Properties of Carbon Nanomaterials Produced by Ultrashort Pulsed Laser Irradiation

by

Michal John Wesolowski

A thesis
presented to the University of Waterloo
in fulfillment of the
thesis requirement for the degree of
Doctor of Philosophy
in
Physics

Waterloo, Ontario, Canada, 2012

AUTHOR'S DECLARATION

I hereby declare that I am the sole author of this thesis. This is a true copy of the thesis, including any required final revisions, as accepted by my examiners. I understand that my thesis may be made electronically available to the public.

Abstract

Two synthesis pathways were employed throughout this work to create a variety of unique carbon materials. The first of these routes involves the photo-dissociation of liquids by direct irradiation with ultrashort laser pulses; while the second entails the bombardment of polycrystalline chemical layers by a pulsed laser induced carbon plasma.

The pulsed laser irradiation (PLI) of liquid benzene (C_6H_6) was found to result in the formation of amorphous carbon nanoparticles consisting of clusters of sp^2-bonded aromatic rings bridged by *sp* hybridized polyyne functionalities. In a complimentary experiment, liquid toluene ($C_6H_5CH_3$) was irradiated under similar conditions leading to the synthesis of a series of free floating methyl capped polyynes, with chain lengths ranging from $C_{10} - C_{20}$. The synthesis of polyynes is an active and cutting edge topic in material science and chemistry. In a more complex experiment, solutions of ferrocene and benzene were irradiated by fs-laser pulses resulting in highly ordered mesoscale structures exhibiting four unique geometries; ribbons, loops, tubes, and hollow spherical shells. After a purification process, the higher order structures were destroyed and replaced with nanoparticles consisting of three distinct species including; pure iron, and two phases in which part of the ferrocene molecule was bound to either carbon or iron/carbon complexes. This material is extremely interesting because it exhibits properties similar to that of an electret and is also ferromagnetic over a large temperature range. In the final liquid phase laser irradiation experiment, a new hybrid deposition technique was originated and used to coat stainless steel electrodes with disordered mesoporous nanocrystalline graphite. This method involves the laser induced breakdown of benzene and the subsequent electrodeposition of the resulting carbon ions.

Another focus in this work involved the synthesis of a special class of polymer-like carbon nanomaterials using a new method that augments traditional pulsed laser deposition. This technique involves the plasma processing of frozen materials with a pulsed laser initiated graphitic plasma. We call this technique "pulsed laser induced plasma processing" or "PLIPP". Various thin film compositions were created by processing alkane and alkene ices. Finally, in a slight departure from the previous experiments, the effects of carbon ion bombardment on water ice were examined in an effort to understand certain astrophysical processes.

Acknowledgements

I would like to acknowledge all of those who have lent me their knowledge, support and companionship over the course of my doctoral work. Firstly, I would like to thank my supervisor Dr. W.W. Duley for introducing me to a fascinating subject that involves aspects of astronomy, physics, chemistry and materials science and for allowing me to chart my own research course while offering guidance and encouragement when needed. Special thanks also go Dr. J.H Sanderson, for access to his laser system, collaboration and many helpful discussions. I would also like to thank the rest of my advisory committee, Dr. K. Bizheva and Dr. M. Mayer for showing enthusiasm in my work, taking the time to meet with me when questions arose and for their informative comments and helpful discussions.

I will be forever grateful to the “Laser Wizards” in Dr. Sanderson’s lab, Reza Karimi and Benji Wales for spending countless hours with me in the lab running and optimizing the Ti:Sapphire, troubleshooting all of her problems and fixing her when she decided to go on vacation for months at a time. I wouldn’t have been able to complete my doctoral work without you guys. I’d also like to thank all of my cohorts in Dr. Duley’s lab, Dr. A. Hu, Stan Kuzmin, and Dr. A. Zaidi for their guidance, and many fun and enlightening discussions. I am also indebted to Brad Moores, Chad Daley and Dr. Z. Leonenko for their collaborations and help with characterizing many of the materials that I have synthesized over the course of my time at UW.

My thanks also goes out to the many great friends I have made over the course of the last 5 years. You have all helped to keep my sanity in check in so many different ways; by sharing a drink with me on the weekend, enjoying a summers day with me on the links, or by helping me fulfill my hoop dreams (Go Demons), I appreciate you all more than I can ever express.

For their unwavering love support and guidance I thank my mother, father and brother from the bottom of my heart. I would not be the person I am today without you three. Finally, for her patience, love and support I thank my everlasting love Debra.

Table of Contents

List of Figures

List of Tables

Chapter 1
Introduction

Nanomaterials research has seen a rapid expansion in the first decade of the twenty-first century, developing into an extremely vibrant field that spans all major scientific disciplines from biology to engineering. A nanomaterial is typically defined as any substance that has at least one physical dimension between 1 and 100 nanometers (nm). At this scale the veil between the classical and quantum worlds begins to fade and as a consequence the well established bulk characteristics of materials become somewhat capricious. For example, as its layers are stripped away and graphite transforms into multi and then single layer graphene its behavior changes from that of a semimetal to that of a zero-gap semiconductor [1]. It is this type of scale dependence and the coinciding discovery of new properties in common materials that has fuelled the rapid development of the field. While numerous nanomaterials have now been discovered they can all be loosely categorized as either carbonaceous, metallic, or composite. Carbon is the fourth most abundant element in the universe. It readily forms strong covalent bonds and as a consequence a large majority of known compounds are carbon based. It is not surprising, therefore, that naturally occurring carbon nanomaterials are also abundant and exist in many different forms. In addition to their natural counterparts these materials can also be readily synthesized and tailored in the laboratory environment and as such have been the focus of a significant amount of research in nanoscience and technology. Thus this thesis is devoted wholly to the carbon branch of nanoscience. More specifically, the focus of this work is on the formation and study of carbon based nanomaterials synthesized through the interaction of femtosecond (fs) laser pulses and matter.

In this primary chapter we follow the advice of the King in Lewis Carroll's *Alice's Adventures in Wonderland* and "begin at the beginning" with a brief history of the development of carbon nanoscience. This is followed by an outline of chemical bonding in carbon materials and a description of the carbon phase diagram. In the section three of this chapter a detailed description of the structure and properties of amorphous carbon is presented. The final section provides an overview of the current project and an outline of the various topics covered in this thesis.

1.1 Historical Perspectives

While the study of nanomaterials is a relatively new branch of science, humans have unwittingly been using them and exploiting their unique properties for millennia. From ancient Egypt [2] to pre-Columbian Mesoamerica [3], the peoples of antiquity were able to synthesize nanostructures even though they lacked a fundamental understanding of the chemical processes used to create them. An intriguing example of this is found in blades crafted from Damascus steel. These weapons developed a legendary reputation during the middle ages due in part to their characteristic wavy patterning, mechanical strength and flexibility and their ability to hold an edge. While the technique used to forge these blades has since been lost, analysis of a seventeenth century Damascus sabre has shown the presence of cementite (Fe_3C) nanowires encapsulated by carbon nanotubes[4]. These carbonaceous inclusions are likely responsible for the blades special mechanical properties. This finding is quite surprising since it appears that medieval blacksmiths were producing nanotubes some four hundred years before they were discovered by modern scientists. Numerous other examples of nanomaterials developed in the ancient world have also been uncovered recently [5-7] however it was not until the mid-nineteenth century that humans began to make serious strides in the scientific study of these materials.

Michael Faraday, in his seminal Bakerian Lecture to the Royal Society in 1857, presented what is considered the first rigorous study on the nature of nanomaterials [8]. Throughout the previous year, in an effort to develop a greater understanding of the nature of light and color, Faraday studied the optical nature of gold [9]. His experiments with gold leaf thin films and colloidal gold, and their interaction with rays of light, showed conclusively that the optical properties of these materials were scale dependent. Investigations of the properties of colloids and thin films continued into the late nineteenth and early twentieth centuries however they were constrained by the limits of that era's technology. It would take a number of theoretical and technological breakthroughs in the first half of the twentieth century to usher in the modern era of materials science and nanotechnology.

The developments of X-Ray crystallography in the 1910s and electron microscopy in the 1930s had a profound effect on our understanding of materials and their nanostructures [10-12]. X-Ray crystallography allowed researchers to study the structure of molecules and deduce the unit cells of crystals while electron microscopy revealed a strange landscape past the diffraction limit in which the morphology of nanomaterials became clear. Advances in spectroscopy during this time, such as

the discovery of the Raman effect, also contributed greatly to the development of nanoscience. It is in this exciting age of exploration that the modern study of carbon materials began.

Pure molecular carbon exists in a number of configurations. These various allotropic forms have unique properties that depend solely on their molecular bonding structure. For example, two of the most well-known carbon allotropes are diamond and graphite. Diamond is mechanically hard, optically transparent and electrically insulating. Conversely, graphite is mechanically soft, optically opaque and electrically conductive. It has been known since the late eighteenth century that both of these materials are equally composed of carbon [13]. How then might they both have the same elemental composition and yet differ in character so greatly? The answer eluded scholars until X-Ray analysis of both materials was completed in the early twentieth century. In 1913, the father and son team of W. H. And W. L. Bragg [14] determined that the arrangement of atoms in a diamond lattice is tetrahedral, with a C-C bond spacing of 0.152 nm. Roughly a decade later in 1924, a student of W.H. Bragg named J.D. Bernal determined the structure of single crystal graphite [15]. While others, using X-Ray diffraction on graphitic powders, had suggested that graphite had a hexagonal lattice it was Bernal who conclusively showed the hexagonal intra-planar and stacked inter-planar structures of the material. Thus it became clear why the mechanical properties of diamond and graphite varied so greatly. In diamond, carbon is bound together in all directions with single covalent bonds, making it an extremely strong bulk material. Graphite, on the other hand, has strong intra-planar bonds however weak van der Waals forces keep adjacent planes together allowing for the material to easily shear and flake. Until the mid-twentieth century diamond and graphite were thought to be the only true allotropes of carbon that existed. This view changed rapidly as new material synthesis techniques became available.

In the late 1960s two new types of carbon were identified. Cowlard and Lewis first synthesized what they called vitreous or glassy carbon (g-C) in 1967 [16]. It was prepared by the thermal degradation of selected organic polymers. These films had an appearance and gas permeability similar to that of glass, however were set apart from it in that they were even less chemically reactive and had a higher mechanical strength. This has made g-C an ideal material for making crucibles as well as coatings for some electronics. The first works on a new form of diamond with a hexagonal lattice structure were also presented in 1967. Hexagonal diamond was first synthesized by two scientists from the General Electric Company named Bundy and Kasper [17]. It was formed through the shock treatment and thermal quenching of single crystalline graphite. Almost

simultaneously, lonsdaleite, a naturally occurring form of hexagonal diamond was identified by Frondel and Marvin who found it in large concentrations in meteorites from Canyon Diablo [18].

The fifth carbon allotrope was discovered soon after the discovery of g-C and hexagonal diamond. In the early 1970s Aisenberg and Chabot [19] used ion-beam deposition to make thin films of amorphous carbon that shared many of the properties of diamond such as transparency, mechanical strength, high electrical resistance, and chemical inertness. As a result this material was labeled tetrahedral amorphous carbon (ta-C) or diamond-like carbon (DLC). Subsequent work in this field has shown that ta-C is actually a subclass of a much broader class of carbon materials known generally as amorphous carbon (a-C). This class of carbon has been studied intensively since its discovery and comes in a variety of forms. The properties of pure a-C, depending on the technique used to synthesize it, can range from diamond-like to those of graphite. With the implantation of hydrogen into the carbon matrix, hydrogenated amorphous carbon (a-C: H), increasingly becomes more polymer-like. It is this ability to easily tailor the properties of a-C that has made it one of the most studied carbon nanomaterials and one of the few to date that has been used in mainstream applications. The nature of a-C materials will be further explored later in this chapter.

A sixth class of carbon was discovered in the mid-1980s by Kroto, Heath, O'Brien, Curl and Smalley [20]. Buckminsterfullerene (C_{60}) was created by the vaporization of graphite using laser irradiation. As a by-product of intense laser matter interaction, vaporized carbon that was stabilized in helium gas was examined using time of flight mass spectroscopy (TOF-MS). Kroto and coworkers found that the carbon plasma was partially composed of stable clusters consisting of 60 carbon atoms arranged in an icosahedron, a polygon with 12 pentagonal and 20 hexagonal faces. These clusters form part of a large class of carbon allotropes called fullerenes which may generally be thought of as cage like molecules that form into spheres, ellipsoids or tubes. Aside from C_{60}, carbon nanotubes (CNT) are likely the most well know of the fullerenes. As mentioned previously they have been fabricated for hundreds of years [4] and have been found to occur naturally in anything from combustion products [21] to ancient meteorites [22]. In the modern era, Iijima is generally credited with their discovery in 1991 [23], however the truth of who actually discovered CNT is somewhat murky [24]. Interest in the fabrication and study of tubular nanoscale carbon filaments has waxed and waned in the scientific community since the early days of the TEM in the 1950s and it is likely that a Russian group was the first to publish result on the topic [24]. Regardless of who discovered them,

Iijima's work sparked the scientific community's interest in CNT and since that time research into their synthesis, properties and applications has comprised a large portion of carbon materials science.

In addition to CNT a number of more exotic forms of carbon have also been identified and examined in the last two decades. In the latter half of the 1990s Rode and coworkers developed low density cluster assembled carbon nanofoam using ultrafast laser ablation [25]. Work with polyynes has potentially paved the road to single crystals of linear acetylenic carbon (LAC) a carbon allotrope that has been envisioned since the 1960s [26, 27]. Most recently, single layer graphite, more commonly known as graphene has garnered a great deal of attention since it was shown that it could be fabricated with nothing more than flakes of graphite and a roll of tape [28]. Taken together all of the aforementioned materials form the diverse base of carbon nanoscience. In the next section of this chapter the nature of carbon bonding and the relationship between those bonds and the various types of carbon materials is explored.

1.2 Carbon Bonding & Phase Transitions

Valence bond (VB) theory is typically employed to describe the structure of carbon materials because it provides a simple qualitative picture of molecular bonding. In basic VB theory, the overlap of pure atomic orbitals (AO) between participating atoms results in the formation of molecular bonds. This approach, however, does not sufficiently account for the structure of certain molecules like methane (CH_4) and therefore the concept of AO hybridization must be employed [29]. A hybrid AO is formed by the linear mixing of two atomic wavefunctions, for example one *s* and one *p* orbital can be combined to form two *sp* hybridized orbitals, as in Figure 1.1a. An unbound carbon atom has a ground state configuration of $1s^2\ 2s^2\ 2p^2$, with two free electrons able to form bonds. In order to form additional bonds an electron must be promoted from the 2*s* valence shell $1s^2\ 2s^2\ 2p^2 \rightarrow 1s^2\ 2s\ 2p^3$, thus freeing four electrons for bonding and leading to orbital hybridization. Figure 1.1 (b-d) shows the three hybridized states, *sp*, sp^2 and sp^3, in which a bound carbon atom can exist. The formation of two *sp* hybridized orbitals by the mixing of one *s* orbital with one *p* orbital leaves two unhybridized *p* orbitals additionally available for bonding. Molecular bonds that occur along the inter-nuclear axis are referred to as σ bonds while those with electron density situated in lobes normal to the axis are called π bonds. In carbon molecules σ and π states behave rather differently and may be dealt with separately. Carbon σ states form into networks of two centered bonds by the lengthwise overlap of

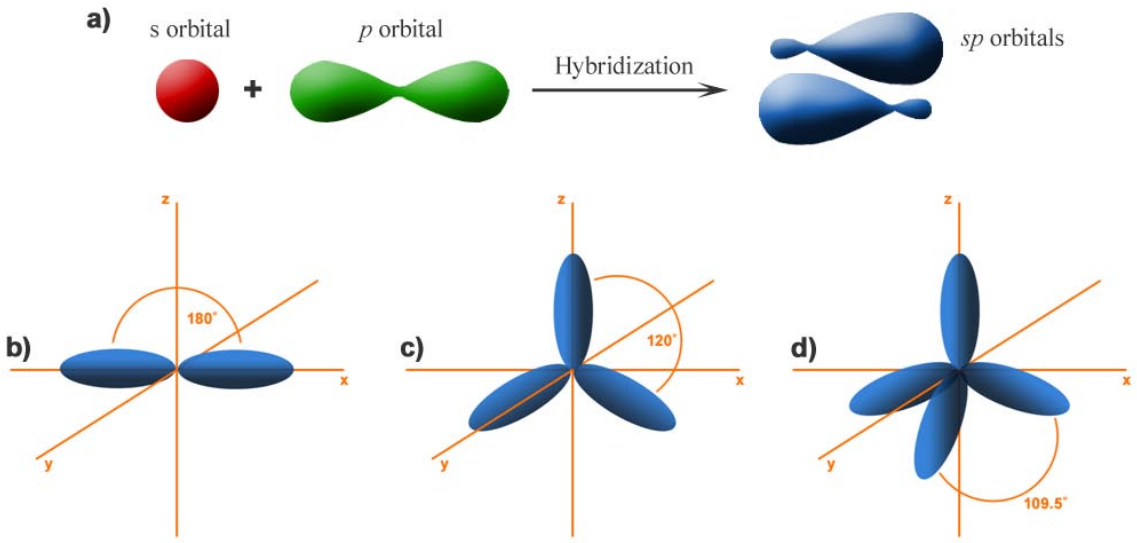

Figure 1.1 - A representation of atomic orbital hybridization is shown in a) along with the various types of hybrid orbitals that occur in carbon materials including b) linear sp, c) trigonal sp^2, and d) tetrahedral sp^3.

two hybridized orbitals. The occupied wavefunction may therefore be expressed as the symmetric combination of bond orbitals,

$$\sigma = \frac{1}{\sqrt{2}}(\varphi_1 + \varphi_2) \tag{1.1}$$

In turn the properties and total energy of the overall occupied σ state can be written as the sum of these independent short range terms. This is not typically the case for π bonds which form between two unhybridized *p* orbitals. These types of bonds can form between multiple neighbors or in continuous conjugated linkages effectively allowing electrons in these orbitals to become delocalized and lead to long range electronic ordering. In this case it is not possible to separate the individual contributions of these bonds to the overall state of the system and therefore it may be written only in general terms as

$$\pi = \sum_i c_i \varphi_i \tag{1.2}$$

A *sp* bonded molecule, such as a polyyne, has a linear structure (180° bond angle) comprised of alternating single and triple bonds. The triple bonds result from one σ bond and two π bonds. Trigonal planar carbon molecules like benzene (120° bond angle) have alternating single and double bonds resulting from bonding between sp^2 orbitals. These hybrid orbitals are formed by the mixing of one *s* orbital and two *p* orbitals. This is one example of a conjugated system with delocalized electrons. Molecules with a fully σ bonded tetrahedral structure (109.5° bond angle) result from sp^3 hybrid bonds which in turn form by the mixing of one *s* orbital and three *p* orbitals. All forms of carbon are assembled from some combination of these hybridized states. Figure 1.3 shows the various carbon allotropes grouped together according to their bond hybridization. The majority of carbon allotropes are either purely sp^2 or sp^3 bonded, however, some like carbon nanofoam or amorphous carbon are assembled from a network containing multiple hybridized states.

Phase transitions between the various states of carbon occur over a wide range of temperatures and pressures and these can be summarized in a P-T diagram. Figure 1.3 shows the thermodynamically stable and metastable phases of bulk carbon as well as their reaction dynamics at high pressures and temperatures adapted from the works of Bundy [30] and Yang [31]. One of its key features is the well established Berman-Simon line that separates the solid phase of graphite (G) from that of diamond (D). Below the line G is thermodynamically stable while the same is true for D above the line. It is of course possible for diamond to exist in a metastable state at standard pressure however if it is heated above a certain temperature its bonds rearrange into those of a graphitic lattice. The analogous first order transition from graphite to diamond can also occur at high pressure. There are a number of these metastable reaction pathways which are indicated on the figure. A reversible phase transition occurs on reaction pathway A when hexagonal graphite is compressed along the c direction at room temperature. In this situation, as pressure is increased G, maintains its compressed structure until roughly 15 GPa after which point it begins to lose some of its characteristic properties such as conductivity and optical opacity. At pressures greater than 23 GPa its Raman spectrum also changes and becomes similar to that of amorphous carbon indicating the partial reversible transformation of hex G to hex D. At 45 GPa if compressed graphite is flash heated from room temperature to roughly 2000 K it then undergoes an irreversible transition to that of cubic D. The grey

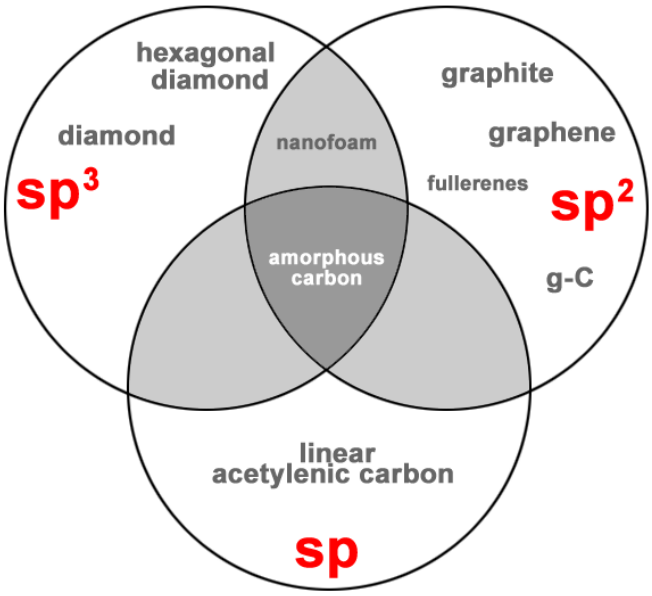

Figure 1.2 - The different carbon allotropes as they relate to bond hybridization. Carbon nanofoam and amorphous carbon are formed from more than one type of hybrid bond.

dotted line marks the activation energy threshold for shock transformations of compressed graphite or hexagonal diamond into thermodynamically stable cubic diamond. The second reaction pathway describes the transition from G to thermodynamically stable hexagonal D. Single crystal hexagonal G gradually transforms into retrievable hexagonal D along reaction pathway B at stresses of 12GPa and annealing temperatures between 800-2000K. There is an upper temperature limit past which hexagonal diamond cannot be retrieved as it transforms into cubic diamond. Commercial synthesis of diamond from graphite occurs in region C but this is not truly a solid-solid phase transition since there is an intermediate step in the fabrication technique in which graphite is dissolved in an ambient catalytic fluid. The end result is; however, the formation of solid diamond. As temperature rises, both D and G melt to form liquid carbon, and the D/G/L triple point for this transition occurs at 5000 K and 12 GPa [30]. While it has been suggested that a number of distinguishable liquid carbon phases exist, experimental results on its electrical properties at various temperatures and pressures have proven contradictory and there is most likely only a single conductive form of liquid carbon. The dependence of the D/G/L triple point on material size has recently been examined by Yang et al. [31]. It was found that as bulk D or G was reduced to the nanoscale the pressure and temperature required

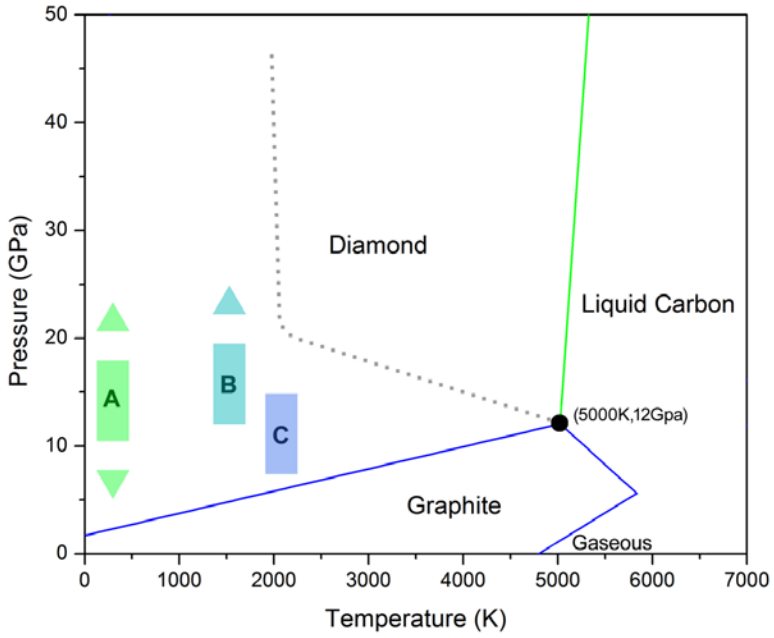

Figure 1.3 - The carbon phase diagram showing thermodynamically stable and metastable states and reaction pathways (A, B, C). Adapted from the works of Bundy and Yang [30, 31].

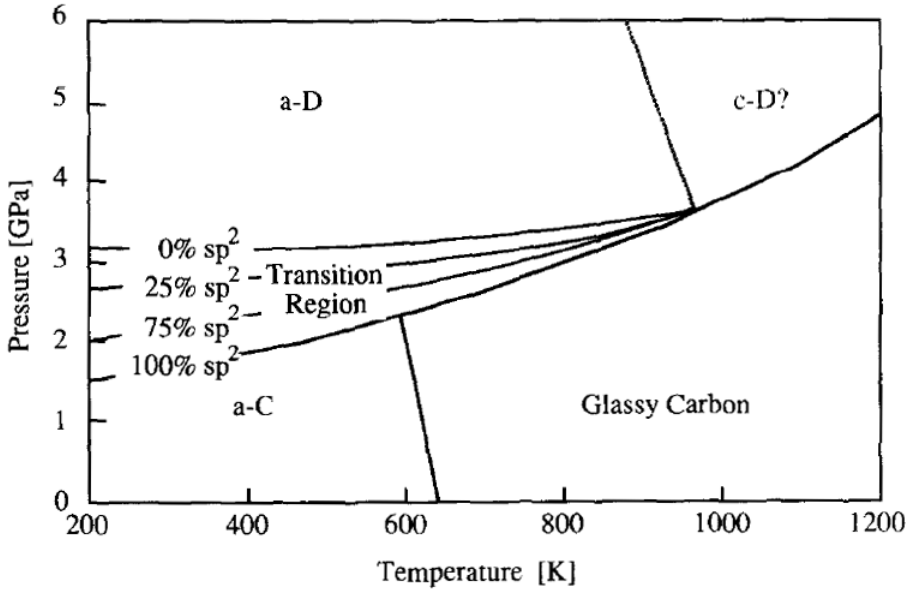

Figure 1.4 - Schematic amorphous carbon phase diagram developed by McKenzie [32]. Above the Berman-Simon line sp^3 amorphous diamond (a-D) occurs while below the line sp^2 amorphous carbon (a-C) is formed. A transition region is also present between purely sp^2 and sp^3.

to melt these materials decreased. The D/G/L triple point for carbon particles with a diameter of 5nm occurs at 4968K and 9.05GPa while particles of 2nm diameter have a triple point at 4000K and 2.74Gpa. The G/D transition line also shifts towards lower temperature and pressure suggesting that, on the nanoscale, diamond is much more thermodynamically stable than graphite.

The low pressure region of the PT diagram of carbon is also of interest. At pressures between 0.01-0.1 GPa and temperatures approaching 5000K graphite vaporizes. However the triple point at which this occurs has only been established to within a few hundred Kelvin (4800 ± 100K, 0.01-0.1GPa). It has also been suggested that a transformation from graphite to solid carbyne occurs in this region just before the melting point of graphite but evidence for this has proven tenuous.

The conditions under which another form of allotropic carbon, amorphous carbon, is typically synthesized are found in the low temperature and pressure region of the PT diagram near the Berman-Simon line. McKenzie et al. [32] developed the phase diagram of metastable amorphous carbon using vacuum arc deposited thin films (Figure 1.4). The internal hydrostatic component of stress was examined as a function of film growth temperature for a variety of films ranging from amorphous diamond (a-D) which is purely sp^3 bonded to purely sp^2 bonded amorphous carbon (a-C). There was found to be a general trend of increased crystalline ordering with increasing temperature but the materials remained amorphous at low temperature. The behaviour of a-C was found to follow the previously established Berman-Simon line exactly, with a-D always occurring at pressures well above the line and a-C occurring at pressures well below it.

1.3 Amorphous Carbon

Depending on the conditions in which it is created, amorphous carbon may have character that is graphite-like (GLC), diamond-like (DLC), or with the addition of hydrogen, polymer-like (PLC). The transition between these three types of *a*-C is not stepwise; rather it is a continuous transition between intermediary forms composed of varying amounts of sp, sp^2, sp^3 bonded carbon and hydrogen. A ternary phase diagram, such as the one presented in Figure 1.5, is typically used to illustrate the relationship between the types of *a*-C and their hybridization or hydrogen content [33, 34]. At the highest levels of sp^3 amorphization (~ 85%), *a*-C is referred to as tetrahedral amorphous carbon (*ta*-C). Thin films made from this material have a density (3.2 g/cm^3), hardness (45-88 GPa), index of refraction (~2.5) and resistivity (10^{10} Ωm) similar to that of diamond [35-37]. The maximum optical band gap of *ta*-C (3.5 eV) differs from that of diamond by approximately 2 eV [38]. This is not

surprising, given that even at the largest sp^3 concentrations; *ta*-C is still partially composed of sp^2 carbon chains (~15%). This has the effect of lowering the optical band gap energy compared to the purely σ-bonded sp^3 diamond system. DLC is of practical interest because of its high hardness and wear resistance and a low friction coefficient making it an ideal coating material for engineering and biomedical applications.

As the amorphization trajectory moves toward the lower left-hand corner of the ternary phase diagram, the sp^3 bonds of *ta*-C are increasingly replaced by sp^2 carbon in rings and chains. At the lowest levels of sp^3 bonding (5-20%), a-C is composed mainly of large clusters of disordered sp^2 rings resulting in a densities (1.6-2.2 g/cm^3), optical gap (0.4-0.8 eV) and resistivities (10^{-3}-10^2 Ωm) that are much closer to those of graphite [34, 39, 40]. The hardness of these materials (3-13GPa) is still an order of magnitude higher than that of graphite [34, 40]. In fact, recent experiments have shown that it is possible to synthesize hydrogen free GLC with comparable hardness to that of DLC (50 GPa) by magnetron sputtering [41]. These films are comprised of highly stressed sp^2 structures with an inter-planar spacing, d_{002} = 0.295-0.305nm, resulting from intrinsic stress induced by ion bombardment. This type of material is currently being utilized as a solid lubricant in the automotive industry and could also be used in future electronic applications. The addition of reactive hydrogen or hydrocarbons during the synthesis of a-C results in the inclusion of hydrogen in the a-C matrix and is represented on the right side of the ternary phase diagram. These materials are typically referred to as hydrogenated amorphous carbon or a-C:H. The effect of hydrogenation on the properties of a-C:H thin films has been well documented by Robertson and Ferrari in a number of review articles [34, 39].

As hydrogen content increases the continuous C-C network forming the backbone of a-C changes. Most sp^3 sites become saturated with one or more H atoms and sp^2 sites exist as small clusters within the new C-H matrix as is represented schematically in Figure 1.6. While *sp* chains do exist as part of a-C:H they typically have small concentrations (~10%) and can be excluded to the first order [39]. There are a number of distinguishable types of a-C:H that depend on the amount of H that has been incorporated into their structures. If low levels of H (10-20%) are added to GLC or a-C, some of the sp^2 C=C bonds become saturated by H forming $\equiv CH_x$ groups rather than forming C-C bonds [39] however the majority are still in the form of unsaturated sp^2 rings and chains. These materials have an optical band gap that is lower than 1eV. At intermediate levels of H (20-40%) a-C:H reaches its most diamond-like character with a maximal density, C-C sp^3 bonding percentage and an optical gap that typically lies between 1-1.8 eV. Increasing the H content even further ($\geq$ 40%) leads to a reduction in sp^2 cluster size and an additional increase in the optical band gap (1.8-4eV).

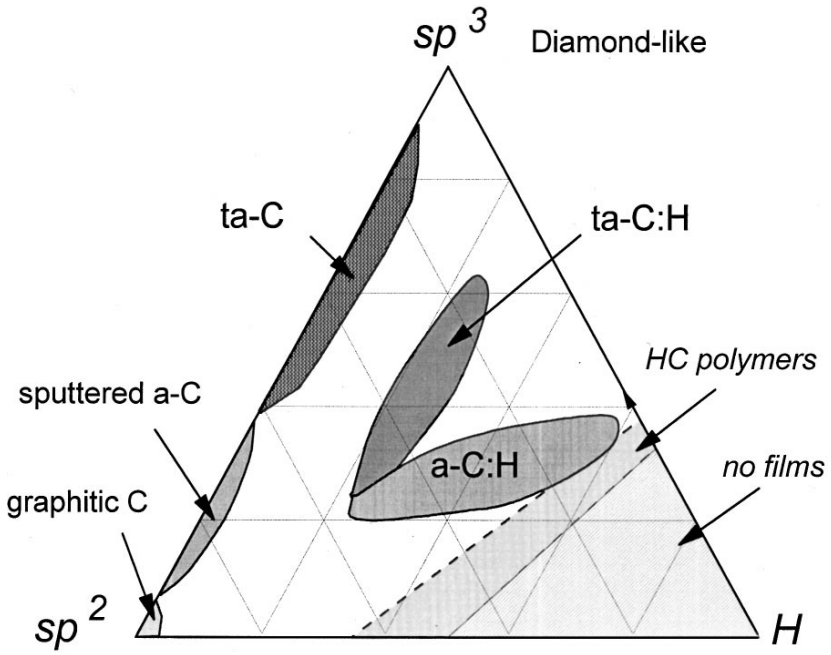

Figure 1.5 - Ternary phase diagram of amorphous carbon [34]. DLC has the highest sp^3 content while GLC has the highest sp^2 content and PLC has the largest amount of hydrogen. Mixed carbon materials occur in most other areas of the diagram.

This soft material is highly polymer-like (PLC) with a large amount of sp^3 bonded CH (60%) a low density (1.2-1.6 g/cm^3) and has been suggested for use is optics as well as electronic applications [39].

In addition to these three types of a-C:H derived from graphite-like carbon a more diamond-like a-C:H has also been synthesized. Under specific conditions, low levels of hydrogen (~10%) can be incorporated into *ta*-C making hydrogenated tetrahedral amorphous carbon (*ta*-C:H). This material is distinguishable from the other types of a-C:H with equal hydrogen content in that it has a much larger percentage of C-C sp^3 bonds (75%). As such it has a higher density (2.4 g/cm^3), hardness (50 GPa) and optical gap (2-3eV) than its counterparts [34, 42]. A variety of other a-C materials such as the nitrogenated analogues of a-C:H have also been studied extensively [43], however; they do not significantly alter the overall description of a-C and ultimately are beyond the scope of this work.

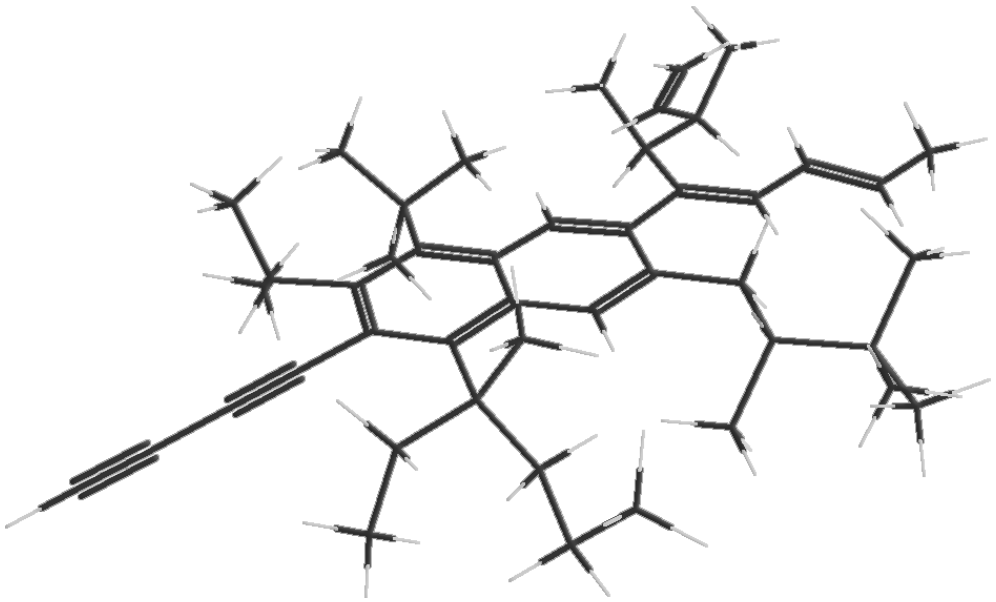

Figure 1.6 - A representative hydrogenated amorphous carbon (a-C:H) structure with *sp*, sp^2 and sp^3 domains.

In general, it is clear that the mechanical, optical and electronic properties of a-C are governed by its microstructure. Accordingly, the three most important microstructural parameters are the sp^2/sp^3 ratio, ordering of sp^2 sites and the concentration of H in the a-C matrix. These parameters are in turn controlled by the choice of synthesis technique and the conditions under which synthesis takes place. There are several techniques available for the production of a-C materials, including ion deposition, vacuum arc, magnetron sputtering, plasma or pulsed laser deposition [40, 44-47]. Of these various techniques, pulsed laser deposition (PLD) offers a number of advantages [48]. A prime advantage is that it is a simple technique that can be applied in vacuum or in gaseous and liquid environments. This allows the formation of a range of a-C and a-C:H materials from all regions of the ternary phase diagram in addition to a variety of other composite carbon materials. Given these advantages and the availability of ultrafast pulsed lasers, PLD is the technique used in the present work; an overview of which is given in the next section of this chapter.

1.4 Overview of the Present Work

The search for new materials and the synthesis techniques used to create them is the main catalyst that drives the advancement of material science. From metallic nanoparticles recruited in the

fight against cancer [49] to carbon nanotubes that may someday provide an inexpensive passageway to the cosmos [50], each newly discovered substance has the potential to dramatically affect human civilization. Keeping that in mind, the main purpose of the present work is the creation and characterization of new carbon based nanomaterials. While there are many methods currently used to synthesize nanomaterials, none are perhaps more dramatic than those facilitated by pulsed lasers. A focused femtosecond laser beam can reach an intensity quadrillions of times higher than that of sunlight striking the Earth. The interaction of such a beam with matter creates conditions that are unique in the universe, stripping atoms of their electrons and causing material breakdown through Coulomb explosion [51]. The theoretical underpinnings that describe these interactions are presented in Chapter 2.

The high energy plasma ejected from a Coulomb explosion is a complex mixture of electrons, ions and neutral atoms that can interact with each other and their environment to form materials that are distinct from their progenitors [47]. Ultimately the properties of these newly formed substances depend on three factors: laser parameters, target material and deposition environment. The parameters of the fs-laser system used throughout my research are outlined in Chapter 3. Also described in this chapter are the many instruments used to characterize the cutting-edge materials that have been synthesized over the course of my doctoral work. The main portion of this thesis concerns the results of that work and is organized into the two chapters that follow Chapter 3.

Chapter 4 deals with the fs-laser irradiation of liquid media. This is an exciting new branch of material science that involves photo-induced plasma chemistry at extreme pressures and temperatures. The first two sections of this chapter are dedicated to the synthesis of straight chain carbon molecules, called polyynes, through the irradiation of a variety of organic liquids. Polyyne synthesis has garnered considerable attention recently because these molecules are thought to be both conductive and rigid [52, 53]. This makes them ideal candidates for components in molecular electronics applications. The final section of Chapter 4 describes the effect of fs-laser irradiation on solutions of ferrocene and benzene. The result of this experiment was the creation of an iron-carbon hybrid nanomaterial with many surprising properties; not the least of which is self-organization. This mysterious black powder appears to be a wholly new substance and a variety of characterization techniques were employed to clarify its composition, structure and properties. Moving away from the irradiation of liquids, Chapter 5 introduces a novel technique that has been developed for the creation of carbon thin films. It involves the processing of frozen materials with plasma created by the pulsed

laser ablation of graphite. Water, its deuterated counterpart and a variety of hydrocarbons have been processed using this method resulting in the deposition of a new form of polymer-like amorphous carbon that is partly comprised of precursory molecules. These carbonaceous deposits have tailored physical and chemical properties based on networks of sp^2 rings separated by specific distances and could be implemented in molecular sieve or gas separation applications.

Overall a considerable amount of research has been undertaken in completion of this work; new materials have been discovered and novel synthesis techniques have been developed. Chapter 6 serves as a summary of all of this research and also approaches the issue of future work. The chapter concludes with a discussion of the potential impact these new materials may have on society and suggests ways in which they could be implemented in scientific and technical applications.

Chapter 2
Light-Matter Interactions and Material Synthesis

The interplay between light and matter lies at the heart of pulsed laser material synthesis. In this chapter, we explore some mechanisms that govern the interaction between ultra-short laser pulses and materials. The photo-induced ionization and dissociation of opaque media by high intensity fs-laser pulses is described in Section 2.1. At high intensities this process leads to the removal of material from a target surface by Coulomb explosion and the subsequent formation of plasma which may then be used for in the synthesis of nano-materials. The plasma created after fs ablation of graphite is described in Section 2.2 and thin film growth mechanisms are detailed in Section 2.3. In transparent dielectrics the spatial zone over which light and matter interact is three dimensional, as opposed to being confined to a surface. At similar intensities this leads to nonlinear optical and acoustic phenomena that are not present in the case of opaque materials. These effects can influence the synthesis process and are described in Section 2.4.

2.1 Interaction of Laser Pulses & Opaque Media

A detailed analytical model of the interaction between fs-laser pulses and opaque materials has been developed over the course of the last twenty years by several authors [54-58]. When a laser pulse is incident on the surface of a solid dielectric, the strength of its electric field $E(x)$ decreases exponentially as the electromagnetic wave penetrates into the material,

$$E(x) = E(0)e^{-x/l_s} \tag{2.1}$$

where l_s is the field penetration length, or skin depth, defined as

$$l_s = \left(\frac{c}{\omega k}\right) \tag{2.2}$$

The skin depth is derived from the imaginary part of the material's refractive index *k*, and the laser frequency ω [58]. The relative permittivity of a solid, which can be used to define its initial state, is expressed as

$$\varepsilon(\omega) = 1 - \frac{\omega_{pe}^2}{\omega\left(\omega + i\nu_{eff}\right)} \tag{2.3}$$

in the dielectric Drude approximation [59]. Here ν_{eff} is the effective collision frequency between electrons and a lattice and ω_{pe} is the electron plasma frequency defined as

$$\omega_{pe} = \left(\frac{4\pi e^2 n_e}{m_e}\right)^{1/2} \tag{2.4}$$

In the ultra-short pulse length regime, the electron plasma frequency and the effective electron lattice collisional frequency are dependent on time and intensity and therefore so is the dielectric permittivity. To understand a materials response to laser irradiation, the dependence of its parameters on the electron and lattice temperatures must first be determined.

The imaginary part of the dielectric function (2.3) is typically of much smaller magnitude than the real part; however, its value may increase due to ionization. There are two prominent mechanisms that can contribute to the ionization of matter in the laser field. These are known as impact-avalanche (*imp*) and multiphoton (*mpi*) ionization. A rate equation describing the contribution of both these mechanisms to the time dependent free electron number density n_e , stripped from atoms in the light-matter interaction zone may be written as,

$$\frac{dn_e}{dt} = n_e w_{imp} + n_a w_{mpi} \tag{2.5}$$

where n_a is the density of neutral atoms, w_{imp} is the time independent probability for avalanche ionization and w_{mpi} is the probability for multiphoton ionization [60, 61]. For the simplified case of single ionization these probabilities may be approximated, having the form

$$w_{imp} \simeq \frac{\varepsilon_{osc}}{J_i}\left(\frac{2\omega^2 \upsilon_{eff}}{\omega^2 + \upsilon_{eff}^2}\right) \tag{2.6}$$

$$w_{mpi} \simeq \omega n_{ph}^{3/2}\left(\frac{\varepsilon_{osc}}{2J_i}\right)^{n_{ph}} \tag{2.7}$$

where ε_{osc} is the electron quiver energy in the laser field J_i, is the ionization potential (eV) and $n_{ph} = J_i/\hbar\omega$ is the number of photons required for ionization in the *mpi* process. The relative contribution of each ionization process to the number density of free electrons clearly depends on the relationship between the quiver energy and the ionization potential. When the quiver energy is greater than the ionization potential the *mpi* process dominates for any relationship between the incident light and the collisional frequencies [58]. The quiver energy may compared to the incident laser intensity by the scaling relation,

$$\varepsilon_{osc}[eV] = 9.3(1+\alpha^2)\frac{I}{10^{14}\left[\frac{W}{cm^2}\right]}(\lambda[\mu m])^2 \tag{2.8}$$

where α accounts for the laser polarization, I is the intensity, and λ is the wavelength. Since the first ionization potential of most dielectrics is typically ~ 10 eV, *mpi* clearly dominates the ionization process at laser intensities above 10^{14} Wcm^{-2}. This is typically the minimum intensity used throughout our experimental work and therefore further discussion is restricted to the *mpi* ionization regime. Figure 2.1 is a schematic representation of *mpi* showing two photon absorption and ionization. The general solution of Eq. (2.5) with the initial conditions $n_e(t=0) = n_0$ is,

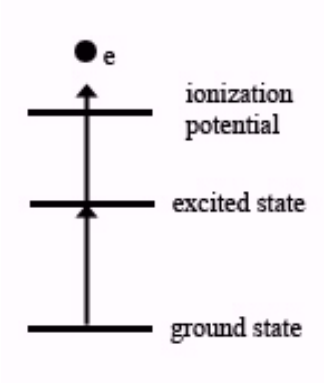

Figure 2.1 - A schematic representation of two photon absorption and ionization.

$$n_e(I,\lambda,t) = \left(n_0 + \frac{n_a w_{mpi}}{w_{mpi}}(1 - e^{-w_{imp}t})\right) e^{w_{imp}t} \tag{2.9}$$

In the *mpi* regime the number of free electrons increases linearly with time and so the time for the first ionization can be shorter than the pulse duration. As suggested in Eq. (2.8) the ionization threshold is dependent on the laser intensity and wavelength and is reached when the electron number density reaches a critical value determined by the incident laser wavelength [61]. When ionization is complete, the plasma formed in the skin layer has a free electron density that may be considered constant and comparable to the ion density which is approximately the density of the solid or ~ 10^{23} cm^{-3} [58].

In order for ablation to occur under fs irradiation conditions, the temperature of the electrons in the skin layer must approach the temperature equivalent of the Fermi energy. Electrons gain energy through optical absorption. Near the ablation threshold, the dielectric function, ε, and refractive index, n, are directly related to the electron plasma frequency

$$\varepsilon' \simeq \frac{\omega^2}{\omega_{pe}^2} \tag{2.10}$$

$$\varepsilon'' \simeq \frac{\omega_{pe}}{\omega}\left(1+\frac{\omega^2}{\omega_{pe}^2}\right)^{-1} \tag{2.11}$$

$$n \simeq k = \left(\frac{\varepsilon''}{2}\right)^{1/2}. \tag{2.12}$$

The absorption coefficient, *A*, of the material at normal incidence can be calculated from the Fresnel [61] formulas and is

$$A = 1 - R \simeq \frac{4n}{(n+1)^2+n^2}. \tag{2.13}$$

The ratio between A and skin depth is only weakly dependent on material parameters and reduces to a simple function of the laser wavelength

$$\frac{A}{l_s} \simeq \frac{2\omega}{c}\left(1+\frac{1}{n}+\frac{1}{2n^2}\right)^{-1} \simeq \frac{2\omega}{c} = \frac{4\pi}{\lambda} \tag{2.14}$$

The energy transfer time between electrons and ions in a dense plasma can be expressed in terms of the electron-ion collisional frequency,

$$\tau_{ei} \simeq \frac{M}{m_e \nu_{ei}} \tag{2.15}$$

where *M* is the atomic mass of the ion and m_e is the electron mass [58]. The collision frequency ν_{ei} (s^{-1}) is estimated for the case of an ideal plasma in which collisions occur due to Coulombic interactions between electrons and ions and is found to relate to the frequency of momentum exchange. Estimates for most materials give an energy transfer time on the order of picoseconds, which suggests that, in

the femtosecond pulse regime, there is no energy transfer between the electrons in the skin layer and ions in the lattice. Thermal diffusion for electrons in the skin layer is described by

$$t_{heat} \simeq \frac{l_s^2}{\kappa} \tag{2.16}$$

and

$$\kappa = \frac{l_e \mathrm{v}_e}{3} \tag{2.17}$$

where κ is the coefficient of thermal diffusion, l_e is the electron mean free path (m), and v_e is the electron velocity (m/s). For dielectrics the electron heat conductivity time, t_{heat}, is on the order of tens of picoseconds which is also much longer than the pulse length. This suggests that, in addition to not being able to transfer energy to the lattice, the electrons cannot transfer energy across and out of the skin layer [62]. The change in electron temperature T_e due to the absorption of laser energy in the skin layer is then derived from the laws of energy conservation

$$c_e(T_e) n_e \frac{\partial T_e}{\partial t} = -\frac{\partial Q}{\partial x} \tag{2.18}$$

$$Q = A I_0 e^{-2x/l_s} \tag{2.19}$$

where n_e is the number density of the electrons, c_e is their specific heat conductivity, Q is the energy flux in the skin layer and $A = I/I_0$ is the absorption coefficient [61]. Solving these equations, while taking the time independent nature of the specific heat, and absorption coefficient into account, gives the spatially dependent electron temperature

$$T_e = \frac{4}{3} \frac{A I_0 t}{l_s n_e} e^{\frac{-2x}{l_s}} \tag{2.20}$$

Once electrons in the skin layer gain sufficient energy (i.e. the Fermi energy), they escape the surface of the solid and an electric field results due to charge separation. The strength of this field, E_a, is directly related to the kinetic energy of the electrons and the gradient of electron density normal to the target surface,

$$E_a = -\frac{\varepsilon_e(t)}{q_e}\frac{\partial \ln(n_e)}{\partial z} \tag{2.21}$$

where ε_e is the electron kinetic energy (J) and q_e is the electron charge (C) [62]. The electric field of the laser beam also produces a pondermotive force, F_{pf}, on the ions in the lattice during the laser pulse where

$$F_{pf} = -\frac{2\pi q_e^2}{m_e c\omega^2}\nabla I \simeq \frac{I}{2n_e c l_s}\frac{\omega_{pe}^2}{\omega^2} \tag{2.22}$$

The time dependent electrostatic force from the charge separation field is given by Coulomb's law

$$F_{el-st} = q_e E_a = -\varepsilon_e(t)\frac{\partial \ln(n_e)}{\partial z} \cong \frac{It}{n l_s l_D} \tag{2.23}$$

where l_D is the Debye length [58]. The ratio of these two forces at the end of the laser pulse is;

$$\left|\frac{F_{pf}}{F_{el-st}}\right| \cong \frac{1}{\omega t_p}\left(\frac{\omega_{pe}}{\omega}\right)\left(\frac{v_e}{c}\right) \tag{2.24}$$

At solid state plasma densities, and with a laser pulse duration of 100 fs the ratio (2.24) is much less than unity, indicating that the pondermotive force does not contribute significantly to the ablation threshold and may be neglected in further calculations. The time necessary to accelerate and therefore remove ions from the surface can be estimated from the required change in ion momentum,

$$\frac{dp_i}{dt} \simeq q_e E_a \tag{2.25}$$

which then leads to

$$t_{acc} = \frac{l_D}{v_i} \simeq \frac{2}{\omega_{pe}} \left(\frac{m_i}{m_e}\right)^{1/2} \left(\frac{T_e - \varepsilon_{esc}}{T_e - \varepsilon_{esc} - \varepsilon_b}\right)^{1/2} \tag{2.26}$$

At energies below the ablation threshold, the time it takes to accelerate the ions out of the target is much longer than the laser pulse duration, but above this threshold, ions may be ablated before the end of the pulse [57, 58]. The minimum energy required for the electron to leave a dielectric target surface is the ionization potential. In order for the electron to additionally drag ions from the surface, it requires additional energy equal to or larger than the ionic binding energy. The threshold fluence required for ablation is therefore

$$I_{th}^{d} = \frac{3}{4}(\varepsilon_b + J_i)\frac{l_s n_e}{A} \tag{2.27}$$

and above this value, in the fs pulse regime, the Coulomb explosion mechanism dominates and plasma production occurs. The ablation threshold for graphite, which is the primary solid carbon source used in this work, has been determined to be ~6×10^{11} W cm^{-2} for 100 fs laser pulses [57].

2.2 Dynamics of Graphitic Plasmas

The plasma created after irradiation of graphite with fs laser pulses, which will often be referred to as "graphitic" plasma, has been the topic of several studies [63-66]. The shape of the plasma plume, as a function of time, may be described by the hydrodynamic expansion of a three dimensional ellipsoid [63, 67]. Figure 2.2 shows a schematic of the typical setup for pulsed laser deposition. Just after termination of the laser pulse, t = 0, the plasma has a flat pancake appearance with a diameter corresponding to the laser spot size and a thickness similar to the skin depth. This suggests that the pressure gradient normal to the surface is much larger than the transverse pressure gradient and therefore plasma expansion occurs primarily normal to the surface. The plasma expansion may described by the equations of gas dynamics [67],

$$\frac{\partial \rho}{\partial t} + \nabla \cdot (\rho \boldsymbol{v}) = 0, \tag{2.28}$$

$$\frac{\partial \boldsymbol{v}}{\partial t} + (\boldsymbol{v}\nabla)\boldsymbol{v} + \frac{1}{\rho}\nabla \cdot p = 0, \tag{2.29}$$

$$\frac{\partial S}{\partial t} + (\boldsymbol{v}\nabla)S = 0 \tag{2.30}$$

where, $\rho, v, p,$ and S are the density, velocity, pressure and entropy per unit mass respectively. The plasma expands at a constant normal velocity away from the ablation target and the ratio between the ellipsoidal axes (longitudinal and transverse), *P*, also remains constant. It can therefore be considered to be "collision free" over the course of the expansion.

The material flux through a surface that is parallel to the carbon source and located a distance *z* away from it, may then be written as

$$h(\theta) = \frac{MP^2}{2\pi\rho z^2}(1 + P^2 \tan^2 \theta)^{-\frac{3}{2}} \tag{2.31}$$

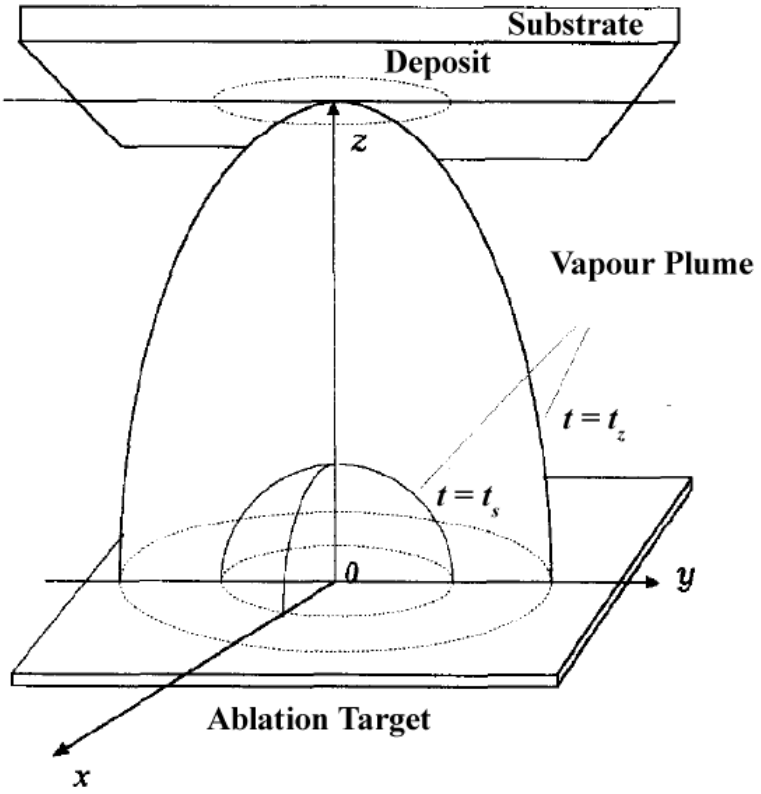

Figure 2.2– Schematic of plasma expansion, in a typical PLD experiment, at two different times. The time at t = ts represents the shape of the plasma shortly after the laser pulse while t = tz represents the plasma as it impacts the substrate [67].

where θ is the observation angle, and M is the mass of the ablated species [63]. In addition to the hydrodynamic model of plasma expansion a variety of experimental techniques have been used to study the composition and kinetic energy of plasma created after fs ablation of graphite.

Optical and UV-VIS plasma emission spectra [66, 68] have shown that the main constituents of these plasmas are neutral C atoms, singly charged C ions and radicals, as well as small clusters like C_2^+, and C_3^+. There is also some evidence suggesting that larger clusters are also present in theses plasmas, however; they have yet to be resolved accurately. The energy of plasma species has usually determined using time of flight mass spectroscopy (TOF-MS) [64, 69]. Figure 2.3 shows the mass spectrum of plasma that resulted from the ablation of graphite with 100 fs pulses of 3×10^{14} Wcm^{-2} intensity [64]. There are two obvious peaks in the spectrum, one of which comes from what have

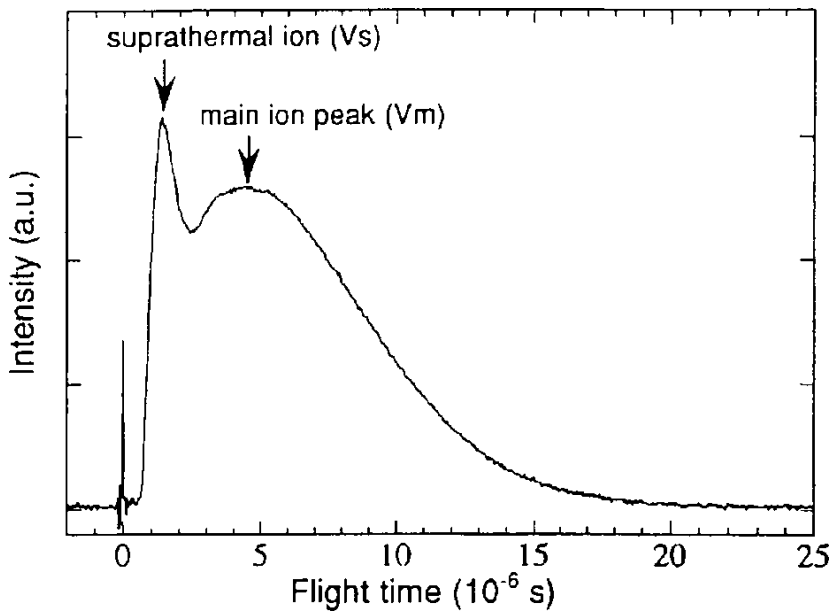

Figure 2.3– Time of flight mass spectrum resulting from ablation of graphite with 100 fs laser pulses at an intensity of 3×10^{14} Wcm^{-2} [64].

been termed "suprathermal" ions by Qian et al. [64] while the other is the main ion peak. The suprathermal ions are thought to be highly charged carbons with energies roughly ten times (3.5 keV) that of ions in the main peak (250 eV). The main ion peak consists of the other plasma species mentioned, typically singly charged carbon ions and clusters. It should be noted that the velocity and therefore the kinetic energy of ablated species has been shown to be dependent on the laser intensity. This relationship is approximately linear from 10^{11}-10^{14} Wcm^{-2} after which point the energy approaches an asymptotic value of 25 keV for suprathermal ions and 2 keV for main peak ions at intensities near 6×10^{15} Wcm^{-2} [64, 69].

2.3 Amorphous Carbon Thin Film Growth Mechanisms

A collisional ion subplantation model is typically employed to describe the deposition and growth of amorphous carbon thin films created through any ion or plasma deposition process. This model was first introduced in the late twentieth century by Lifshitz and coworkers, and has been refined since that time by several authors [34, 70-75].

When hyperthermal plasma species (~10-1000 eV) impinge on a surface they tend to undergo a shallow subsurface implantation process. The cross-section for collisions between incoming species and atoms in the substrate decreases with increasing energy. Ions of higher energy see a smaller potential barrier when approaching the substrate and at some energy E_p, called the penetration threshold, they may pass through an interstice between atoms and penetrate the surface. The ionic penetration depth l, depends mainly on the energy E, of the plasma species and may be approximated as;

$$l(E) \approx c\,(E - E_P)^{1/2} \tag{2.32}$$

where c is a material constant (nm $eV^{-1/2}$) and E_p is penetration threshold in eV [75]. The net penetration threshold is dependent on two other energy values; the displacement threshold E_d, which is the minimum energy required for an incoming ion to displace an atom from a bonded site, and the surface binding energy E_b, which raises the energy of the ion after it enters the surface [34]. The penetration threshold is approximately

$$E_p \sim E_d + E_b. \tag{2.33}$$

For carbon, the displacement threshold is E_d ~ 25eV while the surface binding energy is E_b ~ 7eV, giving a penetration threshold of E_p ~ 32 eV [34]. Thus, according to (2.32) carbon ions with energy equal to or lower than 32 eV will not be able to penetrate the surface and will simply stick to it, remaining in their lowest energy configuration (sp^2). Ions with energies greater than E_p will penetrate the surface and lose their energy mainly through elastic collisions with the subsurface atoms with any excess energy being released as heat. A singly charged carbon ion with an initial kinetic energy of 1 keV will penetrate ~3 nm into the substrate, where it enters an interstitial site and causes a local densification of the subsurface. In the highly energetic environment that exists during ion bombardment it is usually assumed that atomic hybridization in the growing film will adjust readily with changes in local density. Areas where the density is low will favor sp^2 carbon while areas of higher density will become sp^3. This process may be divided into three time scales; the collisional stage at 10^{-13} s, a thermalization stage after 10^{-12} s and relaxation stage at 10^{-10} s.

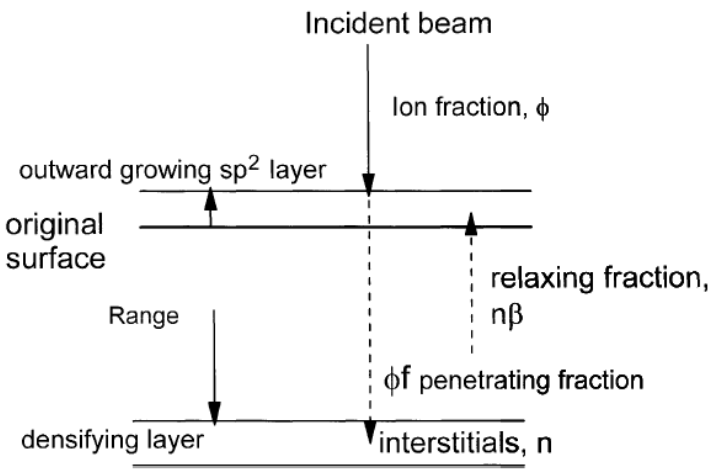

Figure 2.4– Schematic diagram of the subplantation model of amorphous carbon thin film growth [34].

Figure 2.4 outlines the growth process for a plasma of flux F where ϕ is the fraction of ions having kinetic energy E_i [34]. The fraction of ions or atoms that do not have the necessary energy to subplant in the surface may be expressed as

$$a = (1 - f\phi) \tag{2.34}$$

where $f\phi$ is the fraction of ions that can penetrate the surface. A number of the penetrating ions $n\beta$, proportional to the number n of interstitial sites, will relax back to the surface as opposed to implanting. The outwardly growing layer of the film therefore consists of sp^2 bonded carbon while the lowest layers are sp^3 bonded carbon. The area in which relaxation occurs is typically a mixture of sp^2/sp^3 carbon. The overall molecular composition of plasma deposited a-C is therefore dependent on the energy of the incident ions. A plasma with energy near the penetration threshold results in the formation of a graphite-like carbon while plasma of higher energy results in the formation of increasingly diamond-like material. However, there is an ideal range for the synthesis of diamond-like carbon, corresponding to energies of 80-120 eV [72, 76]. At energies above this range ions begin to

cause damage to the sp^3 matrix and facilitate increased diffusion and relaxation to sp^2 bonded material [77].

2.4 Interaction of Laser Pulses & Transparent Media

The intensity dependent ionization mechanism described in the preceding section also governs the material breakdown of transparent media, be they solids, liquids or gases. There are, however, a number of additional phenomena that occur in transparent materials that can have an effect on the formation of nanomaterials. The first of these is laser-induced filamentation. In general, this term is used to denote a dynamic region of laser self-focusing and defocusing that can propagate over distances much greater than the diffraction length [78]. At the focal points the core of a fs-laser filament typically reaches intensities of 10^{13} -10^{14} Wcm^{-2} resulting in ionization of the medium. In terms of material synthesis, this has the effect of dramatically increasing the laser matter interaction volume creating multiple ionization zones along the beam track as shown in Figure 2.5. The formation of a filament is governed by two competing nonlinear physical processes; the optical Kerr effect and multiphoton ionization. The Kerr effect acts to focus the beam and works against beam divergence while multiphoton absorption limits the core intensity and tends to promote defocusing of the beam due to the ionization of the medium and subsequent reduction of the local refractive index.

Electromagnetic beams propagating through free space always tend to diverge. The radius, ω, of a Gaussian laser beam with a planar wavefront is dependent on the propagation distance, x, and may be expressed as [78]

$$\omega(x) = \omega_0 \left(1 + \frac{x}{L_R}\right)^{1/2} \tag{2.35}$$

where ω_0 the beam waist is the minimum value of ω and L_R is the Rayleigh length which corresponds to the distance along the propagation direction from the waist to where the beam cross sectional area is twice as large. This relates directly to laser and material parameters as follows

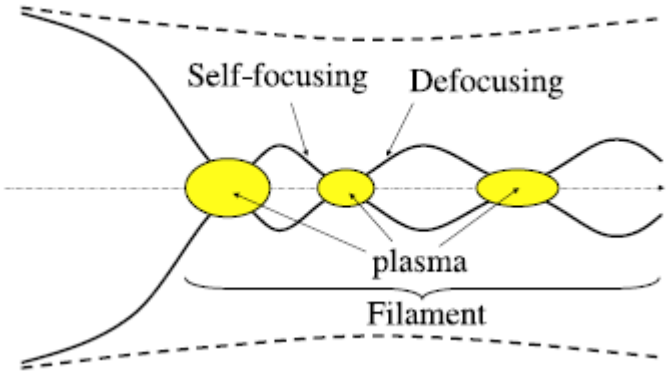

Figure 2.5– A schematic representation of the filamentation process in transparent materials, where the dashed lines represent the beam waist region [78].

$$L_R = \frac{\pi n_0 \omega_0^2}{\lambda_0}, \tag{2.36}$$

where n_0 is the index of refraction of the material through which the laser beam of wavelength λ_0 is propagating [78]. In the presence of a high intensity electromagnetic field, the index of refraction, n, is dependent on linear and nonlinear optical mechanisms and may be written as

$$n = n_0 + n_2 I(r,t) \tag{2.37}$$

where n_2 is a nonlinear Kerr coefficient and $I(r,t)$ is the time dependent laser intensity. The Kerr index is directly related to the third order susceptibility which is in turn connected to a number of other physical parameters including the vacuum permittivity ϵ_0;

$$\chi^{(3)} = \frac{4}{3}\epsilon_0 c n_2 n_0^2. \tag{2.38}$$

The Kerr coefficient is typically positive leading to an increase in the local index of refraction in the presence of an intense field. The intensity of a beam is typically highest along the propagation axis at the beam center and, since the index of refraction is intensity dependent, this leads to curvature of the wave front, similar to a lensing effect, causing convergence and collapse of the collimated beam. One important parameter in self focusing is the initial power of the beam. Self focusing overcomes diffraction only if the initial power reaches a critical threshold [79] given by;

$$P_{cr} = \frac{3.72\lambda_0^2}{8\pi n_0 n_2}. \tag{2.39}$$

Once this occurs, the propagation length, L_c, of the self focusing beam can be approximated semi-empirically and depends on the Rayleigh length as well as the ratio of the initial beam power P_{in} to the critical power,

$$L_c = \frac{0.367 L_R}{\left(\left[\left(\frac{P_{in}}{P_{cr}}\right)^{0.5} - 0.852\right]^2 - 0.0219\right)^2}. \tag{2.40}$$

The intensity of the beam increases dramatically in the beam collapse region, and typically results in photo-ionization of the medium and plasma formation. This plasma in turn causes defocusing and divergence of the beam due to a local change in the refractive index [80], which is given by

$$n \simeq n_0 - \frac{\rho(r,t)}{2\rho_c} \tag{2.41}$$

where $\rho(r,t)$ is the free electron density and ρ_c is the critical plasma density above which the plasma becomes opaque,

$$\rho_c = \frac{\epsilon_0 m_e \omega_0^2}{q_e}. \tag{2.42}$$

The plasma generated during the forward part of the pulse mainly results in defocusing of the trailing end of the pulse and the characteristic length for plasma defocusing may be expressed in terms of the critical plasma density and the neutral atom density ρ_{at}. It has the form;

$$L_p = \frac{2n_0\rho_c}{k_0\rho_{at}}, \tag{2.43}$$

where $k_0 = 2\pi/\lambda_0$ is the vacuum wavenumber. The focusing and defocusing regimes are represented schematically in Figure 2.6. While other processes such as group velocity dispersion or self-phase modulation play a role, it is mainly the balance between Kerr induced focusing and plasma defocusing that results in the formation of long narrow laser filaments. Long range filaments persist if there is enough power ($> P_{cr}$) in the beam after the first defocusing region to initiate another focusing cycle. This sequence continues until the incident power falls below the critical threshold.

Inside these interaction volumes, the electrons created by photo-ionization during the initial pulse phase can be further accelerated by the laser field via a non-resonant inverse Bremsstrahlung process [81]. The cross section for this process is

$$\sigma = \frac{q_e^2}{\epsilon_0 m_e c n_0} \frac{\tau_c}{(1+\omega^2\tau_c^2)} \tag{2.44}$$

where τ_c is the electron collision frequency. After a series of inverse Bremsstrahlung events, a single electron can gain sufficient kinetic energy $K_E \simeq \frac{3}{2}\widetilde{\Delta}$ to generate secondary free electrons through impact ionization. Here, $\widetilde{\Delta}$ is the ionization potential of an atom given as

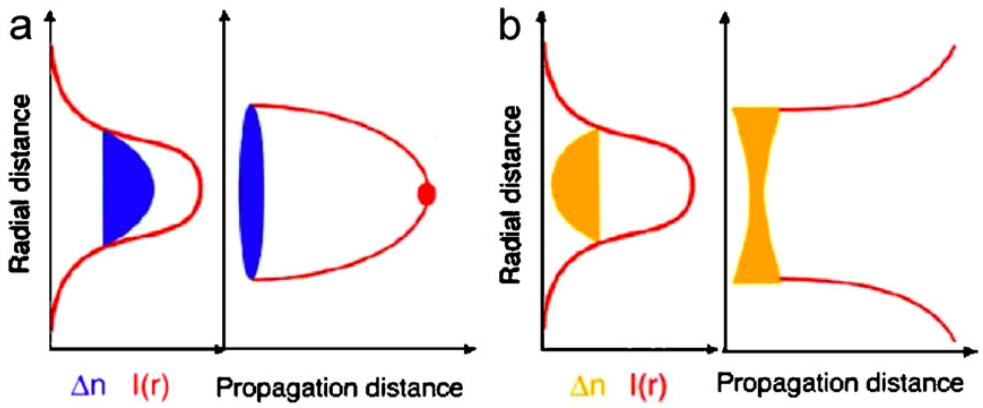

Figure 2.6– Regions of focusing and defocusing initiated by a) the nonlinear Kerr effect and b) plasma formation [78].

$$\widetilde{\Delta} = \Delta + \frac{q_e^2|\mathbf{E}|^2}{4m\omega^2} \tag{2.45}$$

where Δ is the band-gap energy and m is the exciton reduced mass [82]. In turn these electrons may also gain sufficient kinetic energy from the laser field to cause further ionization leading to an avalanche type growth in the number of free electrons in the plasma. The ionization rate per electron, η, participating in the cascade depends mainly on the intensity $I = \frac{1}{2}\epsilon_0 c n_0 |\mathbf{E}|^2$ of the electromagnetic wave and is

$$\eta = \frac{1}{\omega^2\tau_c + 1}\left(\frac{2q_e^2\tau_c I}{3cn_0\epsilon_0 m_e \widetilde{\Delta}} - \frac{m_e\omega^2\tau_c}{M}\right) \tag{2.46}$$

where M is the mass of the molecule being irradiated [83]. Optical breakdown occurs in transparent materials when the total free electron density reaches a critical value $\rho_{crit} \simeq 10^{21}$ cm^{-3}. At higher densities, permanent deformations form in transparent solids and cavitation is observed in liquids.

As is the case when opaque materials are irradiated with fs-laser pulses, electrons in the plasma created within a transparent material cannot transfer thermal energy away from the interaction volume during the pulse and as such their temperature increases dramatically. The mean energy gained by an electron during the laser pulse is the sum of the ionization potential and the increase in its kinetic energy. The total energy density in the plasma at the end of the pulse is then

$$\varepsilon = \frac{9}{4}\rho_{et}\widetilde{\Delta} \tag{2.47}$$

where ρ_{et} is the total number density of free electrons in the plasma. The temperature rise in the interaction volume is

$$\Delta T = \frac{\varepsilon}{\rho_0 C_p} \tag{2.48}$$

where ρ_0 is the density of the medium and C_p is the heat capacity (J K^{-1}) [82]. The plasma pressure also increases within the focal region.

At large intensities, such as those used throughout this work, the plasma formed through photo-ionization and cascade ionization may expand outside the laser matter interaction zone due to the increase in its temperature and the pressure caused by the laser field. This ultimately has the effect of increasing the effective size of the breakdown region and the volume over which new materials may form. The plasma initially expands at hypersonic velocity away from the focal region but as it slows to subsonic velocity as a result of collisions, a shock wave is created [84]. If it exceeds the tensile strength of the medium, this thermoelastic stress wave facilitates the nucleation of cavitation bubbles as the plasma continues to expand. The peak pressure *P* of the shockwave is related to its velocity *u* through the equation

$$P = A\rho_0 u\left(10^{\frac{u-c_0}{B}} - 1\right) \tag{2.49}$$

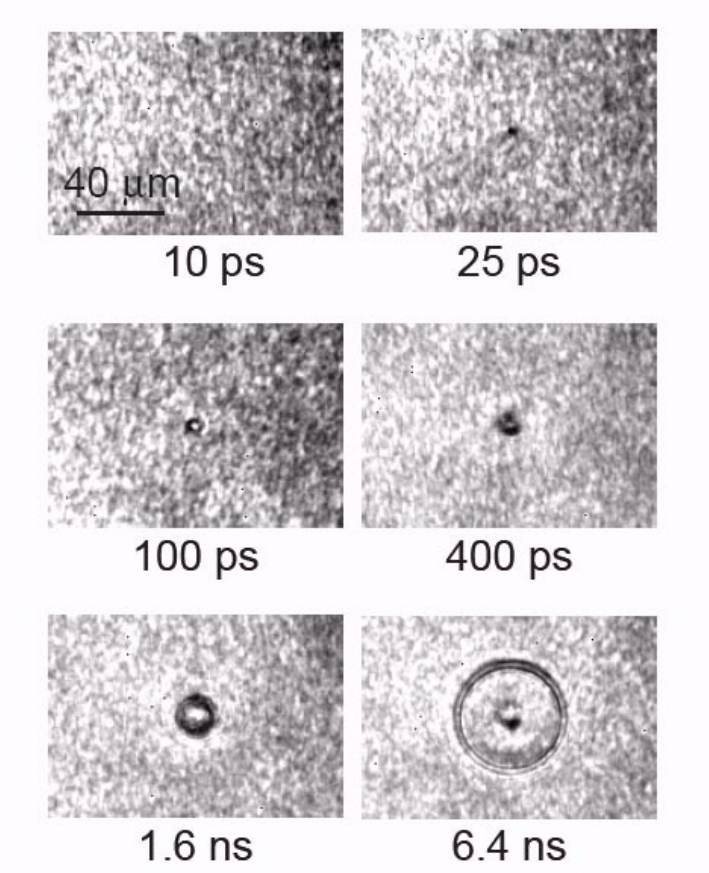

Figure 2.7– Images of the fs induced breakdown in water at various times [85].

where *A* and *B* are empirical constants and c_0 is the speed of sound in the medium [84]. A cavitation bubble forms under these conditions when the kinetic spinodal, (the boundary between superheated metastable fluid states), is surpassed [86, 87]. The maximum radius of a cavitation bubble, R_m , is related to its oscillation period of the bubble T_c and the vapour pressure P_v inside the bubble by

$$R_m = \frac{T_c}{0.915\left(\frac{P_0}{P_0 - P_v}\right)^{1/2}} \tag{2.50}$$

where P_O is the atmospheric pressure. The oscillation period is measured by the time between the shockwave formation due to photo-induced breakdown and the collapse of the bubble. The mechanical energy of a bubble is then

$$E_B = \frac{4}{3}\pi(p_o - p_v)R_m^3 . \tag{2.51}$$

After reaching maximum size, cavitation bubbles implode which can lead to secondary acoustic phenomena such as radially propagating acoustic waves [84]. Figure 2.7 shows the time evolution of a cavitation bubble initiated by a single 100fs, 800nm pulse that was used to dissociate water [85].

Chapter 3
Experimental Systems

A variety of experimental techniques have been employed during the course of this work and the ones that were used most frequently are described in this chapter. Since the fs laser system is the main tool used for the synthesis of the carbon nanomaterials described in this thesis, the design and operation of this system will be outlined first in Section 3.1. As the properties of materials at the nanoscale are affected by their size and shape, the study of their morphology is also important and Section 3.2 of this chapter reviews the basic principles that govern scanning electron microscopy (SEM) and atomic force microscopy (AFM). The optical properties of these materials are often studied using Ultraviolet-Visible (UV-VIS) spectrophotometry, as described in Section 3.3, while their molecular composition can be obtained using various forms of vibrational spectroscopy such as Fourier transform infrared (FTIR), Raman and surface-enhanced Raman (SERS) spectroscopies which are summarized in Section 3.4. Finally, a discussion covering data analysis using the OriginPro 8 software program, which is used throughout the dissertation, is given in Section 3.5.

3.1 Pulsed-Laser Material Synthesis

3.1.1 Laser System

The laser system used in this work was developed by Stephen J. Walker under the direction of Professor Joseph Sanderson of the University of Waterloo [88]. It consists of a mode-locked Ti:Sapphire oscillator pumped by a 5 W Nd:YVO_4 laser. This produces 5 nJ, 800 nm 9.2 fs laser pulses at a repetition rate of 75 MHz. In most chirped pulse amplification schemes, a pulse stretcher is used to lengthen the laser pulses. However in the present system transmissive optical elements in a regenerative amplifier are used for this purpose. The amplifier consists of a Brewster-cut Ti:Sapphire crystal that is pumped by a 20 W frequency-doubled Nd:YLF laser, as well as a number of other optical components. These include a number of polarizing beam splitters, a Pockels cell (quarter or half wave plate) and two curved end mirrors. An overall schematic of the amplifier is given in Figure 3.1. Seed pulses are switched in and out of the amplifier cavity using a set of polarizers and a Faraday rotator (A). The pulse then passes through a half-wave plate that changes the polarization of the pulse to the vertical orientation (B). These vertically polarized pulses are reflected off of a polarizing beam

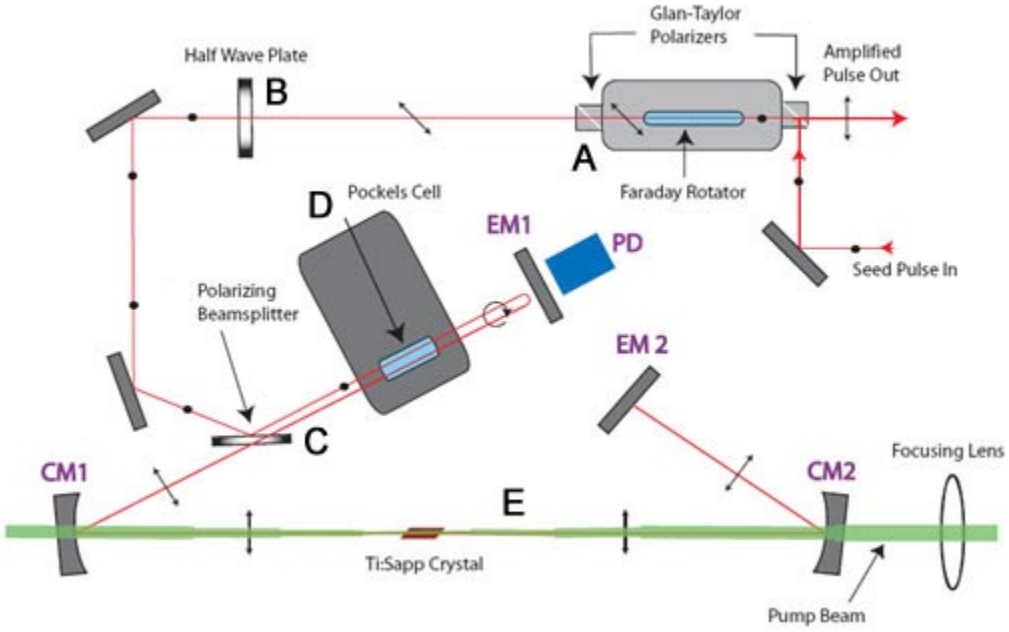

Figure 3.1- Diagram of the regenerative amplifier used to produce 100 fs laser pulses [78].

splitter (C) and pass through a Pockels cell (D) which rotates the pulses by 90°. These pulses are reflected back and now pass through the polarizing beam splitter entering the regenerative cavity (E). The majority of seed pulses from the oscillator are rejected by the Pockels cell, allowing only one seed pulse to circulate within the cavity at any given time. A seed pulse will make sixteen passes through the Ti:Sapphire crystal and acquire an energy of 400 μJ of energy before being switched out of the cavity by the Pockels cell. It then passes back along the optical pathway and out through the polarizers. A double prism pair is then used to compress the output of the amplifier and yields 300 μJ compressed pulses with a typical pulse duration of 100 fs at a repetition rate of 1 kHz. These laser pulses then pass through free space to either the liquid cell or the stainless steel vacuum chamber used for materials processing.

3.1.2 Liquid Irradiation

Two configurations have been used for the irradiation of liquids; pass through (PT) and top down (TD). In the PT configuration the laser beam is focussed using a 0.025 m diameter convex lens with a focal length of 0.040 m. The beam then passes through the transparent sidewall of a rectangular cuvette as shown in Figure 3.2 a). The focal intensity just inside the wall is estimated to be

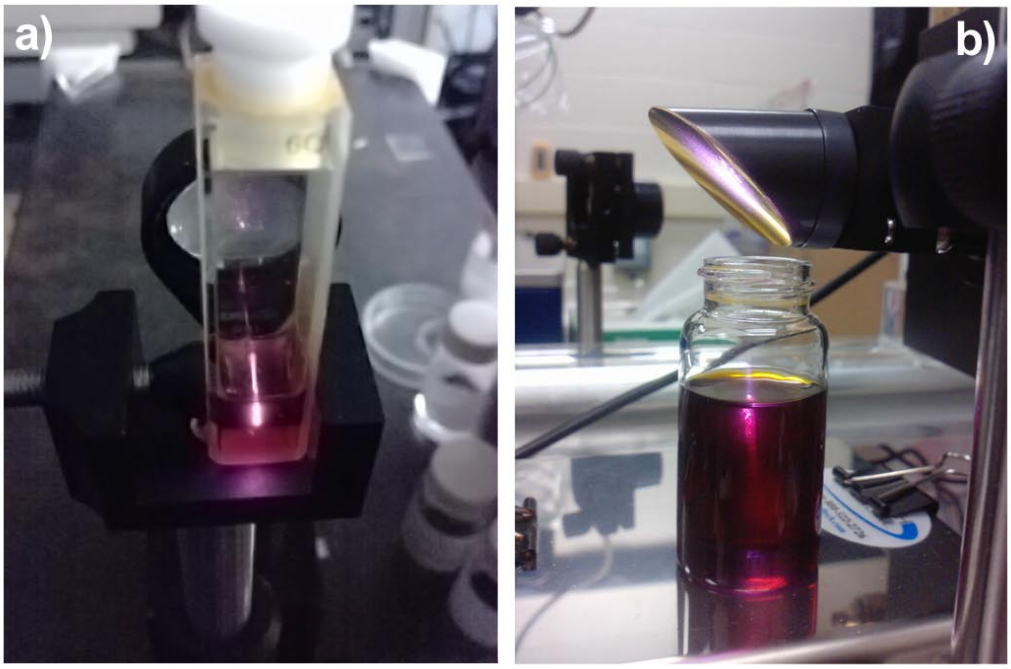

Figure 3.2 - Two configurations are shown for the irradiation of liquids where a) the laser beam is focused and passed through (PT) the transparent wall of a cuvette and b) the laser is focused into the liquid from the top down (TD).

~ 2×10^{14} W cm^{-2}, which is high enough to initiate filamentation in certain liquids depending on the parameters outlined in Chapter 2. As the focal point is moved away from the sidewall and further into the liquid the intensity of light emitted from the plasma forming region decreases noticeably. This suggests that there is attenuation of the light beam as it passes through the liquid, which in turn results in a lower focal intensity and reduced molecular ionization rate. The beam continues to lose energy as the focal point is moved further into the liquid and eventually filamentation ceases as do photo-dissociation and plasma formation. The ideal focal position for material synthesis is therefore as close to the sidewall as possible without initiating ablation of its surface, which can lead to sample contamination. The PT configuration is best suited to the irradiation of hazardous liquids since they can be isolated from the environment.

Irradiating liquids in the TD configuration, as shown in Figure 3.2 b), is typically a more efficient method for nanomaterial synthesis. In this setup the beam is focused using a using a 0.050 m focal length off axis, gold plated, parabolic mirror that results in a laser focal intensity of ~ 1×10^{15} W

cm^{-2}. The higher focal intensity has the net effect of faster material formation. The beam enters an open vial that contains the liquid that is to be irradiated and is focused near the meniscus. Care must be taken when initially focusing the beam, as splashing is liable to occur if the focal point is too close to the air-liquid interface. A bright filament is often observed in this setup, however; it is typically much shorter than those formed in the PT configuration because its path is destabilized by dissociation products in the liquid. As in the PT setup, if the focal position is moved deeper into the liquid the beam becomes attenuated which may lead to the eventual termination of material synthesis.

Specific details for individual liquid phase irradiation experiments can be found in Chapter 4. In general, the parameters were optimized to provide the highest laser intensity during irradiation. The exposure time in all of the experiments ranged from 1 – 4 hrs with irradiation products typically becoming visible in the solutions after ~ 30 min.

3.1.3 Vacuum Deposition

The apparatus for the ablation and deposition of solids is more complex then that required for liquid irradiation because a high vacuum is required to ensure that the effects of atmospheric contamination are mitigated. In this case, the fs-pulsed laser beam is focused into a custom built stainless steel vacuum chamber, shown in Figure 3.3, using a 0.160 m focal length lens (A) giving a maximum intensity of 2.5×10^{14} Wcm^{-2} at the focus. The laser beam enters the chamber through a quartz window (B) and strikes a 0.025 m diameter target disc suspended from the lid of the chamber by a brass cradle (inset) at an angle of ~ 45°. The lateral position of the focal point on the target can be adjusted manually using a micropositioner attached to the base of the lens. Plasma created by ablation travels a distance of 0.040 m before striking the substrate which is positioned parallel to the target. The pressure in the chamber is monitored by an IGM 401 Hornet hot cathode ion gauge which has a measurement range of 1.00×10^{-9}- 5.00×10^{-2} Torr (C). A minimum pressure of 5×10^{-7} Torr is maintained within the chamber using a Varian SD-40 rotary vane roughing pump as well as a Varian TV-60 turbo molecular ion pump (D). During ablation the pressure in the chamber may rise to a value as high as 8×10^{-6} Torr, due to the plasma. Both the target and substrate may be cooled to 77 K by using a liquid nitrogen reservoir (E) connected to the chamber lid. Under ideal conditions, the thin film deposition rate is between 10-12 nm/min. With an average ablation time of 30 min this leads to films that are ~330 nm thick, although samples of varying thickness are often created. After deposition, samples that have been created at low temperatures are typically allowed to warm *in vacuo* over an 8-12 hr period. The warming time may be shortened by pumping warm air into the

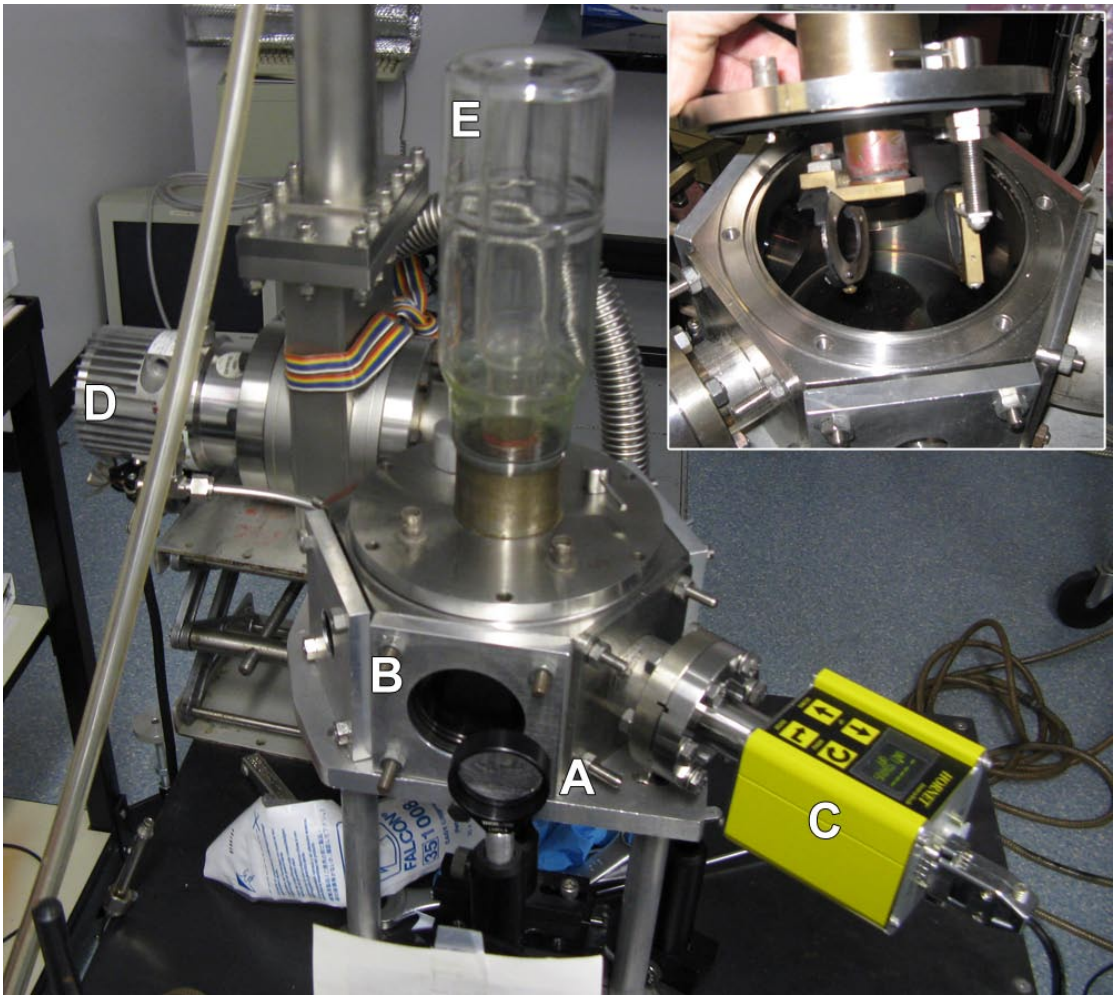

Figure 3.3 - Photograph of the vacuum chamber setup. The laser beam is focused (A) and passes into the chamber (B) striking a graphitic target (inset). The pressure in the chamber is monitored with an ion vacuum gauge (C) and is kept constant using a turbo molecular pump (D). The targets may be cooled using a liquid nitrogen Dewar which is thermally coupled to the target holder (E). The inset shows the inside of the chamber.

nitrogen Dewar. When a sample is ready to be removed from the chamber the turbo pump is turned off first and is allowed to spin down for 10 min before the roughing pump is also turned off. Air is then allowed to enter the chamber through a release valve until the pressure equalizes. After this point the sample can be removed from the vacuum chamber for analysis. Specific details for the individual ablation experiments may be found in Chapter 5.

3.2 Microscopy

3.2.1 Atomic Force Microscopy

One of the main tools used to image and measure the nanomaterials generated throughout the course of this work is atomic force microscopy (AFM). Developed in the late 1980s, AFM is a high resolution scanning probe technique capable of achieving sub-nanometer measurement sensitivities in three dimensions [89]. The main component of an AFM is the scanning probe which is typically a sharp pyramidal tip, with a radius of curvature in the nanometer range, attached to the end of a cantilever. As the tip is brought into close proximity of a sample surface, a number of short and long range forces cause the deflection of the cantilever according to Hooke's Law,

$$F = -kx \tag{3.1}$$

where *k* is the spring constant of the cantilever and *x* is the deflection. Short range repulsive Columbic and longer range attractive van der Waals interactions account for the majority of the cantilever deflection but, depending on the scanning environment, a variety of other forces may also contribute. The deflection of the cantilever is typically measured using a laser spot reflected from the top surface of the cantilever, near the tip, into an array of photodiodes. In this configuration there are three scanning modes that can be used to image the surface. These include contact, tapping, or noncontact modes. Of these, we customarily use the tapping mode, because it provides better lateral resolution under ambient conditions than the contact mode and also causes less damage to samples. In this mode, the cantilever is set to oscillate at or slightly below its resonant frequency at amplitudes up to 100 nm. This changes the separation between the tip and sample surface and, since the forces affecting the tip are distance dependent, the frequency ω of oscillation depends on the tip surface separation as

$$\omega = \omega_0 \sqrt{1 - \frac{1}{k}\frac{d\boldsymbol{F}}{d\boldsymbol{z}}}\ . \tag{3.2}$$

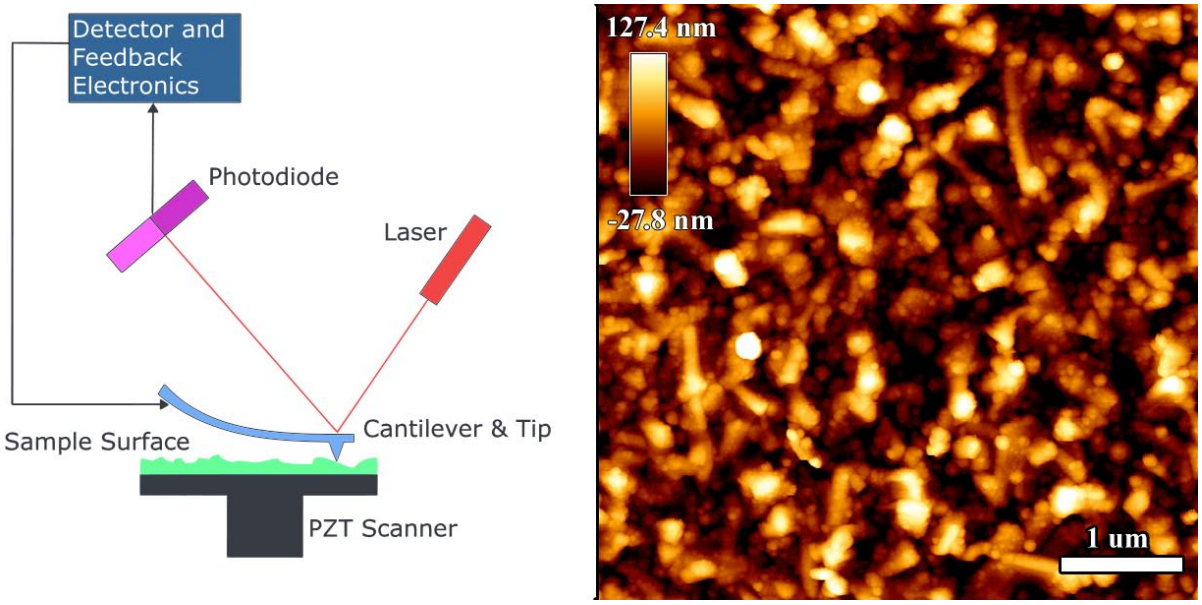

Figure 3.4 - A schematic representation of a typical atomic force microscope [90] and an AFM tapping mode image of the surface morphology of one of the a-C:H thin films created in this work.

Changes in the oscillation frequency can then be used to create a topographical map of the surface by raster scanning across the sample [89]. A simple schematic outlining the operation of a typical AFM system is shown in Figure 3.4 [90], along with an image generated using intermittent contact mode in air. The AFM system used in this work was provided through collaboration with Professor Zoya Leonenko of the University of Waterloo Physics Department. It is a Nanowizard II AFM fabricated by JPK Instruments AG in Germany. The scanning probe tips used throughout this work are made from monolithic silicon which is highly doped to dissipate static charge. They were purchased from NanoWorld Innovative Technologies (NCH tips) and have a spring constant of 42 Nm^{-1}.

3.2.2 Scanning Electron Microscopy

Scanning electron microscopy (SEM), developed during the 1930s, is an important technique for the characterization of the topography and composition of nano-materials. It complements AFM, and yields high resolution, high contrast depth of field images by scanning the surface of a sample with a focused beam of electrons [91]. In a typical SEM, a thermionic tungsten cathode in high vacuum acts as the electron source. Thermionic emission occurs when enough heat is supplied to electrons in the

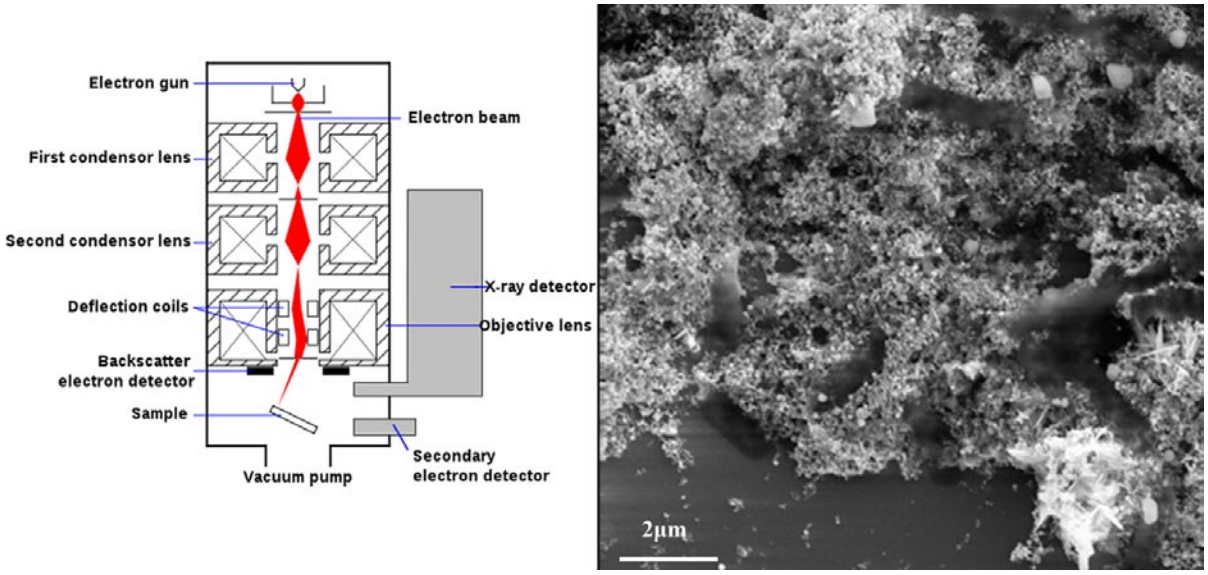

Figure 3.5 - A schematic representation of an SEM [92] and an image generated by secondary electrons, of iron-oxide nanoparticles produced by fs-PLD of iron in water.

filament to overcome the work function of the material. The current density of the emitted electrons is then given by the Richardson-Dushman equation;

$$J = AT^2 e^{\frac{-W}{kT}} \tag{3.3}$$

where A is the Richardson proportionality constant, k is the Boltzmann constant, W is the work function and T is the temperature [93]. Once the electron beam is emitted from the cathode it is accelerated to energies between 0.5-1000 KeV and passes through a series of magnetic condensing and focusing lenses before interacting with the target surface. A set of scanning coils are used to control the x and y position of the beam so that it may be raster-scanned across the sample. Accelerated electrons incident on the target surface can either pass through the sample without interaction or undergo multiple elastic and inelastic scattering events over a tear-shaped interaction volume. Monitoring these various events provides information that can be used to image the sample or to determine the relative concentration of atomic elements present within the sample. For example, secondary electrons and backscattered electrons are frequently used for imaging, while characteristic

X-rays produced by inelastic collisions between incident and atomically bound electrons, are used for elemental analysis. A schematic of a typical SEM system is shown in Figure 3.4 [92] along with an image generated by secondary electrons. One of the benefits of SEM over AFM is that it can quickly scan large areas of a sample surface at magnifications between 10-500,000X. This is very useful when the efficient processing of multiple samples is required.

The SEM used in this work is a Zeiss Leo field emission (FE-SEM) 1530 with an integrated energy dispersive X-ray (EDX) Pegasus 1200 unit for elemental analysis. It is located in the Waterloo Advanced Technology Lab user facility. The accelerating voltage ranges from 0.1-30 KeV resulting in a maximum resolution of approximately 1 nm and magnification of up to 700 kX.

3.3 Spectrophotometry

The transmission of light through a material can be described by the Beer-Lambert Law [94], which for a thin solid film may be expressed as

$$T_\lambda = \frac{I}{I_0} = e^{-\alpha l} \tag{3.4}$$

where I_0 is the initial light intensity, I is the intensity of light after passing through the material, α is the absorption coefficient typically expressed in cm^{-1}, and l is the thickness of the material. The inverse of the transmission is called the absorption and is expressed as $A_\lambda = -\ln T_\lambda$. The absorption coefficient is wavelength λ dependent and is related to the extinction coefficient κ by

$$\alpha = \frac{4\pi\kappa}{\lambda} \tag{3.5}$$

The dimensionless extinction coefficient relates directly to the complex form of a material's index of refraction $\tilde{n} = n + i\kappa$. By measuring the amount of light transmitted or absorbed by a material over a range of wavelengths it is possible to determine the absorption and extinction coefficients and using these values certain characteristics, such as the optical band gap, can be determined. A Shimadzu

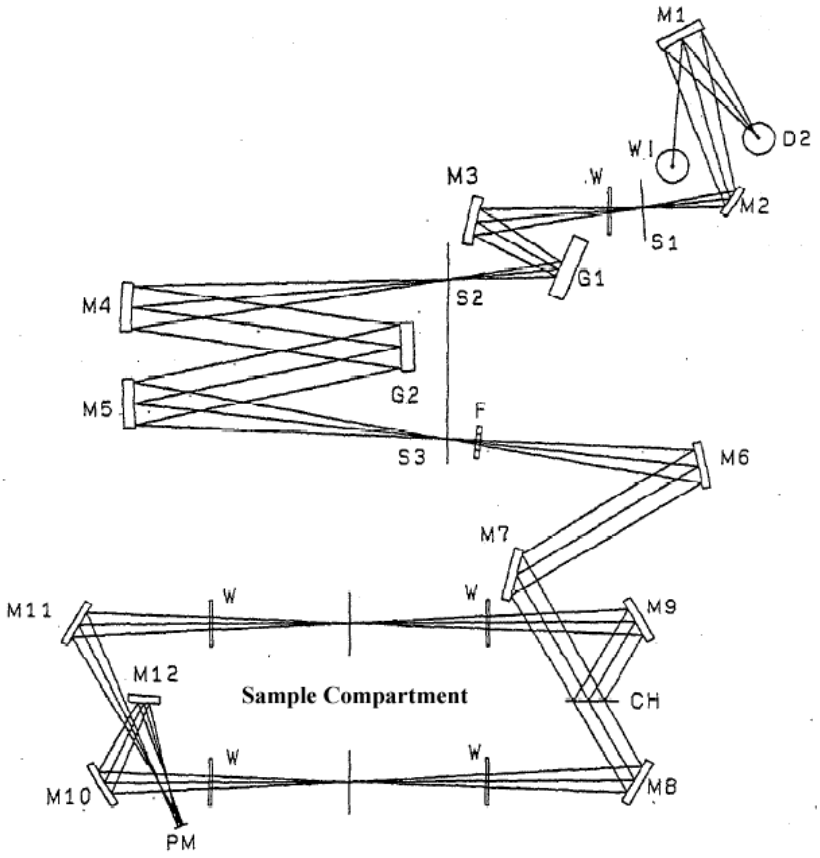

D_2	: Deuterium Lamp	M1~ M10	: Mirrors	S3	: Exit slit
WI	: Halogen lamp	G1	: Grating of first monochromator	F	: Filters
S1	: Entrance slit	S2	: Exit/Entrance slit	CH	: Beam chopper
W	: Quartz windows	G2	: Grating of second monochromator	PM	: Photomultiplier

Figure 3.6 - A schematic of the optical system in the Shimadzu UV-2501PC UV-VIS spectrophotometer taken from the product catalogue.

UV-2501PC UV-VIS spectrophotometer located in the University of Waterloo Giga to Nanoelectronics Center has been used throughout this work to gather absorption and transmission data. It uses a double-blazed, double monochromator with a wavelength range of 190-1100 nm, a resolution 0.1 nm, and an accuracy of ±0.3 nm. A schematic of the optical setup for this device, taken from the product catalogue, is presented in Figure 3.6 as a reference. The double beam configuration of the spectrophotometer allows for automatic subtraction of background absorption from thin film substrates or cuvettes in the case of liquid samples.

3.4 Vibrational Spectroscopy

Vibrational spectroscopy is widely used to study nanomaterials because it is a non-destructive technique that provides information on the given sample's molecular composition. Linear and nonlinear polyatomic molecules have $3n - 5$ and $3n - 6$ degrees of vibrational freedom, respectively. Normal vibrational modes that produce a net change in the molecular dipole moment are infrared (IR) active while those that cause a change in the molecular polarizability are Raman active. Of course, it is also possible that a specific vibrational mode will cause both IR and Raman activity. Optical excitation of these modes results in a vibrational spectrum that is characteristic of a specific molecule. It is therefore possible to identify the molecular species in a material by examination of its vibrational spectrum. In this regard, IR and Raman spectroscopies are often used in conjunction, as they provide complimentary information on molecular composition.

3.4.1 Fourier Transform Infrared Spectroscopy

A Shimadzu FT-IR 8400S spectrometer located in the University of Waterloo Giga to Nanoelectronics Center was used to gather IR vibrational data on the materials created for this work. This system uses a high brightness ceramic as an infrared light source and a helium neon (HeNe) laser for data sampling. It has a spectral range of 7800-350 cm^{-1} with a maximum resolution of 0.85 cm^{-1} and a nominal signal-to- noise ratio of 20,000:1. The optical components of the instrument are kept in a sealed environment and coated with an anti-humidity film to reduce the effects of atmospheric carbon dioxide and water vapor. Alignment and optimization of the system is fully automated and the device is controlled via Shimadzu IRSolution software on a desktop computer. Samples are placed in a small chamber that is held at standard temperature and pressure. A traditional dispersive IR spectrometer measures the change in intensity between reference and sample beams to determine the IR absorption of a sample at a given frequency and then scans each frequency component sequentially. This is not the case in FTIR systems which use an approach based on Michelson interferometry [95].

A schematic of the interferometer used in the Shimadzu instrument is given in Figure 3.7. It basically consists of a beam splitter, one fixed and one movable mirror and a number of detectors. Inside the interferometer the incident HeNe beam is divided by the beam splitter and differences in the optical path length are introduced by varying the relative position of the moving mirror to the fixed mirror. At equal path lengths the two beams are completely in phase and interfere constructively. As the mirror moves from its zero position the two beams begin to interfere

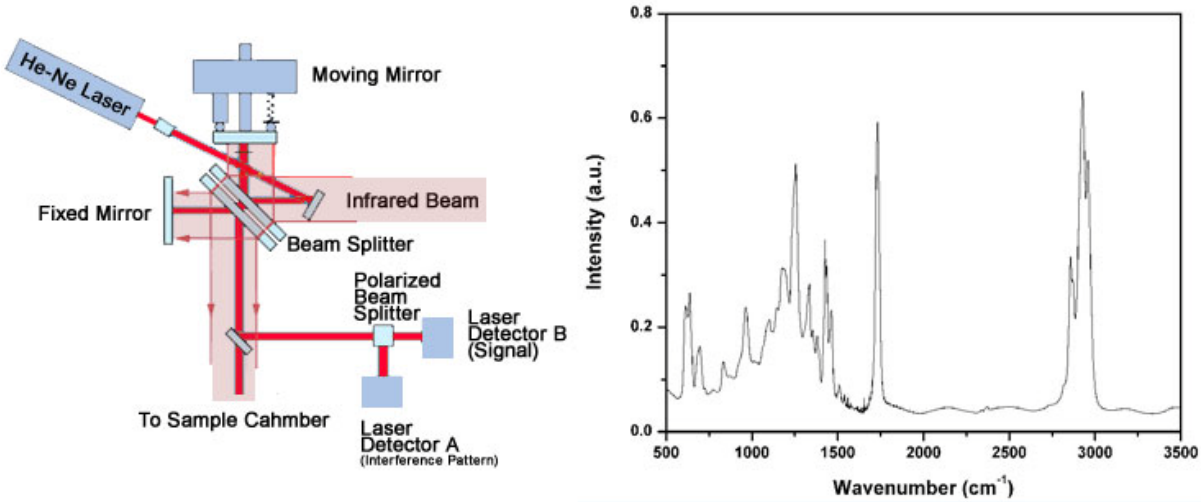

Figure 3.7 - The design of the interferometer in a Shimadzu FT-IR 8400S and the FTIR spectrum of PVC plastic wrap.

destructively until the path length of the movable mirror is half of its original value. At this point the two beams are 180º out of phase and undergo complete destructive interference. The mirror's speed is kept constant so that the intensity of the recombined beam varies sinusoidally, producing a time domain interferogram (intensity vs. time). When a sample is scanned its IR absorption has the effect of changing the amplitude of the interference sinusoid. The interferogram contains information over the entire IR region that the device is capable of scanning. After detection the time domain signal is then converted to the frequency domain (intensity vs. frequency) for analysis using a Fourier transform

$$g(\omega) = \frac{1}{\sqrt{2\pi}} \int_{-\infty}^{\infty} f(t) e^{i\omega t}\, dt. \tag{3.6}$$

To help insure that atmospheric and detector effects do not affect the measurement signal, a background scan is typically taken before the IR absorption of a sample is measured. This is then subtracted from the signal produced from the sample, resulting in a final frequency domain spectrum that can be used to identify molecular vibrational modes.

3.4.2 Raman Spectroscopy

When monochromatic light interacts with a molecule, one of the processes it may undergo is scattering. A classical treatment of this phenomenon is presented briefly to explain the origins of Raman spectroscopy. The incident radiation may be treated as a monochromatic plane wave of frequency ω_i which, to the first order, induces an electric dipolar moment in the molecule. The intensity of light radiated by this oscillating dipole may be written as

$$I = k_\omega \omega^4 p_0^2 \sin^2(\theta) \tag{3.7}$$

where k_ω is a constant, p_0 is the amplitude of the induced electric dipole having frequency ω, and θ is the direction of the incident radiation with respect to the dipolar axis [96]. In classical approximations the frequency dependent induced electric dipole moment of a molecule under the influence of an electric field is given by the vector product

$$\vec{p} = \vec{\alpha} \cdot \vec{E} \tag{3.8}$$

where $\vec{\alpha}$ is the molecular polarizability tensor and $\vec{E}$ is the time dependent electric field vector of the incident radiation. The polarizability tensor relates directly to the vibrational frequencies of the excited molecule and its variation with a single normal vibration, Q_k, is given as the first term of a Taylor expansion

$$\overrightarrow{\alpha_k} = \overrightarrow{\alpha_0} + \frac{d\overrightarrow{\alpha_k}}{dQ_k} Q_k. \tag{3.9}$$

The induced linear dipole moment may then be shown to have three distinct frequency components

$$\vec{p} = \vec{p}(\omega_i) + \vec{p}(\omega_i \pm \omega_k) = \overrightarrow{\alpha_0} \cdot \overrightarrow{E_0} \cos(\omega_i t) + \overrightarrow{\alpha_k} \cdot \overrightarrow{E_0} \cos((\omega_i \pm \omega_k \pm \delta_k)t) \tag{3.10}$$

where the first term gives rise to radiation of the same frequency (Rayleigh scattering) as that of the

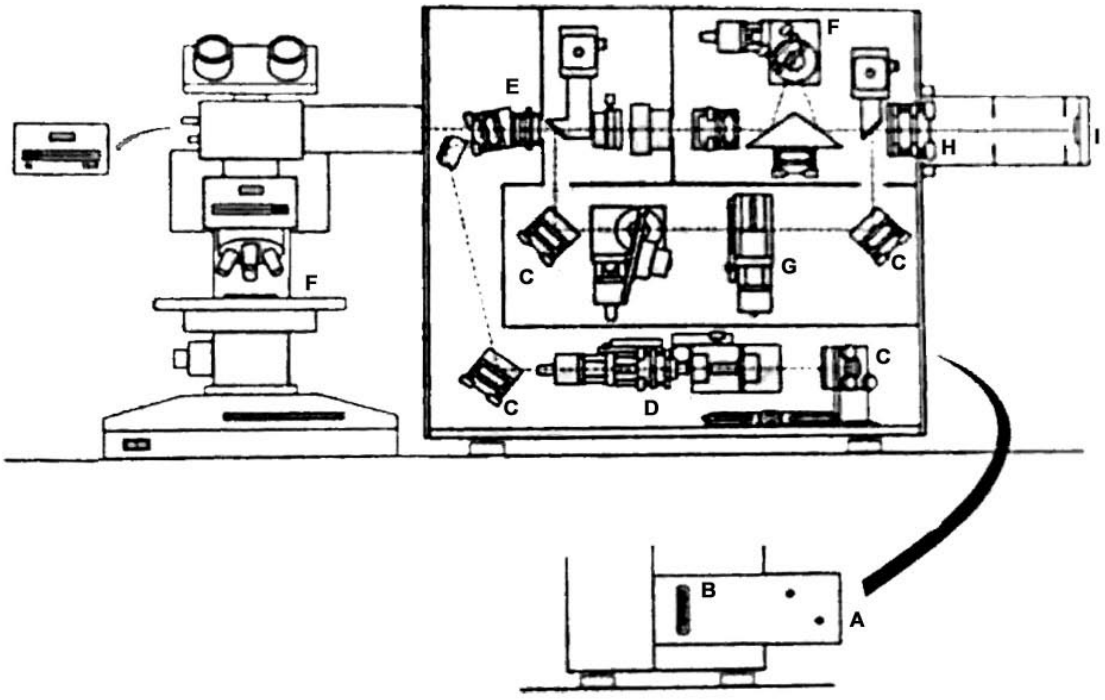

Figure 3.8 - Schematic of the Renishaw micro-Raman 1000 system.

incident light and the other terms result in radiation of higher (anti-Stokes Raman scattering) and lower (Stokes Raman scattering) frequency. The dipoles oscillating at frequencies different from the incident light are phase shifted relative to it and result directly from interaction between the light and the vibrational normal modes of the molecule allowing for the identification of molecular species through Raman spectroscopy.

Figure 3.8 shows a schematic of the Renishaw micro-Raman 1000 Spectrometer used throughout this work. The spectrometer is located in the Giga-to-Nano center at the University of Waterloo and is attached to an Olympus BH2-UMA microscope. The beam, either from a 488 nm Ar ion or a 632 nm HeNe laser, enters the apparatus at point (A) and then passes through an attenuation filter wheel, (B), which allows for the stepwise control of the laser light intensity. The beam is then aligned with the first of a number of adjustable mirrors, indicated at points (C). The light is then fed through a spatial filter assembly (D) that consists of a number of lenses and a pinhole and then

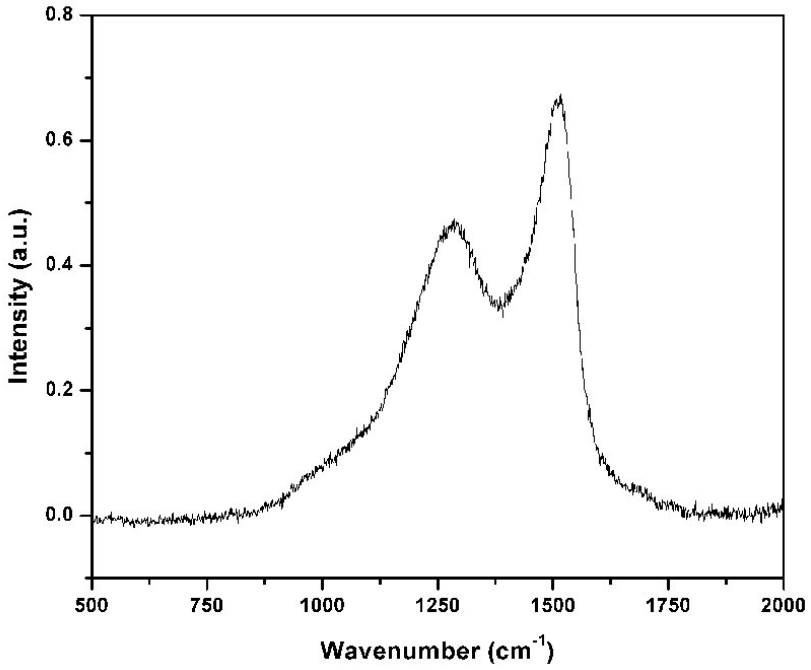

Figure 3.9 - Raman spectrum of amorphous carbon in the D and G mode range.

continues to a holographic notch filter set and polarizer (E). The beam is then sent to the microscope and is focused onto the sample at point (F). The Rayleigh and Raman scattered light then travels back up through the microscope column where the Rayleigh light is removed from the signal beam at the holographic filter. The beam is then split into two arms, one traveling into a spectrograph (F) and the other into a Fabry–Pérot interferometer (G). These beams are then focused (H) onto a CCD array (I) and that data is transferred to a computer for storage and analysis. This type of spectral data is usually expressed in terms of Raman shift which has units of wavenumbers (cm^{-1}) which relates to the original excitation wavelength through the equation

$$\Delta\omega\ (cm^{-1}) = \left(\frac{1}{\lambda_0(cm)} \pm \frac{1}{\lambda_1(cm)}\right) \tag{3.11}$$

where λ_0 is the excitation wavelength and λ_1 is the wavelength of the scattered light. As an example, Figure 3.9 shows the Raman spectrum of an amorphous carbon sample excited by a 488 nm Argon ion laser beam.

3.4.3 Surface Enhanced Raman Spectroscopy

When molecules come into contact with roughened metallic surfaces or metallic nanoparticles, a considerable intensification of the Raman signal has been shown to occur. This phenomenon was first observed in the late 1970s and has proven to be an invaluable technique for the characterization of materials [97]. Surface-enhanced Raman spectroscopy (SERS) is typically reported to cause a 10^6 fold increase of the normal Raman cross-section, thus allowing, under certain conditions, for single molecule sensitivity and the appearance of additional vibrational modes not present in the original Raman spectra [98]. In the laboratory, SERS is typically achieved by either deposition of a sample onto a nano-roughened metallic surface or by the adsorption of metallic nanoparticles onto the sample surface itself. In the experiments described in this work, the second method is employed exclusively. Typically, colloidal silver nanoparticles having a diameter of less than 50nm were drop deposited onto thin film samples and allowed to dry or mixed with liquid samples. The metallic nanoparticles used were either purchased from Sigma Aldrich and dispersed in ultrapure water (0 ppm dissolved solids) or prepared in a chemical process by Dr. Anming Hu of the University of Waterloo Mechanical Engineering Department.

Since its discovery, the exact mechanism responsible for the SERS effect has been the topic of considerable debate. Currently, the general consensus is that the enhancement is considered to result from the contribution of two different mechanisms, one of which is electromagnetic in nature, while the other is chemical [98]. When electromagnetic radiation interacts with a roughened metal surface, it can excite localized surface plasmons. Surface plasmons are quasi particles that may be thought of as coherent oscillations of valence electrons [99]. If the plasmon oscillation frequency matches that of the incident light, a plasmonic resonance occurs and results in the amplification of the incoming and scattered local electromagnetic fields near the surface. The intensity of Raman scattering therefore scales approximately as E^4 and, as a consequence, the signal intensity increase dramatically (~10^4) due to plasmonic coupling.

The remaining enhancement (~10^2) is thought to result due to charge transfer resonances between the metallic surface and the adsorbent. If the Fermi level of the metal falls in between the molecular ground state and one or more of the excited molecular states it reduces the energy required for spectroscopic transitions, leading to an increase in the Raman cross-section. The charge transfer effect only occurs when metals are in contact with certain molecular species, typically those with a lone electron pair, and contributes far less to the overall enhancement than plasmonic resonance. The combined effect of these phenomena is illustrated in Figure 3.10 that shows the a) regular Raman and

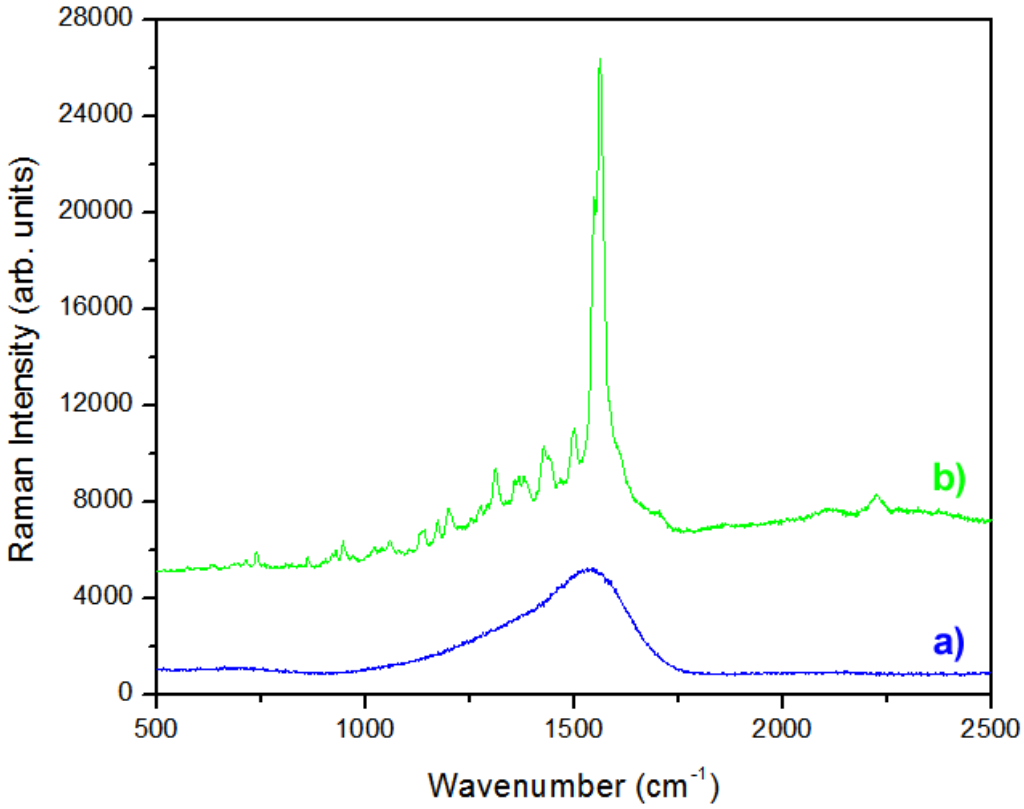

Figure 3.10 - Comparison of the a) normal Raman spectrum of an a-C thin film to that of its b) SERS spectrum.

b) SERS spectra of an a-C thin film deposited using the laser system described in Section 3.1. The SERS spectrum is several times more intense than the normal Raman spectrum and shows a variety of additional features that result from contributions of individual molecular components.

3.5 Data Analysis

Once spectroscopic data has been accumulated using the various methods outlined above it is converted from its native file format to ASCII and imported into the OriginPro 8 software program. This program contains a suite of automated functions for data analysis which will be referred to in italics in the text below. Typically, the first step in the analysis of any spectral data is the removal of contributions from background sources such as water vapour or photoluminescence (PL). This is accomplished by manually fitting a set of linear functions to the spectrum with the aid of the *baseline* algorithm in OriginPro's analysis menu. After a baseline is fit, it may then be subtracted from the

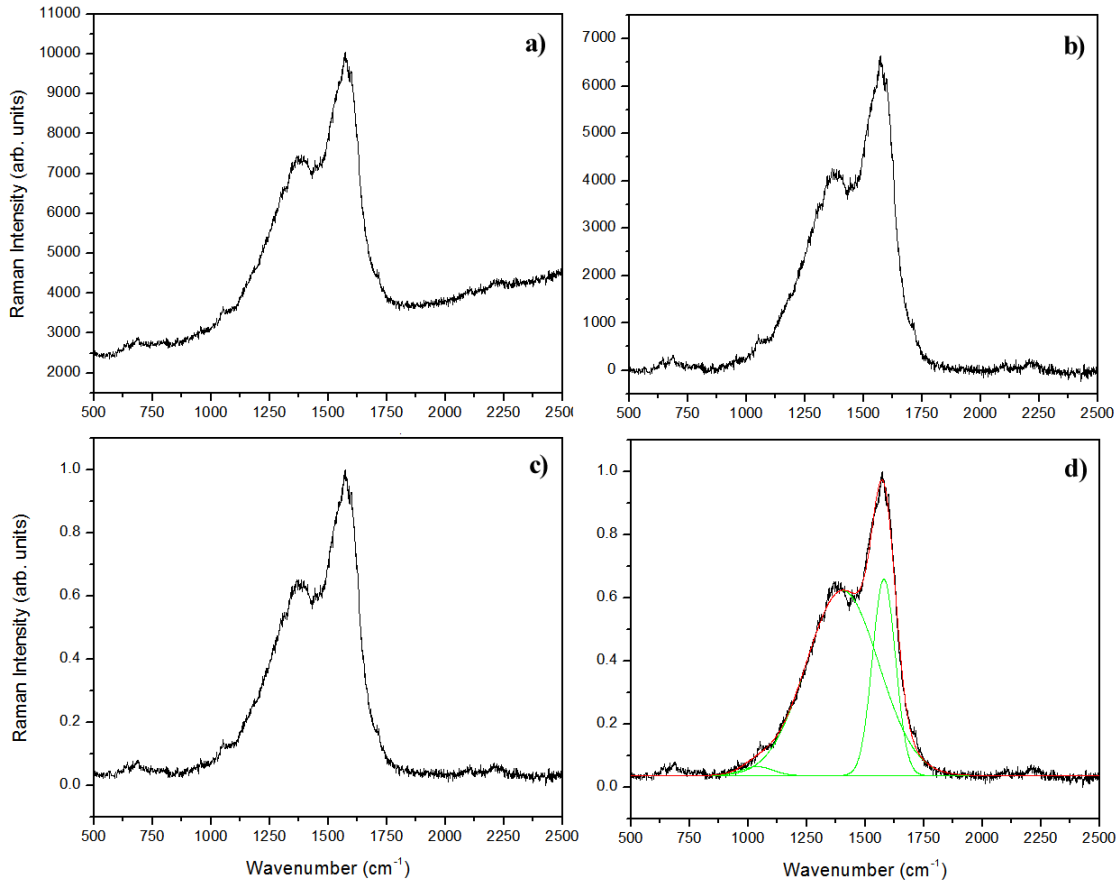

Figure 3.11 - A series of graphs outlining the processing that is usually preformed on spectral data. The first graph a) shows an unaltered Raman spectrum taken from an amorphous carbon sample, while b) shows the same spectrum after background subtraction. The data is then normalized in c) and any peaks are deconvolved into their Gaussian or Lorentzian components in d).

original data using *baseline subtraction*. As an example, the unprocessed Raman spectrum of a hydrogenated amorphous carbon sample is shown in Figure 3.11 a). Due to the hydrogen content there is an underlying PL background that can obscure peaks associated with Raman vibrations. The background is removed in Figure 3.11 b). After baseline subtraction, the data are normalized from 0-1 using the mathematical *normalize* routine, which sets the highest and lowest intensity Y data values to 1 and 0 respectively. The rest of the data are scaled automatically scaled to values between these extrema, as is shown in Figure 3.11 c). This is done to facilitate the comparison of spectra from

different samples. The final step in data analysis is the identification and characterization of spectra features. This is accomplished by fitting line profiles to peaks in the spectrum. Individual peaks can be fit directly with either Guassian

$$I(\tilde{\nu}) = I_0 e^{\frac{-(\tilde{\nu}-\tilde{\nu}_0)^2}{2\Gamma^2}} \tag{3.12}$$

or Lorentian

$$I(\tilde{\nu}) = \frac{I_0 \Gamma^2}{\Gamma^2 + (\tilde{\nu} - \tilde{\nu}_0)^2} \tag{3.13}$$

functions. Here I_0 is the maximum intensity of the feature with a central position of $\tilde{\nu}_0$ and a full width at half maximum (FWHM) of Γ. When peaks are not resolved in the spectrum, as in Figure 3.11 d), they may be deconvolved into their individual components using the *fit multiple peaks* function.

Chapter 4
Material Synthesis through Liquid-Phase Pulsed Laser Irradiation

The production of nanomaterials through high intensity fs laser irradiation of liquids is an exciting new branch of material science that involves photo-induced plasma chemistry at extreme pressures and temperatures. This chapter begins with a brief introduction to liquid phase pulsed laser irradiation (LP-PLI). Of special interest is the formation of one dimensional polyyne chains through the irradiation of liquid hydrocarbons; a portion of Section 4.1 being derived from collaborative work [100]. Section 4.2 provides a detailed description of the various LP-PLI experiments that I have carried out over the course of my doctoral work, with the results of each being described in Section 4.3. In total, four separate experiments have been completed. These include the irradiation of benzene and its deuterated counterpart (Section 4.3.1), toluene (Section 4.3.2), and solutions of ferrocene (Section 4.3.3). A new hybrid pulsed laser electrodeposition technique is also presented (Section 4.3.4). Of these four, I am the principle investigator on the first two experiments. The work on the irradiation of benzene was published in 2011 and as such Section 4.3.1 is based on that article [101]. The third and fourth experiments were carried out in collaboration with Stanislav Kuzmin, a doctoral candidate in our research group. All of the unpublished results, which are summarized in Section 4.4, are being prepared for peer-review. Appendix A also details a variety of peripheral liquid phase experiments that were carried out over the course of my doctorate but do not come under the scope of this chapter.

4.1 Introduction

The ablation of solid materials with pulsed lasers and the subsequent deposition of ablation products, a technique referred to as pulsed laser deposition (PLD), has been employed to synthesize thin films since the mid 1960s [102]. A vast array of these coatings have been fabricated since the seminal work of Smith & Turner, who used a Ruby laser to deposit films from a variety of organic and inorganic target materials, in 1965. In a standard PLD setup the properties of the deposit are controlled by the choice of target material, changing laser parameters such as pulse length, or by adding gasses into an otherwise evacuated environment. A newer pulsed-laser synthesis technique, first introduced in 1987 [103] and called liquid-phase pulsed-laser ablation (LP-PLA), expands on the functionality of standard PLD by allowing for the creation of free floating colloidal nanoparticles.

In LP-PLA a solid target is immersed in a liquid and then its surface is ablated by high powered laser pulses. As a result, energetic plasma is ejected from the target and then rapidly interacts with the molecules of the surrounding liquid producing new substances. A variety of nanomaterials have been produced using this method including metal and metal oxide nano-particles, shells and rods [104-106], diamond-like carbon [107], fullerenes and carbon nanotubes [108]. Surface patterning and chemical modification using LP-PLA have also been explored by numerous authors [109, 110]. LP-PLA has gained considerable prominence as a nanoparticle synthesis technique because it has a number of advantages over other physical or chemical synthesis methods used to create similar nanomaterials. For example, it is a straightforward and clean process, typically producing minimal by-products and often requiring only one pure elemental solid immersed in a simple liquid like water. Ultimately it is this simplicity in design and implementation that makes LP-PLA such a potent synthesis technique; however, it is possible to simplify the process even further by removing the necessity for a solid target all together.

In this case a high intensity, short (nanosecond) or ultra-short (femtosecond), pulsed laser beam can be focused directly into a liquid medium causing photo-ionization, dissociation, plasma formation and, in certain cases, material synthesis. This process can no longer be considered an ablation technique since material is not being removed from a surface and as such it will be referred to as liquid-phase pulsed-laser irradiation (LP-PLI). In general, the laser induced breakdown of liquids in the short pulse regime has been studied extensively over the past thirty years [111-114]. The majority of work in this field can be separated into two categories. The first relates to the study of the fundamental mechanisms responsible for photo-ionization and dissociation of molecules [111, 112] while the second, often in congruence to the first, involves the spectroscopic identification of photo-induced atomic dissociation products for the purpose of material characterization [113, 114]. This technique is referred to as laser induced breakdown spectroscopy (LIBS). Excluding these topics there has been little to no exploration in the literature of the other possible aspects of LP-PLI such as the one central to this work; nanomaterial synthesis. That situation is slowly changing with a number of articles being published on the topic within the last five years.

In 2008, Hu et al. [115] presented the findings of a project that involved the direct laser induced photo-dissociation of acetone ($(CH_3)_2CO$). It was found that, by irradiating the solvent with focussed 90 fs pulses ($\sim 10^{15}$ Wcm^{-2}) from a Ti:Sapphire laser, *sp*-hybridized molecules called polyynes ($C_{2n}H_2$) could be produced in significant quantities. Polyynes are linear carbon molecules

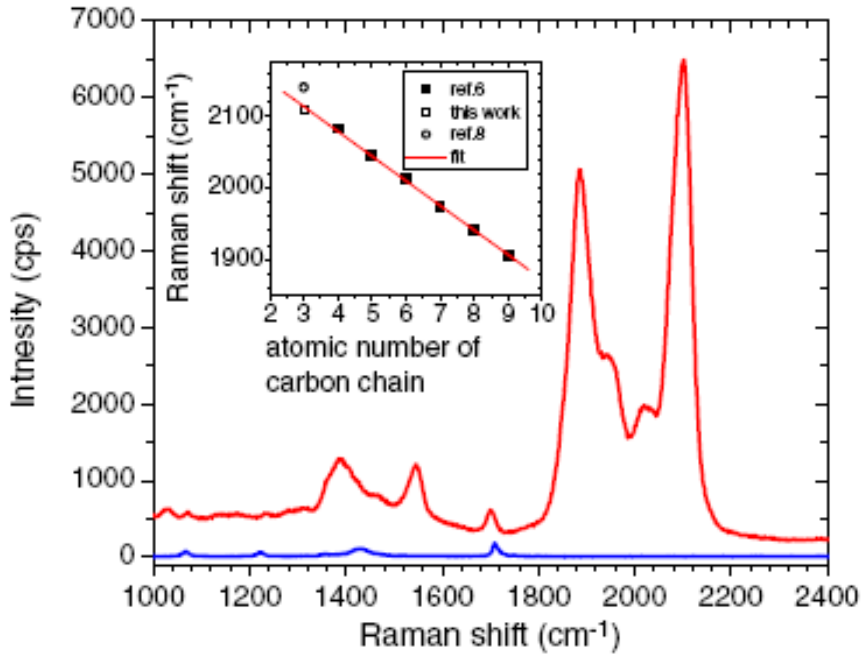

Figure 4.1 - SERS spectra of hexane (bottom) and irradiated hexane (top) showing the presence of polyyne stretching modes in the region between 1800-2200 cm^{-1} [115]. The insert shows peak position as a function of polyyne chain length.

that are comprised of alternating single and triple bonds. The synthesis of these molecules has garnered considerable attention because of their unique properties and potential applications in nanotechnology. For example, polyynes show good molecular conductance [53] and high mechanical strength [52]. These properties are highly desirable in molecular electronics applications where they could serve as wires. Such applications however, require the development of generic synthesis methodologies whereby molecules having specific lengths can be generated in a reproducible manner.

Figure 4.1 shows the spectral region (1800-2200cm^{-1}) in which the primary stretching vibrations (−C≡C−) of polyynes were identified. Features in this area correspond to polyynes with different chain lengths and the correlation between peak position and chain length [115] is shown in the inset of the figure. It was suggested that the formation of polyynes occurred after the dissociation of acetone and was due to carbon addition reactions. While it is likely that polyynes longer than 6 C were produced by the irradiation of acetone this could not be confirmed definitively because of ambiguity in the Raman data. Two years after these initial results, Sato et al. [116] showed that the

irradiation of hexane (C_6H_{14}), using a similar laser system (Ti:Sapphire, 100fs, 0.9 mJ/pulse), also results in the formation of polyynes. Molecules with chain lengths ranging from 6-12 C atoms were identified using UV absorption spectroscopy and high performance liquid chromatography. To uncover the polyyne formation mechanism the authors also examined irradiated decane ($C_{10}H_{22}$). It was assumed that if polyyne formation resulted from a single step hydrogen elimination induced by photo-ionization of the parent molecule then the irradiation of decane would lead to an enrichment of $C_{10}H_2$. This was not the case. In fact, a smaller concentration of $C_{10}H_2$ was found in irradiated decane than in irradiated hexane. This led the authors to suggest that the previous mechanism outlined by Hu et al. [115] was likely responsible for the formation of polyynes in their samples.

In that same year, molecular chains as long as $C_{14}H_2$ were discovered in irradiated octane (C_8H_{18}) by Zaidi et al. [100]. Using the laser system described in Chapter 3.1, the authors irradiated high purity liquid octane for two hours with 100 fs pulses in a focused laser beam that had a maximum intensity of 4×10^{13} W cm^{-2}. This resulted in a colorless transparent liquid that was examined using SERS. To facilitate this, a solution of nano-silver particles was added to the irradiated octane in a ratio of 1:5. The SERS spectra were then gathered, using the Renishaw Raman system outlined in Chapter 3.3, by focusing the laser on the interface between the Ag solution and the irradiated octane. The SERS spectra of pure and irradiated octane are shown in Figure 4.2 a). The irradiated spectrum shows complex spectral features in the polyyne fingerprint region which were shown to be associated with the polyynes C_8H_2, $C_{10}H_2$, $C_{12}H_2$ and $C_{14}H_2$. To further expand on the understanding of the polyyne formation mechanism, the gas phase ionization and dissociation of octane was studied using time of flight mass spectrometry (TOF-MS). Figure 4.2 b) shows the TOF spectrum that resulted from the irradiation of octane with 100 fs laser pulses (~10^{15} W cm^{-2} at focus). It shows that the decomposition of octane results in the formation of numerous radical ions. In liquid octane, these radicals will likely undergo secondary reactions with neutral octane molecules in the surrounding liquid. Despite the inherent complexity of the decomposition products, secondary reactions are likely dominated by reactions involving C, CH, C^+, CH^+, CH_2^+, $C2^+$, C_2H^+, etc. Recombination with electrons and negative ionic species is also expected to occur. Since 100 fs pulses result in the decomposition of octane into fragments smaller than the parent molecule, it is clear that the C_8H_2 polyyne is not produced directly from simple dehydrogenation of the parent. This data also suggests that polyynes are not produced directly by laser induced ionization because they are not visible in the TOF spectrum. It is therefore likely that polyynes are formed due to C_2 and C_3 insertion reactions with smaller chains outside of the laser focus. The reaction between octane and

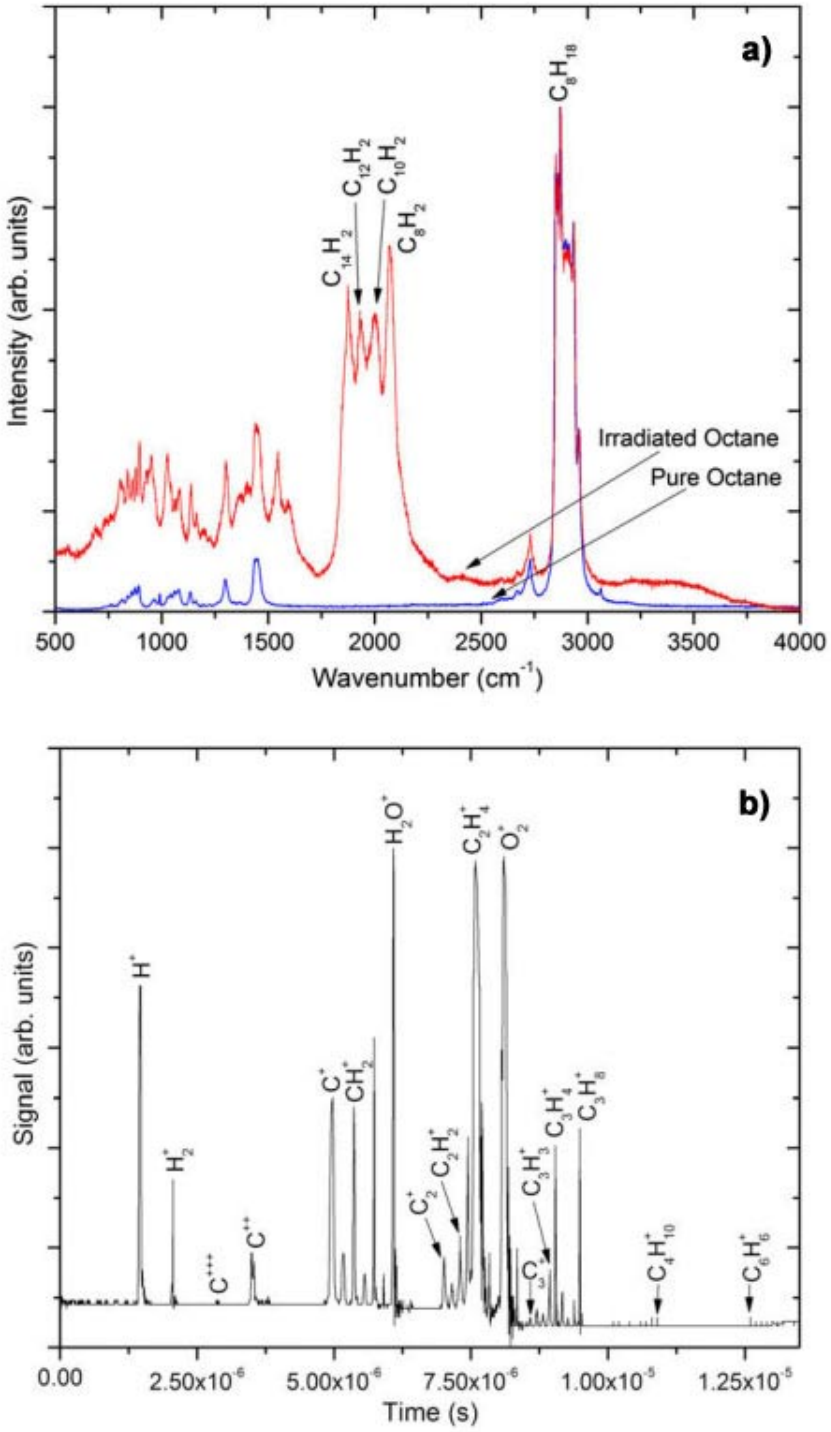

Figure 4.2 - The a) SERS spectra of pure and irradiated liquid octane and b) TOF mass spectrum of dissociated gaseous octane [100].

any of the species listed above will lead to the formation of a variety of hydrocarbons including the long polyyne molecules that were identified in SERS measurements. These, and other small molecules and molecular ions, are generated in the dissociation of the hydrocarbon precursor by multi-photon excitation. The dissociation of the precursor molecule is then a critical step in the formation of polyynes via fs laser irradiation. This process is expected to be more difficult in ring compounds because of the inherent stability of the ring structure. Previous studies [117-119] have shown that $C_6H_6^+$ is the dominant ion produced in the fs dissociation of benzene, although other molecules, indicative of ring opening have also been detected in mass spectra. Given these constraints, it is of interest to see if polyyne molecules analogous to those seen in the fs irradiation of other hydrocarbons can also be generated in the irradiation of ring molecules such as benzene and its derivatives or more exotic materials like ferrocene. It is also intriguing to examine if similar effects can be produced in proto-typical organo-metallic compounds such as ferrocene.

4.2 Experimental

A total of four separate experiments are described in this chapter. The first involves the irradiation of liquid benzene and per-deutero benzene (Section 4.3.1), while the second explores the effects of irradiation on the benzene derivative toluene (Section 4.3.2). The third experiment is slightly more complex; exploring the effects of irradiation on a solution of ferrocene and benzene, as opposed to a pure solvent (Section 4.3.3). The fourth and final experiment presented in this chapter is focused on the application of a new technique for the deposition of porous carbon that involves a combination of electrodeposition and pulsed laser irradiation (Section 4.3.4). The common thread weaving all of these experiments together is LP-LPI, with each experiment building on the complexity of its predecessor. The specific procedures employed to carry out these experiments are outlined below. It should be noted that all of the chemicals used in the present experiments were purchased through Sigma Aldrich and were of the highest possible purity. Also, if not specifically mentioned it may be assumed that the equipment used during each experiment is the same as that outlined in Chapter 3.

1) High performance liquid chromatography (HPLC) grade benzene (≥ 99.9% CHROMASOLV®) and deuterated benzene (99.96 atom % D) were irradiated for 1.5 hr using the Ti:Sapphire laser system. The liquids were placed in separate rectangular polished quartz

cuvettes (3.5 ml capacity, 1 cm path length). The incident beam was focused through the side wall of the cuvette with a 4 cm focal length convex lens resulting in a peak intensity of 10^{14} W cm^{-2} at the focus. After irradiation dark particulate matter was observed within the cuvette containing benzene; however, no such deposits occurred in deuterated benzene. The topography of this material was examined by AFM. This was accomplished by depositing a 50 μL droplet of extracted solution onto a standard glass microscope slide and allowing it to dry in air. The composition of the irradiated liquid was studied using SERS by mixing a solution of nano-Ag into the quartz cuvette. Time of flight mass spectrometry (TOF-MS) was used to study the atomic and molecular species produced from fs-irradiation of gaseous benzene. The dual stage TOF system is of Wiley- McLaren type with a drift region of 0.92 m. The same Ti:Sapphire laser used for irradiation of liquid benzene was utilized as the dissociation source in the TOF system.

2) Similar to the first experiment, HPLC grade toluene (≥ 99.9% CHROMASOLV®) was placed in a rectangular polished quartz cuvette and irradiated using the same pass through configuration. A slight colour change, from transparent to pale yellow, was observed after 1.5hr of irradiation. This change intensified with time and after 4hr a very small amount of particulate matter was observed within the cuvette. It was not possible to isolate this material and as a consequence only the irradiated liquid was examined. The photoluminescent, UV-Vis, PL, and Raman properties of this liquid were examine to determine if polyynes had formed.

3) Solutions of ferrocene $Fe(C_5H_5)_2$ were prepared by dissolving the powder in HPLC grade benzene. The typical concentration of these solutions ranged from 0.04 g mL^{-1} to 0.14 g mL^{-1}. The resulting orange liquid was then held in 25 ml glass bottles for irradiation. A top down irradiation configuration was used in which the laser beam was focused into the liquid directly using a 5 cm focal length off axis parabolic mirror that resulted in a focal intensity of ~ 1×10^{15} W cm^{-2}. This material was studied both in an unaltered and purified state. After irradiation the unaltered material was pipetted directly out of the bottles along with the irradiated liquid and studied. Purification of the powder was accomplished by repeatedly centrifuging the solution, pipetting away the excess liquid, and fluxing the remaining material with benzene until no trace of the original ferrocene solution remained. The black powder

that remained in the bottom of the centrifuge vials was covered in benzene until it was removed for study. The surface structure of these samples was studied using AFM and SEM by drop deposition onto quartz discs or silicon wafers depending on the application. Vibrational data were gathered using Raman and FTIR spectroscopies. The atomic structure was examined using a Bruker D8-Advance powder x-ray diffractometer (XRD) with a Cu K-alpha radiation source (wavelength = 1.5406 Å). This device is located in the laboratory of Prof. Linda Nazar who is part of the University of Waterloo Chemistry Department. Finally, the magnetic properties of the purified powder were also examined using a Quantum Design MPMS SQUID Magnetometer situated in the Brockhouse Institute for Material Research at McMaster University.

4) A new technique is presented which combines LP-PLI with electrodeposition. HPLC grade liquid benzene was placed in a quartz cuvette (3.5 ml capacity, 1 cm path length) that contained two stainless steel electrodes separated by a 4 mm gap. The fs laser beam was focussed between these electrodes using a 4 cm focal length convex lens (10^{14} W cm^{-1}). This initiated ionization and dissociation of the benzene. At the same time a potential of 600V was passed between the electrodes. After roughly 20 min a coating was seen to form on the electrodes and became more prominent after continued irradiation. After 1 hr the electrodes were removed from the cuvette and allowed to dry in air. They were then examined using SEM and Raman spectroscopy to determine the nature of the deposits.

4.3 Results & Discussion

4.3.1 Irradiation of Benzene

When the laser beam was focused into liquid benzene an intense region of filamentation was immediately observed as shown in Figure 4.3 a). After approximately 20 min of irradiation the liquid began to develop a light yellow/brown hue. This was followed by the appearance of precipitates after further irradiation. Figure 4.3 b) is an image of the cuvette after irradiation. A similar result was recently reported by Nakamura et al. [120] when liquid benzene was irradiated with 780 nm, 100 fs laser pulses having a maximum intensity of 9×10^{18} Wcm^{-2}. They found that the liquid contained a mono-disperse solution of amorphous carbon nanoparticles that had a 10 nm diameter. The typical

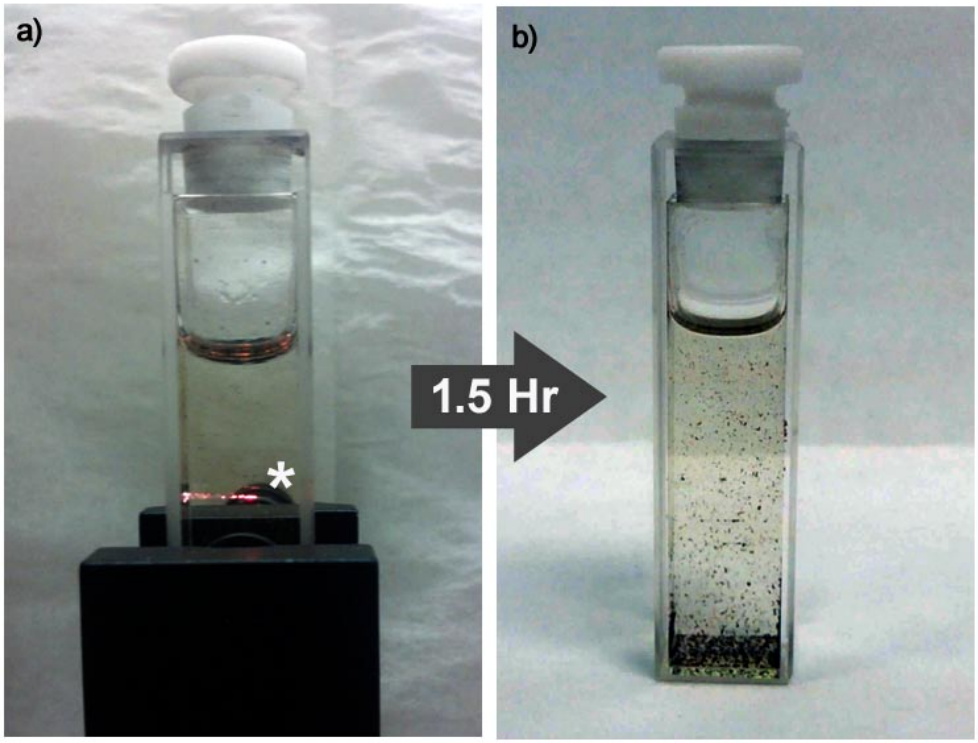

Figure 4.3 - Irradiation of benzene with fs laser is shown in a) and the laser filament is indicated by a star in the image. The precipitate that forms after 1.5 hrs of irradiation is shown in b).

topography of precipitates produced in the current experiment is shown in Figure 4.4. Numerous nanoparticles of varying size are shown in these micrographs. The diameter of particles cannot be accurately determined due to probe broadening however it is common practice to assign particles a given geometry and then use a height profile to attain approximate estimate of their size [121].

A representative cross-sectional height profile (Figure 4.4 a) indicates that the smallest particles in our samples are ~ 1 nm in height while the largest structures, which appear to be cluster assembled from smaller particles, are about 25 nm in height. A higher resolution (1 μm × 1 μm) image of the smallest particles was taken to better characterize their shape and size. Three distinct types of nanoparticles are visible (Figure 4.4 b); spherical particles with heights ranging between 1 and 3 nm, prolate spheroids with similar heights, and toroidal particles that occasionally encircle a

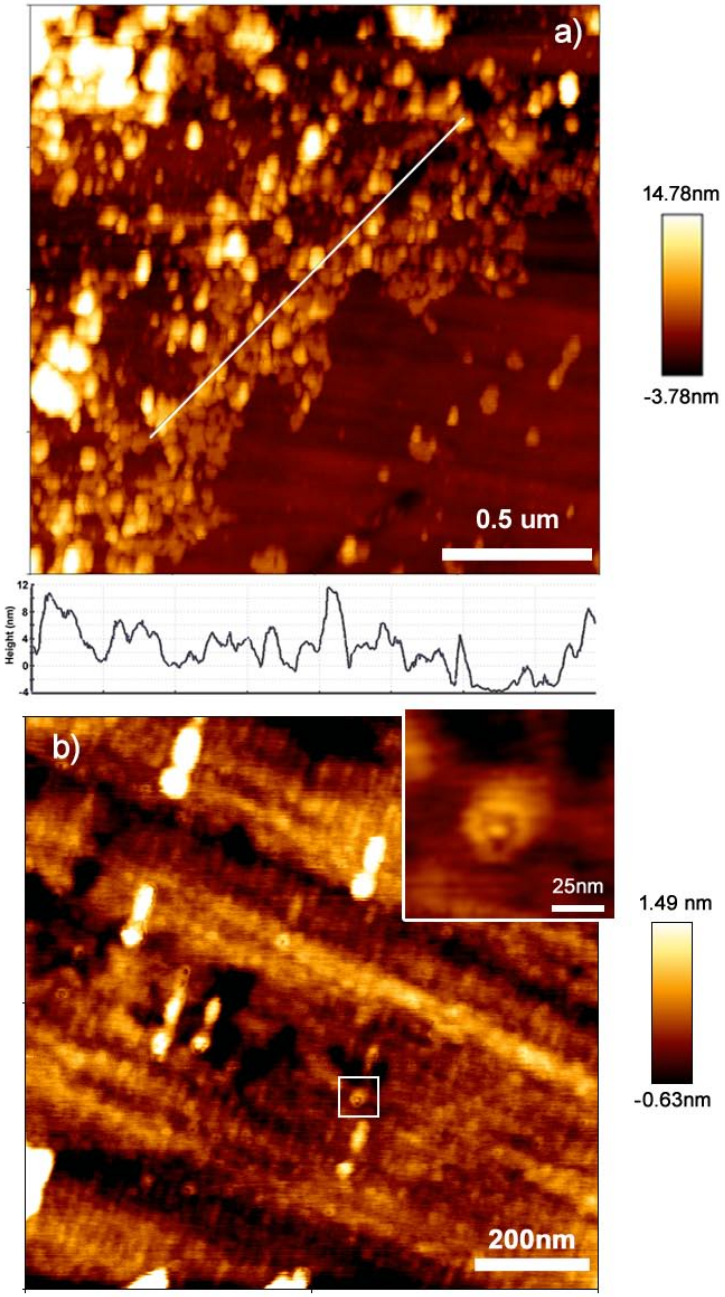

Figure 4.4 - A low resolution atomic force micrograph showing the height profile for the nanoparticles extracted from irradiated benzene is shown in a), while a higher resolution scan showing three distinct types of nanoparticles is presented in b). The inset is a magnification of the structure inside the small white square.

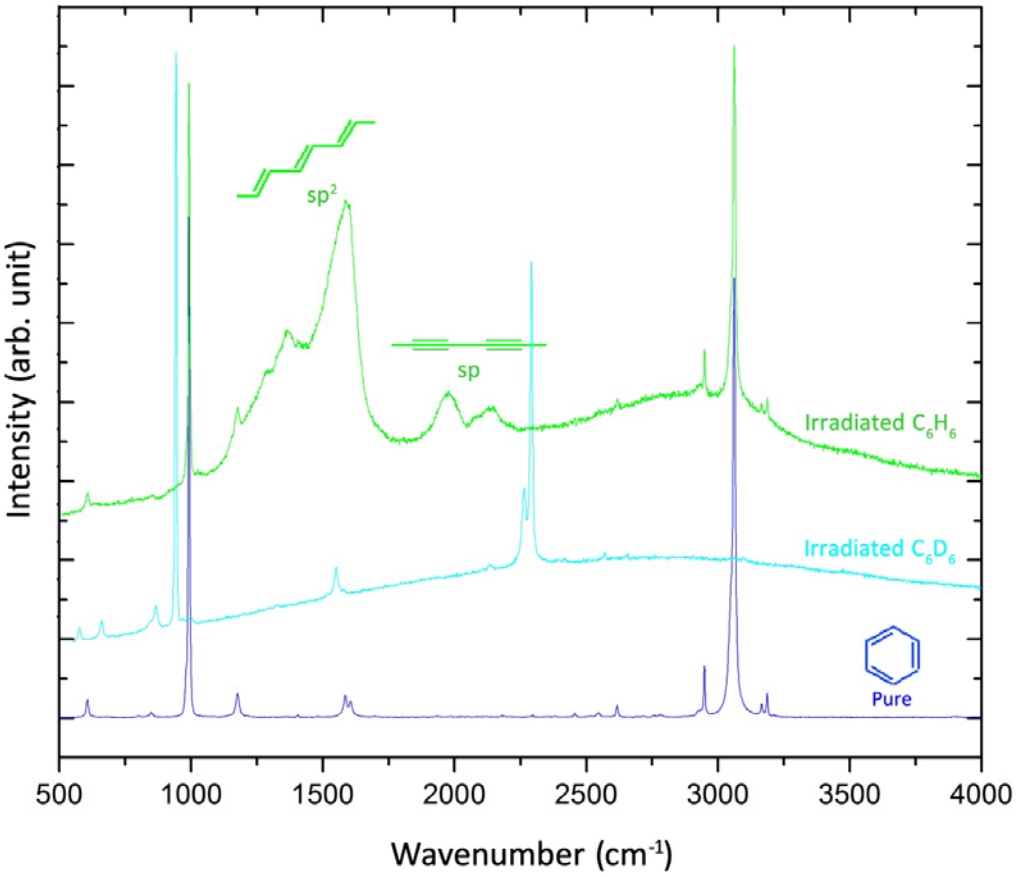

Figure 4.5 – Surface enhanced Raman spectra of pure benzene (blue), irradiated deuterated benzene (cyan), and irradiated benzene (green). Vibrational modes in the fingerprint regions of sp (polyynes) and sp^2 (amorphous) carbon are clearly present in the irradiated benzene solution.

small spherical particle with heights of 1 nm (Figure 4.4 b inset). The spherical and prolate particles appear similar to those previously observed in fs irradiated benzene [120] and are composed of amorphous carbon. The toroidal particles on the other hand exhibit a novel quasi- molecular morphology. These may consist of fullerenes [122] or cyclic polyynes [123] however it is also possible that these structures are assembled from smaller amorphous carbon nanoparticles. In order to determine the molecular structure of these particles and of the overall irradiated benzene solution surface enhanced Raman spectroscopy (SERS) was used.

Figure 4.5 shows the SERS spectra for both pure and irradiated liquid benzene. The spectrum of the pure sample shows all of the characteristic benzene peaks with the two strongest modes being the α-ring stretching mode (991.6 cm^{-1}) and the β C–H stretching mode (3060.7 cm^{-1}). The irradiated sample has spectral features associated with benzene, amorphous carbon and polyynes. The energies of features present in the SERS spectrum of irradiated benzene were determined by fitting with Gaussian or Lorentzian functions and are summarized in Table 4.1. The disorder induced D (1363 cm^{-1}) and combination G (1560 cm^{-1}, 1601 cm^{-1}) bands clearly indicate the presence of amorphous carbon in this material. The additional peak in this region at 1289 cm^{-1}, has been previously associated with acetylene or poly-acetylenic compounds [124, 125]. The fingerprint region for linear chain polyynes occurs from 1800 to 2200 cm^{-1}, and within this region there are three large spectral features in the spectrum of irradiated benzene occurring at 1974, 2075 and 2135 cm^{-1}. The first two peaks can be attributed to $C_{14}H_2$ and C_8H_2 respectively [126], while the third peak at 2135 cm^{-1} is most probably the carbyne anti-symmetric stretching mode [127]. It is also possible that this feature may originate from the C≡O bond of carbon monoxide [128] as the irradiation was carried out in air. The vibration modes of medium sized monocyclic polyyne isomers also occur in this region [129, 130], and suggest that cyclic polyynes could also be present in the irradiated sample. These data indicate that the nanostructures present in the residue extracted from irradiated benzene are primarily amorphous carbon but that they also contain a variety of polyynes. These polyyne molecules are the result of laser-induced dissociation of benzene together with subsequent radical reactions in solution.

The dissociation of benzene in the gaseous phase by fs-pulsed laser irradiation has been studied extensively [117-119]. Pulses from a Ti:Sapphire laser operating at 800nm produce little ionization in benzene at intensities in the 10^{13} Wcm^{-2} range. For both 50fs [117] and 200fs [118] pulse durations the parent ion, $C_6H_6^+$, was the predominant species in TOF spectra at this intensity. At higher intensities (up to 2.5 x 10^{14} Wcm^{-2}) the benzene ring was found to dissociate into numerous molecular fragments, $C_nH_n^+$. At intensities between 10^{16} W cm^{-2} and 10^{17} W cm^{-2} it was found that multiply charged carbon ions dominated in time of flight mass spectra [119]. The relative role of ionization and fragmentation in irradiated benzene is therefore a strong function of intensity, so that the products produced as the result of irradiation will be dependent on the particular laser system used. Figure 4 shows the TOF spectrum resulting from the irradiation of pure gaseous benzene with the present Ti:Sapphire laser. As reported by Castillejo [117] the predominant carbon species are seen to be the parent ion $C_6H_6^+$, as well as fragments such as $C_3H_n^+$, CH_n^+, C^+, and C^{2+} produced from the

Table 4. 1 – SERS peak positions for irradiated benzene	
Peak Position (cm^{-1})	Assignment
991.6	C_6H_6 (α)
1175.7	C_6H_6
1288.6	C_2H_2 (sp)
1363.7	D (sp^2)
1560.0	G (sp^2)
1601.0	G (sp^2)
1605.9	C_6H_6
1974.3	$C_{14}H_2$ (sp)
2075.1	C_8H_2 (sp)
2135.0	C≡C or C≡O (sp)
2948.2	C_6H_6
3060.7	C_6H_6 (β)
3165.4	C_6H_6
3186.2	C_6H_6

dissociation of the benzene ring. The same distribution of dissociation products is also seen in the TOF spectrum of C_6D_6 obtained under identical radiation conditions (Figure 4.6 bottom), but significantly we do not detect polyynes or amorphous carbon in the SERS spectrum of irradiated liquid C_6D_6 (Figure 4.6 top). The clamping intensity of a fs-laser filament depends inversely on the nonlinear refractive index, n_2, and is given as $I = \rho(I)/2n_2\rho_c$, where, $\rho(I)$, is the photo-generated electron density and, ρ_c, is the critical plasma density [117]. The ratio of intensities within each liquid is $I_D/I_B \approx 0.4$ indicating that the maximum intensity within the C_6D_6 is less than half of that of the C_6H_6 which accounts for the lack of fragmentation within the liquid benzene-d6. Laser-induced multi-photon ionization is the source of fragmentation of the benzene ring and is the process that dominates in the generation of the reactive fragments that initiate a complex chemistry in irradiated liquid

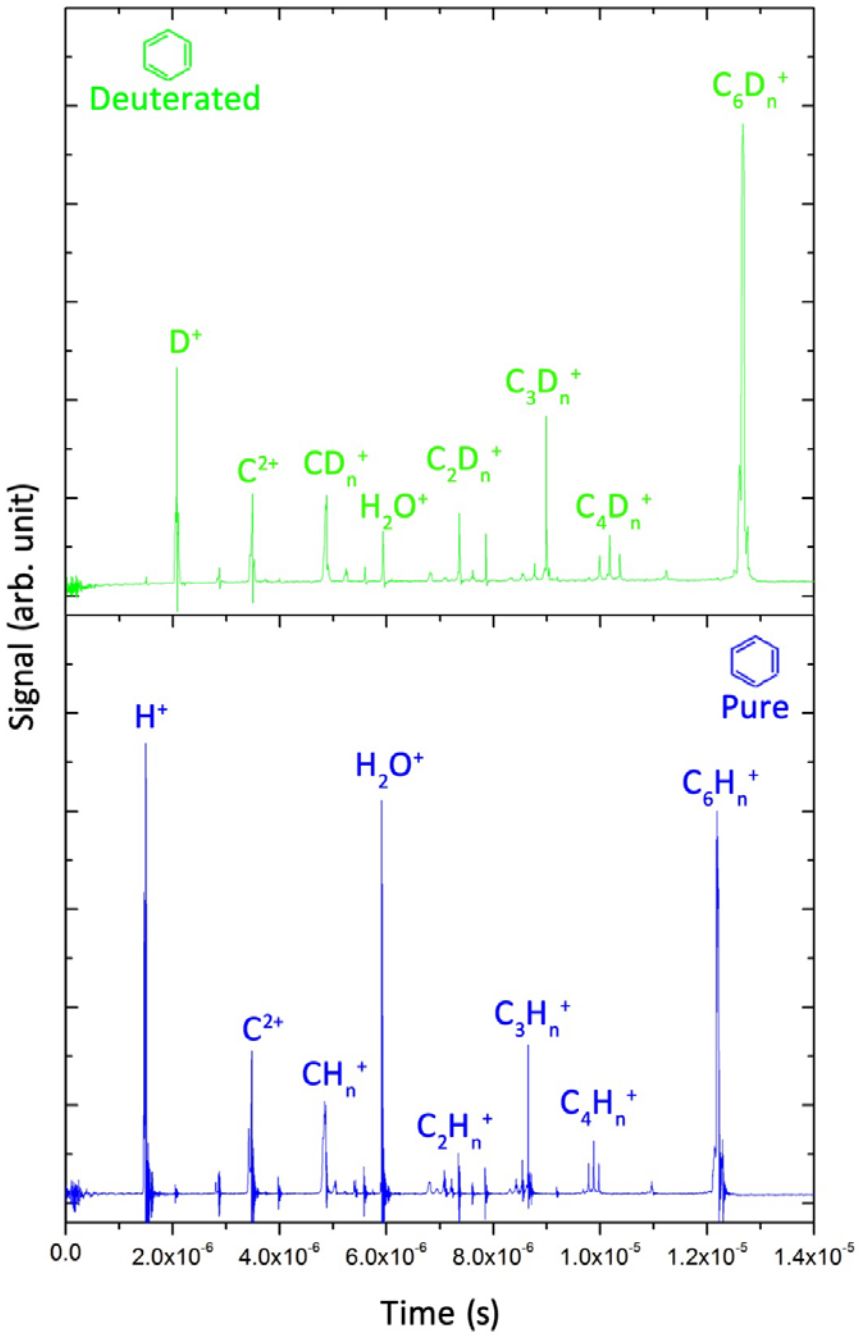

Figure 4.6 - Normalized time of flight mass spectrum resulting from the irradiation of gaseous benzene (bottom) and per-deutero benzene (top) by a 120 fs pulse at 800 nm and peak intensity of 10^{14} Wcm^{-2}.

benzene. The products of this chemistry include an amorphous carbon precipitate as observed in AFM images and detected in the SERS spectrum. While polyynes have been detected in solution after irradiation of alkane and acetone liquids, [100, 115] no evidence has previously been found for the formation of amorphous carbon. In a model proposed recently [100] to explain the formation of polyynes in the fs irradiation of liquid alkanes, long chain polyynes are the result of the insertion of C, C^+, C_2, and other primary dissociation products into small carbon chains. The present study shows that the formation of amorphous carbon is initiated by the reaction of primary dissociation products with C_6H_6 molecules in solution. A variety of substituted ring compounds would result from these reactions leading eventually to amorphous carbon. Polyynes appear to be the *sp*-bonded component of this structure, and it seems likely that the compounds seen in the SERS spectrum are not separate molecular species, but take the form of chains attached to aromatic rings. These chains probably act as bridges between clusters of sp^2-bonded rings. We note that SERS spectra do not show a feature at 3330 cm^{-1} that would be typical of terminal CH groups attached to free polyyne molecules. There is also no evidence for spectral features at 2946 cm^{-1} and 2924 cm^{-1} associated with CH_3 and CH_2 groups suggesting that the amorphous carbon generated by fs irradiation of liquid benzene has a sp-sp^2 bonded structure rather than the sp^2-sp^3 bonded structure that is characteristically observed in amorphous carbons [34]. A similar composition has also been observed in the fs irradiation of graphite surfaces [131]. The absence of amorphous carbon and polyynes in solution after fs irradiation of C_6D_6 is consistent with this reaction scheme, since the laser intensity in liquid C_6D_6 is insufficient to produce fragmentation.

4.3.2 Irradiation of Toluene

Figure 4.7 shows the irradiation setup for toluene (right) as well as the conical emissions (CE) typically associated with the filamentation process (left). Compared to the filament observed in benzene the filament formed in toluene was very bright indicating higher white light conversion efficiency. This is not surprising given that the nonlinear refractive index of toluene is lower than that of benzene [132, 133]. An interesting feature of CE is the radial order of spectral components. If CE was the result of diffraction, the light rings would tend to redden from the inside to the outside of the circle. The opposite is observed, with rings of bluer frequency appearing on the outer edge of the emission area. Several mechanisms have been put forth in the literature to describe the CE phenomenon, including four-wave mixing, self-phase modulation, Cerenkov radiation, and X-waves [78]; however there has been no definitive explanation of this phenomenon.

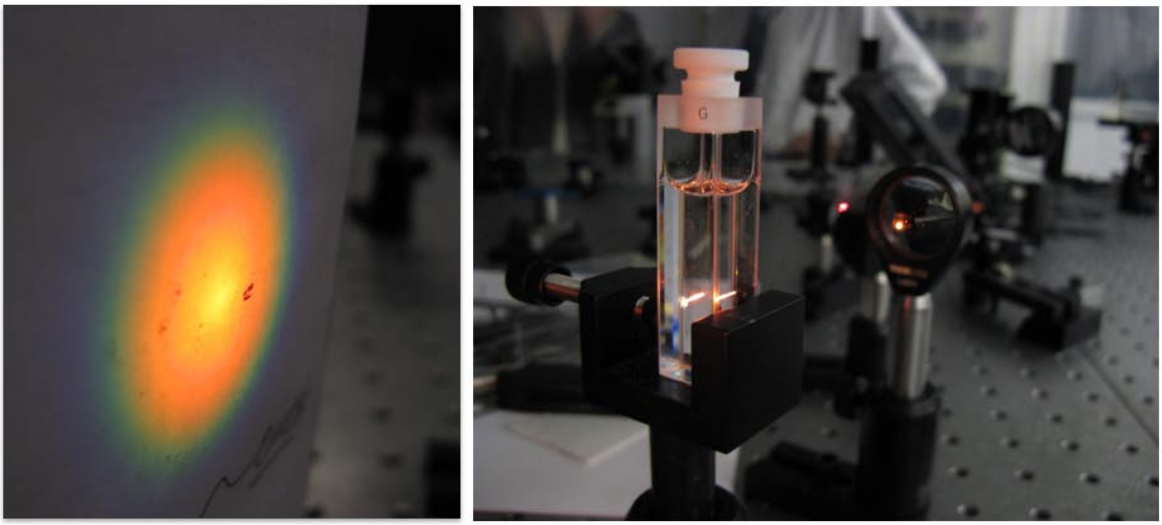

Figure 4.7 - The irradiation of toluene with fs laser beam (right), and the resulting white light and conical emissions (left).

After 1.5 hr of irradiation the liquid attained a yellowish hue. No particles were observed during this time period. With increased irradiation time the color of the fluid deepened slightly and a small amount of string-like particulate matter was observed after 4 hr; however, it was not possible to isolate this material for examination. The composition of the irradiated liquid was studied using Raman spectroscopy and its spectrum was compared to that of pure toluene (Figure 4.8). Toluene ($C_6H_5CH_3$) is a mono-substituted benzene derivative that has one hydrogen atom replaced by a methyl group and as such its vibrational spectrum appears similar to that of benzene (Figure 4.8 a). The most prominent mode occurs at 1003 cm^{-1} and results from the C=C ring breathing vibration (992 cm^{-1} in benzene). Other C=C stretching modes appear at 1030 and 1605 cm^{-1} [134]. In addition to these modes, features associated with ring-methyl vibrations arise at 784 cm^{-1} and 1208 cm^{-1}, while modes in the 2600 – 3200 cm^{-1} region are typical of the CH vibrations that occur in most hydrocarbon compounds. As with the previous experiment the energies of these features were determined through Gaussian or Lorentzian curve fitting. The spectral profile of irradiated toluene (Figure 4.8 b) is remarkably quite similar to that of pure toluene. While there is a large background photoluminescence, no appreciable change is detected in the energies of spectral features associated with the vibrational modes of toluene; however, a number of low intensity features do appear in the

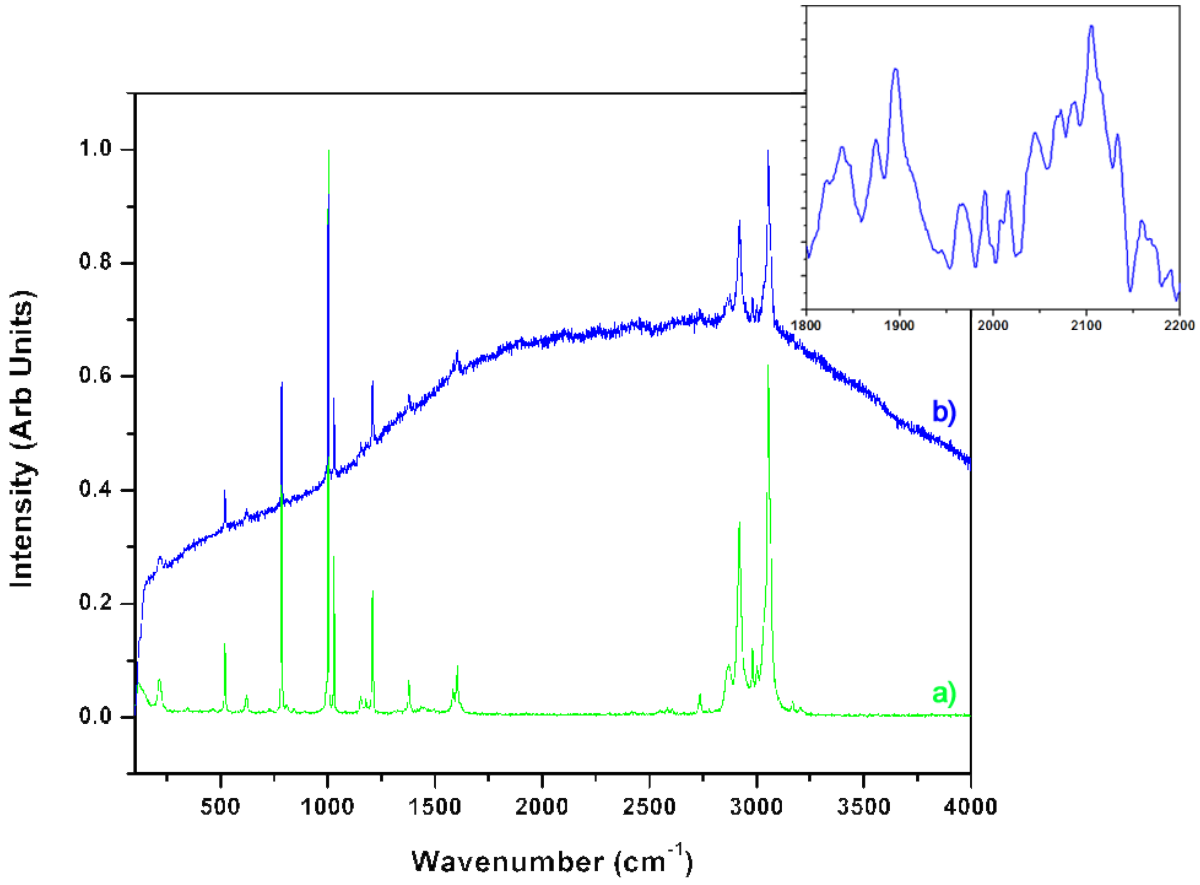

Figure 4.8 - The Raman spectra of a) pure and b) irradiated toluene. The inset is multi-accumulation scan of the 1800-2200 cm-1 region in the spectrum of irradiated toluene.

1800-2200cm^{-1} region. The appearance of these peaks without the need of surface enhancement suggests a high concentration of linearly hybridized carbon, which may be a result of the extended irradiation time. A multi-accumulation scan of this area is presented in the inset of Figure 4.8. Over a dozen well resolved features are shown, indicating a variety of polyyne and cumulene molecules have formed in the irradiated liquid [126, 130]. Not surprisingly, the strongest feature in this spectrum is centered at 2105 cm^{-1}. This mode generally occurs in acetylenic compounds with C≡C vibrations [135]. In samples with many spectral features such as this one, the identification of specific molecular species can be quite challenging due in part to the fact that there is often overlap of the fundamental vibrational modes. For example, it is well established that as the length of the polyyne chain

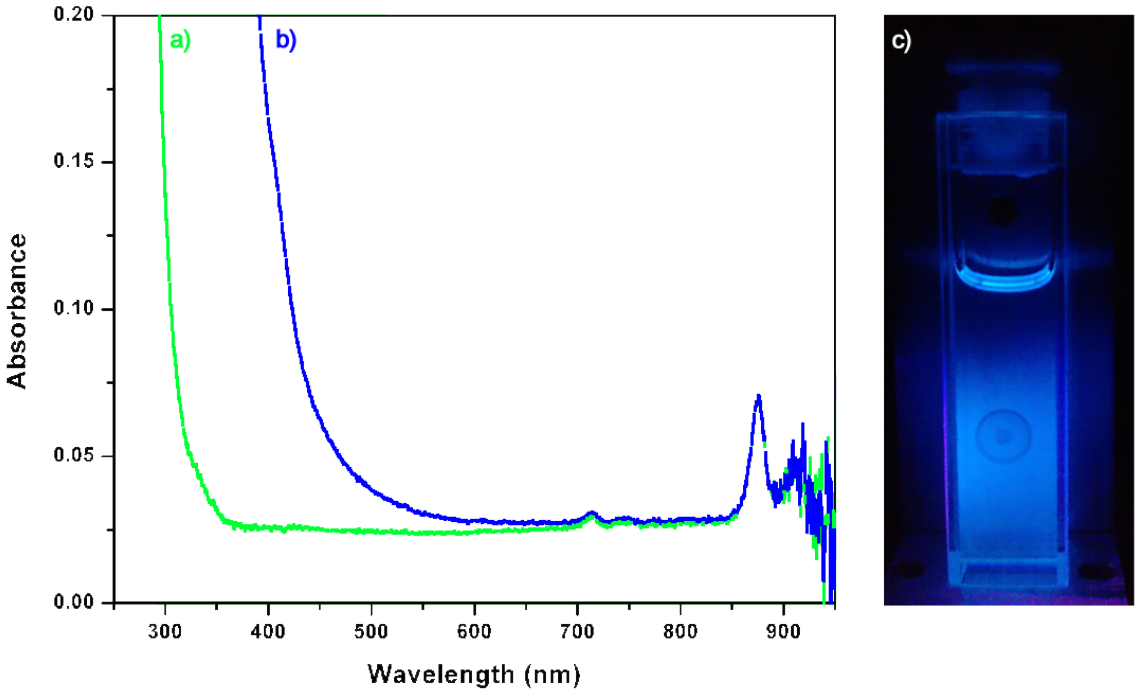

Figure 4.9 - The absorption spectrum of a) pure and b) irradiated toluene, as well as c) a photograph of the photoluminescence that results from the UV excitation (λ_{ex} = 365 nm) of the irradiated liquid.

increases, the frequency of its primary vibrational mode decreases [126]. This may result in the primary modes of long polyynes overlapping modes that belong to shorter cumulenes. Despite these difficulties, a number of chains have been conclusively identified, the most significant of these being $C_{20}H_2$. Density functional simulations suggest that this molecule has four totally symmetric vibrational modes in the polyyne fingerprint region [130]. These match to within a wavenumber with four features found in the present sample at frequencies of 2188, 2133, 2086, 1911 cm^{-1}. To date this is the longest polyyne molecule fabricated using the LP-PLI method. Spectral features associated with $C_{18}H_2$, $C_{16}H_2$, $C_{14}H_2$, $C_{12}H_2$ and $C_{10}H_2$ have also been identified in these samples [126, 136, 137].

The broadband photoluminescent (PL) background appearing in the Raman spectrum of irradiated toluene (Figure 4.8 b) is similar to that which appeared in irradiated benzene (Figure 4.5). This type of background PL was also reported in other liquid phase irradiation experiments where polyynes were an end product but was attributed to some unknown by-product of the laser irradiation

process [138]. To investigate the possible origins of this feature the UV-Vis absorption spectrum of irradiated toluene is shown in Figure 4.9. Pure toluene (Figure 4.9 a) begins to strongly absorb radiation at wavelengths below 350 nm. After irradiation (Figure 4.9 b) a bathochromic shift of over 100 nm is observed in the absorption spectrum, moving the lowest energy absorption edge well into visible wavelengths. A similar change was also reported, by Sato et al. [116], in the UV spectrum of irradiated hexane containing polyynes, where a red shift of 50 nm was reported. Red shifts in the absorption spectra of hydrocarbon molecules generally occur due to increasing bond conjugation which in turn results in a greater number of delocalized π-electrons present within the system [139]. Since the only appreciable change in the Raman spectrum of irradiated toluene is the appearance of polyyne modes it is reasonable to assume that the shift in the absorption spectrum is related to the formation of these substances. In fact, a relationship in which the HOMO-LUMO energy gap decrease with increasing chain length has been established for polyynes synthesized using other techniques [140, 141]. The longest polyyne observed in the Raman spectrum of irradiated toluene ($C_{20}H_2$) has a lowest absorption energy of ~ 3.3 eV [141] and therefore cannot account entirely for the absorption edge in Figure 4.9 b). It is possible that longer polyynes or polyynes with more complex end groups, such as methyl or butyl groups, exist in the sample and simply have not been identified due to the complexity of the features in the Raman fingerprint region. These could account for the observed absorption feature and future work should include simulation of these molecules and their vibrational features to determine if their profiles are present in the Raman data. Even without knowledge of the exact nature of the absorption mechanism, the generation of fluorescent liquids by LP-LPI could prove useful. Materials such as these could be used as fluorescent dyes, or as markers in biological applications. In that vein Figure 4.9 c) shows a photograph of the PL emission from irradiated toluene after excitation with 365 nm (3.40 eV) radiation from a UV LED. The PL appears blue and has a central maximum of ~ 450 nm (2.75 eV). Exciting the same sample with lower energy, 488 nm (2.54 eV), light from the Ar^+ laser used in the Raman system resulted in the background shown in Figure 4.8 b). A precise measure of the PL emissions was accomplished by deconvolution of that background into two broad Gaussian PL emission bands, one of low intensity centered at 522 nm (2.38 eV) and one of high intensity at 568 nm (2.18 eV). The appearance of multiple emission features suggests the presence of several absorption bands and higher resolution studies of the UV-VIS absorption, and PL characteristics of these samples is recommended as future work.

One of the other curious aspects of this experiment is the relative lack of an amorphous phase in irradiated toluene. In irradiated benzene it was suggested that amorphous carbon formed when laser

initiated dissociation products interacted with benzene molecules outside of the laser focus forming substituted benzenes that eventually built up into a more complex sp-sp^2 matrix. This did not occur in irradiated benzene-d6 because the intensity inside the laser filament was not high enough to initiate dissociation of the molecule. The ionization potential of toluene (8.82 eV) is lower than that of benzene (9.24 eV), and it has been shown to readily fragment in the gas phase at the laser intensity used in this work [117]. In the liquid phase the clamping intensity of a laser filament in toluene is estimated to be nearly double that of benzene ($I_T/I_B \approx 1.8$) suggesting that there should be enough energy inside the focal regions of the filament to initiate dissociation [78, 132, 133]. The formation of polyynes also implies that dissociation of the parent molecule must be taking place. The reason for the preferential synthesis of polyynes over amorphous carbon in irradiated toluene is still unclear. One possible explanation involves the additional methyl group that is attached to the toluene molecule. It is generally accepted that the stability of polyynes is greatly improved by the addition of end groups [142, 143]. These groups prevent the reactive polyyne cores from cross-linking or reacting with other species by providing steric bulk and electronic stabilization [143]. The dissociation of toluene produces many fragments including, CH_n^+ $C_3H_n^+$, $C_4H_n^+$ and the singly and doubly charged parent ions $C_7H_8^+$ and $C_7H_8^{2+}$ [117, 144]. Importantly, many of these ions still contain the methyl group and when polyynes form via carbon addition reactions with these ions, it is possible that they are stabilized by these groups. As such they would not be reactive and would be unavailable as building blocks to form an extended amorphous network. As suggested earlier this may also account for the large red shift in the UV-Vis data; however additional work must be completed to elucidate this mechanism.

4.3.3 Irradiation of Ferrocene

Ferrocene is an organometallic compound that consists of two cyclopentadienyl (Cp^-) groups ($C_5H_5^-$) bound to a central iron atom in a sandwich configuration. In its stable form it exists as a light orange powder and is widely used in material science as either a catalyst or precursor molecule in the synthesis of carbon nanotubes [145-147]. Ferrocene is soluble in benzene and at the concentrations used in this work the resulting solutions had a yellow to deep orange colour. Irradiation of a 0.14 g mL^{-1} solution, in the top down configuration, is shown in Figure 4.10a. When the fs-laser beam was focused near the surface of the liquid a very intense region of dissociation and ionization was observed. Bubbles containing plasma, which appear as bright streaks in the photo, were ejected

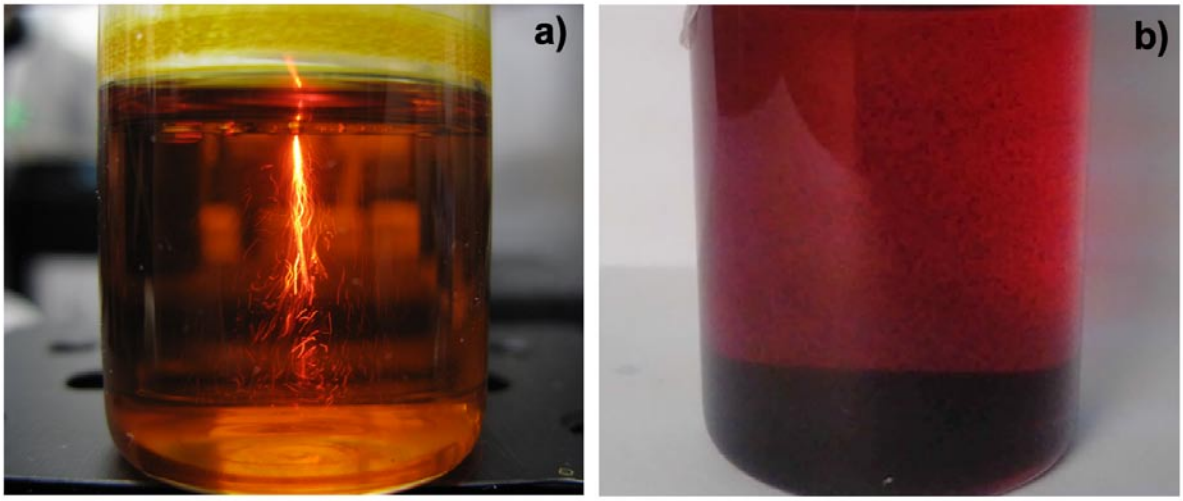

Figure 4.10– The irradiation of ferrocene in the top down configuration is shown in a), while the black dissociation product formed during irradiation is displayed in b).

violently from the focal region. Material synthesis occurred very rapidly in this scenario with clusters of black nanoparticles becoming visible in the solution within the first ten minutes of irradiation (Figure 4.10 b). On average, samples were irradiated for 1 hr, which resulted in the production of a few milligrams of powder. While further irradiation led to additional material synthesis a saturation point was eventually reached where the particulate matter disrupted the focus and arrested ionization.

The nanoscale morphology of the synthesized material, both in an unaltered and purified state, is shown in a series of scanning electron and atomic force micrographs (Figures 4.11-4.18). A fascinating array of nano and microstructures are present in the unaltered samples. For example, dendritic crystalline regions, which appear orange under an optical microscope, have formed sporadically on the sample surface. These are shown in Figure 4.11 and likely result from the evaporation of the irradiated solvent and crystallization of remnant ferrocene. Energy-dispersive X-ray spectroscopy (EDS) does indicate, however, that additional carbon is present in these regions, with an atomic ratio of 16:1, carbon to iron. In all probability the six extra carbon atoms manifest due to benzene dissociation products that remain after the solvent has evaporated. At the highest magnification (100 KX) these structures appear to be comprised of fused nanoparticles that individually range in diameter from 50-70 nm (Figure 4.11 d).

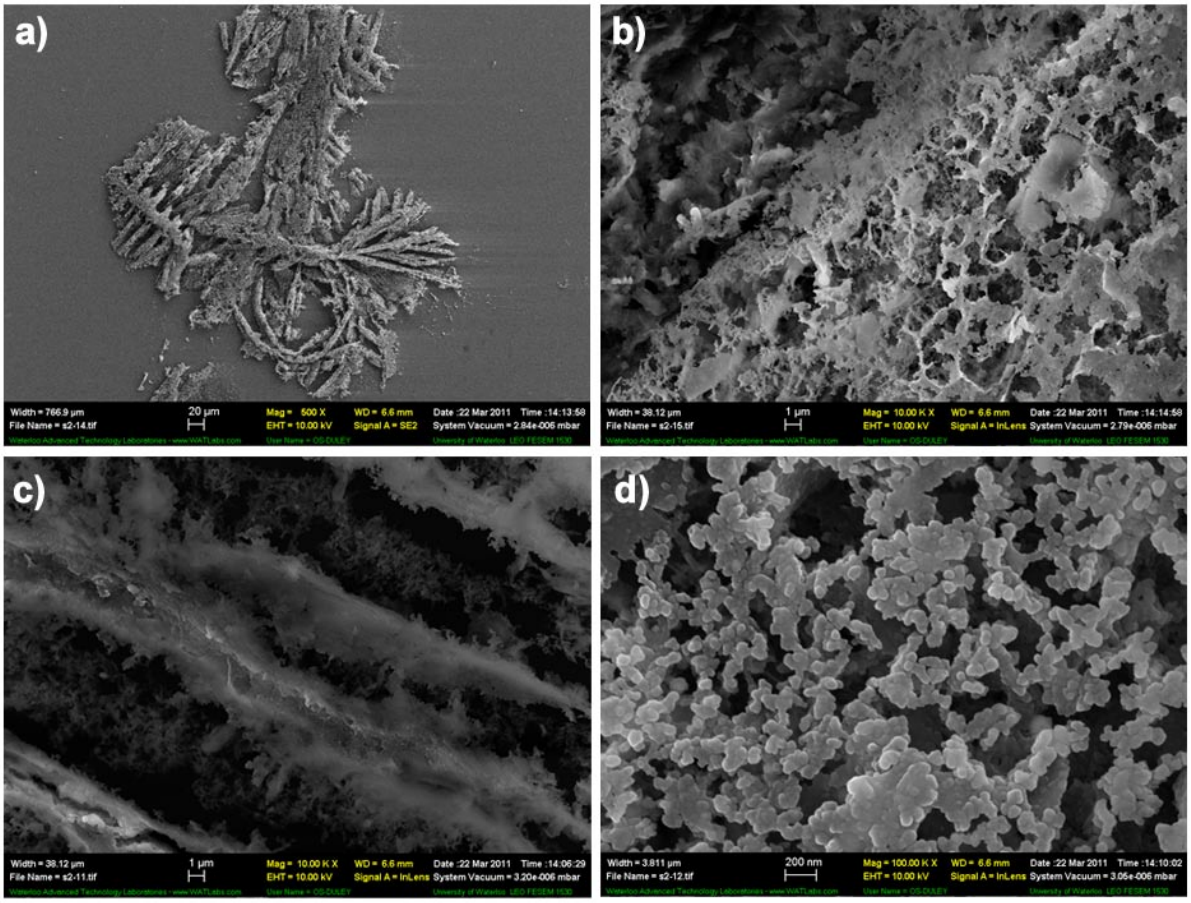

Figure 4.11– Micrographs showing the dendritic crystal growth of remnant ferrocene after evaporation of irradiated solution. At the highest magnification d) shows that these structures are composed of fused nanoparticle.

Other regions of the substrate are blanketed in large swathes of nanoparticles that are on average 50 nm in diameter (Figure 4.12). Carbon coated iron nanoparticles have been reported as products in many reactions involving ferrocene including pyrolysis [148] and co-carbonization [149]. It is possible; therefore, that the nanoparticles produced in the LP-PLI of ferrocene are similar to those synthesized using other techniques. Lying above the particles in Figure 4.12 is an interconnected network of nanoribbons. The nanoribbons range in width from 50 - 400 nm, are between 30-60 nm thick, and appear to be atomically smooth. In 2008, Campos-Delgado et al. [150] reported the production of thin graphite ribbons by the aerosol pyrolysis of solutions containing ferrocene dissolved in thiophene (C_4H_4S) and ethanol (CH_3CH_2OH). Those ribbons were found to

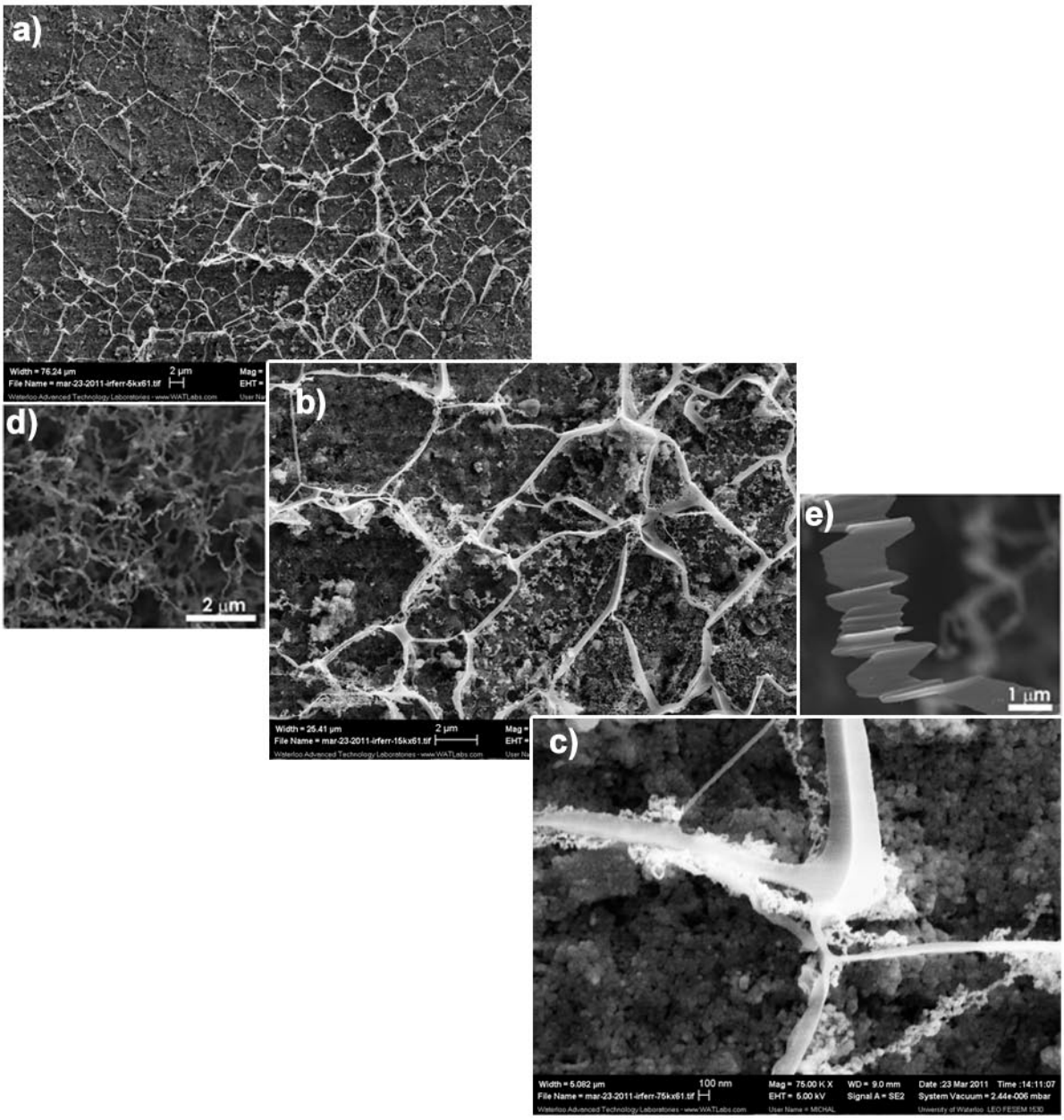

Figure 4.12 – Images a), b) and c) show nanoparticles covered by an interconnected nanoribbon network at increasing magnification. Images d) and e) show the graphite nanoribbons fabricated by Campos-Delgado et al. [150] for comparison.

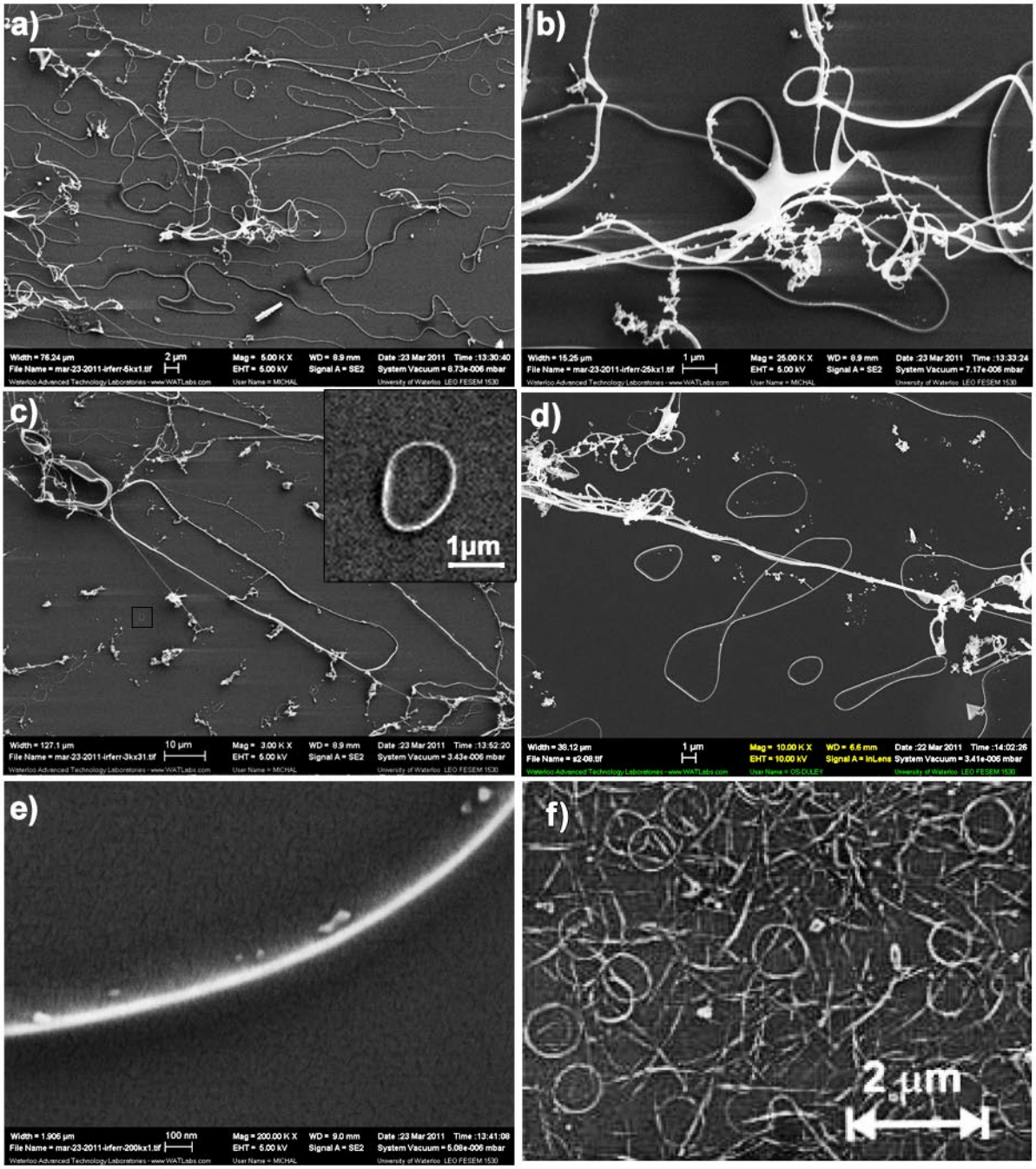

Figure 4.13 – Examples of the loop structures formed in irradiated solutions of ferrocene and benzene (a-e). Rings are present both, on and partially above the surface of the substrate as seen in b) and c). The inset in c) is a magnified view of a small ring on the surface. Rings formed of bundled carbon nanotubes appear somewhat similar to those synthesized here and are presented in f) for comparison [154].

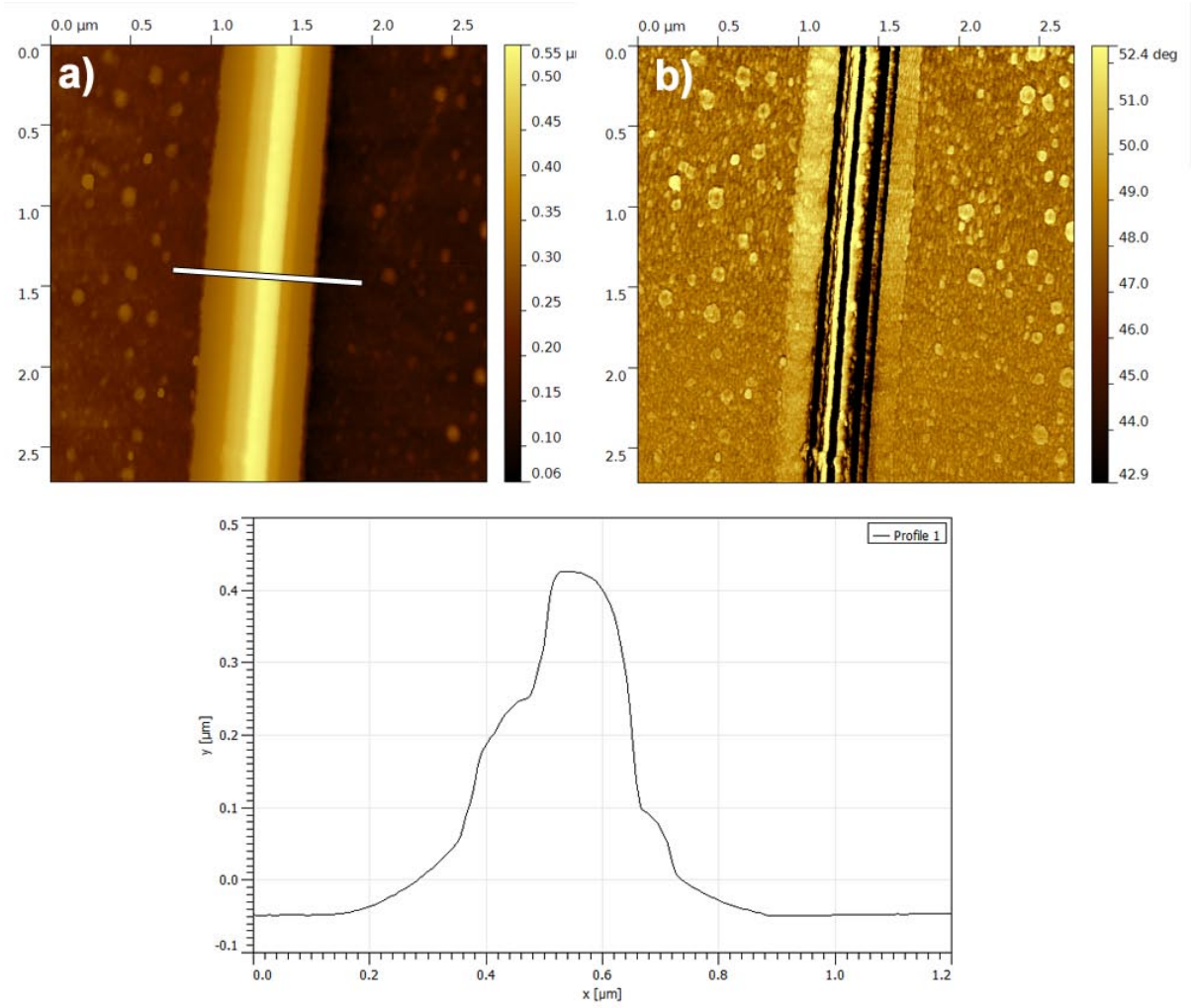

Figure 4.14– Atomic force micrographs of a loop structure formed in irradiated ferrocene. The height scan is shown in a) while the phase image is shown in b). The inset at the bottom of the figure is the cross sectional height profile that corresponds to the white bar in a).

exhibit lengths of several micrometers, widths ranging from 20 to 300 nm and thicknesses of less than 15 nm. The ribbons also exhibited perfect ABAB graphitic stacking and it was concluded that they were comprised of 2-40 layers of graphene. For comparison to the ribbons created here they are shown in Figure 4.12 d) and e).

Areas with a lower particle density are often covered in more exotic surface features including; loops, microtubules and spherical structures. A representative sample of the continuous

loops is presented in Figure 4.13. The shape and size of these structures vary considerably, with the smallest having path lengths and diameters on the order of a few micrometers (Figure 4.13 c inset). The largest loops, meanwhile, can stretch for hundreds of micrometers and have wire-like outer rims that range in diameter from 40 – 1000 nm (Figure 4.13 e). These structures are reminiscent of the ring-like stains formed by contact line deposition [151]; however, some loops are suspended partially above the surface of the substrate (Figure 4.13 b and c) and therefore are not likely to result from this mechanism. To determine if the loop edges are particulate they were also examined using atomic force microscopy. The high resolution topographical image of a ring located directly on the surface of the substrate and its corresponding phase scan are shown in Figure 4.14 a) and b) respectively. A cross-sectional line profile of the ring edge shows that it has a heterogeneous structure, a maximum height of 470 nm and an average roughness of 1.1 nm along the rim. Often taken in conjunction with topographical scans, phase images display the phase lag between the driving oscillations sent to the cantilever and its actual oscillation. Phase delays occur when energy is lost due to interaction of the scanning tip and the sample and changes in lag can indicate variations in a material's physical or mechanical properties [152]. Figure 4.14 b) shows striations of differing phase along the length of the wire that correspond to the changes in slope seen in the topographical image. These results suggest that the loop edges are made of bundled fibers and this could account for the large range in observed edge diameters (Figure 4.13). The only analogous structures to these are carbon nanotube rings formed by sonification and chemical treatment of straight carbon nanotube bundles or catalytically by thermal decomposition of hydrocarbon gas [153, 154]. An example of these rings is shown in Figure 4.13 f) for comparison to the structures synthesized here [154].

A series of increasingly magnified images showing a microtubule are presented in Figure 4.15 a) - c). This hollow tube is 38 μm long, has an average diameter of 2 μm, is riddled with holes, and is entangled in a number of nano fibers and ribbons. Spherical nodules with a 500 nm diameter are also attached to the outer surface of the tube as illustrated in Figure 4.15 c). It appears, given the inset in Figure 4.15 a), that the tube may have formed when a nanoribbon curled in on itself; however, this has not been determined conclusively. Hollow carbon microtubes of similar diameter have been fabricated through the thermochemical decomposition of ZnS and activated carbon [155]. Those tubes are highly symmetrical and crystalline in nature with surprisingly thin walls (10-20 nm) and good field emission properties. They are shown in Figure 4.15 d) and e) for reference.

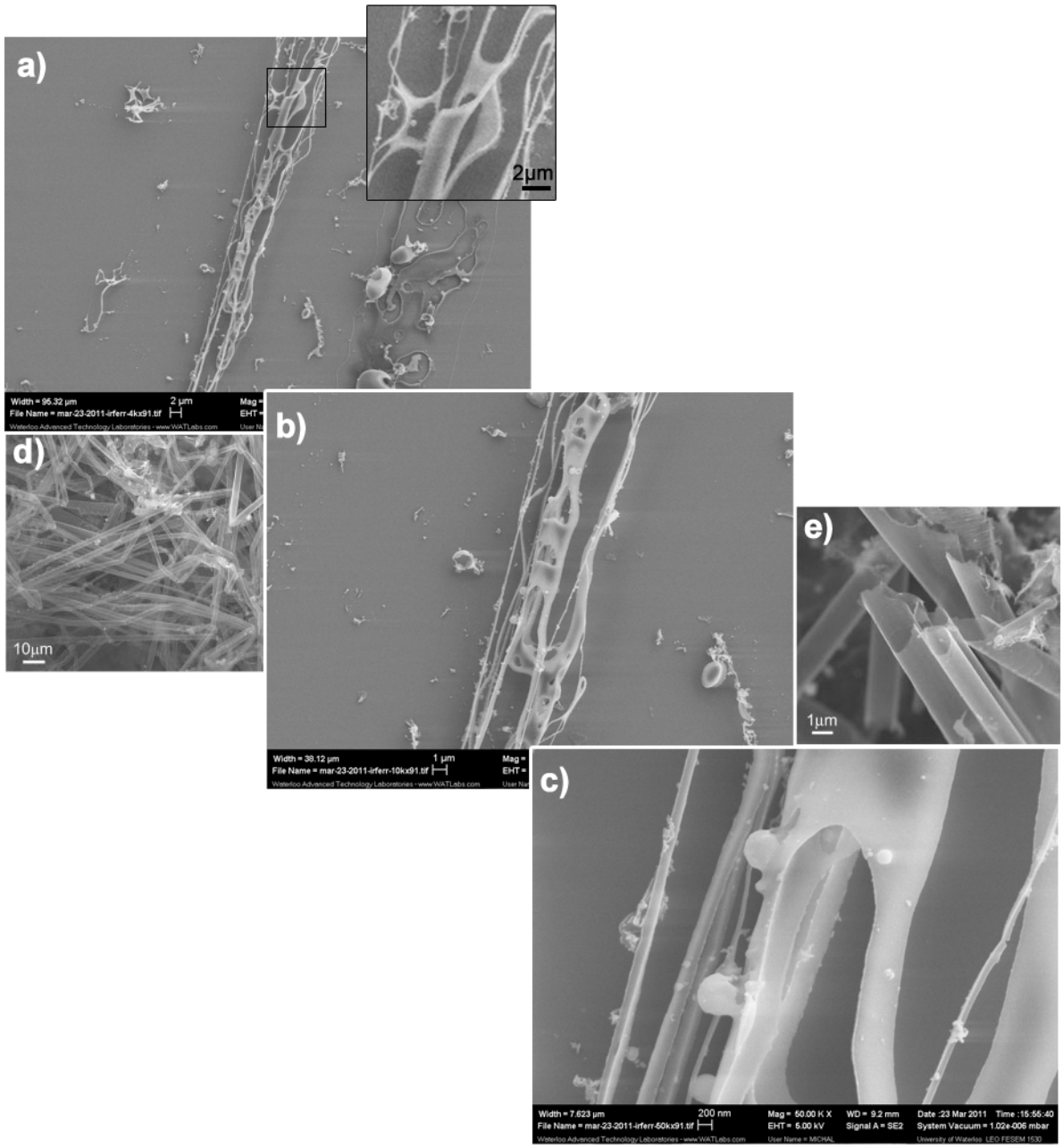

Figure 4.15– Increasingly magnified images of hollow microtubule structures (a-c). The inset in a) shows a magnified view of the end of a tube that appears to have curled in on itself. Small spherical nodules also appear to have grown on the outer wall of the tube in c). Hollow carbon tubes created by thermo-chemical decomposition are shown for reference in d) and e) [155].

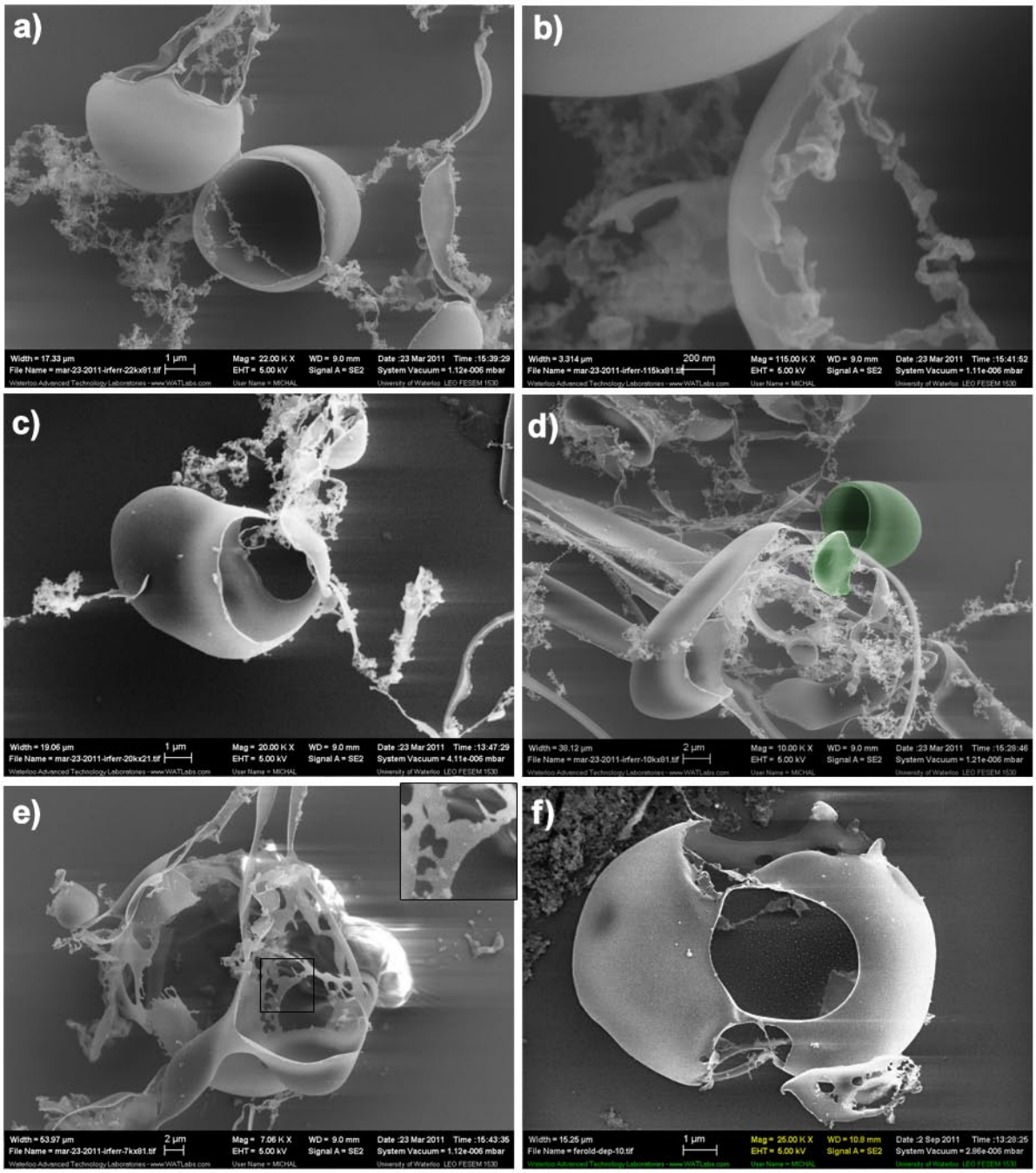

Figure 4.16– Micrographs of the spherical shaped microstructures formed in irradiated ferrocene. Two touching hemispheres that are each attached to furled nanoribbons are shown in a) and b). Egg shaped microshells are shown in c), and d) with false colour added to d) indicating the top and bottom of a shell that has become separated. The largest spherical objects are shown in e) and f).

Perhaps the most surprising structures formed in the irradiated solution are shown in Figure 4.16. These objects range in appearance from hollow hemispheres to ruptured prolate spheroids and can grow to be a large as 25 μm in diameter. They occur frequently on the substrate and always appear either attached to, or very near, nanoribbons. Two open hemispheres are shown in Figure 4.16 a), with a magnified image of them shown in Figure 4.16 b). Even at high magnification the outer wall of these microshells is very smooth and its diameter is in the same range, 30-60 nm, as observed in the nanoribbons in Figure 4.12. The ribbons seen in both of these images are curly and appear to result from unfurling of the hemisphere walls (Figure 4.16 b). Microshells that are more egg shaped (prolate spheroids) are presented in Figures 4.16 c) and d). False colour has been added to outline a shell and its top that have become separated in Figure 4.16 d). The structures in the first four images all have relatively similar dimensions (~4-6 μm diameters). The final two images (Figure 4.16 e and f) are of spheres that are considerably larger than the others shown (~10-25 μm diameters). The shell in Figure 4.16 e) is spherical, with a 25 μm diameter, but does not have a continuous outer wall with jagged edged holes dominating the structure as seen in the inset of the image. The prolate spheroid in Figure 4.16 f) has a polar axis that is 10 μm long, an equatorial diameter of 8 μm and a large rupture in its center.

The higher order structures observed in previous samples appear to be destroyed during the purification process. A series of images showing the morphology of the purified dissociation product are presented in Figure 4.18. The substrate is littered with micron sized clusters of light and dark material (Figure 4.18 a-d). At high magnification the cluster shown in Figure 4.18 d) has the appearance of a porous matrix that according to EDS is a mixture of carbon and iron. The round white nanoparticles embedded in the matrix range in diameter from 10-100 nm and are lighter in appearance because they are composed of a larger percentage of iron which has a higher atomic mass than carbon. Microfibres and nanotubes are also present in these samples but occur infrequently. The fibre in Figure 4.18e has a diameter that ranges between 6-15 μm and is over 300 μm long. The nanotube in Figure 4.18 f) is 76 nm in diameter and stretches across a 1.3 μm long gap to attach to nanoparticle clusters at either end. It also appears that a faceted nanoparticle is embedded in one end of this tube (Figure 4.18 f inset). The spontaneous formation of highly ordered mesoscale structures that exhibit four unique geometries (loops, ribbons, tubes, and spheres) in the unaltered samples is quite interesting. Their absence after the purification process, which includes centrifugation, suggests that they are somewhat delicate. The synthesis of micro structures from molecular building blocks is generally thought to be governed by the interplay of two processes: crystallization and aggregation

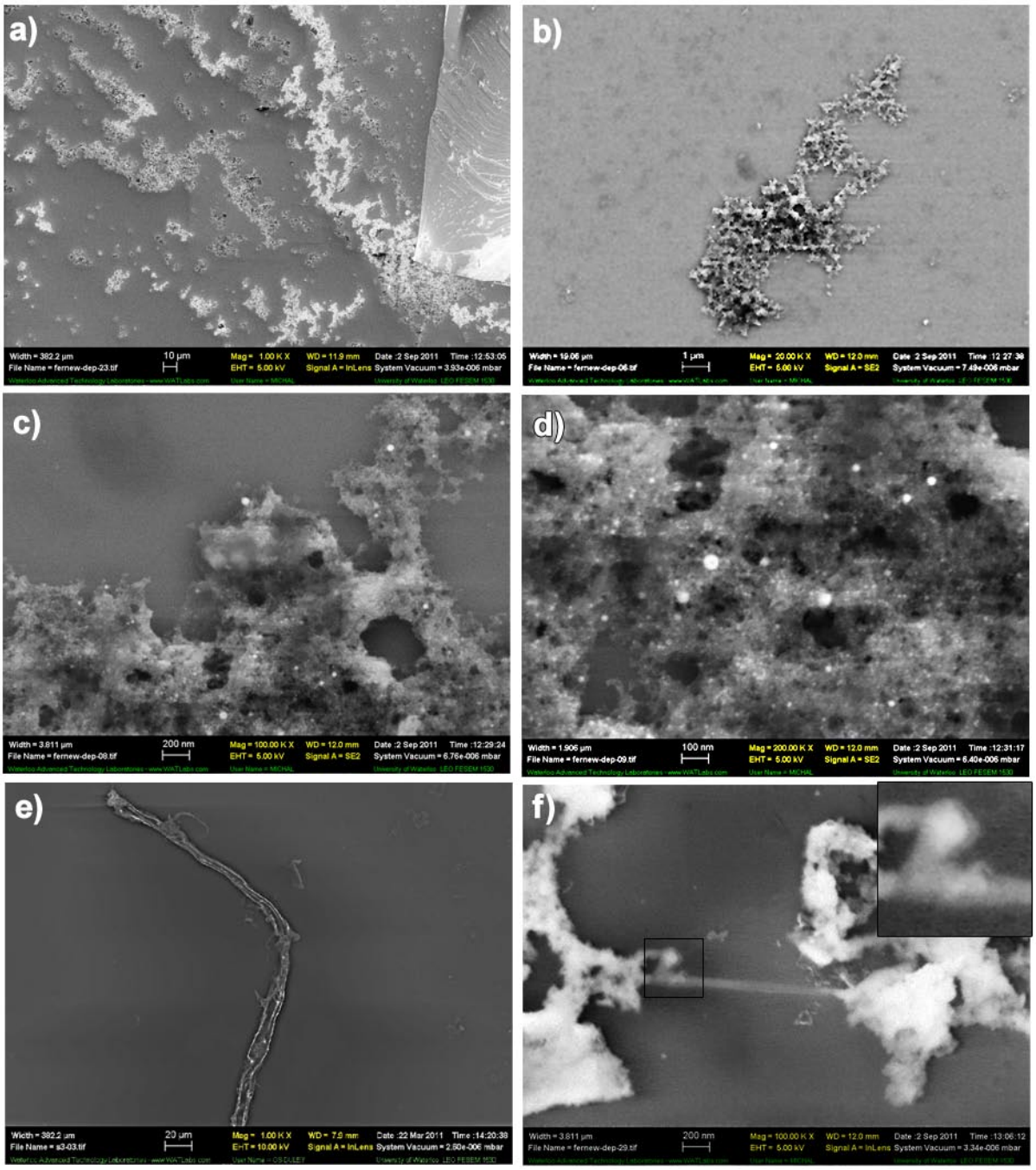

Figure 4.17– Micrographs showing the nanostructures present after purification of the black dissociation products. The main products are nanoparticles (a-d), while long microfibers e) and nanotubes f), are also present in low quantities.

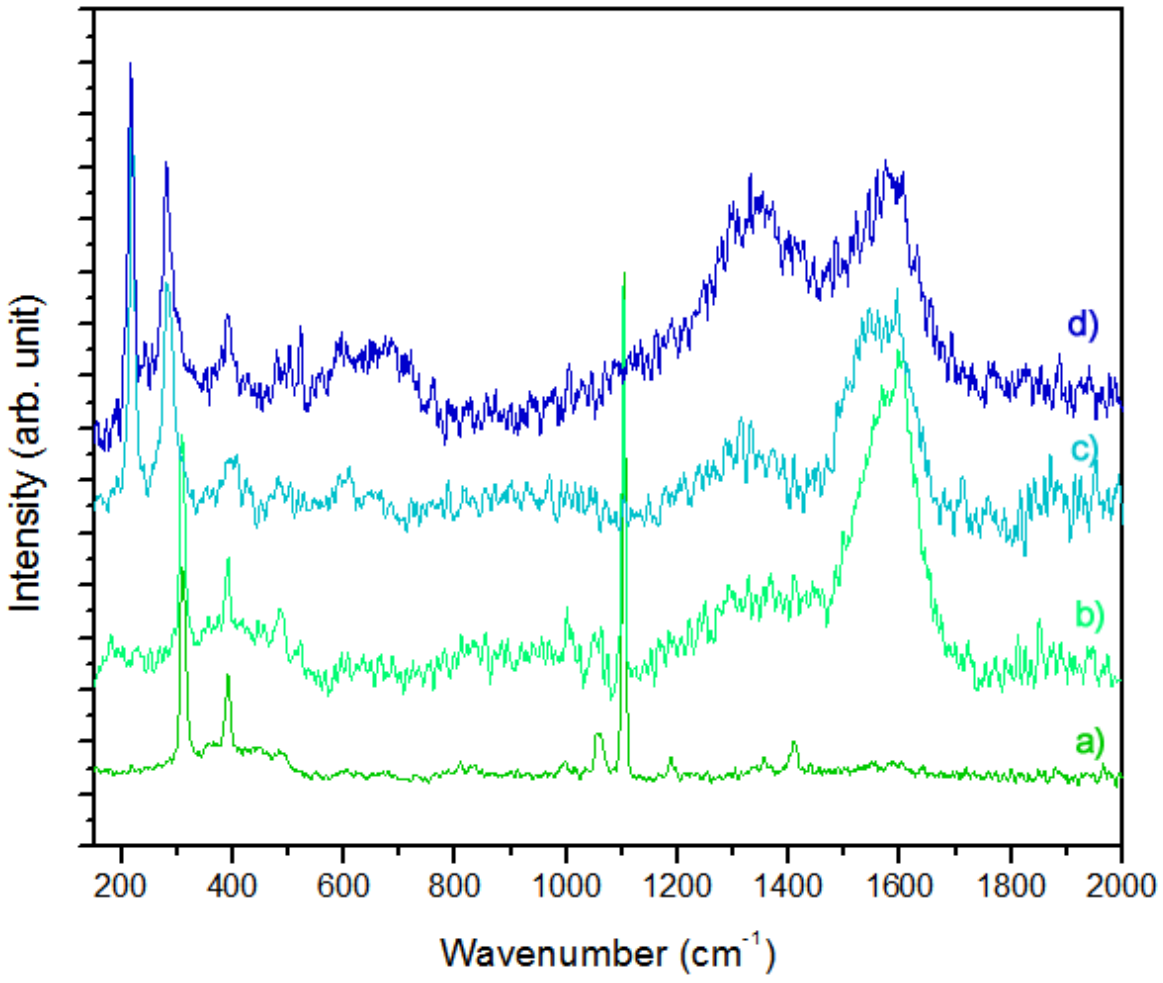

Figure 4.18– Raman spectra of a) ferrocene crystals, b) ferrocene crystals from irradiated solution, c) unaltered dissociation products, d) purified dissociation products.

[156]. While these two mechanisms are likely at play here, it is impossible to elucidate the formation process using microscopic data alone and therefore the vibrational properties of these materials were also studied.

Figure 4.18 shows the normalized Raman spectra (488 nm Ar^+ laser excitation) of a) virgin ferrocene crystals, b) crystals from irradiated solution, c) unaltered irradiation products and d) purified irradiation products. The peak positions in each curve and their probable assignments are summarized in Table 4.2. Ferrocene has a number of prominent vibrational modes. At higher energies the two strong features seen in Figure 4.18a arise due to ring-metal A_{1g} stretching (310.5 cm^{-1}) and

Table 4.2 – Vibrational modes identified in by-products of ferrocene irradiation				
Peak Positions (cm^{-1})				Assignment
Virgin Ferro Cryst	Irrad Ferro Cryst	Irrad Powder	Pure Irrad Powder	[157-168]
		217.8 s	216.4 s	Fe-Fe?
		283.2 s	280.9 s	Fe-C?
310.5 s	308.6 s			Sym. Fe-Cp str.
390.9 s	390.7 s	393.7 m	391.6 s	Sym Cp tilt
485.8 w	485.7 m	484.8 w	479.2 m	Asym. Fe-Cp str.
		602.8 w	594.5 m	C=C bend
		649.6 m	673.4 m	C-C str.
808.7 w				C-H bend
829.5 w				C-H bend
994.3 w	1000.8 m			C-H bend
1060.6 m	1055.4 m			C-H bend
1102.4 s	1102.1 s			Cp breathing
1188.2 m				C-H bend
1354.5 w	1330.0 m	1316.4 m	1340.4 s	C=C str., D
1407.8 m				C-C str.
1551.6 w	1556.7 s	1562.3 s	1578.9 s	C=C str., G
	1604.9 s	1603.5 s	1603.8 s	
s = strong, m = medium, w = weak, str.=stretching,				

symmetric E_{1g} ring tilting (390.9 cm^{-1}) vibrations, while the strongest feature in the spectrum (1102.4 cm^{-1}) is associated with the breathing mode of Cp rings [157]. The weaker modes all result from either C-H bending (1060.6, 1188.2 cm^{-1}) or C-C stretching vibrations (1354.4, 1407.8 cm^{-1}). The crystals shown in Figure 4.11, which formed after evaporation of the irradiated solution, have Raman spectra (Figure 4.18 b) that are very similar to that of the virgin ferrocene. The ring-metal, ring tilt

and ring breathing modes are all present at approximately the same energies; however, new features have also arisen while others have disappeared. The most obvious new peaks are the well known D and G modes associated with vibrations of clustered sp^2 carbon [34]. Amorphous carbon is typically viewed as a collection of independent sp^2 clusters bonded to a sp^3 carbon matrix. The size of these clusters, L_a, may be determined by through the Tuinstra and Koenig relation [158], which relates the ratio of the intensities of the D and G modes to the cluster size, $I_D/I_G = C(\lambda)/L_a$ where $C(\lambda)$ is a wavelength dependent fitting parameter which for the wavelength used here is $C(488\text{ nm}) = 35.04$ Å [159]. In Figure 4.18 b) the D mode is centered on 1330.0 cm^{-1}, while the G mode is deconvolved into two peaks at 1556.7 and 1604 cm^{-1}. The ratio of the intensity of these two peaks is $I_D/I_G = 0.32$, corresponding to a cluster size of 11.0 nm. These results corroborate the EDS analysis of Figure 4.11 which showed six additional carbon atoms for each iron present in these structures. Given the synthesis of amorphous carbon in irradiated benzene (Section 4.3.1) it's probable that this additional carbon comes from dissociation of the solvent. The disappearance of some C-H bending modes suggests dehydrogenation of the original ferrocene and it is possible that some hydrogen is being replaced with carbon leading to the observed spectrum. Instead of being bound in a sp^3 matrix, as would be expected in traditional amorphous carbon, the sp^2 clusters are likely cross-linking ferrocene molecules. Similar structures such as dibenzoferrocene (bis-indenyliron(II)) have been prepared chemically [160, 161], although information on their Raman spectra does not appear to be available in the literature.

A representative spectrum of unaltered black irradiation products is shown in Figure 4.18 c) while the spectrum of the purified powder is shown in Figure 4.18 d). The spectra differ significantly from those of the crystals, although two modes associated with the Cp ring are still present (394.7 and 484.8 cm^{-1}). Both the unaltered and purified materials contain significant amounts of sp^2 carbon with D modes at 1316.4 and 1340.4 cm^{-1} respectively. The G modes each have two components with peaks occurring at 1562.9 and 1603.5 cm^{-1} in the unaltered spectrum and 1578.9 and 1603.8 cm^{-1} in the purified samples. The intensity ratios of the D and G bands are $I_D/I_G = 0.41$ and $I_D/I_G = 0.96$ for each sample respectively. These values correspond to a cluster size of 8.5 nm in the unaltered samples and 3.7 nm in the purified powder. A decrease in the size of the sp^2 clusters makes sense given the shrinking size of the structures, observed microscopically, in two types of samples. Bending and stretching modes associated carbon double and single bonds are also present in both spectra. By far the most pronounced features in either spectrum are two low frequency peaks at 217.8 and 283.2 cm^{-1} in the unaltered samples and 216.4 and 280.9 cm^{-1} in the purified ones. A number of substances have

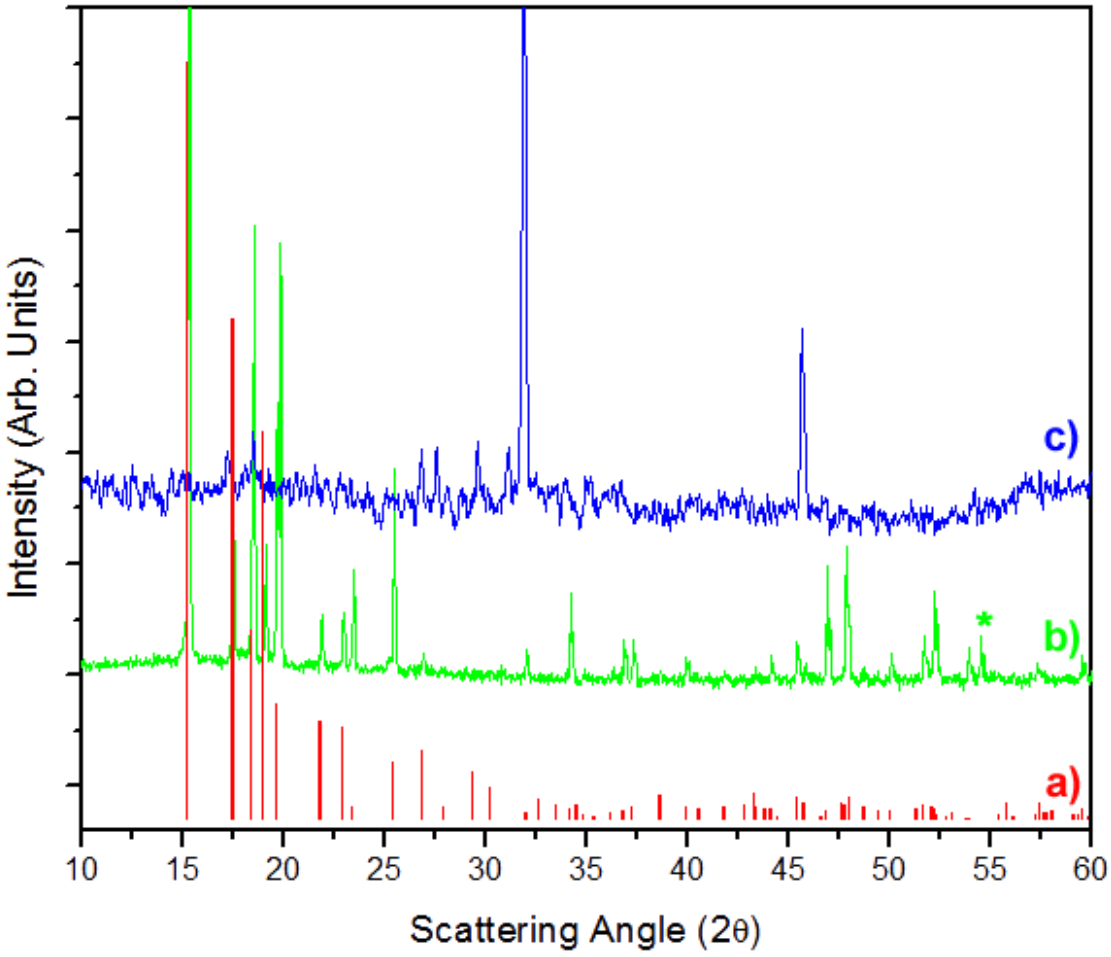

Figure 4.19– XRD pattern of ferrocene from COD [169] is shown in a) while b) and c) show powder XRD data obtained from unaltered and purified irradiation products respectively.

vibrational modes in this region including, iron oxides, iron carbides, or even carbon nanotubes (CNT) so identification of these modes may be somewhat ambiguous [162-164]. Iron oxides can likely be excluded as potential candidates responsible for these modes since EDS data showed very little evidence of oxygen. The high degree of crystallinity in CNT typically results in a very narrow G mode that is significantly more intense than the radial breathing or D modes. This is obviously not the case in the spectra here; however, given the appearance of a nanotube-like structure in Figure 4.17 f), the presence of CNT in the purified powder cannot be discounted. The continued manifestation of some Cp modes in the irradiation products implies that they may in fact be some type of ferrocene

Table 4. 3– X-Ray Diffraction Peaks in Purified Powder				
Peak (2θ)	*d*-spacing (Å)	*B* (2θ)	*L* (nm)	Assignment
17.260	5.133	0.00292	48.0	Ferrocene
17.447	5.079	0.00247	56.7	Ferrocene
18.529	4.785	0.00292	48.1	Ferrocene
26.845	3.318	0.00257	56.0	Ferrocene
27.596	3.230	0.00299	48.1	Hex C
29.637	3.012	0.00257	56.8	Fe-C_4
31.151	2.869	0.00409	35.2	bcc Fe
31.934	2.801	0.00564	25.6	Fe-Fe
45.718	1.983	0.00582	25.8	α-Fe

derivative. Compounds that contain two iron atoms bonded to carbons often have modes in the region of the unidentified spectral peaks and modes with these energies have been assigned to non-terminal Fe-Fe, and Fe-C stretching vibrations [165-168]. Since this is the simplest explanation, given the experimental parameters, for the appearance of these modes they are tentatively assigned to Fe-Fe (217.8, 216.4 cm^{-1}) and Fe-C (283.2, 280.9 cm^{-1}) vibrations.

Complimentary information about the structure of these nano-composite materials was obtained using powder XRD. The diffraction pattern of ferrocene was obtained from the Crystallography Open Database (COD) [169] and is shown in Figure 4.19 a). The diffraction patterns of the unaltered and purified irradiation products are presented in Figure 4.19 b) and c) respectively. It is clear that the majority of peaks in the diffraction spectrum of unpurified powder result from the presence of crystalline ferrocene. On average the peak positions in this spectrum differ from those of the reference pattern by less that 1%; however, there are two features in the unaltered spectrum that do not match with ferrocene. These occur at 2θ = 54.52, 54.67° (indicated by a star). Values of 2θ correspond to the spacing between scattering planes, *d*, through the Bragg equation $d = \lambda / 2\sin(\theta)$ where λ is the excitation wavelength [170]. These two peaks result from d-spacings of d = 1.68, 1.67 Å respectively and may correspond to scattering from Fe_3C iron carbide [169, 171]. The

spectrum of the purified powder (Figure 4.19 c) is significantly different from that of pure ferrocene or the unaltered material with only nine diffraction peaks visible. The scattering angle, corresponding d-spacing, and width, B (2θ Radians), of these features are listed in Table 4.3. Using these values the size of the crystalline particles was estimate using the Scherrer equation, $L = K\lambda/B\cos(\theta)$ where K is the dimensionless shape factor. For a perfectly spherical nanoparticle particle the shape factor has a value of 1 with a value of 0.9 being used in most cases [172]. The overall diffraction pattern of the purified samples was searched for in the COD to determine if it corresponded to any existing materials. This was not the case; however, a number of peaks have been identified and it is apparent from the estimates of L that there are at least three different compositions present in the sample. The sharp peak at 2θ = 45.72° comes from α-Fe, while the strong peak at 2θ = 31.93° corresponds to a very weak ferrocene peak [173]. In large iron complexes the upper limit on the length of Fe-Fe single bonds is 280 pm which corresponds to the d-spacing of this peak [174]. The unit cell edge of bcc Fe has a length of 287 pm matching the small peak at 2θ = 31.15° [148, 175]. All of the other peaks in the purified spectrum can be attributed iron carbides, hexagonal carbon rings, or ferrocene [169, 173, 175-178]. The diffraction peaks associated with iron and iron carbide corroborate the assignment of the low wavenumber Raman modes in Figure 4.18. The overall structure of these materials is still somewhat mysterious however it is apparent that there is a pure iron phase, as well as two phases in which part of the ferrocene molecule is bound to either carbon or iron-carbon complexes.

The probable formation mechanism for the highly ordered dissociation products can now be described by taking into consideration their molecular composition, physical structure and the synthesis environment. Inside the laser focal region both ferrocene and benzene are ionized and dissociated, resulting in plasma that is comprised mainly of electrons, Fe_n^+ and C_n^+ ions, and a variety of ring fragments as well as iron-carbon complexes. This glowing material is violently ejected from the focal region, as shown in Figure 4.10 a) and travels through the surrounding liquid in the form of a hot, spherical plasma packet. A schematic of this proposed mechanism is presented in Figure 4.20. Similar “plasma bullets” have been observed in atmospheric plasmas as well as in interstellar space [179, 180]. As it travels the outer region of the laser produced plasma packet interacts with the fluid, loosing energy due to collisions, which results in the condensation and subsequent crystallization of an Fe-C outer shell. This would correspond to the spherical structures shown in Figure 4.16. The diameters of these objects are similar to that of the diameter of the focal region and their size variation can be accounted for by the chaotic conditions under which the plasma is created. It is apparent that some of the shells are hemispherical while others are fully ovular. The hemispherical

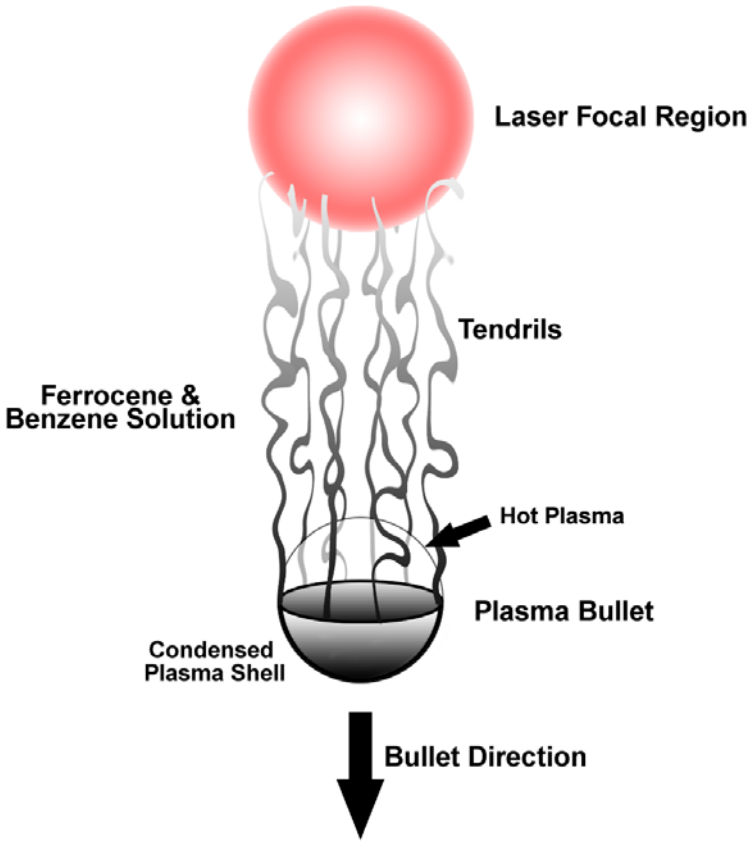

Figure 4.20 - Schematic of the proposed plasma bullet condensation and crystallization mechanism. A hot plasma packet is ejected from the dissociation region and travels through the comparatively cold liquid solution of ferrocene and benzene. The surface of the packet condenses and crystallizes forming a nanometer thick shell around the plasma.

shells are likely travelling faster through the liquid and therefore undergo turbulent flow which would prevent the stable formation of a shell around the whole bullet. This would also account for the "streamers" that are attached to the back of these objects. Plasma packets that do not experience turbulent flow become fully encased in shells but these are then torn open by temperature and pressure gradients.

All of the other structures that have been observed in these samples likely result from a similar process, which ultimately involves the crystallization of transient plasma structures. For

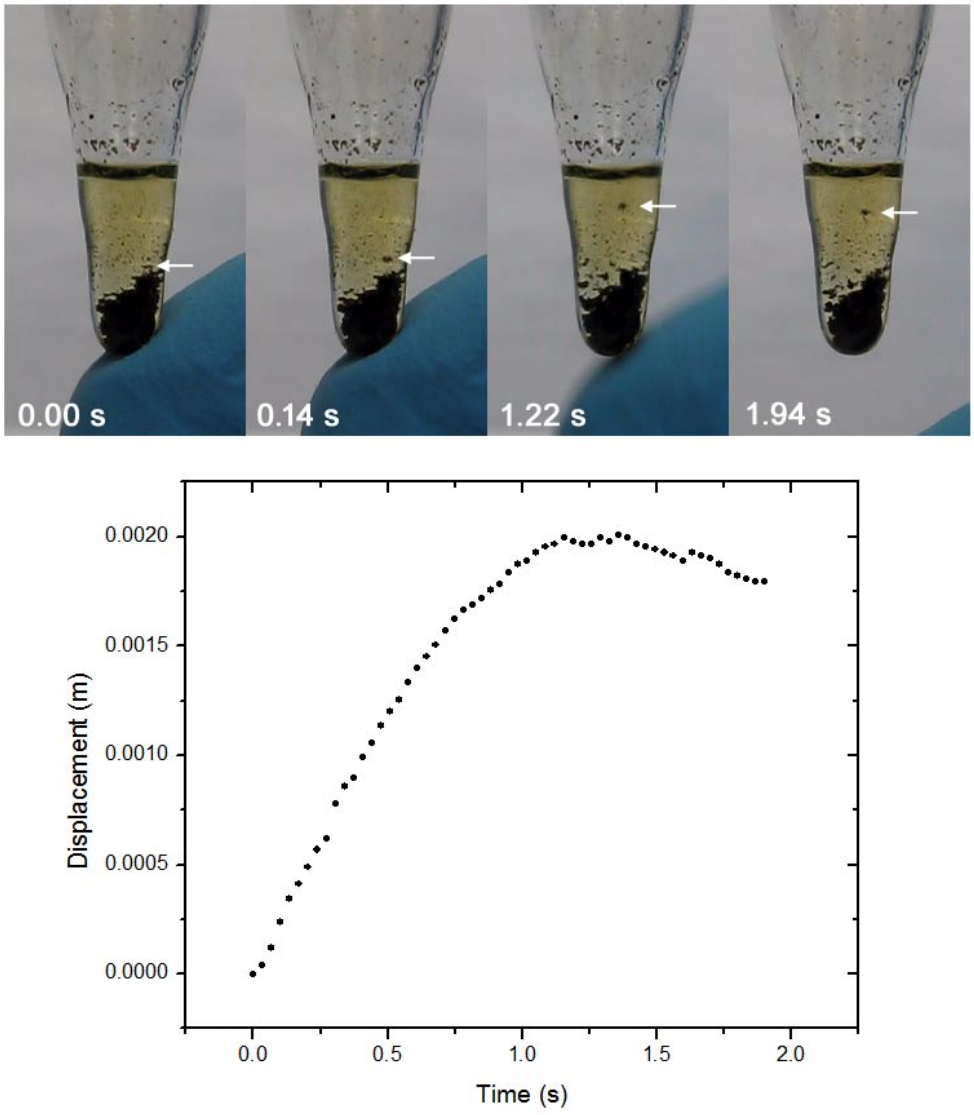

Figure 4.21 - Series of time lapse still images extracted from a video recording of the response of purified dissociation products, in benzene, to a static electric field. A single cluster is tracked and indicated by a white arrow. The graph shows the position of the cluster as a function of time.

example, the microtubules, shown in Figure 4.15, have a very similar appearance to “keyholes” that are often observed in laser welding applications [181] and could result from crystallization around plasma filaments. The fact that these types of structures do not appear in irradiated benzene suggests

that they form exclusively due to the catalyzing effects of the iron that is present in the plasma created from ferrocene. It is widely understood that iron promotes the crystallization and organization of carbon into nanostructures such as carbon nanotubes [182-184]. In the present experiment iron is also acting as a catalyst for crystallization but in addition to this the plasma itself is acting as a scaffold for the creation of larger structures. This is the first example of this type of nano-micro material growth and should be explored further in the future. Presently, however, it is of interest to study a number the other characteristics of the purified material to determine if it could be relevant for technical applications.

One curious property of purified powder is its response to a static electric field. During the handling of vials containing purified powder submerged in benzene, nanoparticle clusters were observed receding from a gloved finger. This response was recorded digitally using a video camera shooting at 30 frames per second. An analysis of the movement of a small nanoparticle cluster is presented in Figure 4.21. The cluster was approximately spherical with a diameter of 2.5×10^{-4} m and an estimated mass of 167 μg. It is indicated by a white arrow in the four time lapsed frames presented in the figure. The position of the particle was extracted in a frame by frame analysis and the position as a function of time is shown graphically in the inset of the figure. The cluster began to rise in the liquid within 0.034 s of the initial contact with the vial. Over the first 0.75 s of interaction it had a constant velocity of 2.2×10^{-3} m s^{-1}. After climbing 1.6×10^{-3} m through the fluid the cluster's velocity began to decrease until it reached a maximum height of 2.0×10^{-3} m after 1.16 s. Near the 1.22 s mark the finger was removed from the bottom of the vial and the cluster began to fall under the influence of gravity. Initially it was surmised that the origin of this interaction may have been the thermal; however, the response time is much too fast and the temperature gradient much too low for this to be the case. The interaction must then be electrostatic which suggests that this material is a dielectric with a quasi-permanent electric dipole, or electret. Given the properties of electret materials they are used extensively in the electronics industry (microphones, transducers, etc.) and nanoscale electrets could have many important future applications [185]. A more quantitative characterization of the electrical properties of this material is planned for the future.

In the mean time, the magnetic properties of the purified material were studied using a SQUID magnetometer after a sample was observed reacting to the field from a neodymium magnet. Figure 4.22 a) shows the room temperature magnetic hysteresis loop of the purified powder. The remnant magnetization of this material is M_r = 0.12 emu/g while the coercivity, H_c, and the saturation

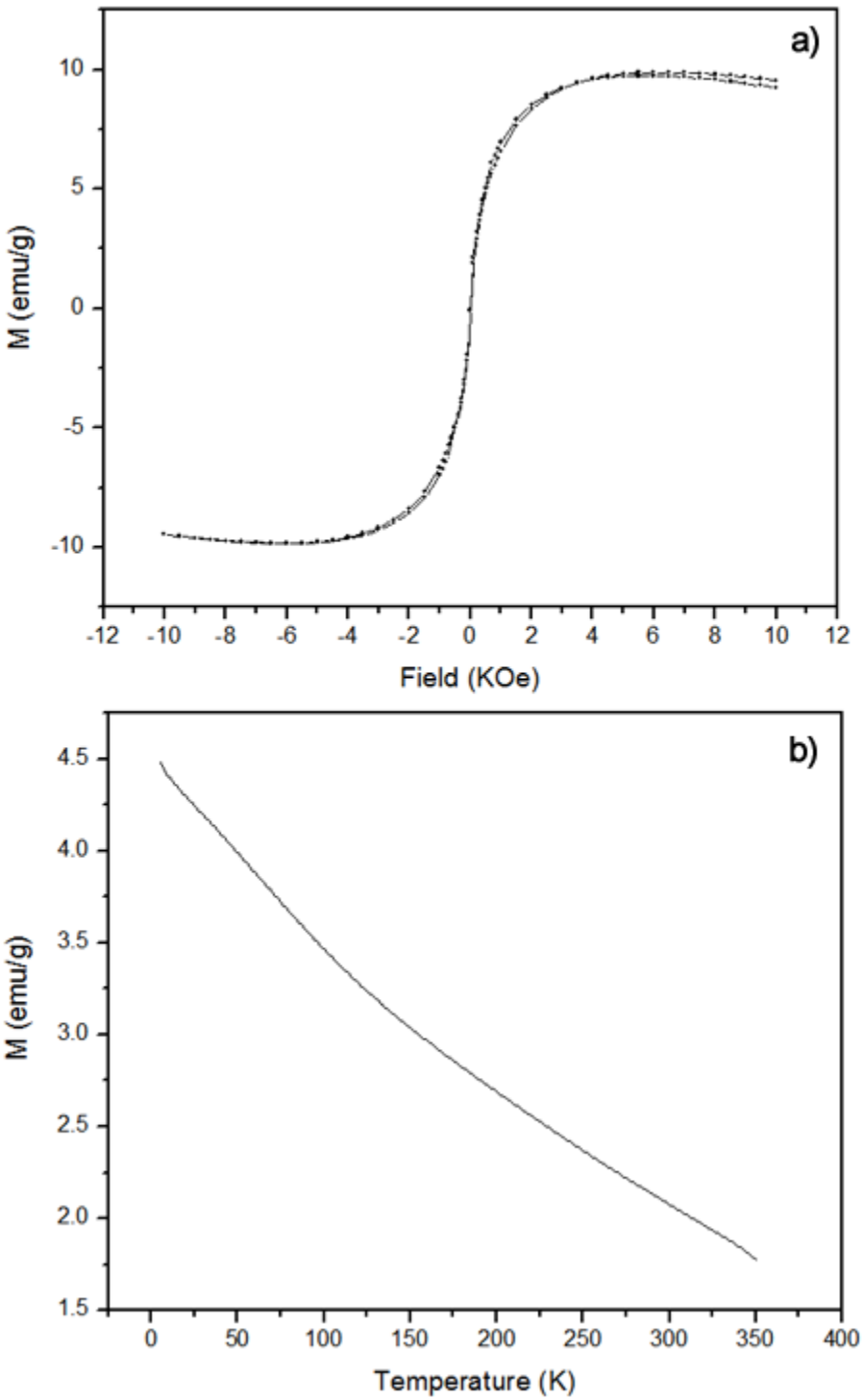

Figure 4.22 - Magnetic hysteresis loop of the purified powder is shown in a) while the magnetic moment as a function of temperature is shown in b).

magnetization, M_s, are 6.85Oe and 9.87 emu/g respectively. The coercivity is a measure of the applied magnetic field required to return the material to zero magnetization while the remnant magnetization is the residual magnetization after the applied field is reduced to zero [186]. These values are determined directly from the hysteresis loop and determine the type of magnetism present in a given material. The values of M_r suggest that the purified samples are softly ferromagnetic. There is also a small diamagnetic component present in the hysteresis loop. This is not unexpected given its constituents are iron and carbon. Compared to other magnetic materials prepared using ferrocene these values a quite low, however, the coercivity is significantly higher than that of iron (~1 Oe) [178]. Figure 4.22 b) presents a graph of magnetization as a function of temperature given an applied field of 100 Oe. The sample continues to be ferromagnetic over the whole temperature range, with no evidence of a magnetic phase change. A ferromagnetic electret material is quite unique and could have many potential applications in electronics.

4.3.4 Pulsed Laser Initiated Electrophoresis

Porous carbons are high surface area materials that have garnered a great deal of attention in the last twenty years because of their applications in chemistry, electronics and medicine. They have been used commercially as catalysts, molecular sieves, and water filters, and have also been suggested for use as electrodes in supercapacitors or as bio coatings to promote osteogenesis [187-190]. To create a porous carbon coating, benzene was ionized by LP-LPI, under the influence of a 600 V electric potential. A photo-ionization current of 0.77 nA was induced in the fluid resulting in the deposition of a dark material onto the stainless steel electrodes.

The nano-structure of this deposit was examined using SEM. Figure 4.23 shows a series of electron micrographs taken of the deposited material at various magnifications. The images show that the coating is disordered and highly porous. The white circle in the bottom right image indicates an area of nanoparticle contamination. These particles were identified as iron oxide (Fe_3O_4) through EDS. Overall EDS analysis showed that the samples were over 90% carbon with up to 10% contamination in some areas from stainless steel based dissociation products. It should be noted that these images were gathered without gold coating of the surface. The lack of charging artifacts in the images suggests that this material is highly conductive. The main parameter which determines the utilization of porous carbon in specific applications is the pore size distribution (PSD) and as such it is used to group these materials into three categories: micro ($\leq$ 2 nm), meso (2-50 nm) or macroporous ($\geq$ 50 nm). Data on the pore diameters in this sample were gathered by analyzing the

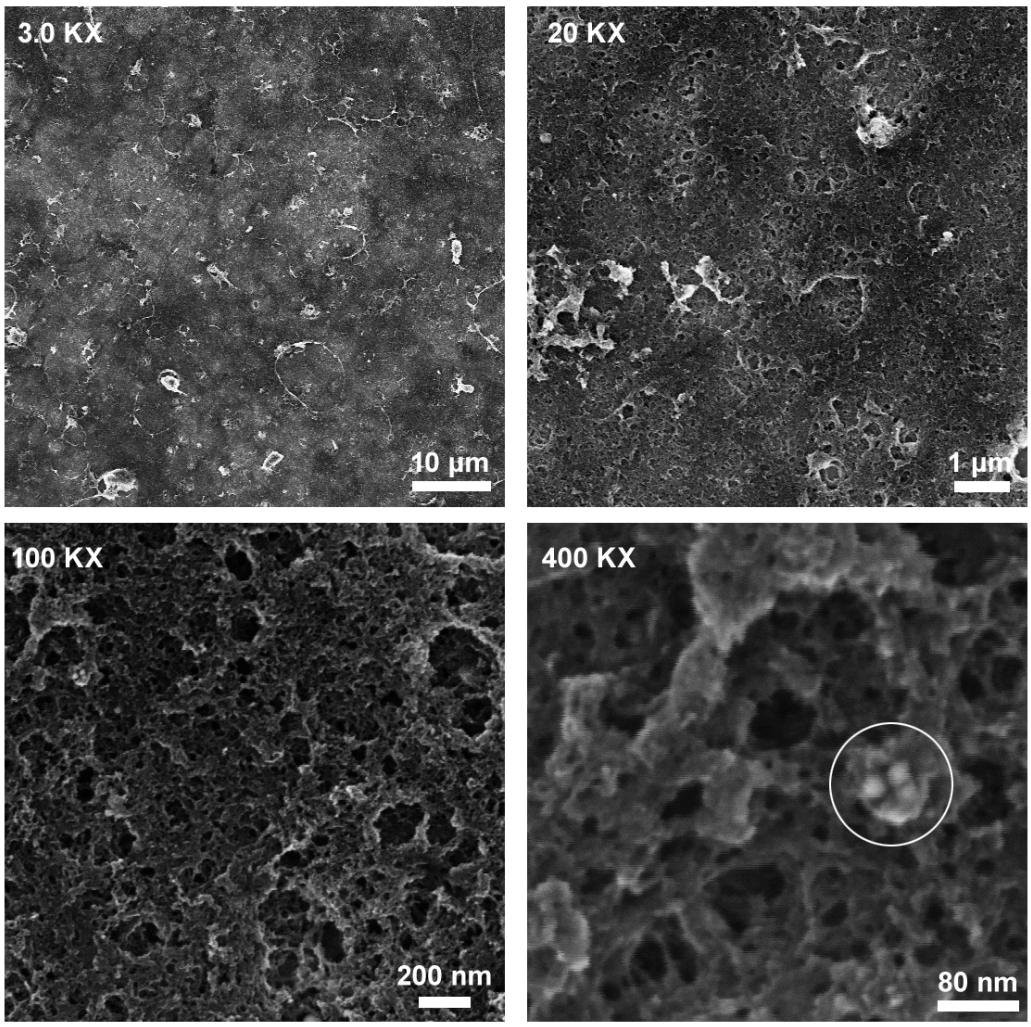

Figure 4.23– Scanning electron micrographs taken of the porous carbon electrodeposited on stainless steel electrodes during the liquid phase laser irradiation of benzene. The white circle indicated iron oxide nanoparticle contamination.

micrographs using an edge selection algorithm available in the ImageJ software program [191]. A histogram of the pore diameters is shown in Figure 4.24. A total of over 1600 pores were counted in a 1.5 × 1.5 µm area. The diameters ranged from 2-100 nm with an average pore size of 15.0 nm, putting this material in the mesoporous category. The composition of the samples was studied then studied using Raman spectroscopy.

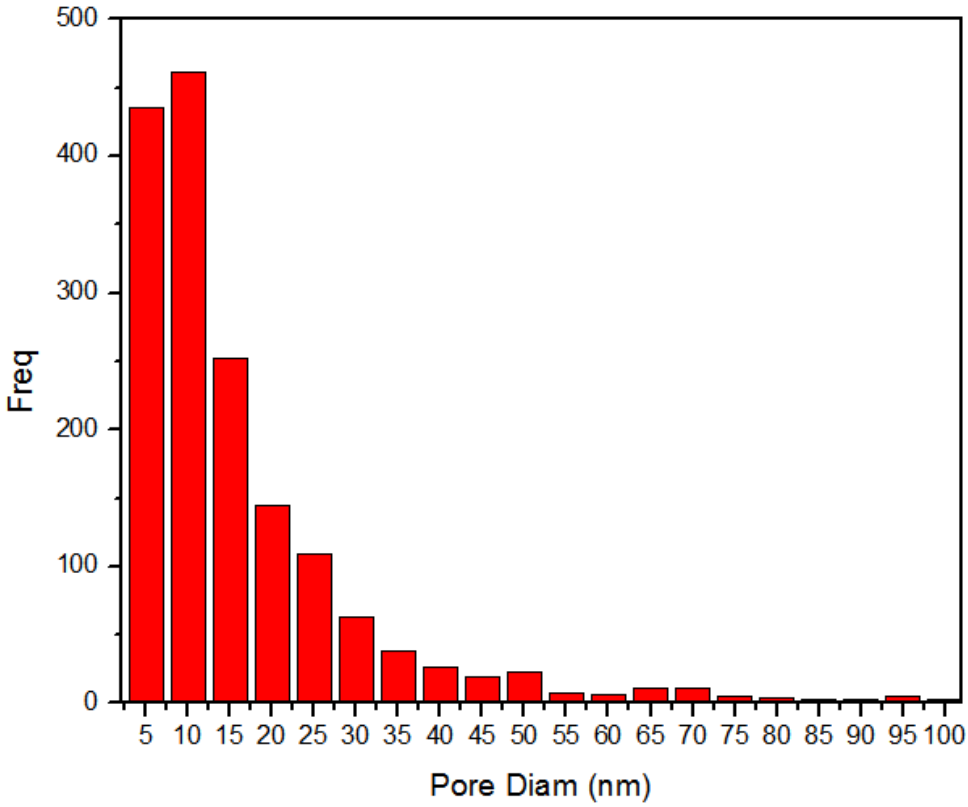

Figure 4.24 - A histogram of the pore size diameter in disordered porous carbon. The data were gathered from an area of 2.25 μm^2.

Figure 4.25 shows the normalized Raman spectra from three different spots on the sample. The background signal from the stainless steel electrode is also presented as a reference (bottom curve). The prototypical D and G modes dominate the spectra indicating that this material is composed of sp^2 carbon. To determine the parameters of the Raman peaks in this region each spectrum was deconvolved using four Gaussian curves (see inset). The energies of the D (1370 cm^{-1}) and G (1588 cm^{-1}) peaks stay relatively constant, with less than a 1% variation in wavenumber over the entire substrate. This indicates that the composition of the sample is homogenous. The ratio of the D and G intensities fluctuates from I_D/I_G = 0.6 - 0.7 over the sample which correlates to a cluster size range of 5 - 6 nm according to the previously outlined Tuinstra and Koenig relationship (Section 4.3.3). This corresponds to clusters comprise of approximately 18-22 rings. A three-stage phenomenological model has been developed by Ferrari and Robertson [39] to classify the various

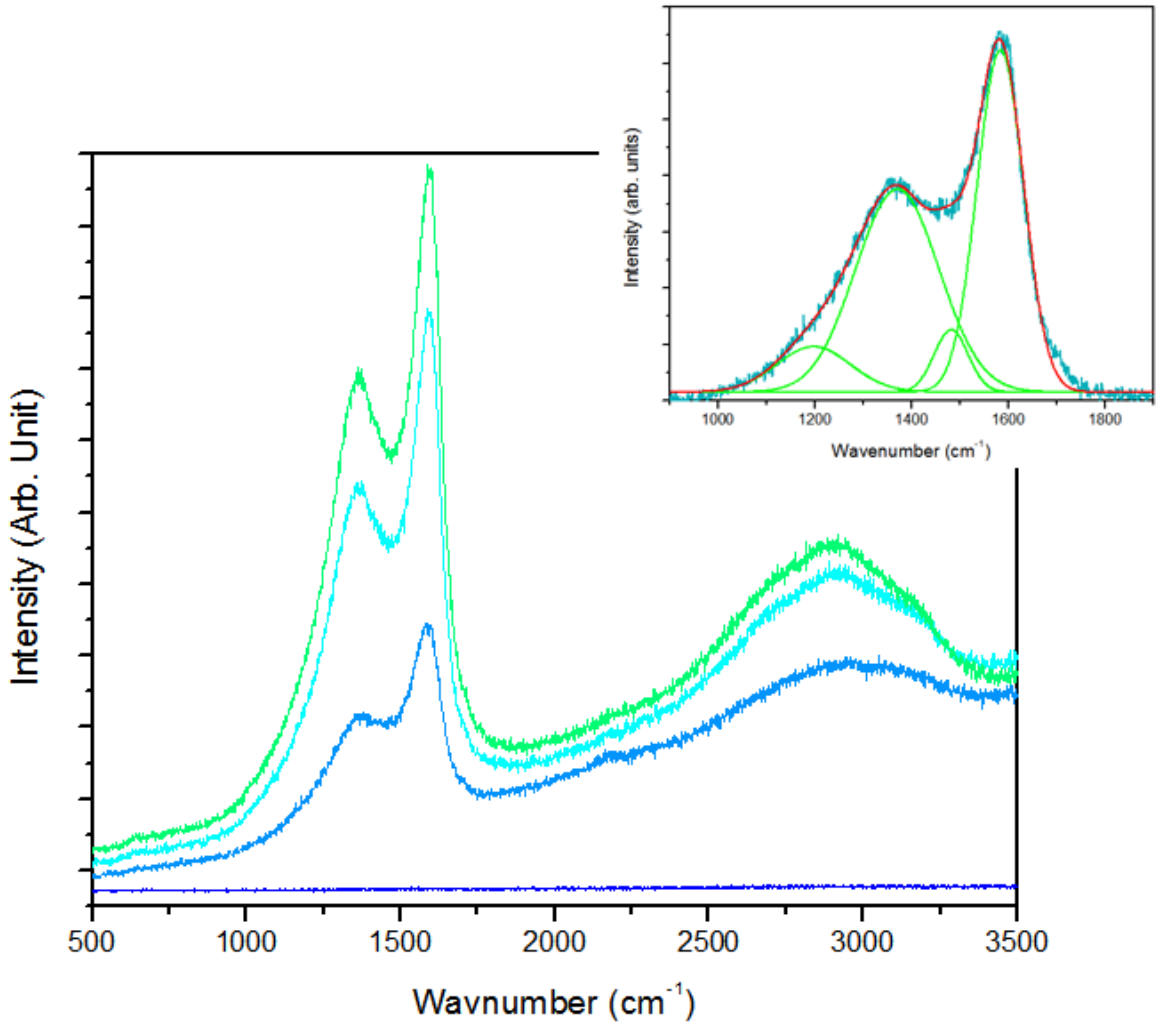

Figure 4.25 - The Raman spectra of porous carbon deposited on the electrodes. The lowest curve is the background spectrum of the electrode and the top three curves are spectra taken from different areas of the sample. The inset shows an example of the four parameter Gaussian fit applied to spectrum after subtraction of the background photoluminescence.

classes of amorphous carbon using the position of the G mode and the I_D/I_G ratio. According to this model, the deposited material is classified as nanocrystalline graphite. Two additional vibrational modes centered around 1180 cm^{-1} and 1490 cm^{-1} are also present in the spectra. These peaks have been previously identified in hydrogenated amorphous carbon. The lower wavenumber mode is

usually attributed to nanocrystalline diamond or hexagonal diamond and corresponds to sp^3 bonding in amorphous carbon thin films; however, a parallel C-H bending mode of benzene is also found at this energy [101, 192]. The higher wavenumber mode can be attributed to the semicircle ring stretch vibration of benzene or condensed benzene rings. It has also been suggested that this mode arises in graphite crystals of finite size due to critical points in the phonon density of states [193]. Since this material forms through the LP-PLI of benzene it is likely that these two peaks occur in the spectra of Figure 4.25 due to benzene related vibrational modes. The background photoluminescence observed in all of the spectra indicates that the porous nanocrystalline graphite is partially bonded to hydrogen. A convenient way to estimate the hydrogen concentration in carbon films was proposed by Marchon et al. [194]. The slope parameter S (μm), may be calculated by taking the ratio between the slope m of the fitted linear background in the D and G mode region and the intensity of the G peak or $S = m/I_G$. The slope parameter depends exponentially on the hydrogen concentration, and in the present samples ranges between 1.5 - 3.8 μm which corresponds to a hydrogen content of 36 - 38%.

The ability to easily coat conductive materials that can conceivably have any shape, in porous nanocrystalline graphite could have important applications in a variety of industries. Traditionally, porous carbon has been fabricated by either an activation process or a template method [187, 188]. These procedures can be quite complex, requiring multiple steps and processing of materials at high temperatures. The porous carbon materials synthesized using these methods typically come in the form of powders and therefore must be further processed to be utilized in technical applications. While other methods, such as glancing angle laser deposition (GLAD) have been used to coat substrates in porous carbon [195], the single step process developed here has the added advantage of working in three dimensions. Graphite-like amorphous carbon has recently been shown to be an excellent biomaterial that could be applied to dental and orthopedic implants to improve biocompatibility and osteogenesis [190]. There is an extensive list of other potential applications for conductive porous carbon coatings [187, 188, 196-198]. LP-PLI electrodeposition is therefore an extremely powerful technique that in the future could prove to be the preeminent method for the deposition of conductive porous carbon.

4.4 Summary

Four liquid phase-pulsed laser irradiation experiments have been outlined in this chapter. The irradiation of pure liquid benzene by fs-laser pulses leads to the formation of nanoparticles with three distinct morphologies. Spherical, prolate and toroidal nanoparticles ranging in height from 1 to 25 nm were observed by AFM. The composition of these nanoparticles was determined by SERS to be amorphous carbon, however not of the characteristic (sp^3, sp^2)-bonded structure. Linear or cyclic polyynes (C_8, C_{14}), appear to act as bridges between clusters of sp^2-bonded aromatic rings resulting in a (sp, sp^2)-bonded amorphous carbon material. The dissociation of gaseous benzene by fs-laser pulses was shown by TOF-MS to produce a number of predominant carbon species including the parent ion $C_6H_6^+$, as well as fragments such as $C_3H_n^+$, CH_n^+, C^+, and C_2^+. In liquid benzene laser-induced ionization is the source of fragmentation. The formation of (sp, sp^2)-bonded amorphous carbon is initiated by the reaction of primary dissociation products with C_6H_6 molecules in solution. A variety of substituted ring compounds result from these reactions leading eventually to the observed amorphous carbon. This process was not observed in deuterated benzene since the laser intensity in liquid C_6D_6 is insufficient to produce fragmentation due to its higher nonlinear refractive index.

In a complimentary experiment, liquid toluene was irradiated by fs-laser pulses under similar conditions. After an extended period of irradiation a series of polyynes, with chain lengths ranging from C_{10} –C_{20} were identified in the liquid through Raman spectroscopy. No amorphous carbon phase was detected in these samples. The dissociation of toluene produces many fragments including, CH_n^+ $C_3H_n^+$, $C_4H_n^+$ and the singly and doubly charged parent ions $C_7H_8^+$ and $C_7H_8^{2+}$. Importantly, many of these ions still contain the methyl group and when polyynes form via carbon addition reactions with these ions, it is possible that they are stabilized by these groups. As such they would not be reactive and would be unavailable as building blocks to form an extended amorphous network. The irradiated solutions also exhibited a wide band strong room temperature photoluminescence and could therefore prove useful as a fluorescent dye or as a marker in biological applications.

In a more complex experiment, solutions of ferrocene and benzene were irradiated by fs-laser pulses. Highly ordered mesoscale structures exhibiting four unique geometries; ribbons, loops, tubes, and spheres were observed in the evaporated deposits of the irradiated solution using atomic force and scanning electron microscopy. Lying above beds of nanoparticles the nanoribbons exist as an interconnected network and individually range in width from 50 - 400 nm, are between 30-60 nm thick, and appear to be atomically smooth. The shape and size of the continuous loops vary

considerably, with the smallest having path lengths and diameters on the order of a few micrometers and the largest stretching for hundreds of micrometers. These structures have wire-like outer rims that range in diameter from 40 – 1000 nm, have an average roughness of 1.1 nm and appear to be formed from bundles of smaller wires or tubes. A hollow tube like structure was also observed and was 38 μm long, with an average diameter of 2 μm, riddled with holes, and entangled in a number of nano fibres and ribbons. Spherical nodules with a 500 nm diameter were also attached to the outer surface of the tube. Spherically shaped microspheres occurred frequently on the substrate and always appear either attached to, or very near, nanoribbons. These objects range in appearance from hollow hemispheres to ruptured prolate spheroids and can grow to be a large as 25 μm in diameter. Even at high magnification the outer walls of these structures are very smooth and have diameter that range from 30-60 nm. These higher order structures are destroyed after a purification process and replaced with micron sized clusters of light and dark material that appear to be a porous matrix of carbon and iron. Round, white nanoparticles embedded in the matrix range in diameter from 10-100 nm and are lighter in appearance because they are composed of a larger percentage of iron. The composition of the purified material was examined using Raman and x-ray spectroscopy and it was determined that there are three species in this material including; pure iron, and two phases in which part of the ferrocene molecule is bound to either carbon or iron carbon complexes. The purified material also exhibited properties similar to that of an electret and was shown to be ferromagnetic over a large temperature range and could therefore have many interesting applications.

Finally disordered mesoporous nanocrystalline graphite was deposited onto the surface of stainless steel electrodes through the ultrafast laser induced breakdown of benzene and subsequent deposition of carbon ions. This coating was examined using SEM and was shown to have an average pore size of 15 nm. A lack of charging artifacts in the micrographs suggest that the material is conductive and Raman spectroscopy confirmed it is composed of nanocrystalline graphite with an average cluster size of 5.5 nm. It was also determined that this material contained approximately 35% hydrogen. The ability to easily coat conductive materials that can conceivably have any shape, in porous nanocrystalline graphite could have important applications in a variety of industries.

Chapter 5
Pulsed Laser Induced Plasma Processing of Frozen Materials

The experimental procedures involved in the synthesis of amorphous carbon (a-C) through pulsed laser deposition (PLD) have not changed significantly since the formative years in which the technique was developed [199-201]. This chapter introduces a new variation of the PLD technique in which the carbon plasma produced by the fs laser ablation of graphite is used to process frozen chemicals such as hexane or water. This method, entitled pulsed laser induced plasma processing or PLIPP, leaves behind an amorphous carbon material that has a unique composition and nanostructure. The introduction of this chapter (Section 5.1) consists of a review of the wide variety of a-C materials synthesized through traditional PLD, from the earliest works of Marquardt et al. [200] in the 1980s through to those recently published by our research group [202]. Following this, the PLIPP technique is described in detail as are the various experiments preformed during the course of my doctoral work (Section 5.2). A variety of alkanes, alkenes and water have been processed using this technique and the effects of changing plasma processing time, and the processed material have been examined. The results of those experiments are outlined in Section 5.3. Characterization of the carbon plasma produced through Ti:Sapphire fs laser ablation of graphite is presented in Section 5.3.1 while the effect of plasma processing time on layers of solid hexane is described in Section 5.3.2. The content of the first two subsections are partially contained in our recent paper on this subject [203]. A comparison of the structure and composition of films produced by PLIPP of solid hexane, octane and decane layers is given in Section 5.3.3. This is followed by an exploration of the characteristics of the deposited material that results when the alkane base layers are replaced with alkenes (Section 5.3.4). Finally, the effect of PLIPP on water ice, which may be of astrophysical significance, is examined in Section 5.3.5. The chapter then concludes with a summary of the PLIPP technique, the experiments that have been carried out, and a discussion of the future potential of this technique.

5.1 Introduction

Amorphous carbon (a-C) thin films have been successfully fabricated using pulsed laser deposition (PLD) since the mid-1980s, with a number of authors contributing to the early exploration of the field including the pioneering work of W.W. Duley in 1984 [199]. The advantages of this technique over other deposition methods such as chemical vapor deposition (CVD) are simplicity and the ability

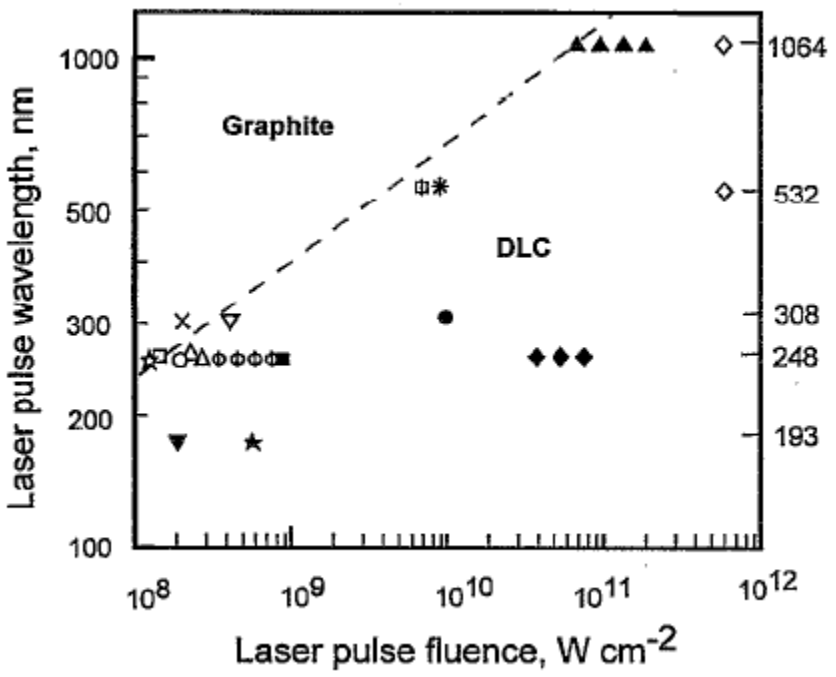

Figure 5.1 - The relationship between laser intensity, wavelength and the microstructure of a-C thin films produced through the ns-PLD of graphite. The dashed line represents the transition between graphite-like and diamond-like thin films. The data points were compiled by Voevodin and Donley [205].

to synthesize pure a-C with very little contamination [47]. The synthesis of a-C thin films using PLD typically involves focusing a high intensity pulsed laser onto a carbon based target material and allowing the resulting carbonaceous plasma to condense onto a substrate. There are relatively few experimental parameters involved in controlling this process and these may be grouped into three general categories; laser parameters, deposition environment and target material. Variation of a single parameter can have a dramatic effect on the structure and composition of the deposited material and combinations of parameters can be used to produce a-C from any area of the ternary phase diagram (Figure 1.5).

The majority of early research in the synthesis of a-C through PLD was carried out by the ablation of graphite with nanosecond laser pulses (10-100 ns), at temperatures ranging from 77-800 K, and in high vacuum [47]. Many of these initial studies examined the interdependent relationships between laser intensity, wavelength and the molecular structure of a-C. Films have typically been

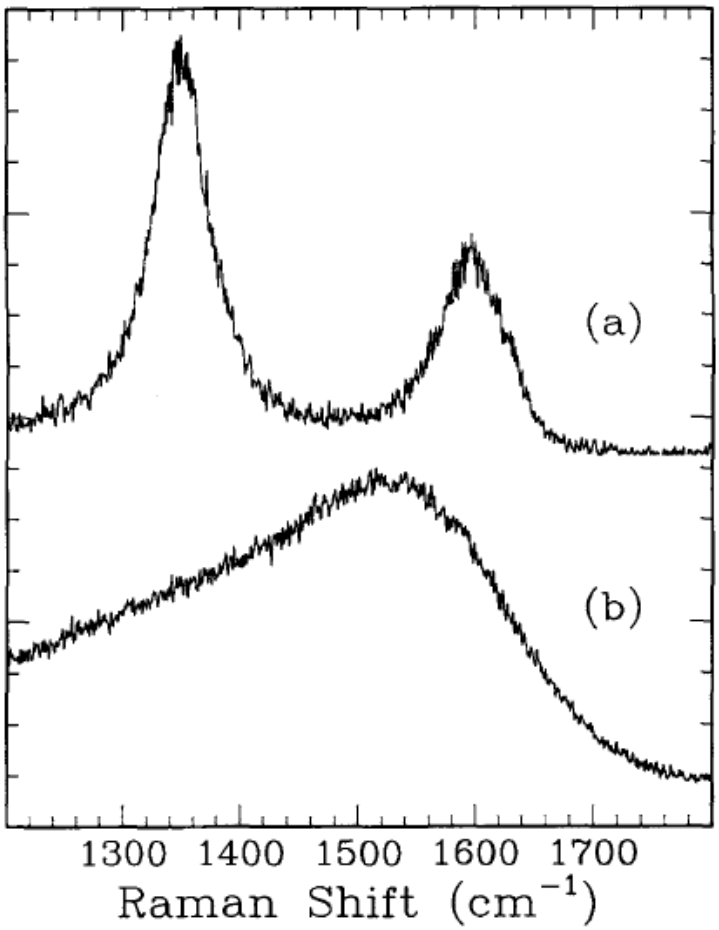

Figure 5.2 - Raman spectra of a) GLC synthesized by the PLD of graphite using 15 ns 1064 nm and b) DLC produced with 15 ns 248 nm laser pulses. The intensity of laser pulses in either case was fixed at 2×10^{8} Wcm^{-2} [206].

grown using laser pulses with intensities between 10^{8}-10^{12} Wcm^{-2} and wavelengths ranging from 193-1064 nm [47]. In 1985, Marquardt *et al*. synthesized thin films by ablation of a carbon rod with 1064 nm Nd:YAG laser pulses. A transition from soft graphite-like (GLC) to hard diamond-like a-C (DLC) was shown to occur in films produced at intensities greater than 5×10^{10} W cm^{-2} [200]. This so called "Nagel criterion" was confirmed by Danvanloo et al. in 1990 [204] using comparable experimental parameters; however, others have shown that the value of the critical intensity is dependent on laser wavelength [47]. An analysis of the correlation between ns laser intensity, wavelength and the formation of DLC, derived from the work of many authors, was carried out Voevodin and Donley and

is summarized in Figure 5.1 [205]. The dashed line in the figure represents the combination of intensity and wavelength required to initiate the transition from GLC to DLC material. One of the earliest examples of this phenomenon was described by Murray and Peeler [206] who synthesized thin films by ablating graphite with either 15 ns Nd:YAG (1064 nm) or 15 ns excimer (248 nm) laser pulses. The intensity in both cases was fixed at 2×10^8 W cm^{-2} significantly lower than the Nagel transition. Visible Raman and electron energy loss spectroscopies (EELS) were used to characterize the resulting thin films and it was shown that films deposited with IR laser pulses were graphitic, in accordance with previous reports. However, films synthesized using UV laser pulses were found to have considerable diamond-like character. A comparison of the Raman spectra for both films is shown in Figure 5.2. These seemingly contradictory results can be reconciled if the kinetic energy of the plasma species is considered. As discussed in Chapter 2, the local conversion from sp^2 to sp^3 carbon bonds in plasma deposited a-C occurs due to metastable densification of the thin film induced by local carbon ion subplantation [71]. This begins to take place when the kinetic energy of ions in the plasma exceeds ~32 eV, and the ideal ion energy for maximal sp^3 formation is thought to be between 80-120 eV [76]. At 2×10^8 Wcm^{-2} the plasma generated by IR laser pulses was found, by Murray and Peeler, to consist primarily of carbon clusters C_n^+ $(1 \leq n \leq 30)$ with kinetic energies of less than 5 eV. Other authors have shown that carbon ions in plasma produced by IR laser pulses at 5×10^{10} W cm^{-2} have energies on the order of 50 eV [69, 200]. This effectively explains the origin of the Nagel transition; below a certain value of intensity the ions formed in the IR laser initiated plasma do not have enough energy to penetrate the surface of a growing film and initiate the formation of sp^3 bonded species. Murray and Peeler also characterized the UV plasma and showed that it was dominated by C_2^+ and C_3^+ ions with energies 60 eV and 18 eV respectively. This suggests that UV irradiation is more efficient at producing small energetic clusters that are in the proper energy regime for the creation of hard diamond-like thin films. It is therefore clear that both of these parameters dramatically influence the properties of ns laser deposited a-C thin films. The increased availability of high intensity ultrashort lasers has recently made it possible to study the influence of another laser parameter; pulse duration, on the formation of a-C.

There have been several studies on the deposition of a-C through femtosecond (fs) laser ablation of graphite [64, 207-209]. Typically, thin carbon films synthesized using shorter laser pulses are smoother with few surface particles, (seen in Figure 5.3), and have a significantly lower volume fraction of sp^3 bonded carbon, (40-60%), than those produced with longer pulse length lasers [64]. This decrease in diamond-like character can be understood by taking into account the effect of the

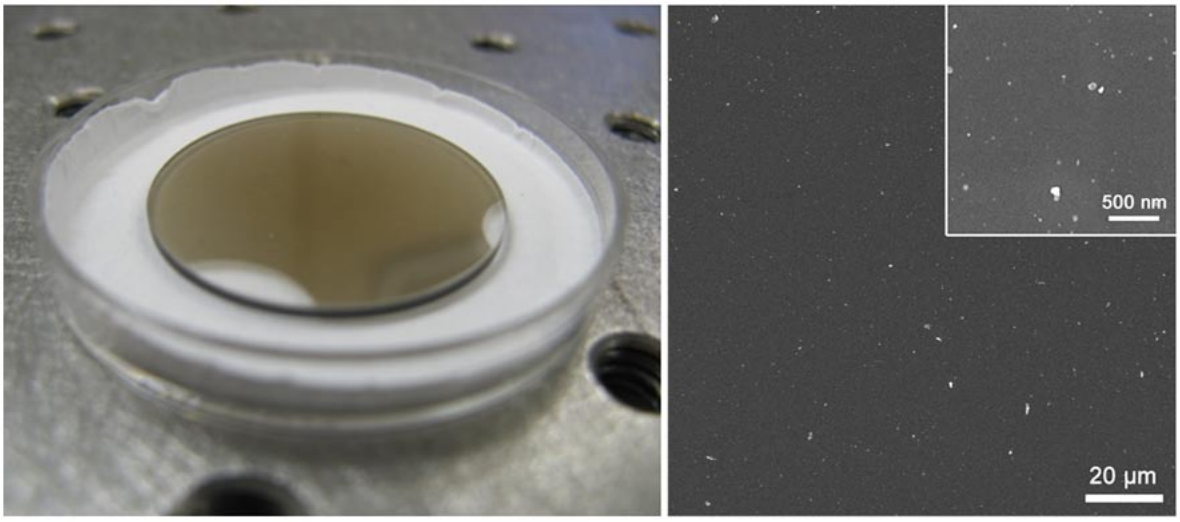

Figure 5.3 - A photograph (left) and electron micrograph (right) of a film synthesized through pulsed laser deposition of graphite using the laser and vacuum systems described in Chapter 3.

higher laser intensities required to initiate ablation in the ultra-short pulse regime. A simple theoretical relationship describing the dependence of the intensity (I) required for optimum laser evaporation of a solid target on pulse duration (t_p) was put forth by Gamaly, Rode and Luther-Davies in 1999 [57]. For graphite, this relationship is $I = (1.89\times10^5/\sqrt{t_p})$ W cm^{-2} resulting in a value of 5.98×10^{11} W cm^{-2} for 100 fs laser pulses. Experimentally, the ablation threshold of graphite for 800 nm, 100 fs Ti:Sapphire laser pulses has been determined to be somewhat higher (~ 2×10^{12} W cm^{-2}) than the theoretically predicted value [63]. Carbon plasmas arising from the fs laser ablation of graphite are therefore considerably more energetic than their ns laser generated counterparts, with reported ion energies ranging between 0.5-25 keV [64, 68]. These energies lie well outside the optimal range for the formation of sp^3 carbon bonds in a-C thin films. In addition to a reduced *sp*^{3} percentage, a-C thin films synthesized using ultrashort laser pulses have recently been shown to contain a significantly enhanced component of *sp*-bonded carbon. Figure 5.4 (Hu et al.) [207], shows the UV Raman spectra of a-C thin films produced by XeCl excimer (λ = 308 nm, t_p = 30 ns) and Ti:Sapphire (λ = 800 nm, t_p = 120 fs) laser ablation of graphite. The relative concentrations of *sp*, *sp*^{2} and *sp*^{3} carbon present within the fs sample was ~ 6%, 43% and 51%, respectively, while the corresponding fractions in the ns sample were 0%, 27% and 73%. Changing environmental

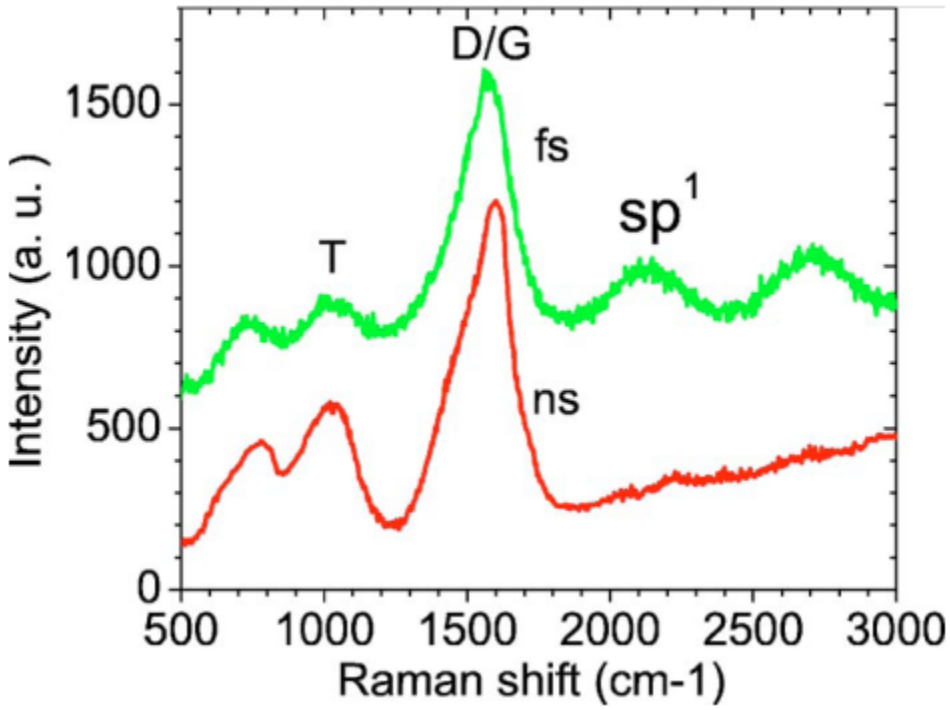

Figure 5.4 - A comparison of the UV Raman spectra of a-C thin films resulting from the ablation of graphite by 30 ns and 120 fs laser pulses [207].

parameters such as substrate temperature and gas pressure can also dramatically alter the properties of PLD synthesized a-C thin films.

The influence of substrate temperature on a-C structure has been the subject of a number of research articles [201, 202, 210-212]. After allowance for the effects caused by changing laser parameters, the deposition of carbon ablation products onto substrates held at temperatures between 77 and 373 K generally leads to the formation of DLC. The optimum temperature range for the formation of DLC was established to be 293-323K by Sato et al. [201] and Malshe et al. [212] for ns pulse lengths. Above this temperature range, the diamond-like character of the a-C begins to degrade with a transition from DLC to GLC stating at 423 K. According to a model put forth by Lifshitz and coworkers [72], subsequent to subplantation, a diffusion activated mechanism is responsible for the phase transition from sp^3 to sp^2 -bonded C at temperatures exceeding the transition substrate temperature. Recently, analogous results have been reported by Hu et al., for films deposited at various substrate temperatures using fs laser pulses [202]. The topography of these films was shown

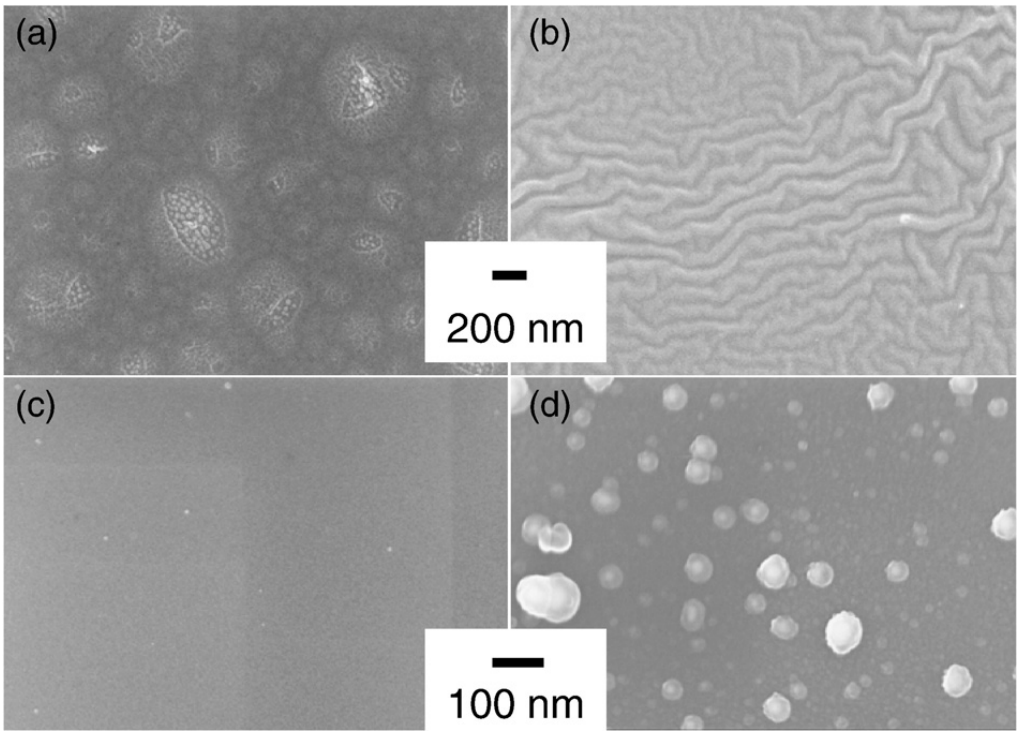

Figure 5.5 - Typical SEM images for fs-DLC films of various thicknesses deposited at representative temperatures: (a) a 200 nm thick film deposited at 77 K; (b) a 600 nm thick film deposited at 77 K; (c) a 100 nm thick deposited at 573 K in vacuum; (d) a 400 nm film deposited at 573 K in a He atmosphere [202].

to be dependent on film thickness as well as temperature, (Figure 5.5), with stress relief patterns occurring in films deposited at 77K. In addition to confirming the relationship between sp^3/sp^2 content and temperature previously established in the ns regime, Hu showed that the concentration of *sp* -bonded carbon in a-C films also varied with temperature. The highest concentrations occurred in thin films synthesized at cryogenic temperatures.

The inclusion of non-reactive buffer gases such as He in the sample chamber during the ablation process can result in the growth of structures not typically associated with a-C. For example, Bolgiaghi et al. [213] showed that columnar, nodular and dendritic, highly porous microstructures evolved as a function of increasing He pressure in glass-like, sp^2 bonded a-C films synthesized using KrF laser pulses (λ = 248 nm, t_p = 20 ns). While buffer gases change the deposited material by affecting the dynamics of the carbon plasma they are not typically incorporated into the resulting thin

films. Reactive gases on the other hand often combine with the a-C matrix effectively doping the material. By far the most common gas used to dope a-C is hydrogen which leads to a materials known as hydrogenated amorphous carbon, or a-C:H. There are two methods which have historically been used to incorporate hydrogen into PLD a-C materials; ablation of graphite in a gaseous environment or irradiation of solid hydrocarbon target materials in vacuum. The resulting material has a unique blend of optical, electronic and mechanical properties analogous to non-hydrogenated a-C. These can range from graphite or polymer-like to diamond-like, depending on the initial conditions under which it was fabricated and subsequent hydrogen content. Owing to this versatility, a-C:H has already been applied in a variety of industrial settings [214].

In one of the earliest articles on the subject, Malshe et al. [215] produced a-C:H by the ns-PLD of graphite under a constant partial pressure of hydrogen (0.45 Torr) using a ruby laser. The resulting amorphous thin films were smooth, chemically inert, weakly absorbing in the infrared and had an increased optical band gap when compared to non-hydrogenated PLD films. Several similar studies on the ns-PLD of a-C:H have shown that the properties of a-C:H films depend on substrate temperature, laser fluence, and gas pressure [216-218]. More recently Hu *et al*. [219] have explored ultrashort fs-PLD of graphite in a variety of hydrocarbon gases using a Ti:Sapphire laser system. Thin films deposited in the presence of hydrogen, acetylene or ethylene gases shared a unique composition that was shown to include polycyclic aromatic hydrocarbons and polyyne chains. The shape and size of these molecular inclusions was found to be dependent on the type of gas present during ablation. These results differed significantly from those of similar a-C:H films synthesized by ns-PLD.

The ablation of a target material containing both carbon and hydrogen, such as a carbon polymer or a frozen hydrocarbon gas, is another method that has been used to make a-C:H thin films by PLD [205, 220-222]. Voevodin et al.[205] showed that a-C:H films, deposited by the KrF ns-pulsed laser irradiation of a polycarbonate target, undergo a structural transformation from graphite-like to diamond-like at laser fluences between 10^8-10^9W/cm^2. Budai et al. [220] defined a parameter called the volumetric intensity (intensity over optical penetration depth), I_{vol}, to compare a-C:H deposited by the PLD of polymer targets using ns- and fs-pulsed laser systems. It was found that films deposited at the lowest I_{vol} values (10^{12}-10^{13} W/cm^3) resembled the original polymer targets while those produced at the highest I_{vol} (~10^{16} W/cm^3) were increasingly amorphous. Finally, the composition of a-C:H from the PLD of frozen hydrocarbon targets has been studied by the Hanabusa group. In their initial work, chemically inert, highly resistive a-C:H was fabricated by the ns-PLD of

frozen acetylene [221]. Later, it was shown that the fs-PLD of frozen acetylene produced black conductive films, and the properties of deposited a-C:H could be changed by using frozen targets of differing composition [222].

This chapter outlines the results of a new technique developed for the synthesis of a-C:H thin films. This method involves the plasma processing of pre-existing solid hydrocarbon layers by the carbon plasma generated from the fs-pulsed laser ablation of a graphite target. The morphology and composition of these deposits has been determined using atomic force microscopy (AFM), as well as by a variety of spectroscopic techniques including photoluminescence (PS), Raman, surface enhanced Raman (SERS), and Fourier transform infrared (FTIR) spectroscopies.

5.2 Experimental

Thin films were synthesized by the deposition of energetic carbon plasma, generated from the fs-pulsed laser ablation of graphite, onto pre-existing frozen chemical layers, in vacuum. A variety of chemicals, purchased from Sigma-Aldrich and of the highest available purity were processed in this way. These included; hexane (C_6H_{14}), octane (C_8H_{18}), decane ($C_{10}H_{22}$), hexene (C_6H_{12}), octene (C_8H_{16}), and water (H_2O). A schematic of this technique is shown in Figure 5.1 and from this point forward the plasma processing of any solid using this method will be referred to as pulsed laser induced plasma processing (PLIPP). In the first step of this process a liquid such as hexane is vacuum evaporated and injected into a stainless steel vacuum chamber raising the base pressure from 5×10^{-7} to 5×10^{-4} Torr. This gas is then allowed to condense onto a cryogenically cooled substrate forming a polycrystalline layer (Figure 5.6a). Optical grade fused quartz or potassium bromide (KBr) disks in thermal contact with a liquid nitrogen reservoir were used as substrates. The thickness of the frozen material was controlled by monitoring the time that the substrate was exposed to the gas. Once a layer is formed the excess gas is evacuated from the chamber. At this point the laser beam is focused onto a target within the vacuum chamber using a 0.16 m focusing lens which results in a peak focal intensity of 2×10^{14} W cm^{-2}. Inside the chamber, a disk of highly oriented pyrolytic graphite (HOPG) serves as the laser ablation target and is positioned parallel to the covered substrate at a distance of 0.04 m (Figure 5.6b). The energetic carbon plasma, resulting from pulsed laser ablation, is then deposited on top of the frozen layer over a set amount of processing time, t_p (Figure 5.6c). In the first experiment layers of hexane were processed for 5, 10 and 20 min. After deposition the samples were then kept *in*

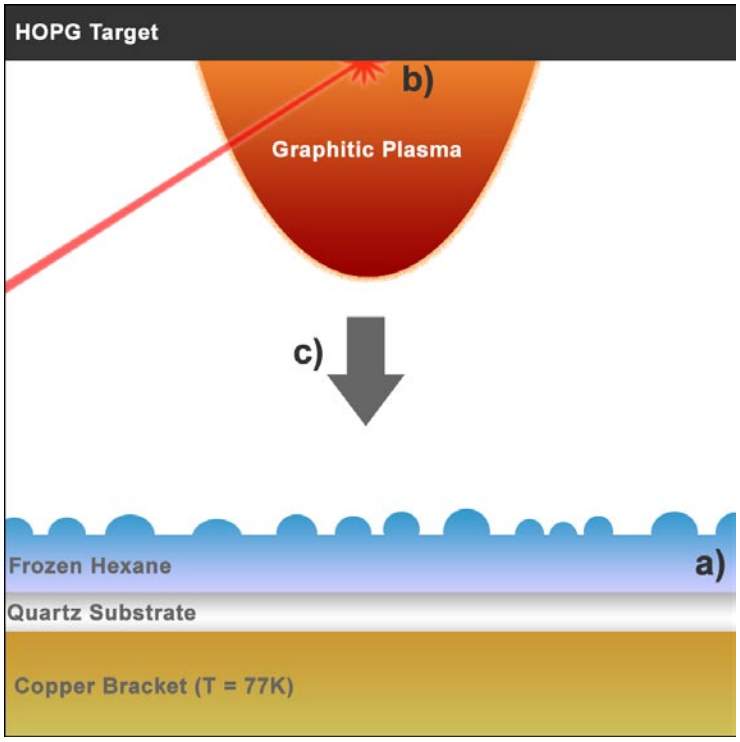

Figure 5.6 - A schematic of the PLIPP process in which a) polycrystalline layers of hexane are initially deposited onto a substrate held at 77K. After these frozen layers are deposited, b) fs-laser pulses ablate a HOPG target forming plasma. This plasma is then used c) to process the frozen hexane layers, resulting in a residual hydrocarbon deposit.

vacuo until their temperature reached 293K after which time they were exposed to atmosphere for analysis. After this initial work, other thin films were produced by 5 min PLIPP of pentane (C_5H_{12}), isopentane (C_5H_{12}), decane ($C_{10}H_{22}$) and docasane ($C_{22}H_{46}$). The effect of warming time and atmospheric exposure on the structure of decane films has also been studied, however; for the sake of continuity the results of these secondary studies are relegated to Appendix B.

The carbon plasma generated with the Ti:Sapphire laser system was characterized using a custom built time of flight mass spectrometer (TOF-MS) with a micro channel plate detector (MCP) at the end of 1 m long flight tube. A detailed description of this system can be found in the doctoral thesis of A.D. Scott, a former member of our group [223]. The time of flight for H^+ and C^+ ions ablated from the target were typically 1.4 and 4.25 µs, respectively. TOF spectra were recorded at delays of up to 100 µs with a mass resolution $\Delta m/m = 10^{-3}$. Thin film morphology was determined

using the JPK atomic force microscope, however; in some cases the Leo field emission scanning electron microscope was also used. The optical properties of the films were determined from UV-Vis absorption and photoluminescence spectroscopy while the molecular bonding structure was studied through (FTIR), Raman, and surface enhanced Raman spectroscopies (SERS). UV-Vis and IR measurements were performed on Shimadzu UV-2501PC and FT-IR 8400S spectrophotometers, respectively. Raman data was gathered on the Renishaw micro-Raman Spectrometer with an objective magnification of 50× and an excitation wavelength of 488 nm (0.5 mW). To facilitate surface enhancement, colloidal silver nanoparticles, with diameter less than 50 nm, were deposited onto the surface of film samples. Photoluminescence (PL) data were obtained using the same Renishaw system.

5.3 Results & Discussion

5.3.1 Plasma Characterization

As outlined in Chapter 2, the plasma generated by laser ablation of graphite has been studied extensively [63-66]. Of relevance to the present work, Qian et al. [64] has reported an intensity dependent low resolution TOF-MS study of graphite ablation products using a laser system similar to the one used here (Ti:Sapphire λ = 780 nm, t_p = 100 fs, $I = 1\times10^{14} - 6\times10^{15}$ Wcm^{-2}). Two strong features were seen in the mass spectrum; a broad peak, considered to be the main ion source, and a narrow "suprathermal" ion peak that preceded it. Due to the low resolution of this study the specific composition of the plasma was not determined, however; to estimate the velocity and kinetic energy of the ionic species corresponding to the two features it was assumed that the main constituents were atomic carbon ions. At a laser intensity of 3×10^{14} Wcm^{-2} the suprathermal ions had an estimated velocity of 250 km s^{-1} corresponding to a kinetic energy of 3.5 keV while the slower moving ions in the main peak traveled at 60 km s^{-1} with an estimated energy of 250 eV.

Figure 5.7 shows a typical TOF spectrum that results from plasma generated by ablation of a HOPG target using the laser system described in Chapter 3. The data were averaged over five pulses with an intensity of 2×10^{14} Wcm^{-2}. The overall spectral envelope (shown in red) is very similar to that described by Qian et al. and consists of a suprathemal feature followed by the main ion peak consisting of the bulk of the plasma. Due to the high mass resolution of the current data, the spectrum itself is quite complex with each peak representing an individual ion or charged cluster. The time of

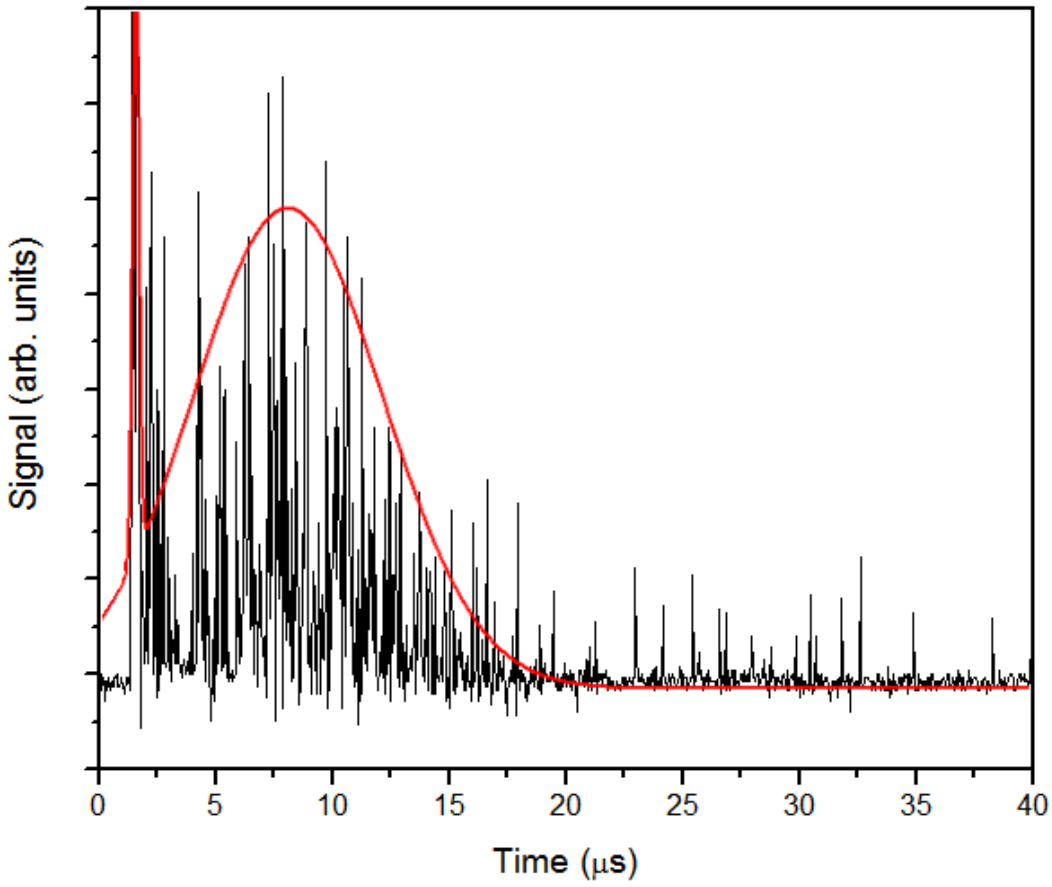

Figure 5.7 - Time of flight mass spectrum of plasma resulting after the ablation of HOPG with 100 fs pulses from the Ti:Sapphire laser. This spectrum results from the averaging of five laser pulses having a focal intensity of ~10^{14} Wcm^{-2} and the red curve represents the overall spectral envelope.

flight of an ion in the plasma is proportional to the square root of its mass-to-charge ratio. Given this value and the experimental parameters, individual plasma species can be identified. A list of the most prominent ions present in the plasma is given in Table 5.1 along with information on their mass-to-charge ratio, initial velocity and kinetic energy. The velocity v_i and kinetic energy E_i of the ions were calculated using the standard equations of electrostatics and kinetics. The suprathermal region of the spectrum is comprised of peaks that result from fast moving hydrogen (H^+, H_2^+) and multiply charged carbon ions (C^{2+}, C^{3+}, C^{4+}). The kinetic energy of species in this region ranges from 2.0-5.5 keV,

Table 5.1 - Some carbon ions and clusters present in the graphite plasma				
Ion	**m/q [kg/C]**	**Time [10^{-6} s]**	**Velocity [km/s]**	**Kinetic energy [keV]**
C^{4+}	3.11×10^{-8}	2.16	297.6	5.50
C^{3+}	4.14×10^{-8}	2.48	254.9	4.04
C^{2+}	6.21×10^{-8}	3.04	208.5	2.70
C^{+}	1.24×10^{-7}	4.24	143.3	1.28
C_2^{+}	2.48×10^{-7}	5.96	100.0	1.24
C_3^{+}	3.73×10^{-7}	7.36	83.1	1.29
C_4^{+}	4.97×10^{-7}	8.52	72.4	1.30
C_5^{+}	6.21×10^{-7}	9.44	63.5	1.25
C_6^{+}	7.45×10^{-7}	10.40	58.2	1.26
C_{16}^{+}	1.99×10^{-6}	16.91	35.6	1.26
C_{22}^{+}	2.73×10^{-6}	19.63	29.6	1.19
C_{60}^{+}	7.45×10^{-6}	32.48	18.0	1.20
C_{70}^{+}	8.70×10^{-6}	34.95	16.5	1.18
C_{84}^{+}	1.04×10^{-5}	38.27	15.0	1.18
H^{+}	1.04×10^{-8}	1.45	626.4	2.04
H_2^{+}	2.09×10^{-8}	2.04	440.7	2.02
CH^{+}	1.35×10^{-7}	4.40	135.4	1.25
CH_2^{+}	1.45×10^{-7}	4.56	131.6	1.26
C_2H^{+}	2.59×10^{-7}	6.12	99.3	1.27
C_3H^{+}	3.83×10^{-7}	7.44	85.0	1.34
$C_3H_5^{+}$	4.26×10^{-7}	7.76	75.8	1.22
$C_4H_4^{+}$	5.39×10^{-7}	8.84	69.0	1.28
$C_5H_3^{+}$	6.52×10^{-7}	9.72	62.6	1.28
$C_6H_2^{+}$	7.66×10^{-7}	10.64	58.5	1.31

which is in good agreement with the results of other authors [63, 64]. The slower component of the plasma (t = 3-20μs) is comprised of singly charged carbon ions (C^{+}) and clusters (C_n^{+}, n = 2-22). Charged carbon clusters that contain up to several hydrogen atoms are also apparent in this region of

the spectrum ($C_nH_m^+$ n = 2-22, m = 1-10). Ions in the main peak have an average kinetic energy of 1.3 keV which is well above the sp^3/sp^2 transition threshold, as expected from our previous work [219]. Trailing the main feature are peaks associated with slower moving, singly charged, large carbon clusters (up to C_{84}^+) that have kinetic energies comparable to ions in the main plume. The presence of large graphite clusters in fs laser plasma plumes has not been previously reported and may have an impact on the formation of a-C:H thin films. Bombardment of solid hydrocarbons by this type of plasma could have many interesting consequences and is examined in the next section of this chapter. In order to simplify the overall chemistry the discussion is initially limited to the time dependent effects of plasma exposure on polycrystalline layers of *n*-hexane.

5.3.2 Plasma Processing Time

To determine the effects of ion bombardment on solid hydrocarbon layers, frozen hexane was processed using the laser plasma as outlined in the previous section. Figure 5.8 shows representative surface morphologies of thin films after PLIPP for 5 (Figure 5.8a), 10 (Figure 5.8b), and 20 (Figure 5.8c) minutes. The surface of thin films remaining after 5 min exposure is densely covered with dendritic-type structures. The shape and size of these features was found to vary but they can be separated into two general categories, which we will refer to as either fern or island-like. Fern-like dendrites (arrow in Figure 5a) consist of a long central axis that can grow in excess of 50 μm in length, and 200 nm in height. Branching structures appear to originate from nucleation sites along the entire length of the central axis. Island-like dendrites are more compact than their fern-like counterparts with branches protruding from a central nucleation site rather than from an elongated stem (circle in Figure 5.8a). Individually, these structures cover a surface area ≤ 25 μm^2, and reach a maximum height of 200 nm. Fractal aggregates generated by diffusion limited aggregation (DLA) often have a very similar appearance to the dendritic structures seen in these films [224]. After 10 minutes of plasma processing, these features become smaller, reaching a maximum height of 160 nm and length of 10 μm, and are more widely spaced on the film surface indicating that structural damage is being caused by the plasma. After exposure for 20 minutes, all long range surface features have disappeared leaving only individual nanoparticles, ranging in height from 2-60 nm, and small nanoparticle clusters. These high-exposure films appear quite similar to a-C deposited by standard fs-pulsed laser ablation of graphite. Overall, the average thickness of all films generated using this method was found to decrease from ~ 48 nm after 5 min to ~ 32 nm after 20 min. This indicates that

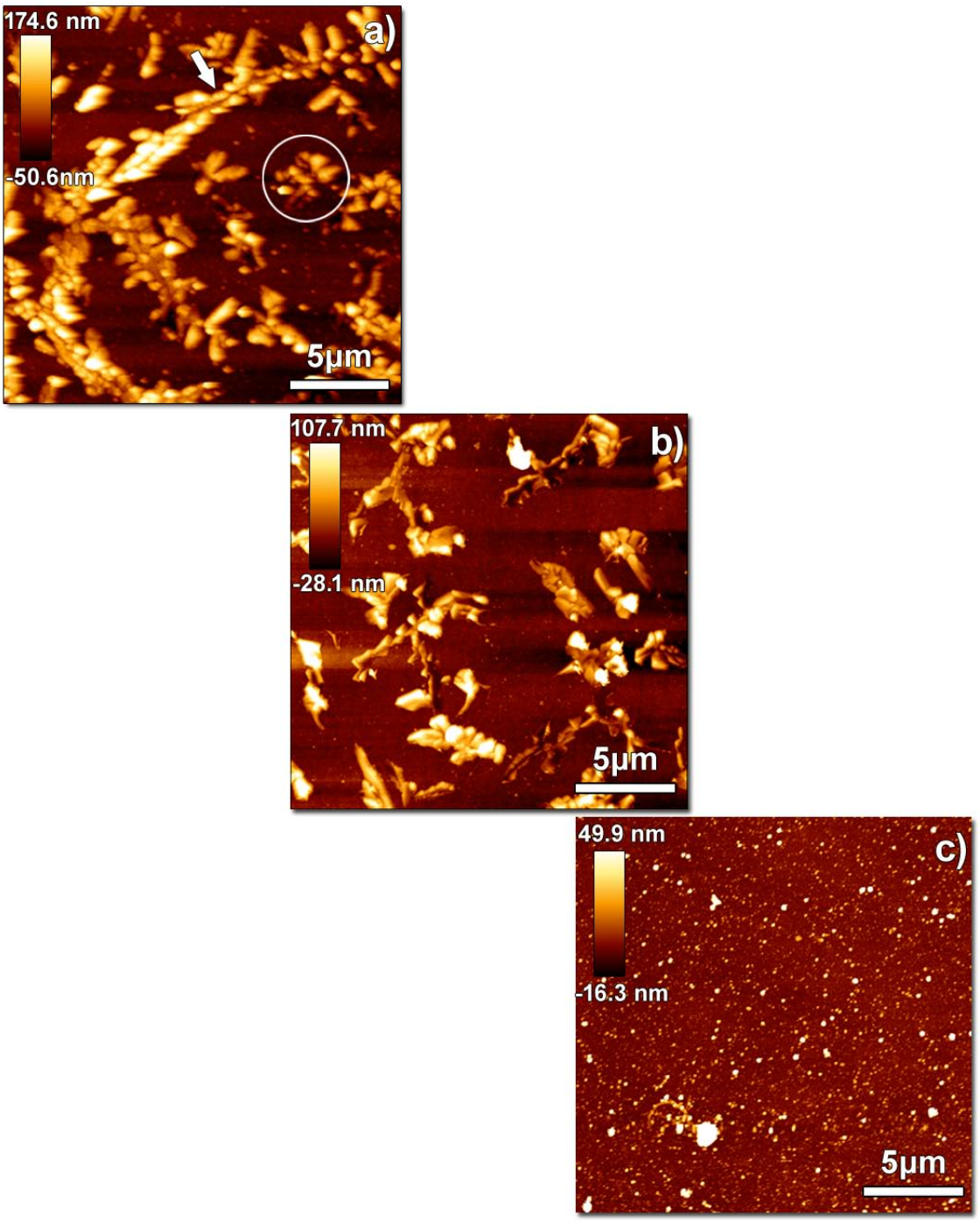

Figure 5.8 - The surface structure of a-C:H thin films remaining after fs pulsed laser induced plasma processing of cryogenic hexane for a) five, b) ten, and c) twenty minutes of plasma exposure. The white arrow indicates a fern-like dendrite while an island-like structure is encircled.

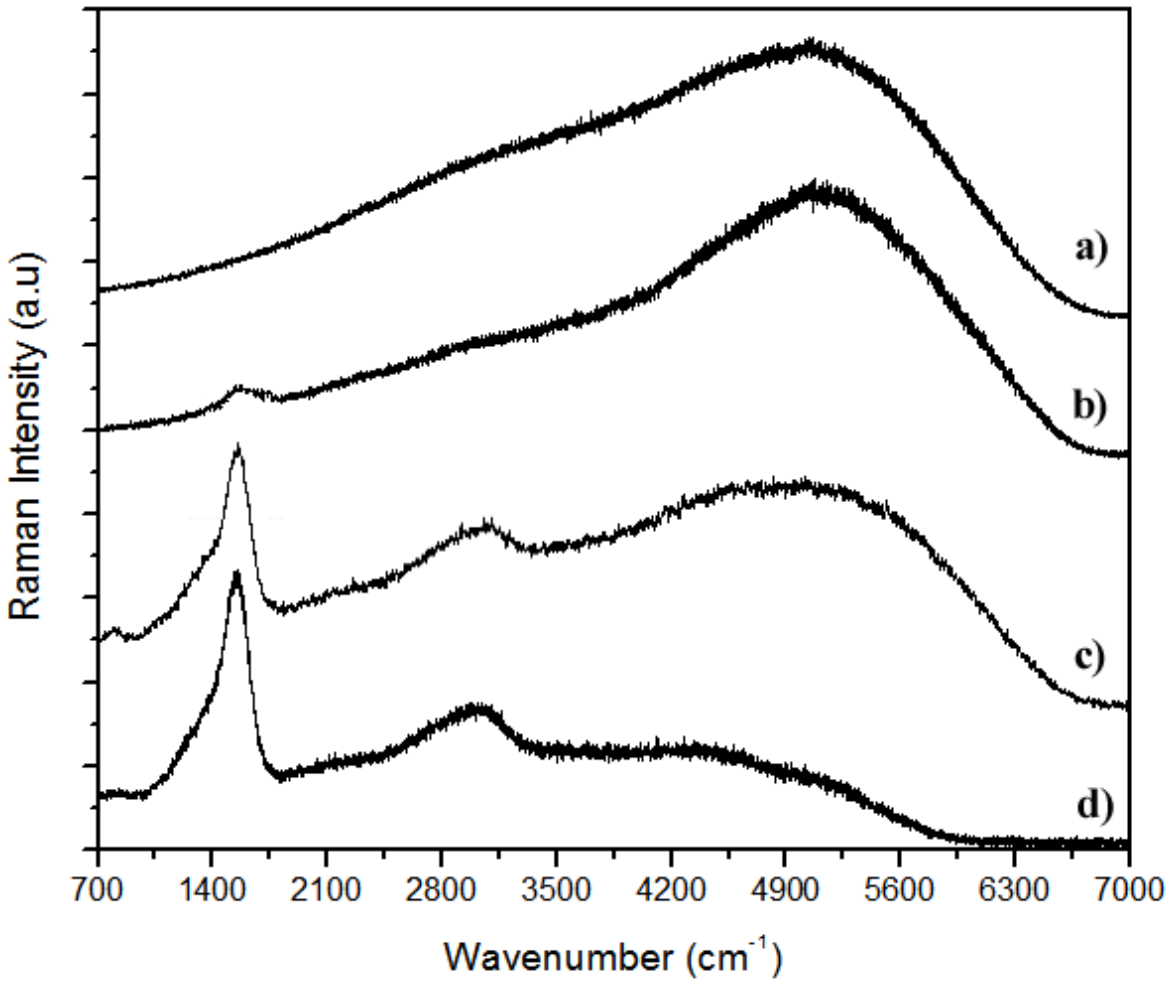

Figure 5.9 - Normalized micro-Raman spectra of PLIPP thin films after a) five, ten (high/low density of surface structure) b/c) and d) twenty minutes of deposition onto hexane at 77K. All spectra have been normalized and were obtained at an excitation wavelength of 488 nm.

the surface structures are residual hydrocarbon deposits left over after processing of solid hexane by the plasma accompanying the ablation of graphite with fs-laser pulses.

The normalized micro-Raman spectra of a-C:H thin films resulting from the PLIPP of hexane at various t_p are shown in Figure 5.9. It is clear that these films change significantly as t_p increases. The spectrum of samples remaining after 5 min of processing is rather featureless and is dominated by a strong photoluminescent (PL) background (Figure 5.9a). Similar Raman spectra have been

Table 5.2 – Summary of Raman and optical data from processed films						
Thin Film	G_{pos} [cm^{-1}]	G_{FWHM} [cm^{-1}]	D_{pos} [cm^{-1}]	D_{FWHM} [cm^{-1}]	I_D/I_G	E_{04} (eV)
5 min (Fig 2a)	n/a	n/a	n/a	n/a	n/a	2.4
10 min (Fig 2b)	1556 ± 1	102 ± 3	1389 ± 2	201 ± 3	0.21	1.9
10 min (Fig 2c)	1556 ± 1	126 ± 1	1391 ± 3	335 ± 10	0.46	1.9
20 min (Fig 2d)	1554 ± 1	136 ± 1	1396 ± 1	309 ± 2	0.51	1.6

reported from polymer-like a-C:H, a soft, low density material that has a structure containing a significant number of H terminated sp^3 C bonds (60%) characterized by a high H content (40-50%), large optical band gap (2-4 eV) and low IR absorption [194, 225, 226]. It is well established that the PL intensity in a-C:H thin films relates directly to H concentration and complete obscurement of the prototypical D and G Raman modes occurs at H concentrations over 42 at.% [39, 194]. This indicates a high level of H in films after short PLIPP. Two spectra are shown for films after 10 min of processing. In areas where there are still many surface features (Figure 5.9b) the large PL background continues to persist but the D peak, due to the breathing mode of six-fold sp^2 C rings and the G peak, resulting from the stretching of sp^2-bonded carbon, begin to appear at ~1500 cm^{-1}. This indicates that in these areas the H concentration has dropped to < 42 at. %. In regions with a lower density of surface features (Figure 5.9c) the PL background is further reduced and the Raman modes are enhanced. The spectrum of films after 20 min of processing (Figure 5.9d) is practically devoid of PL and resembles the spectrum typical of a-C:H with ~20 at. % H [226]. The optical gap, E_{04}, which may be obtained directly from UV-Vis absorption data, also correlates strongly to the hydrogen content in a-C:H [227].We find that the optical gap decreases from 2.4 eV in films processed for 5 min to 1.6 eV in films processed for 20 min. This is an indication that the hydrogen decreases with processing time. Additional information about thin film composition can be gained by examining the evolution of the

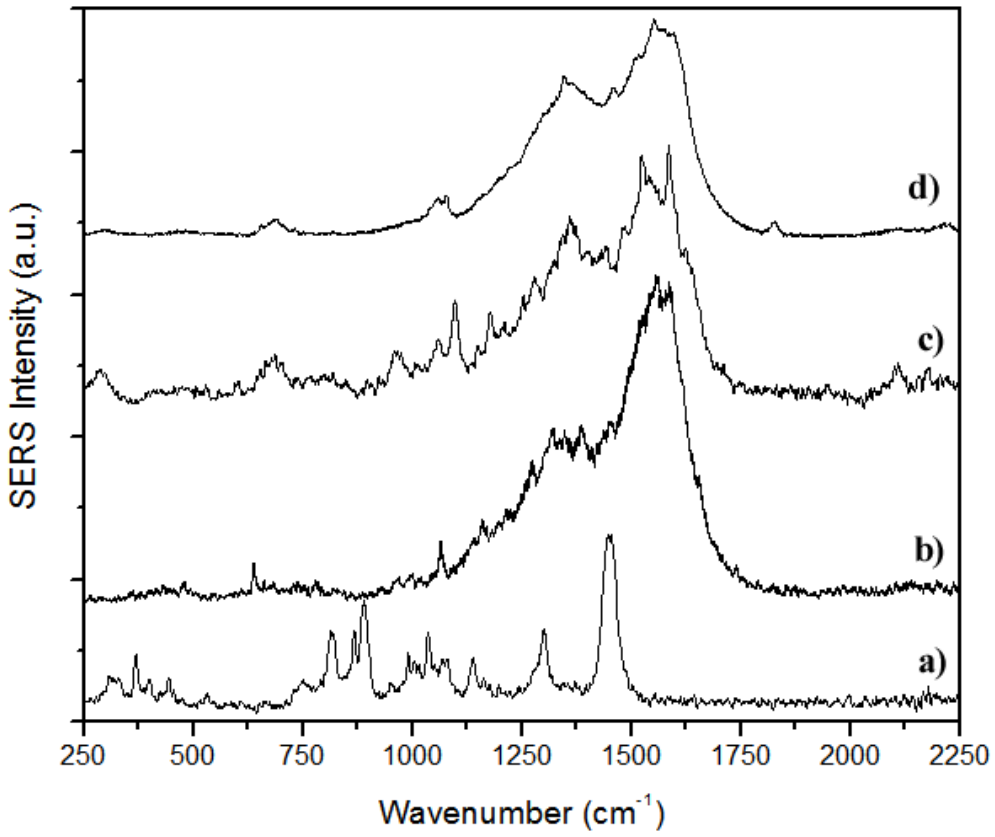

Figure 5.10 - The normalized Raman spectrum of liquid hexane a) and the surface enhanced Raman spectra of thin films processed for b) five, c) ten, and d) twenty minutes, excited by 488 nm Ar^+ laser line.

D and G mode Gaussian fitting parameters; as summarized in Table 5.2. While the energies of the G and D modes are relatively constant, there is a significant increase in the width of both features with t_p signaling an increase in internal stress within the a-C:H matrix. This can be attributed to a decrease in hydrogen content and/or an increase in bond disorder [192, 228]. Amorphous carbon is typically viewed as a collection of independent sp^2 clusters bonded to a sp^3 carbon matrix. The size of these clusters may be determined by taking the ratio of the intensities of the D and G modes, $I_D/I_G = cL_a$ where c is a fitting parameter. The value of this ratio increases with the number of rings (size) forming the clusters and therefore indicates the degree of graphitization of the material [39]. In our films this value scales with t_p and changes from $I_D/I_G = 0.21$ when $t_p = 10$ min to $I_D/I_G = 0.51$ after $t_p = 20$ min suggesting that plasma processing causes graphitization of the underlying hexane layer.

Information concerning the specific molecular content of polymer-like a-C:H cannot normally be obtained with visible Raman spectroscopy but the SERS effect enhances the intensity of vibrational modes in many molecular species allowing for their identification using visible wavelengths. Figure 5.10 shows SERS spectra of films after various t_p as well as the Raman spectrum of liquid hexane over the 250-2250 cm^{-1} range. In this region the spectral profile of hexane (Figure 5.10 a) results mainly from methyl ($-CH_3$) and methylene ($-CH_2-$) group deformations (1300-1480 cm^{-1}), C-C stretching (600-1300 cm^{-1}) vibrations and longitudinal acoustic modes (250-400 cm^{-1}) [229, 230]. The most prominent feature occurs at 1448 cm^{-1} and results from the symmetric scissor type deformation of methylene. This vibration occurs in numerous hydrocarbon molecules and its spectral position can vary from 1440-1480 cm^{-1}. In the SERS data from thin film samples, discrete spectral features not present in conventional Raman appear due to selective plasmonic enhancement and the most prominent vibrational modes with their probable assignments are summarized in Table 5.3. The overall spectral envelope of films processed for 5 min (Figure 5.10 b) resembles that of a-C:H obtained by conventional Raman but the PL background has been suppressed and a large number of small sharp peaks appear. In the G mode region (1500-1640 cm^{-1}) there are a series of peaks that can be attributed to different sp^2 bonded species, with ring vibrations resulting in lower frequency peaks and contributions from conjugated C=C chains giving peaks > 1600 cm^{-1} [39]. Some care must be taken when considering the origin of peaks in the D region (1300-1400 cm^{-1}) as visible Raman C-H modes do not normally contribute to the D mode intensity as they are not optically active; however, this is not the case in SERS. Therefore, peaks occurring in this region may arise not only from six-fold ring breathing vibrations but also from the deformation modes of methyl, ethyl ($-C_2H_5$), butyl ($-C_4H_9$), and propyl ($-C_3H_7$) groups [230]. The appearance of skeletal modes associated with alkyl groups (1100-1300 cm^{-1}) helps to confirm that this is in fact the case. Given that hexane is a fully sp^3 bonded hydrocarbon containing two methyl groups it is not surprising that similar group vibrations are also present in thin films synthesized through PLIPP. It is also significant that a number of peaks in lightly processed films are almost exactly coincident with hexane vibrational modes and include the symmetric methylene scissor vibration occurring at 1449 cm^{-1} [230, 231]. Combined with the presence of additional methylene modes such as the wagging vibration at 1301 cm^{-1}, this suggests that hexane molecules are being incorporated into the a-C:H matrix in a relatively intact state. After further processing, it is expected that these molecules may be dissociated. This should result in additional methyl and methylene vibrational modes since their spectral position is somewhat dependent on chain length. This does appear to be the case in the spectrum of films that

Table 5.3 – SERS data and peak assignments for processed films				
Vibrational Modes	5 min[a)] Peak Position (cm^{-1})	10 min[b)] Peak Position (cm^{-1})	20 min[c)] Peak Position (cm^{-1})	Reference
Hexane	1449, 1301, 1287, 1196, 1178, 1162, 1079, 1068, 1049, 887, 790	1302, 1286, 1177, 1137	1301,1287,1197, 1163	Figure 5.10 a, [229, 230]
sp C		2176, 2155, 2109, 2100	2219, 2208, 1826	[126, 232]
sp^2 G	1586, 1558, 1522	1601, 1585, 1546, 1522	1616, 1549,1522	[39]
$(-CH_3)_n$ def.	1422, 1385	1483, 1452, 1445, 1440, 1400, 1371	1458, 1430	[229.230]
sp^2 D	1347	1360	1346, 1365	[39]
C-C str.	1271, 1168, 1064	1252, 1211, 1190, 1148, 1100, 1096	1246, 1226, 1076, 1057	[229,230]

have been processed for 10 min (Figure 5.10c). In addition to the peaks in the D, G and C-C stretching regions there are now several additional peaks in the 1400-1500 cm^{-1} range which result from different configurations of the asymmetric methyl and methylene scissor deformation vibrations. An additional feature that is of interest in the spectra of thin films processed for 10 min is the appearance of modes in the 1800-2200 cm^{-1} region associated with the vibrations of straight chain *sp* carbon polyynes ($C_{2n}H_2$) or cumulenes (C_nH_4) [126, 232]. These modes are consistent with the formation of polyynes and polycumulenes in a-C:H at low hydrogen content [207]. The spectrum of films processed for 20 min (Figure 5.10d) resembles that of a more traditional a-C:H with low hydrogen content and contains fewer peaks in the methyl and methylene spectral range. These are likely to result from sp^2 bonded carbons given the increase in the D mode intensity seen in the visible Raman spectra of these films (Figure 5.10d).

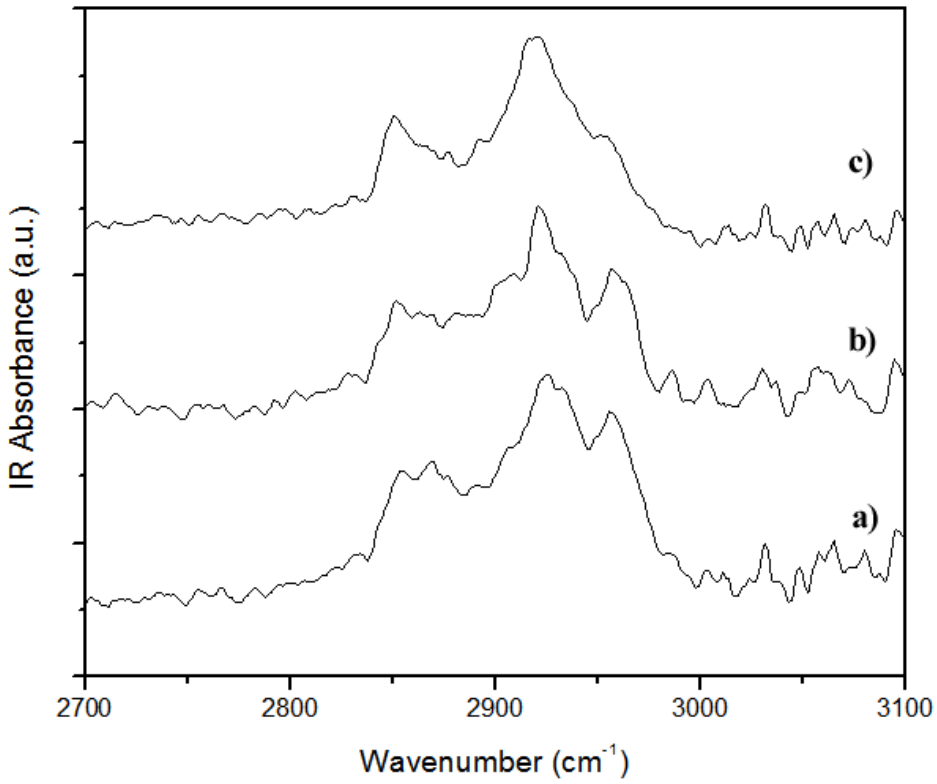

Figure 5.11 - The IR spectra of films produced by a) five, b) ten, and c) twenty minutes of plasma processing of hexane.

Figure 5.11 shows IR spectra of as-produced a-C:H thin films in the 2800-3100 cm^{-1} range. This spectral region can be separated into two sub-regions; the stretching modes of sp^3 CH groups near 2850-2955 cm^{-1} and that of sp^2 bonded CH at 2975-3085 cm^{-1} [233, 234]. The most prominent band in all spectra occurs near 2920 cm^{-1} and results from the anti-symmetric methylene stretching mode. It is paired with the weaker symmetric mode at 2853 cm^{-1}. The symmetric and anti-symmetric stretching modes of the methyl group at 2883 and 2958 cm^{-1}, respectively, are also present in the spectra of films processed for 5 and 10 min. These modes are missing or have reduced intensity in films after with t_p = 20 min. This trend follows that found in the SERS data and the presence of these modes helps to confirm the previous peak assignments. A variety of other modes such as those from olefinic CH_2 at 2975 and 3078 cm^{-1} are also present in these samples but are of much lower intensity. Olefinic CH, with modes in the 2986-3002 cm^{-1} range and aromatic CH arising from 3032-3059 cm^{-1} are also present in IR spectra of all samples.

An additional issue that should be mentioned when discussing the composition of any plasma deposited thin film is the possibility of oxidation and aging due to exposure to atmospheric oxygen and water. It is well established that plasma polymerized thin films contain high concentrations of free radicals which readily react with oxygen to form chemically bonded species within a given film [235-237]. The present samples show no evidence of oxidation within the first 24hr after deposition. Typically, features associated with C=O occur in the 1640-1900 cm^{-1} IR spectral region [238] but no such features were apparent in our data. This is not wholly unexpected since it has been recently shown that a-C:H thin films deposited using different methods, do not react strongly with oxygen [238, 239]. This of course does not preclude the presence of a small percentage of oxygen (< 3%) within the present films, and more sensitive techniques could be employed to determine the role of oxygen. It would be interesting to study this effect, as well as the long term temporal stability of films formed by PLIPP.

Plasma deposited a-C:H thin films produced using traditional synthesis techniques, such as plasma enhanced chemical vapor deposition (PECVD) or PLD, lack long range order and have a relatively simple molecular composition due to the inherently disordered mechanism by which they are formed. When carbon and hydrocarbon plasma species impact a surface they may undergo a variety of physical and chemical interactions including physisorption, H abstraction, dissociation, addition, and ion subplantation. All of these processes are thought to contribute to the growth of a-C:H thin films; however, under most deposition conditions, subplantation is dominant [72, 73, 240]. In many cases, these films have a very simple surface morphology. Some have atomic smoothness while others are rough and are assembled from individual nanoparticles. The overall structure has been found to be a strong function of ion energy and substrate temperature [72]. The surface structure of thin films formed by PLIPP of solid hexane after short exposure times are remarkably different from those of standard a-C:H thin films. For example, the appearance of long range dendritic ordering in carbon films has not been reported previously and likely results from the interaction between the laser produced plasma and the surface of solid hexane.

When the plasma, discussed in the previous section, impacts the polycrystalline surface of solid hexane, it is expected to result in dehydrogenation and the production of a variety of volatile species including CH_4. Additionally, dehydrogenation and photo-dissociation can be initiated by processing as a result of UV radiation emitted by the plasma, although this effect is considered to be small compared to that of ion bombardment [241]. While there have been no direct studies on the

effects of carbon ion bombardment on frozen hexane, a number of authors have examined the effects of He^+ bombardment on frozen butane and benzene. In both cases a-C:H residues were formed with progressive carbonization due to increasing ion dosage [242, 243]. In the present configuration, sub-surface carbon ion implantation and carbon insertion reactions will build larger carbon networks. It appears that hexane molecules are incorporated at this early stage and are retained in the solid after warming to 300K. Continued exposure to the plasma eventually results in the formation of an amorphous carbon film. This sequence is confirmed through the spectroscopic analysis of the PLIPP films preformed ex-situ. After brief plasma exposure, the composition of these films is similar to that of polymer-like amorphous carbon with a significant hexane component. Upon additional plasma processing, SERS and FTIR data indicate that the hexane molecules within the carbon matrix begin to dissociate, likely due to further reaction with C atoms. This also leads to erosion of the dendritic structures (Figure 5.8b) and a decrease in H content through abstraction as evidenced by a decreasing PL background and optical band gap. At long t_p, all distinct long range surface features have been destroyed and the remaining deposits have a surface structure similar to that of traditionally synthesized a-C:H.

Dendritic films, produced after short plasma processing time appear to retain the parent hexane molecules which become incorporated in the solid. This suggests that it may be possible to use the PLIPP technique to generate carbonaceous materials with tailored physical and chemical properties based on networks of sp^2 rings separated by specific distances defined by the length of individual alkane chains. It is therefore of interest to determine if other materials can also be incorporated in a similar way. In the next section the structure and composition of films produced by PLIPP of a variety of alkanes is discussed.

5.3.3 Structure & Composition of Alkane Based Films

The dendritic nanostructures present in thin films remaining after PLIPP of solid hexane (C_6H_{14}), shown over a large area in Figure 5.12, do not appear in PLIPP films of longer chain alkanes. Figures 5.13-5.14 show representative structures present in samples remaining after short PLIPP of octane, and decane, respectively. Octane (C_8H_{18}) films exhibit a number of unique morphologies including needle-like protrusions, spherical particles, faceted crystallites and flat platelets. The needle-like objects occur on the film surface amongst a variety of flat structures (Figure 5.13 a) and are shown at higher resolution in Figure 5.13 b). The needles range in height from 10-40 nm, in width from 80-120 nm and in length between 340-850 nm. Most of these structures are linear and separated,

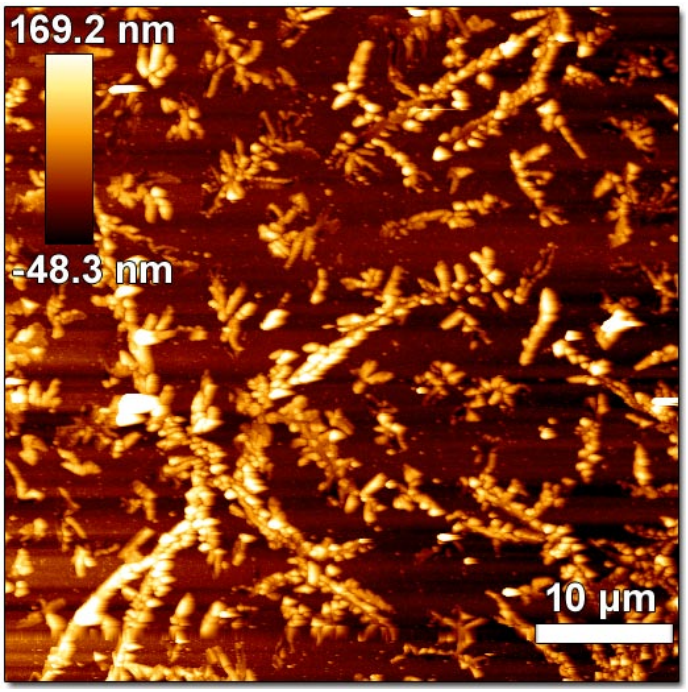

Figure 5.12 - Atomic force micrograph of nanostructures present in films produced by PLIPP of hexane.

however; occasionally needles are either directly connected to each other at 90° angles or to a central parent particle at 120°. In other regions, the surface of the sample is completely covered in a disordered agglomeration of nanoparticles and microstructures (Figure 5.13c). At high resolution (Figure 5.13 d) it is apparent that these structures consist of spherical nanoparticles ranging in diameter from 25-125 nm. Octane films also exhibit structures reminiscent of crystallites, as shown in Figure 5.13 e). These particles are randomly oriented and typically have either a cuboidal or tetrahedral shape. While most of these objects appear to consist of single structural units, some look like they have ridges and are assembled from stacks of smaller objects. This does in fact seem to be the case, with Figure 5.13 f) showing a height scan of a stack of two flat rectangular platelets. Structures comprised of up to six stacked platelets have also been observed, although they are not shown in the figure. Individually, the platelets are relatively thin, ranging in thickness from 20-40 nm, and extremely smooth with an average surface roughness of $\leq$ 1 nm. They also range in width from 150-350 nm and can reach lengths approaching 1 µm.

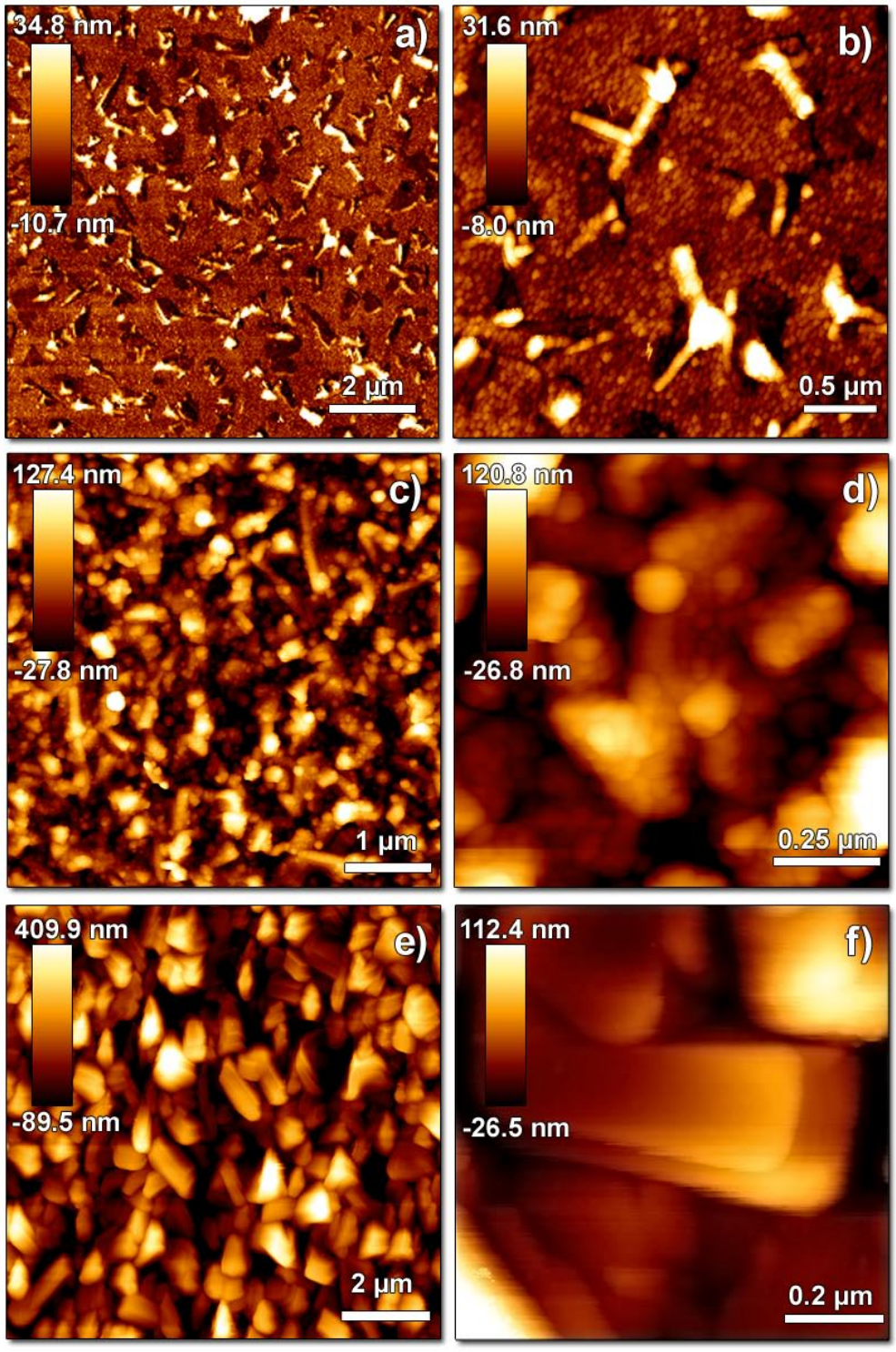

Figure 5.13 - Atomic force micrographs showing the nanostructures present in thin films produced after a 5 min PLIPP of octane.

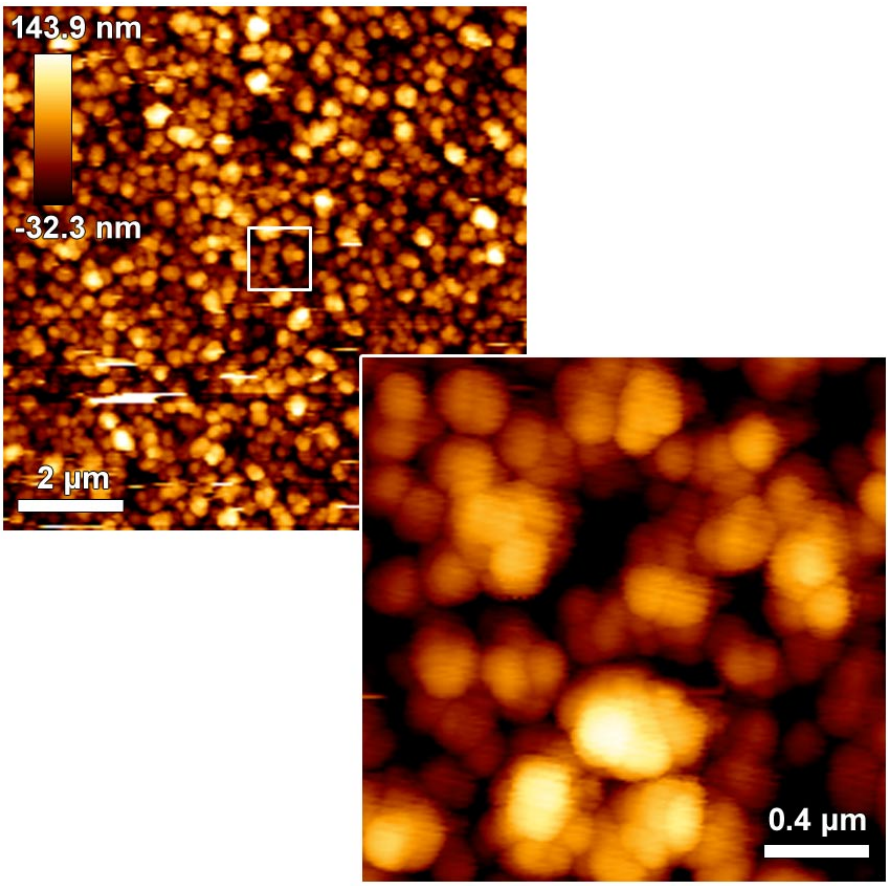

Figure 5.14 - Height scan showing the cauliflower-like clusters that form on films produced by PLIPP of decane.

Figure 5.14 shows the surface structure of films produced after PLIPP of decane. There is far less shape diversity in these samples, with the majority of the surface covered in cauliflower shaped clusters of spherical nanoparticles. Individually the particles, shown in greater detail in the inset, are approximately 150 nm in diameter. The clusters can grow as large as 450 nm in diameter and contain over ten individual components.

Taking into consideration all of the structures present in these samples it is apparent that there are regions in which vastly different nanostructures have formed during PLIPP, as was shown in Figure 5.13. However, this is not necessarily always the case, as some films appear to be relatively homogenous (Figure 5.14). This may point towards potential deficiencies in the current experimental setup. While there is rough control over the formation of the initial frozen hydrocarbon layers, the

system could be adjusted in the future to ensure that flow rates and layer thickness are kept constant between experiments. It is therefore likely that in the current setup there are variations in the physical characteristics of the initial hydrocarbon layers (thickness, substrate coverage etc.) and it would be of great benefit to study these layers *in situ*, before PLIPP, to determine if these parameters have any effect on the deposited film nanostructure. This would require significant refinement of the experimental setup, which is not possible at this time, however; other researchers have examined the growth of vacuum deposited alkane solids and a similar mechanism is assumed to be taking place in the present experiments. For example, Wu et al. [244] have described a Stranski-Krastanov type growth mechanism for a number of short chain, vacuum deposited, *n*-alkane films on single crystal cryogenically cooled substrates. Similar growth has been shown to occur with longer chain alkanes at the liquid-solid interface on disordered fused quartz substrates, suggesting that this model may be applicable on a more general basis [245]. When an alkane vapor is condensed at substrate temperatures well below its bulk melting point, it has been shown to initially form a crystalline monolayer consisting of molecules oriented with their long axis parallel to the substrate. At the solid-gas interface above this layer, alkane nanoparticles grow epitaxially at nucleation sites along crystal planes parallel to the co-existing monolayer film [245]. If the initial deposition of the alkane is insufficient to completely cover the substrate in a single solid monolayer, localized monolayer regions may form. Knüfing et al. have shown these regions often form fractal domains through diffusion limited aggregation [246]. This is probably the mechanism which results in the structures seen in PLIPP films; three dimensional alkane crystals form on the fused quartz substrate which then act as templates for the final a-C:H structures. In areas where there is complete coverage of the substrate, a higher density of nanostructures results, while in areas with lower coverage dendritic and needle-like structures form. As in the previous section the composition of these films was examined using a variety of spectroscopic techniques.

While the thin film nanostructure varies dramatically between samples, there appears to be very little divergence in molecular composition. This is not wholly unexpected, given that the only difference between the starting compounds is chain length. The normal Raman spectra of octane and decane films are nearly identical to those previously observed in hexane films and are characterized by a large PL background that completely masks the D and G modes as in Figure 5.9 a). This again indicates a high level of hydrogenation in these films (> 42%). Additionally, the optical properties of the various samples are very similar; with the optical gap, E_{04}, of all films falling between, 2.3-2.5

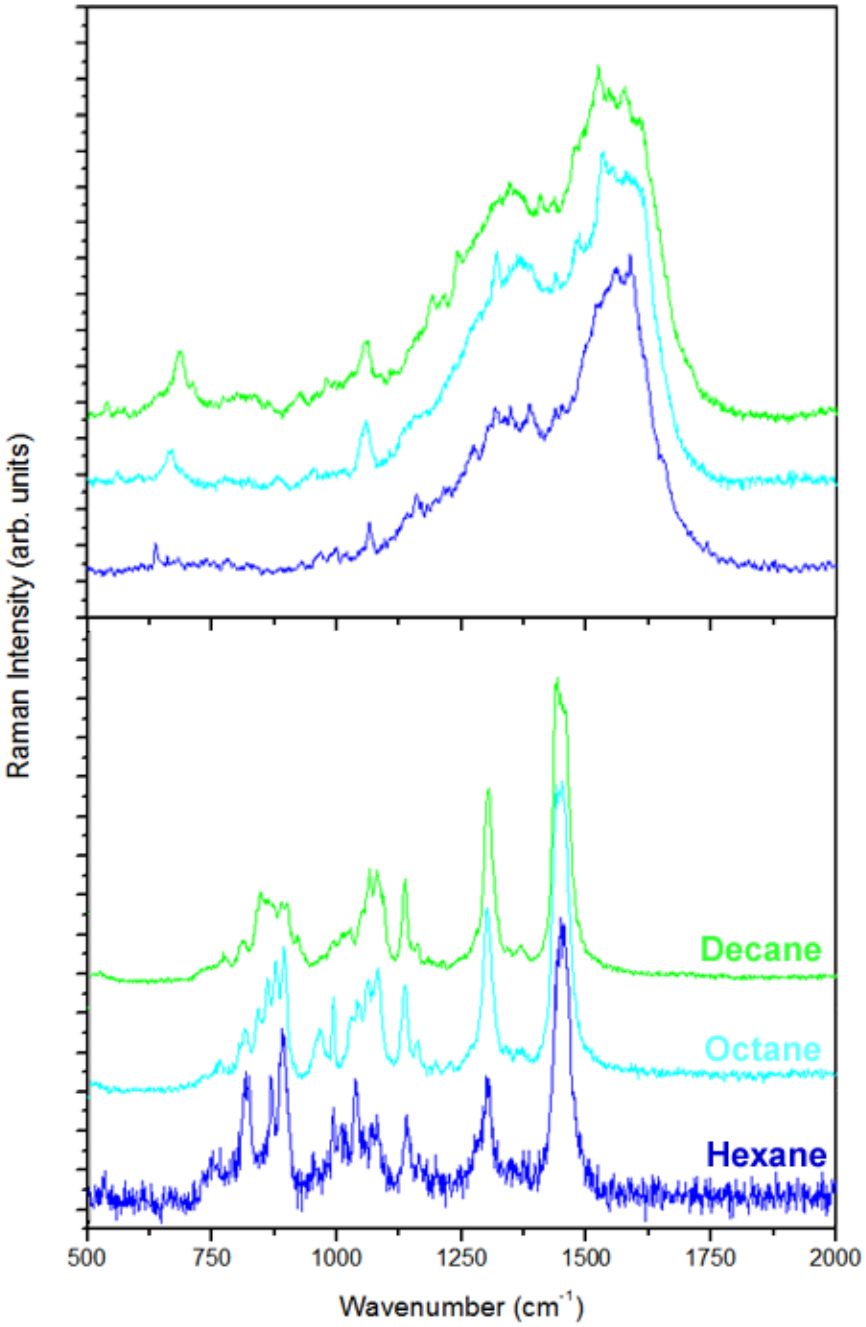

Figure 5.15 - The Raman spectra of pure, size selected alkanes (bottom), and the surface enhanced Raman spectra of the a-C:H thin films produced by PLIPP of the corresponding solid alkane layers.

eV. As was the case in the previous section, to gain specific information about the molecular composition of each thin film sample, surface enhanced Raman spectra are examined.

A comparison of the visible Raman spectra of the liquid alkanes used in this work (bottom) and the SERS spectra of thin films that were produced by their plasma processing (top) is shown in Figure 5.15. The alkane spectra appear very similar in the 500-2000 cm^{-1} range, however; subtle changes occur with increasing chain length. For example, the frequency of the methylene scissor vibration decreases slightly. In alkanes with an even number of carbon atoms this mode is usually split into two maxima that are centered at 1441 and 1457 cm^{-1} in hexane while in octane they occur near 1438 and 1455 cm^{-1}. In decane the peak positions decrease even further to 1436 and 1452 cm^{-1} respectively. The torsional methylene vibration, on the other hand, stays relatively constant, occurring at 1301, 1300, and 1302 cm^{-1} in hexane octane and decane respectively. Also of note is the behavior of peaks in the carbon backbone region between 1000 and 1100 cm^{-1}. As the number of carbon atoms in the chain increases, the individual sharp maxima in this region tend to merge and become poorly resolved near 1080 cm^{-1} [229]. Given the similarities in the spectra of the precursor alkanes it isn't surprising that there is little variation between the spectra of the thin films samples. As was the case in the spectrum of thin films derived from hexane (Figure 5.10 b and Figure 5.15), many of the alkane vibrational modes are present in spectra of films produced by PLIPP of longer alkanes. For example, the methylene scissor vibrations occur near 1437 and 1455 cm^{-1} in octane films while their positions are 1435 and 1452 cm^{-1} in films produced by PLIPP of decane. These features are within a wavenumber of the corresponding values in the liquid suggesting that longer chain alkanes become incorporated into the carbon matrix in a similar way to that which was described for hexane based films. The alkane backbone vibration at 1080 cm^{-1} is also seen in all of the spectra, as is the torsional methylene mode near 1300 cm^{-1}. In addition to the alkane vibrations, a new mode arises in the film samples in the 600-700 cm^{-1} region. Peaks corresponding to carbon ring deformations typically occur in this range [230] and the position of this mode appears to be dependent on chain length increasing from 638 cm^{-1} in hexane films to of 686 cm^{-1} in decane films.

To determine the overall nature of these newly formed films, the spectral envelope from 1000-2000 cm^{-1} was used to extract the positions of D and G modes. The positions of these modes were found to be relatively constant between samples, with values of 1350 ± 5 cm^{-1} and 1570 ± 6cm^{-1}, respectively. However the ratio of the intensities of these features, I_D/I_G, was found to increase

significantly with chain length i.e. 0.53, 0.64 and 0.72 for hexane, octane and decane films respectively. An increase in this ratio generally corresponds to an average increase in number of C_6 rings present in a sp^2 cluster, which, given the present values changes from 10-12 rings between hexane and decane films. These findings help to confirm that by changing the length of the alkane chain in the initial base layers the structure of the carbon network can be tailored. This suggests that these networks could be used in molecular sieve or chemical sensing applications.

5.3.4 Compositional Dependence on Unsaturated Bonds

Now that it has been shown that fine control over the molecular composition of a-C:H is possible using alkanes of different length during PLIPP, it is useful to determine if this technique can be applied to other materials. Alkenes are chemical compounds that are closely related to alkanes. They differ only by the presence of a single unsaturated bond (-$CH=CH_2$ vinyl group) in the carbon chain. Alkenes such as 1-hexene (C_6H_{12}) and 1-octene (C_8H_{16}) are often used in the synthesis of polymers, either through catalytic co-polymerization with ethylene to produce polyethylene or through electric arc plasma polymerization [247, 248]. The addition of carbon double bonds to the initial frozen base layer should have a significant effect on the final nanostructure and molecular composition of the thin film samples.

The nanostructures of thin films derived from hexene and octene are shown in Figure 5.16. Hexene films appear to be composed of large nanoparticle clusters (Figure 5.16 a) about ~150 nm in diameter assembled from smaller round nanoparticles that are ≤ 50 nm in size (Figure 5.16b). These films have a similar appearance to the films produced by PLIPP of decane, but the size of the constituent nanoparticles is smaller and there is less of a hierarchical structure. The appearance of thin films derived from octene (Figure 5.16 c) differs significantly from that of samples produced by PLIPP of other materials. The surface has the appearance of a relatively uniform sheet of material that is crumpled and ridged in many areas. Large micron sized holes in the film are also visible in image. Strangely, at higher resolution (Figure 5.16 d), the surface does not appear to be particle assembled; rather it forms a somewhat smooth, continuous film. This suggests that the PLIPP technique may have caused large scale polymerization of the octene base layers. It is unclear why this has occurred in the octene samples but not in those produced by PLIPP of hexene since hexene has been shown to undergo plasma polymerization [248]. In an effort to determine if there is any difference in the molecular composition of these samples their vibrational spectra were examined using SERS.

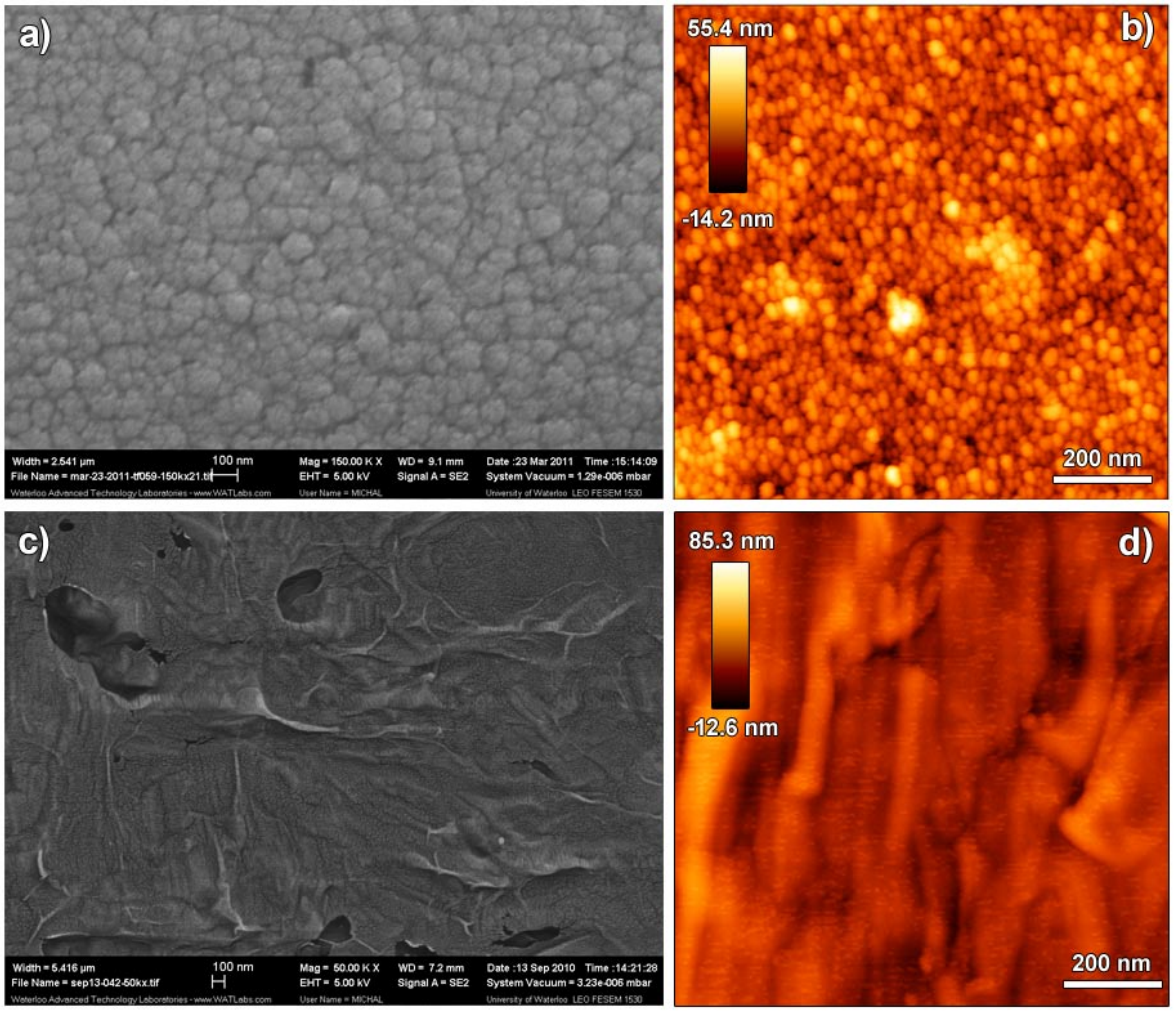

Figure 5.16 - SEM images of the nanostructure of thin films remaining after PLIPP of a) solid hexene and c) solid octene. Higher resolution AFM topographical scans of the corresponding films are presented in b) and d) respectively.

A comparison of SERS spectra taken from thin films made by PLIPP of a) hexane, b) hexene, c) octane, and d) octene is shown in Figure 5.17. The spectra of all film samples are comparable, as expected given the similarity of the starting materials. There are, however, some key differences between alkane and alkene based thin films. A C=C stretching vibrational mode, typically found between 1640 and 1650 cm^{-1} occurs in spectra of alkenes due to their vinyl group [230]. Peaks associated with this mode are found in both hexene and octene based thin film samples (Figure 5.17 b and d) at 1642 and 1640 cm^{-1} respectively. The presence of this mode in both alkene films suggests

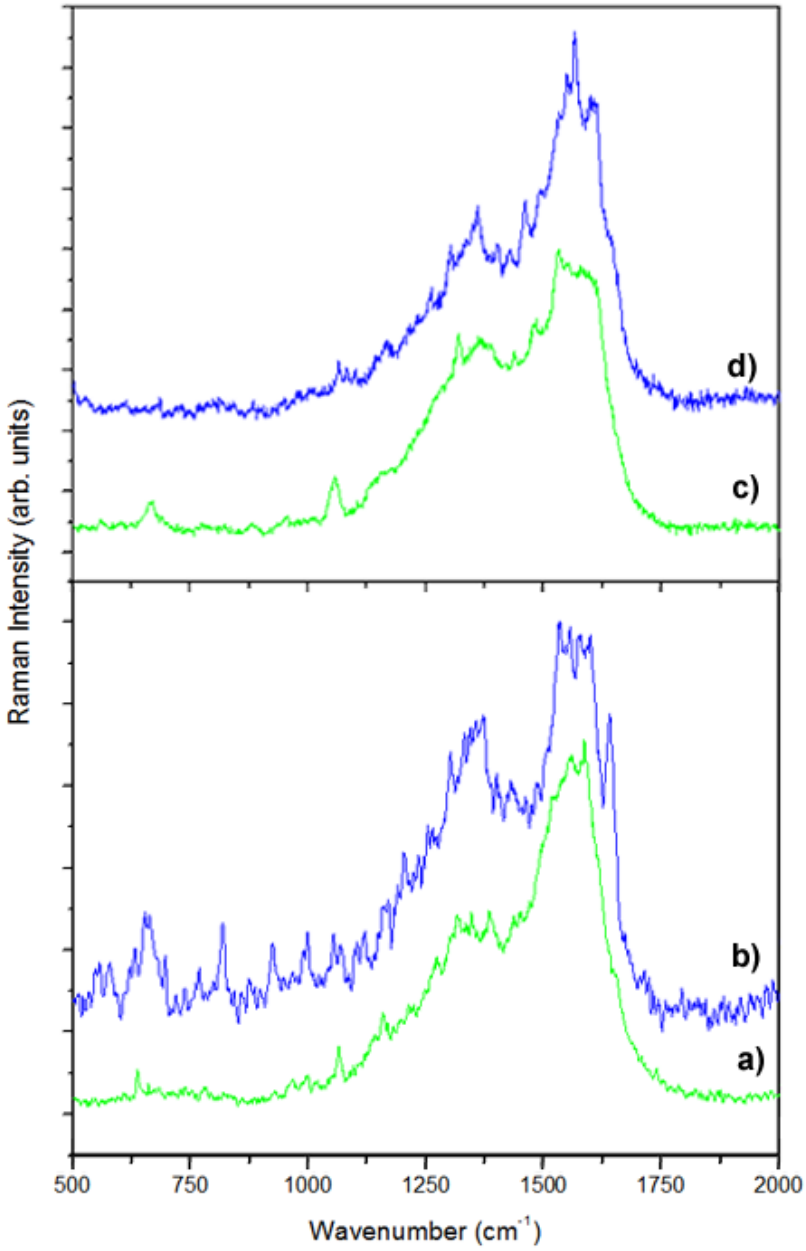

Figure 5.17 - The SERS spectra of thin films produced by PLIPP of solid a) hexane, b) hexene, c) octane and d) octene.

that they have been incorporated into the film matrix in a relatively intact state, as was the case for the alkane films. Aside from this feature, a stretching mode from conjugated chains is also present in both spectra near 1608 cm^{-1} [39]. At slightly lower wavenumbers there are several peaks present in the

1530-1600 cm^{-1} region. These are associated with the multi-component G mode and arise from the stretching vibrations of various conformations of sp^2 carbon [34, 39]. Group vibrations arising from methylene and methyl vibrations in the 1300-1480 cm^{-1} range are also present in these samples, as expected. Common features include the sharp peaks associated with methylene deformation vibrations near 1450 and 1435 cm^{-1} as well as a number of methyl deformation modes (~1400 and 1386 cm^{-1}). The D mode (~1350 cm^{-1}), resulting from sp^2 ring vibrations, is also observed in this range. As was the case in alkane based films a number of skeletal modes associated with alkyl groups (1100-1300 cm^{-1}) are also present in the alkene thin films. Vinyl twisting modes are present in both alkene films and occur in the 990-1010 cm^{-1} range, however; the C-C ring stretching vibrations also occur in this region and therefore definite assignment of these modes is not possible [230, 249]. Unbranched 1-alkenes typically have ethylene type twisting and wagging skeletal vibrations between 550 and 700 cm^{-1} and there are several features present in this range in the spectra of thin films samples [249]. It is then likely that alkene molecules are being incorporated into a carbon matrix that is mainly comprised of sp^2 chains and rings.

The topography and the overall molecular composition of these samples suggest that the material formed after PLIPP of alkenes may be akin to an allyl or styrene based polymer [250]. While this is not a definitive classification, these samples are, at the very least, a new form of highly polymer-like amorphous carbon. It is clear that precise control over the structure of the deposited thin films may be achieved by altering the molecular composition of the initial frozen base layer. Like the alkane based films, this material may be of use in molecular sieve or chemical sensing applications. In that context, it would be of interest to explore the reactivity of both alkane and alkene based thin films to determine if they are reactive with respect to different chemical substances. It would also be useful to process other types of hydrocarbons using this technique. To examine this possibility, the next section describes a preliminary study of the effect of PLIPP one of the most common inorganic polar solvents; water.

5.3.5 Ionic Bombardment of Water Ice

Water ice is one of the most common constituents of circumstellar (CM) and interstellar medium (ISM). It has been detected in comets, on planets and moons, and in interstellar clouds [251, 252]. In many regions, ice and ice covered surfaces are exposed to bombardment by energetic carbon ions from shocks [253, 254]. The experimental techniques developed here afford a unique opportunity to simulate this type of environment and is the basis for the research covered in this section. As in

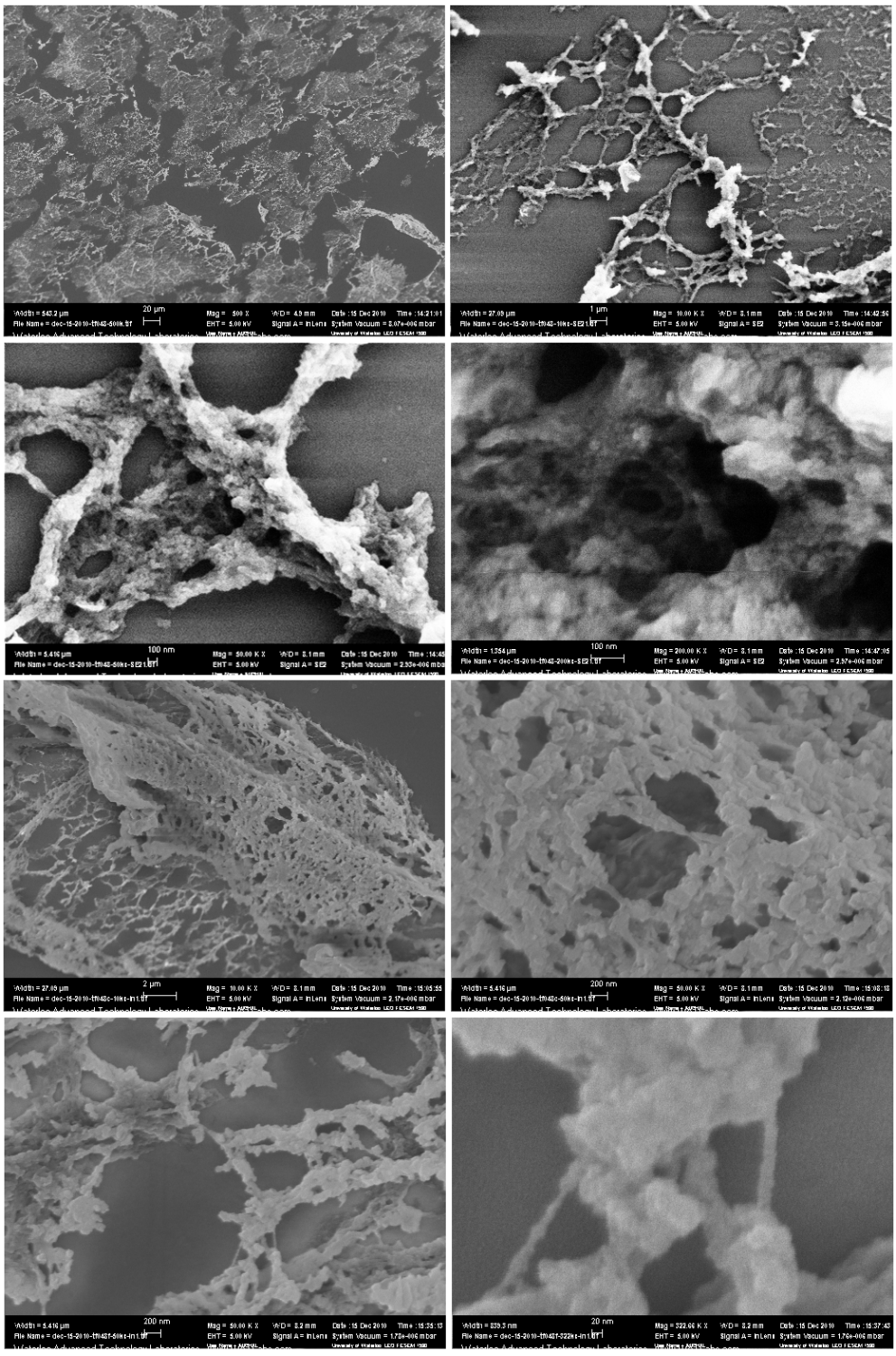

Figure 5.18 - Scanning electron micrographs of the nanostructure of thin films produced by PLIPP of water ice in vacuum at 77K.

previous PLIPP experiments, ultra-pure water was deposited onto a substrate at 77K in vacuum and subsequently exposed to the laser induced carbon plasma for five minutes. The deposited material was then allowed to warm naturally *in vacuo* until it reached room temperature, after which it was removed for examination.

A number of electron micrographs of the surface of this material are shown in Figure 5.18. Large areas of the substrate are covered in a lacy network, which at higher resolution appears to be an interconnected web of nano-sized fibers. Individually, these structures range in diameter from ~15-500 nm. The smallest fibers (bottom of figure) have diameters that range from 15-25 nm and can stretch to cross a gap of 300 nm. In some regions this network appears to have rolled over itself forming three dimensional cage-like objects. This likely occurs due to delamination of the film from the substrate during the warming phase after plasma processing. While hydrogen cannot be detected by energy-dispersive X-ray spectroscopy (EDS), heavier elements such as carbon and oxygen may be readily identified. Quite unexpectedly, these samples were found to contain little to no oxygen, and have only a single EDS peak in the spectrum, resulting from pure carbon. This indicates that water molecules are not being incorporated into the carbon matrix and differs significantly from the results of previous PLIPP experiments. In previous experiments where water ice has been bombarded by noble gas ions or charged C_{60} molecules of similar energy to the carbon plasma used here, it was shown that two processes take place at the target; molecular sputtering and dissociation [255, 256]. The sputtering yield has been demonstrated to be proportional to the square of the energy lost by ions in electronic collisions with the ice molecules. This process leads to the formation of pores and to progressive erosion of the target [254, 257]. Water also dissociates readily under ionic bombardment in the keV-meV ion energy range, giving H atoms and hydroxyl radicals which may then react with other target or ionic species. It is apparent therefore, that water molecules do not become trapped in the deposited carbon material because water is either sputtered away from the surface or is dissociated. One possible explanation for the lack of oxygen in the deposited carbon samples is the formation of hydrogen peroxide ($2H_2O \rightarrow 2H + H_2O_2$) in the target. This has been shown to be the main product of water ice bombardment by noble gas ions [254], although the relative abundance of H_2O_2 in H_2O was found to be only 0.02. The excess hydrogen from this reaction may then react with other ions from the plasma. After plasma processing, any excess water or hydrogen peroxide remaining on the substrate will evaporate on warming to room temperature leaving behind the deposited carbon network. To determine if hydrogen is in fact incorporated into material a variety of spectroscopic techniques were employed.

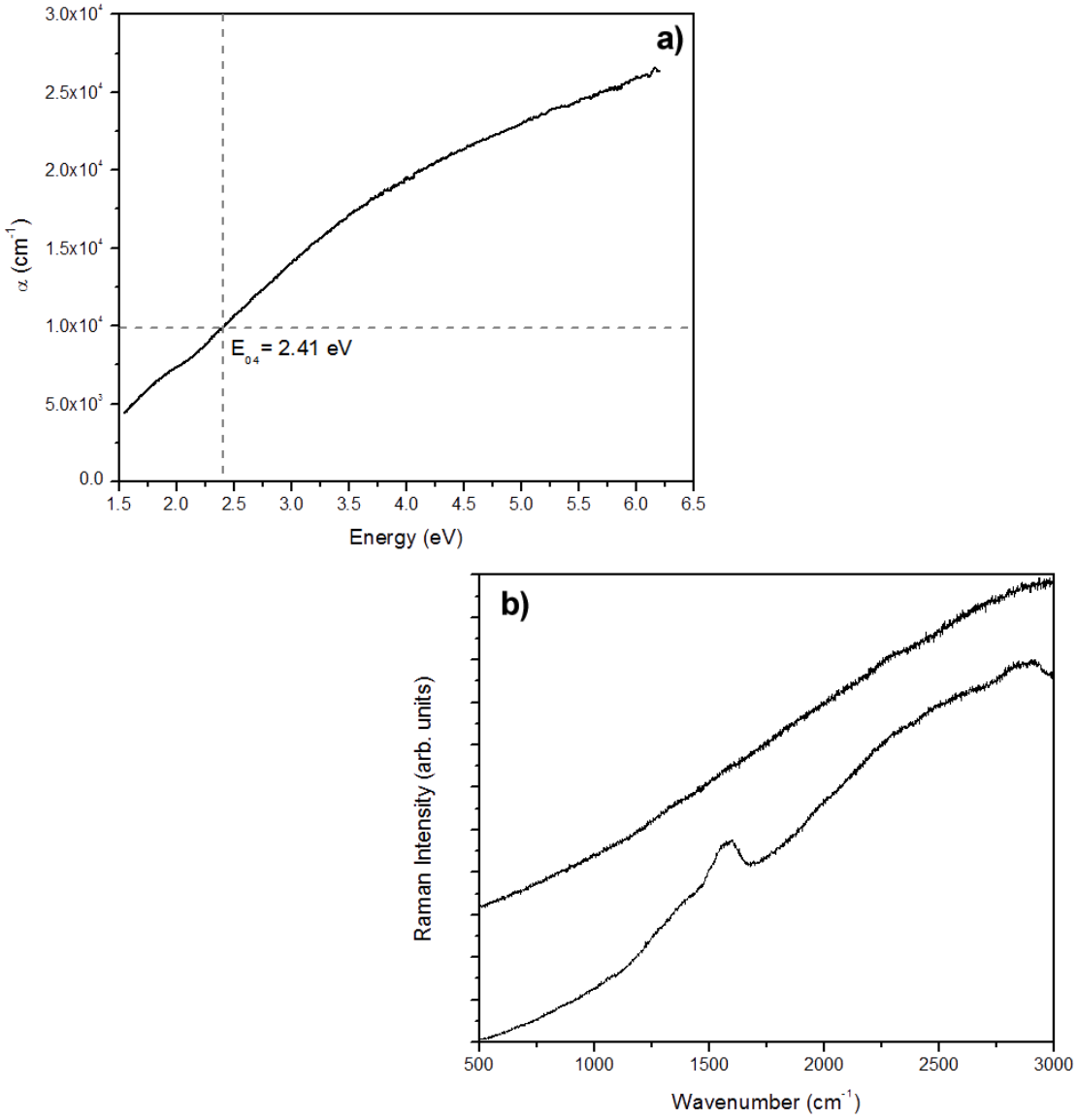

Figure 5.19 - The E_{04} optical gap of thin films produced by PLIPP of water ice can be determined directly in a) by plotting absorption coefficient as a function of energy. The photoluminescent emission spectrum on excitation of the thin film with 488 nm laser light is shown in b) where the top curve results from an area of high H content and the bottom curve is taken from a region of slightly lower H concentration.

The value of the E_{04} optical band gap may be obtained by plotting the absorption coefficient (α), derived from the UV-VIS absorption spectrum, as a function of energy (eV) in Figure 5.19 a). The sample thickness was determined using AFM line scans. For this sample E_{04} = 2.41 eV, which is similar to that of other hydrogenated amorphous carbon thin films created by PLIPP. The Raman spectrum varies slightly across the sample as seen in Figure 5.19b). In most cases the Raman vibrational modes are completely obscured by a large photoluminescent background. This indicates that the hydrogen content is > 42% according to the Marchon slope parameter [194]. In some areas on the film the hydrogen content drops slightly to ~ 40% and the Raman modes become visible. The energies of the D and G modes appear at 1389 cm^{-1} and 1571 cm^{-1} respectively, and I_D/I_G = 0.52. According to the Tuinstra and Koenig relationship defined previously, this I_D/I_G ratio corresponds to a cluster size of 6.7 nm [158]. The relatively high energy of the D mode indicates that there is less disorder in the carbon matrix in these films than in traditional amorphous carbon. Combined with the position of the G peak and the measured I_D/I_G ratio, this suggests that this material is a poly- or nano-crystalline graphite according to the three stage Ferrari and Robertson model [39]. This composition is similar to the mesoporous nanocrystalline graphite described in Chapter 4.3.4.

For a more detailed analysis of the molecular structure, SERS and FTIR spectra are presented in Figure 5.20. The SERS spectrum (Figure 5.20 a) contains a number of well defined peaks, the most prominent being associated with the D and G modes. The G mode region can be decomposed into three Lorentzian features with peak values at 1615, 1583 and 1529 cm^{-1}. The feature occurring at 1615 cm^{-1} can be attributed to vibrational modes of olefinic chains or to the breakdown of local lattice symmetries at grain boundaries in micro and nanocrystalline graphite [39]. The other spectral features in this region likely arise from sp^2 ring vibrations, with the 1583 cm^{-1} band corresponding directly to the E_{2g} mode of graphite. Another spectral feature with medium intensity is found near 1475 cm^{-1} and may arise due to the semicircle ring stretch vibration of carbon rings. The most prominent spectral feature in the D region occurs at 1344 cm^{-1} with a weaker band near 1378 cm^{-1}. Both of these features correspond to disorder induced radial ring vibrations [34]. A number of medium to low intensity features are present in region from 1100-1300cm^{-1}, with the most intense peak at 1204 cm^{-1}. Vibrational modes in this region typically result from C-H deformation or C-C stretching vibrations, however; the band near 1200 cm^{-1} has also been associated with vibrations in the amorphous diamond lattice [192, 258]. Features in the region below 1100 cm^{-1} (magnified in the figure) typically result from C-C stretching, ring deformation modes in substituted benzenes, or a variety of fullerene and nanotube vibrations [207, 230, 259]. In fact, the intermediate frequency modes that

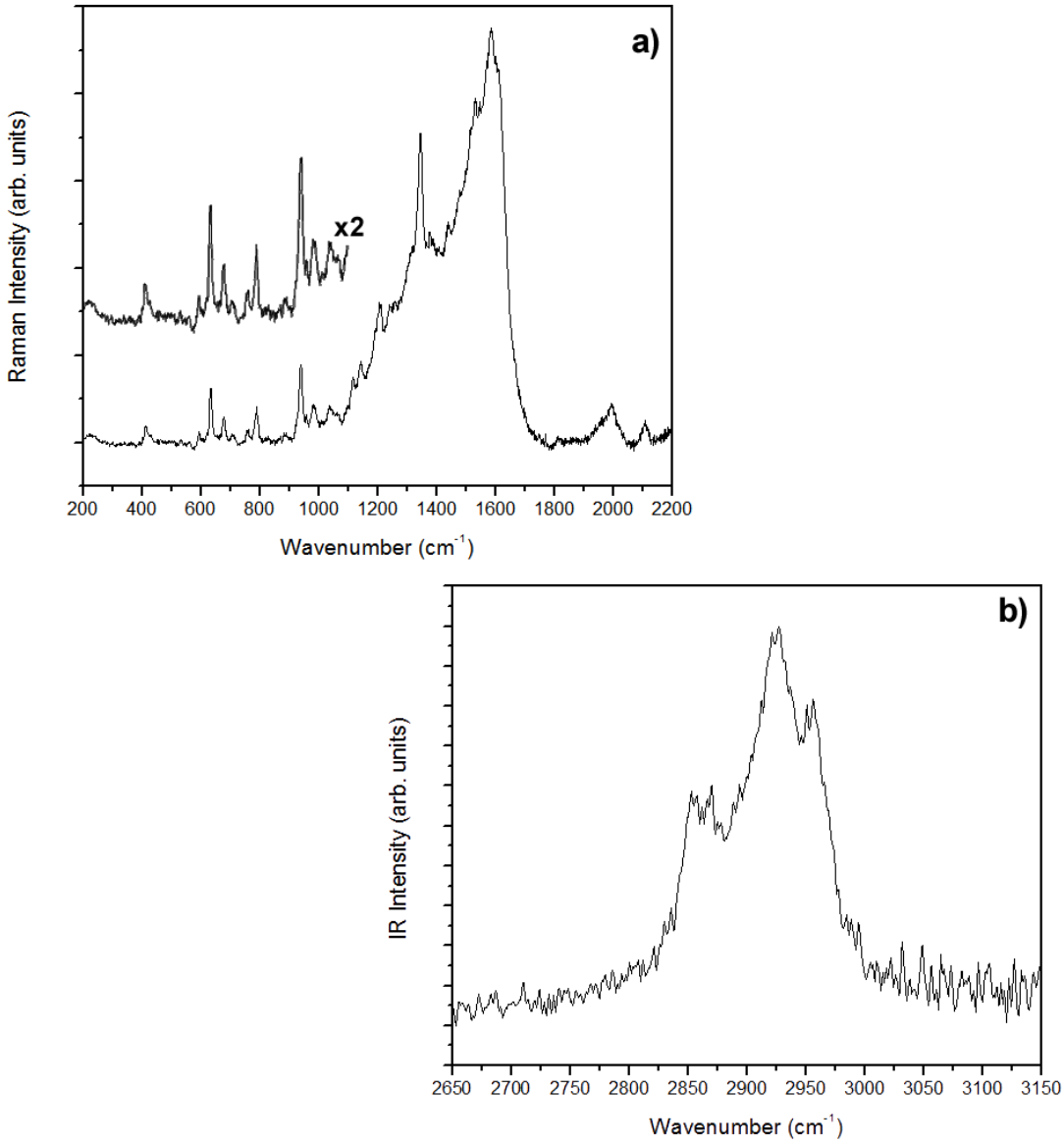

Figure 5.20 - The a) SERS, and b) FTIR spectra of thin films produced by PLIPP of water ice at 77K.

arise in highly defected carbon nanotubes match very well with the observed spectral features in this region [259]. Figure 5.20 b), shows a representative FTIR spectrum in the 2650-3150 cm^{-1} range. The spectrum can be deconvolved into five Lorentzian peaks corresponding to symmetric and/or asymmetric vibrations of CH (2910 cm^{-1}), CH_2 (2854, 2926 cm^{-1}) and CH_3 (2869, 1958 cm^{-1}). This suggests that hydrogen is bonded to the nanocrystalline carbon matrix at sp^3 sites.

Many complex carbonaceous materials have been identified in interstellar carbon dust including; graphitic onions, a-C, a-C:H, polycyclic aromatic hydrocarbons and fullerenes [260, 261] . It has been suggested that another constituent of the ISM could be the hydrogenated analogue of fullerenes; fulleranes [262]. It is quite possible that these types of molecules are being formed during the current experiments, given the fiber-like nanostructures shown in Figure 5.18 and their overall molecular composition. Bombardment of water ice by highly energetic carbon ions may therefore be a possible route to the natural formation of complex carbon structures throughout the interstellar medium.

5.4 Summary

A new method has been developed for the synthesis of polymer-like and nanocrystalline carbon materials. This technique is an augmentation of traditional pulsed laser deposition and involves the plasma processing of frozen materials with pulsed laser initiated graphitic plasma has been named pulsed laser induced plasma processing (PLIPP). The effects of plasma processing time on polycrystalline hexane layers were studied initially. After short processing times (5 min) the resulting thin film had a unique dendritic surface morphology and was polymer-like with strong room temperature photoluminescence. These films were also found to retain the parent hexane molecules which became incorporated in the solid. Upon further processing these surface structures were gradually destroyed resulting in a nano-particle assembled amorphous carbon film.

After this initial study, other alkane and alkene molecules including; octane, decane hexene and octene, were processed using this technique for short periods to determine if chemical control over the a-C:H molecular network was possible. The nanostructure of each sample was found to be significantly different, ranging from nano-needles, to platelets and spheres in alkane based films. These films all contained a similar hydrogen concentration and were found to be partially composed of their parent molecules. Slight changes in the intensity of the D and G Raman modes of these films showed that the size of carbon clusters in the polymer-like a-C:H matrix was dependent on chain length. Films produced by the PLIPP of alkenes were similarly composed of their parent molecules and also had nanostructures that were unique from those of the previous films. The addition of an unsaturated bond in the base layers increased the sp^2 content of the resulting films and may have lead to the plasma polymerization of the initial molecules. This suggests that it could be possible to use the

PLIPP technique to generate carbonaceous materials with tailored physical and chemical properties based on networks of sp^2 rings separated by specific distances defined by the length of individual alkane or alkene chains. Amorphous carbon thin films have been suggested for use as molecular sieves, and tailored carbon networks generated by PLIPP could potentially be useful in this type of application.

Finally, in a slight departure from the previous experiments, the effects of carbon ion bombardment on water ice were examined in an effort to understand certain astrophysical processes. The resulting deposited material had the appearance of an extended web-like network of nanofibers. Unlike the previous sample, whole water molecules were not incorporated into the material due to the ready dissociation of water under ion bombardment. Instead the carbon plasma was found to react with free hydrogen and formed a nanocrystalline carbon material. It is possible that the smallest of the fibers, which were found to be ~20 nm in diameter could be hydrogenated fullerenes.

Chapter 6
Summary and Critical Perspectives

Mille viae ducunt homines per saecula Romam. Just as a thousand roads lead men forever to Rome, it has been shown in this dissertation that at least two roads, built upon the interaction of light and matter, lead to the creation of nanomaterials. The first of these synthesis pathways involves the photo-dissociation of liquids by direct irradiation with ultrashort laser pulses, while the second entails the bombardment of polycrystalline chemical layers by a pulsed laser induced carbon plasma. A variety of carbon nanomaterials were created using these techniques as summarized here.

The pulsed laser irradiation (PLI) of liquid benzene (C_6H_6) was found to result in the formation of spherical, prolate and toroidal nanoparticles. These particles ranged in size from 1-25 nm and consisted of clusters of sp^2-bonded aromatic rings bridged by *sp* hybridized polyyne functionalities (C_nH_2, n = 8, 10) molecules. In a complimentary experiment, liquid toluene ($C_6H_5CH_3$) was irradiated under similar conditions. After an extended irradiation period, a series of free floating methyl capped polyynes, with chain lengths ranging from C_{10} – C_{20}, were identified in the resulting liquid. Under these conditions, no amorphous carbon components were produced. The synthesis of polyynes is an active and cutting edge topic in material science and chemistry. The ultimate goal of this branch of science is to establish a reliable route for the synthesis of the long sought after allotrope of carbon called carbyne, which is essentially a *sp* hybridized carbon chain of infinite length [127]. Interest in this material derives from the technological breakthroughs afforded by other recently discovered carbon allotropes, such as fullerenes, graphenes and carbon nanotubes. While the molecules identified in this work are much too short to be considered carbyne, their synthesis serves as an important first step in the direction of its formation. Polyynes themselves are also of considerable interest because some of their predicted properties, including their high strength and conductivity, make them ideal candidates for use as wires in molecular electronics [53, 141]. The work presented here could be extended in a number of ways. For example, it would be productive to study the irradiation of other chemical compounds to determine if longer chained polyynes can be synthesized through PLI. For example, it would be interesting to melt and irradiate long chain alkanes that are typically solids at room temperature. A more immediate experiment would involve the irradiation of toluene for longer periods of time to determine if the concentration of polyynes in solution can be increased and if these polyynes can also be extracted from the solution to form a high

concentration sample. Ultimately a macroscopic sample containing mostly polyynes would be very useful in determining if these molecules could, in fact, be useful in technological applications.

In a more complex experiment, solutions of ferrocene and benzene were irradiated by fs-laser pulses. Highly ordered mesoscale structures exhibiting four unique geometries; ribbons, loops, tubes, and hollow spherical shells were observed in the solid deposits remaining after evaporation of the irradiated solution. The spherical shell structures are of special interest because it appears that they result due to the condensation of plasma bullets as they travel through the ferrocene solution. This is the first example of this type of transient phenomenon being recorded in this way and may provide important new insight into the dynamics of plasmas as they travel through condensed media. After a purification process, the higher order structures were destroyed and replaced with micron sized clusters of light and dark material that appear to be a porous carbon-iron composite material. The purified material was found to consist of three distinct species including; pure iron, and two phases in which part of the ferrocene molecule is bound to either carbon or iron/carbon complexes. This material is extremely interesting because it exhibits properties similar to that of an electret and is also ferromagnetic over a large temperature range. The first and perhaps most obvious extension of this work would be to study, in greater detail, the electronic properties of these irradiation products to determine if in fact they are electrets. If this is found to be the case then a nanoelectret material could find application in a variety of industries, including the construction, electronics and energy sectors [185].

In the final liquid phase laser irradiation experiment, a new hybrid deposition technique was originated and used to coat stainless steel electrodes with disordered mesoporous nanocrystalline graphite. This method involves the laser induced breakdown of benzene and the subsequent electrodeposition of the resulting carbon ions. The material created in this experiment could be useful as a coating for orthopedic or dental implants and a study of its osteogenetic and tribiological properties could be very useful. This technique is in its infancy and a number of experimental parameters still need to be examined. For example, the effects of laser intensity and voltage on the final deposited material should be studied. Also this method could be expanded to other liquids to see determine if other types of coatings can be created. The value of the global electroplating market is projected to grow to nearly $14 billion by 2015 and pulsed laser initiated electrodeposition could very well find niche applications in this market, however; a considerable amount of work is still required to move this technique out of the research and development stage.

Another focus in this work involved the synthesis of a special class of polymer-like carbon nanomaterials using a new method that augments traditional pulsed laser deposition. This technique involves the plasma processing of frozen materials with a pulsed laser initiated graphitic plasma. We call this technique "pulsed laser induced plasma processing" or "PLIPP". Various thin film compositions were created by processing alkane and alkene ices. It was found that short exposure (5 min) to the plasma resulted in the formation of polymer-like amorphous carbon (a-C:H) deposits, with unique surface morphologies, that were partially composed of the parent molecules. These molecules were shown to bond to the a-C:H matrix in a relatively intact state as bridging groups between sp^2 clusters. Observation of this novel result suggests that it is possible to use the PLIPP technique to generate carbonaceous materials based on networks of sp^2 rings separated by specific distances as defined by the length of individual alkane or alkene chains. These networks would have tailored physical and chemical properties. For example, it was found that the average cluster size in these samples increased from 10 rings in hexane based films to 12 rings in decane based films. In addition, replacement of the initial alkane layers with alkene layers resulted in thin films with increased sp^2 content that were found to be very polymer-like. In fact, it is possible that some polymerization of the pre-placed molecules may have occurred in the plasma during preparation of these films. Amorphous carbon thin films have been suggested for use as molecular sieves, or chemical sensors, and tailored carbon networks generated by PLIPP could potentially be implemented in this type of application. There is still, however, quite a bit of uncertainty as to the physical and chemical mechanisms involved in the PLIPP process. This suggests that there is lots of opportunity for further productive research. For example, the reason for the large variability in the nanostructure of samples has yet to be determined accurately. Parameters such as the role played by the structure and thickness of the frozen base layers could be studied in this regard. The effect of ion energy on the composition of the deposited material could also be studied by altering the laser intensity, or provision of an accelerating voltage between the substrate and the target. The greatest range of new experiments could come from simply changing the chemicals used as the frozen base layer and examining the properties of the resulting thin films under standard PLIPP conditions.

Finally, in a slight departure from the previous experiments, the effects of carbon ion bombardment on water ice were examined in an effort to understand certain astrophysical processes. The resulting deposited material had the appearance of an extended web-like network of nanofibers. Unlike the previous sample, water molecules were not incorporated into the material due to the ready dissociation of water under ion bombardment. Instead the carbon plasma was found to react with

hydrogen atoms and molecules to form a nanocrystalline carbon material. Many complex carbonaceous materials have been identified in the interstellar carbon dust including; graphitic onions, a-C, a-C:H, polycyclic aromatic hydrocarbons and fullerenes [260, 261]. Recently, it has been suggested that another constituent of the ISM could be fulleranes, which are essentially fullerenes that have become hydrogenated [262]. It is quite possible that these types of molecules are being formed during the current experiments. Bombardment of water ice by highly energetic carbon ions may therefore be a possible route to the natural formation of complex carbon structures throughout the galaxy.

The results of several of these experiments, including those involving the irradiation of benzene and the plasma processing of frozen hexane, have recently been published in peer reviewed journals. Notably, the work on benzene which was published in the prestigious journal Carbon has garnered considerable attention, being cited six times to date. Several other articles are currently being prepared for submission based on the unpublished results of liquid phase and plasma processing experiments. These are listed below, along with a listing of the various presentations that have been given at national and international conferences, several of which were award winning.

In preparation

- Wesolowski, M.J., Kuzmin, S., Karimi, R., Wales, B., Sanderson J, Duley W.W., "*Plasma bullet remnants: Carbon jellyfish emerging from an ocean of ferrocene*".
- Wesolowski, M.J., Kuzmin, S., Duley W.W., "*Pulsed laser induced electrophoresis and the deposition of conductive mesoporous nanocrystalline graphite*".
- Wesolowski, M.J., Sanderson J, Duley W.W., "*Formation of web-like carbon nanofiber networks through carbon ion bombardment of water ice*".
- Kuzmin, S., Wesolowski, M.J., Duley, W.W., "*The enhanced filamentation in media with resonance absorption of the third harmonic: Study of the ionic photocurrent in liquid benzene irradiated by femto-second laser pulses*".

Published

- Wesolowski, M.J., Moores, B., Leonenko, Z., Karimi, R., Sanderson J, Duley W.W., "*Synthesis of polymer-like hydrogenated amorphous carbon by fs-pulsed laser induced plasma processing of solid hexane*" Plasma Processes and Polymers, *In Press 2012 DOI: 10.1002/ppap.201100206*
- Wesolowski, M.J., Kuzmin, S., Moores, B., Wales, B., Karimi, R., Zaidi, A.A., Leonenko, Z., Sanderson, J.H., Duley, W.W., "*Polyyne synthesis and amorphous carbon nano-particle formation by femtosecond irradiation of benzene*" Carbon, 2011, Volume 49, Issue 2, pp. 625-630.
- Zaidi, A.A., Hu, A., Wesolowski, M.J., Fu, X., Sanderson, J.H., Zhou, Y., Duley, W.W., "*Time of flight mass spectrometry of polyyne formation in the irradiation of liquid alkanes with femtosecond laser pulses*" Carbon, 2010, Volume 48, Issue 9, pp.2517-2520.

Presentations

- International Scanning Probe Microscopy Conference – Toronto, ON. 2012, Poster Presentation "*Nanostructures in Polymer-Like Amorphous Carbon Thin Films Created by Pulsed Laser Induced Plasma Processing of Frozen Alkanes*."
- Canadian Association of Physicists Congress – St. John's, NL. 2011, Award winning oral presentation (3rd place Division of Condensed Matter and Materials Physics) entitled "*Synthesis of polymer-like a-C:H thin films by laser induced plasma processing of cryogenic hydrocarbon layers.*"
- Waterloo Graduate Research Conference – Waterloo, ON. 2011, Award winning oral presentation "*Characterization of a-C:H thin films created by fs-PLD of graphite onto cryogenic hydrocarbon layers.*"
- International Conference on Diamond and Carbon Materials – Budapest, Hungary 2010, Poster presentation "*Characterization of new a-C:H nanostructures created by fs-PLA of graphite onto cryogenic alkane layers.*"

- Waterloo-Osaka Nanotechnology Workshop – Waterloo, ON. 2009, Invited speaker "*Laser induced dispersion of single walled carbon nanotubes.*"
- Canadian Association of Physicists Congress – Moncton, NB. 2009, Oral presentation entitled "*Pulsed Laser Deposition of Amorphous Diamond-like Carbon Thin Films.*"
- Waterloo Graduate Research Conference – Waterloo, ON. 2009, Oral Presentation "*Creation and Characterization of New Materials using Laser Light*."

In summary, the synthesis techniques and materials developed over the course of this work are on the cutting edge of a new branch of material science that combines aspects of optics, physics, chemistry and material science. Laser light that is over a quadrillion times more intense than that of the sunlight striking the Earth was used to dismantle materials at the molecular level. Emerging from this violent and unique process is an extremely energetic plasma comprised of the most basic components of the target; charged atoms, ions and molecules. This chemical "soup" was then used to synthesize an array of fascinating new materials that differed significantly from their progenitors. In the future, these materials may find uses in a variety of industries and could potentially foster revolutionary advances in molecular electronics, medicine and chemistry. Yet for all that has been accomplished in this pioneering work, we have all but scratched the surface of a science that is in its infancy. Many new discoveries surely lie just over the horizon and the potential of the new materials created by pulsed laser material synthesis techniques is seemingly limitless. It has been both exciting and humbling to be an explorer at the forefront of this field, standing at the precipice of discovery.

"*To know that we know what we know,*

and to know that we do not know what we do not know,

that is true knowledge."

Mikołaj Kopernik

1473 – 1543

Appendix A

Liquid Phase Pulsed Laser Ablation of Metals and Metalloids

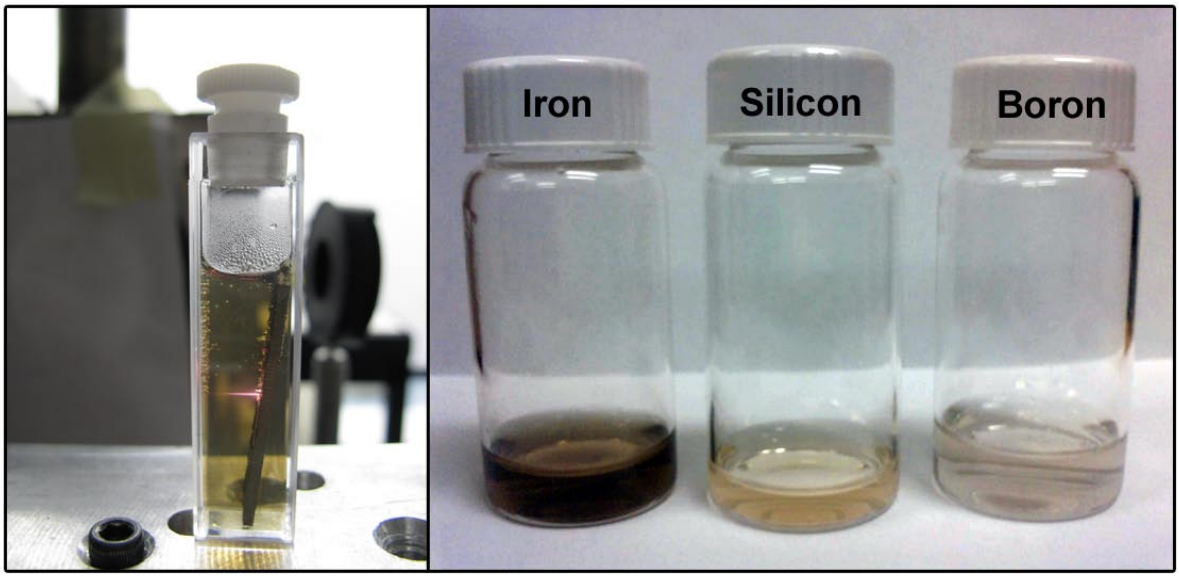

Figure A1 - The liquid phase pulse laser ablation of iron, silicon and boron and the resulting particle suspensions.

While the majority of my doctoral work has involved the liquid phase irradiation of pure solvents, a number of liquid phase ablation experiments were also carried out. The analysis of these experiments is still in the preliminary stage. Solid targets of pure iron, silicon and boron were immersed in ultrapure water and ablated in the pass through orientation using the laser system described in Chapter 3. An example of this process is shown in the left hand side of Figure A1, where the laser beam is focused onto the surface of a bar of iron. Material is ejected from the surface due to the laser solid interaction and then forms nanoparticles in suspension, as shown in the right hand side of Figure A1. These suspensions each have a distinct color which depends on the initial target. The nanostructure of these materials was examined using SEM while their composition was determined using Raman spectroscopy. Figure A2 shows the nanoparticles that are created during the ablation of iron. The majority of particles appear to be spherical, however; a number of other structures are also present.

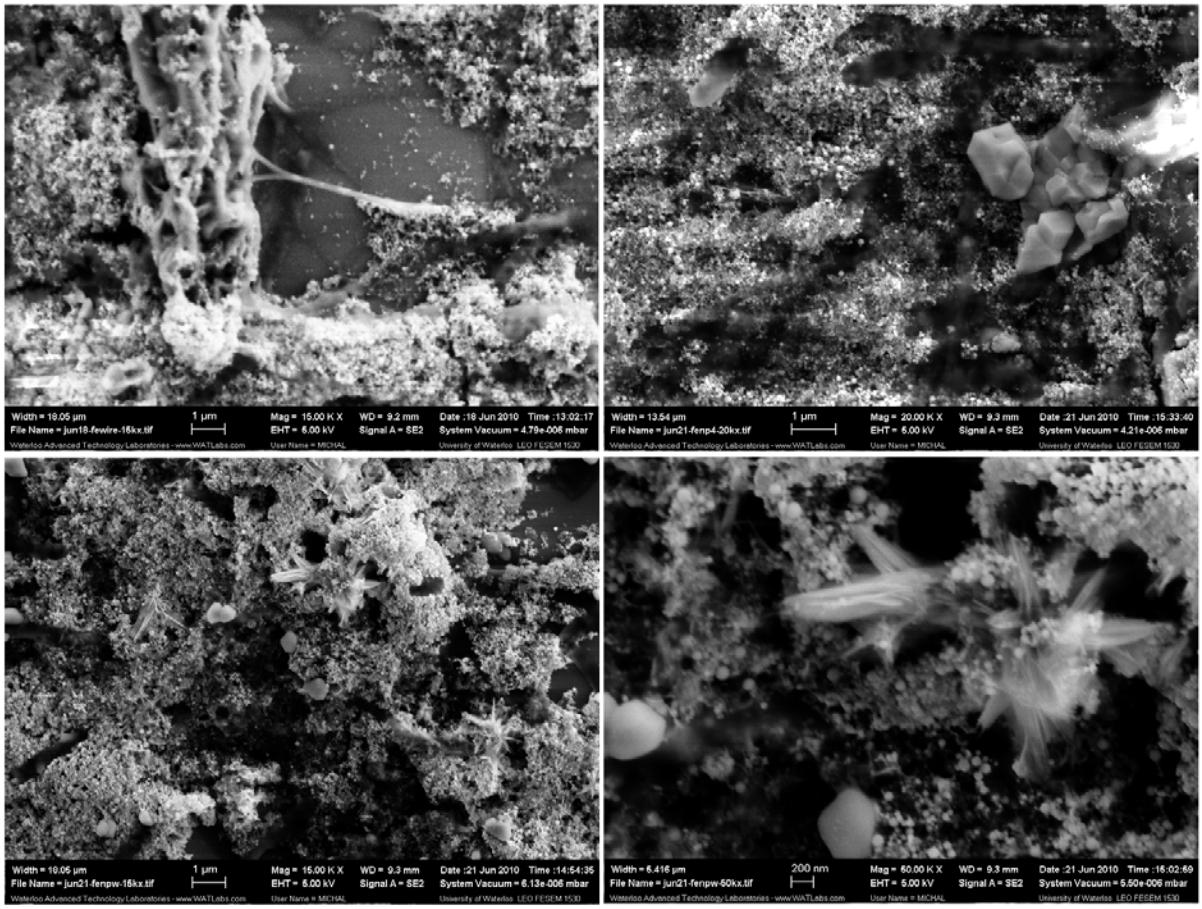

Figure A2 – Scanning electron micrographs of the various nanoparticles that form as a result of liquid phase pulsed laser ablation of iron in water.

These include nanowires, faceted microparticles and nanocrystalline spear-like objects. These structures are all likely to be comprised of either pure iron or iron oxide, as is shown by the Raman spectrum of Figure A3 (left). As was discussed in Section 4.3.3, the lower frequency vibrational modes between 150-300 cm^{-1}, may be associated with Fe-Fe, Fe-O, or Fe-C bonds. In the present case since no carbon is present during ablation so these modes must belong to either pure iron or iron oxide.

Figure A4 presents the structures that result after the boron suspension is drop deposited and dried onto a silicon wafer. These micron sized structures have the appearance of droplets and at higher magnification they appear to be continuous solids that are somewhat porous. The Raman

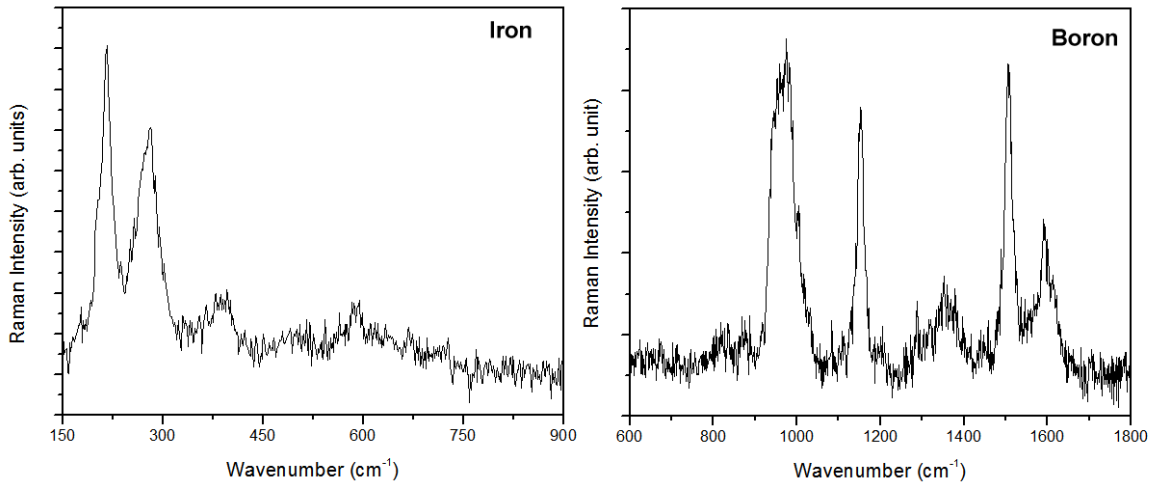

Figure A3 – The Raman spectra of material formed after LP-PLA of either iron (left) or boron (right) in ultrapure water.

spectrum of these structures is shown in Figure A3 (right). There are five strong features in this spectrum centered at 962, 1152, 1353, 1506 and 1594 cm^{-1}. Given the initial conditions of this experiment it is likely that these peaks result due to vibrational modes associated with boron oxides.

The nanoparticles created by the liquid phase ablation of silicon have yet to be examined, however; interesting surface patterning was noticed during an examination of the irradiated target under SEM. In areas where the surface of the target was exposed to the laser beam three dimensional ridged nanostructures have formed, as shown in Figure A5. The shape and size of these ridges appears to be entirely dependent on the number of pulses that the target is exposed to. In areas of light exposure the surface is relatively flat with 100 nm wide ridges spaced evenly across the surface. In areas of heavy ablation, larger micron sized structures form, and are separated by deep pits and grooves. On the edge of the ablation zone, Figure A6 shows that ring-like structures have formed and the target surface in this region appears to have melted and re-solidified.

A great deal of work is left in this project, however; it would be of interest to continue for a variety of reasons. One of the main benefits of LP-PLA is that it is a simple and relatively clean technique that allows for the creation of nanomaterials with very few byproducts. This makes it desirable in certain industrial settings. The surface patterning of substrates is an added benefit that in the case of silicon could have direct application in increasing the efficiency of photovoltaic cells.

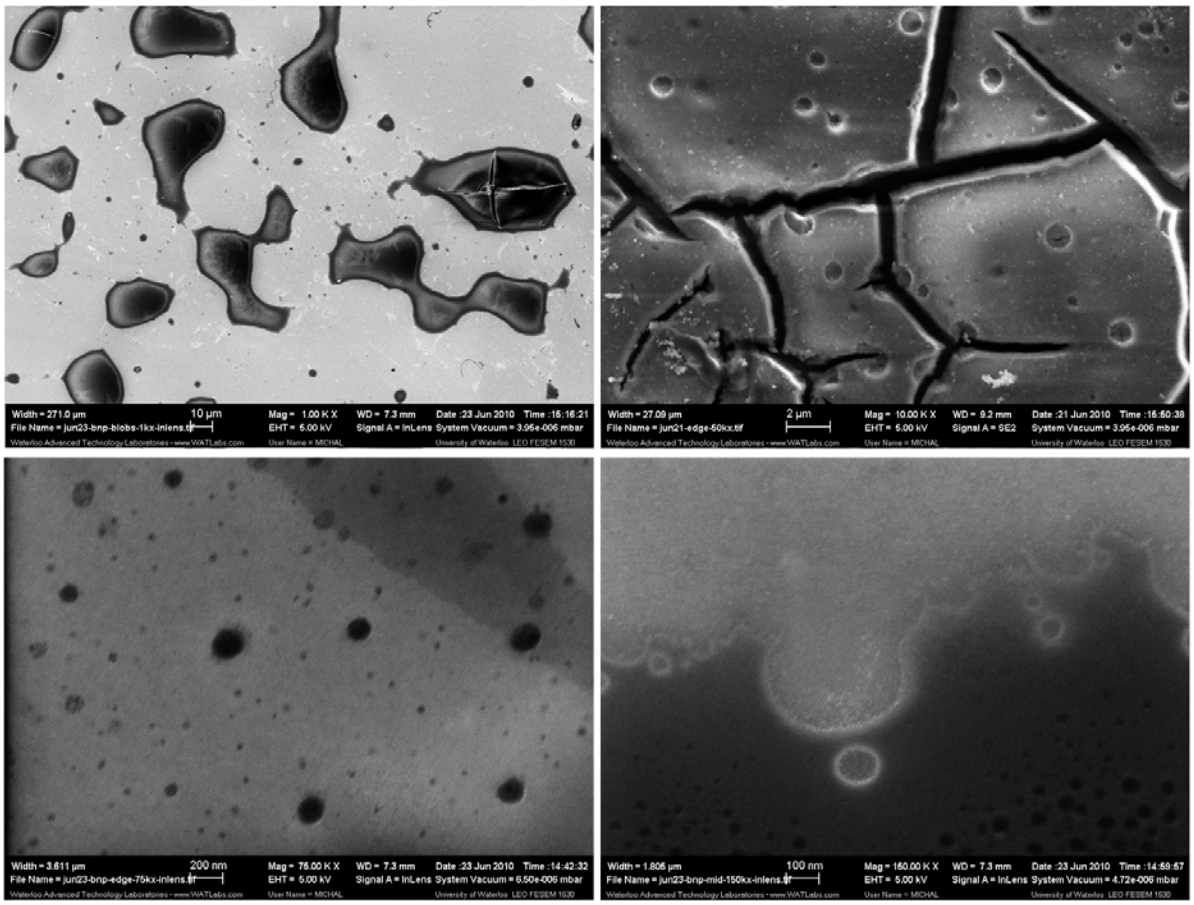

Figure A4 – Scanning electron micrographs of the structures that form as a result of liquid phase pulsed laser ablation of crystalline boron in water.

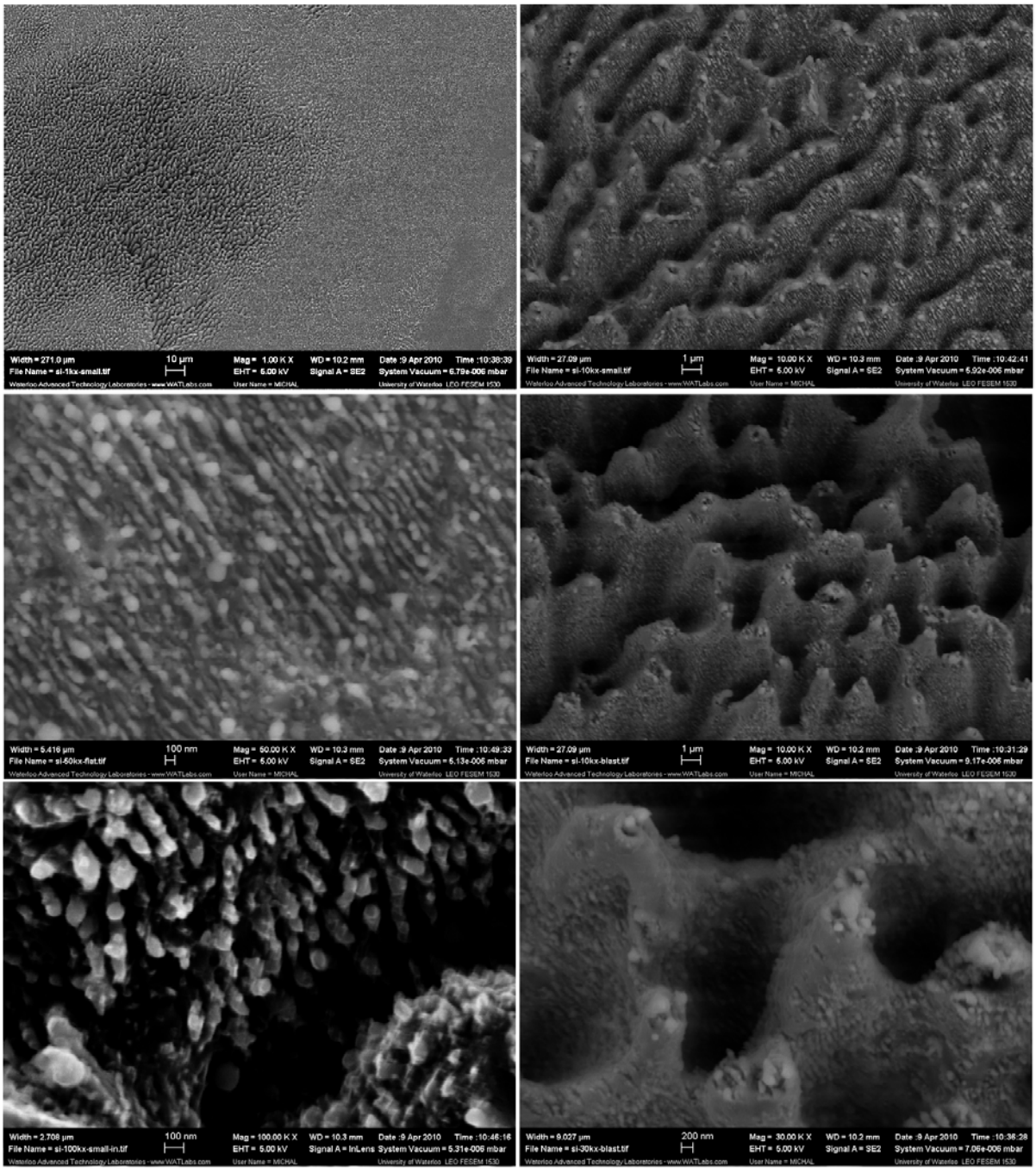

Figure A5 – Scanning electron micrographs of the surface patterning on the silicon target after it has been processed with fs laser pulses.

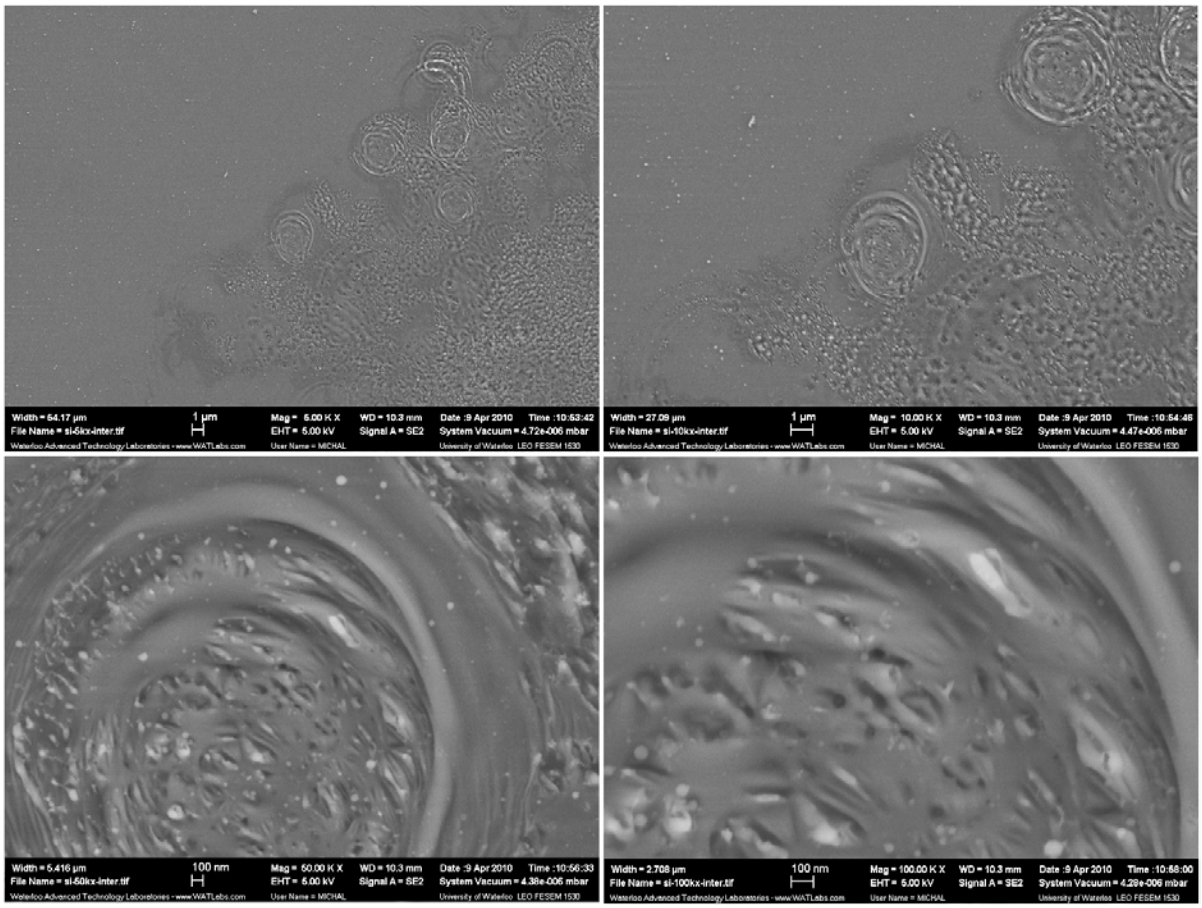

Figure A6 – Scanning electron micrographs of the melt regions left on the silicon target after it has been processed with fs laser pulses.

Appendix B
Secondary Pulsed Laser Induced Plasma Processing Experiments

In addition to the materials discussed in Chapter 5, a number of other frozen chemicals were also processed using the PLIPP including; pentane (C_5H_{12}), isopentane (C_5H_{12}), decane ($C_{10}H_{22}$) and docasane ($C_{22}H_{46}$). As with the experiments outlined in Appendix A, these experiments are not in a completed state, with only the most preliminary analysis presented here.

As with the even chained alkanes, pentane was found to be incorporated into the a-C:H matrix after short PLIPP. Films of isopentane were created to examine the effects, if any, of isomerism on the PLIPP process. No significant differences were observed in the Raman spectra of these two types of films. The surface of a film created by PLIPP of pentane was examined using SEM, and the most interesting structures are presented in Figure B1. The surface is littered with large micro sized objects, including; faceted particles, columns and ribbons. Small arrays of loosely connected nanoparticles are also present on the surface. The faceted nanoparticles likely result from large portions of graphite that were ripped from the surface of the HOPG target during ablation. The columnar structures are typically 3 μm tall, although they seem to have detached from their base structures and lie prone on the substrate. The appearance of these types of structures in polymer-like amorphous carbon is quite unique and suggests significant epitaxial growth can occur during PLIPP. The appearance of curled ribbons on the surface of the substrate is also somewhat surprising and the origin of these structures is not well understood.

In an effort to examine the effects of PLIPP on a long chain alkane, docosane was first heated past its melting point (317K) and then spin coated onto a substrate before being secured in the vacuum chamber and processes in the same as that of the other samples. Docosane is a long chain, waxy alkane that is solid at room temperature and should normally have a smooth surface after spin coating. After PLIPP the surface is pitted and disordered indicating that the plasma has degraded the material as shown in Figure B2. No obvious nanostructures are present; even in higher resolution scans (see inset) the sample appears to be comprised of faceted micron sized objects. This could be due to the fact that the initial alkane layer in this sample was much thicker, on the order of 100 μm, than those of previous samples. The composition of this sample was examined in the usual way using Raman spectroscopy.

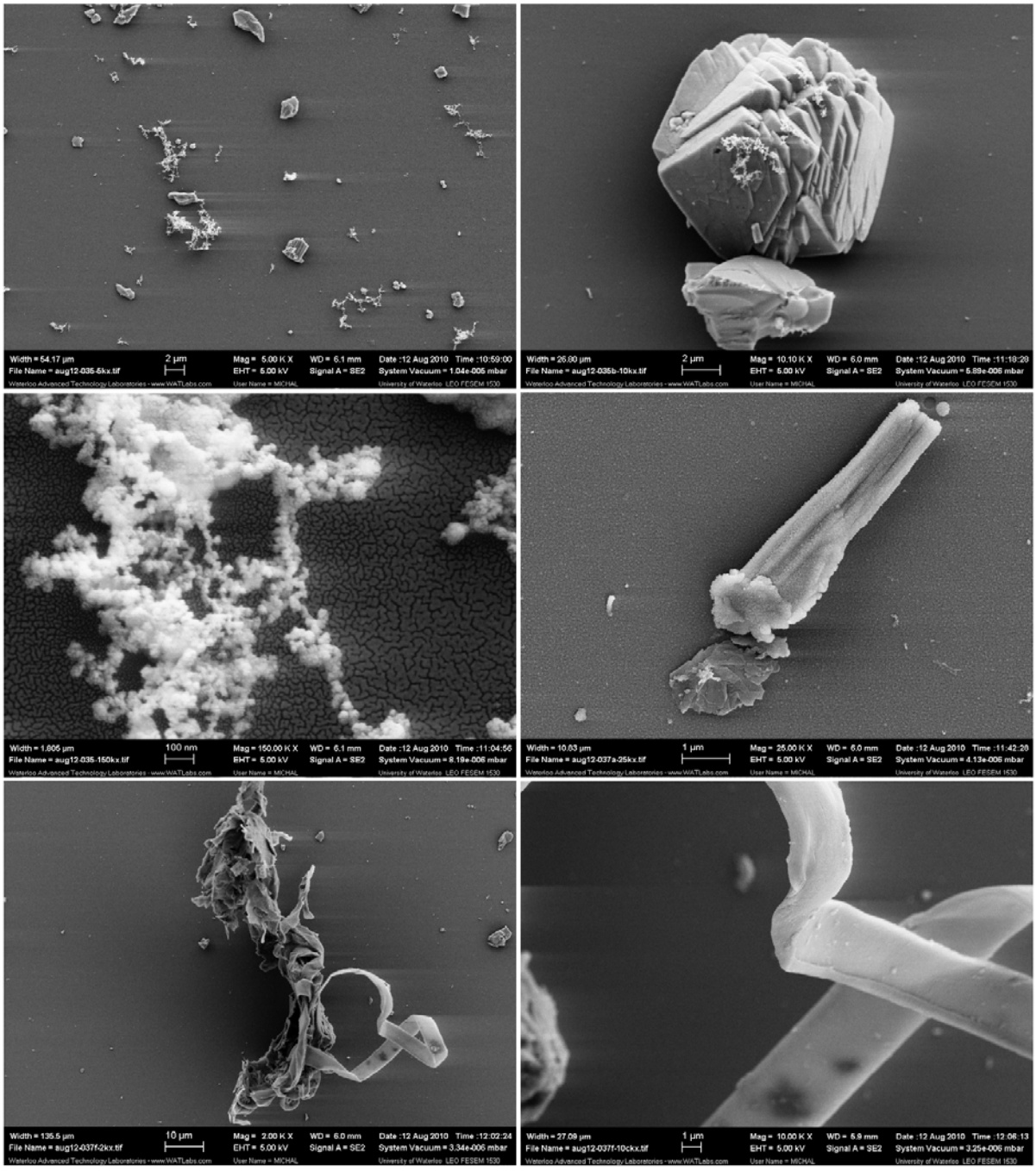

Figure B1 – Scanning electron micrographs of the various nanostructures present in thin films created by the PLIPP of pentane.

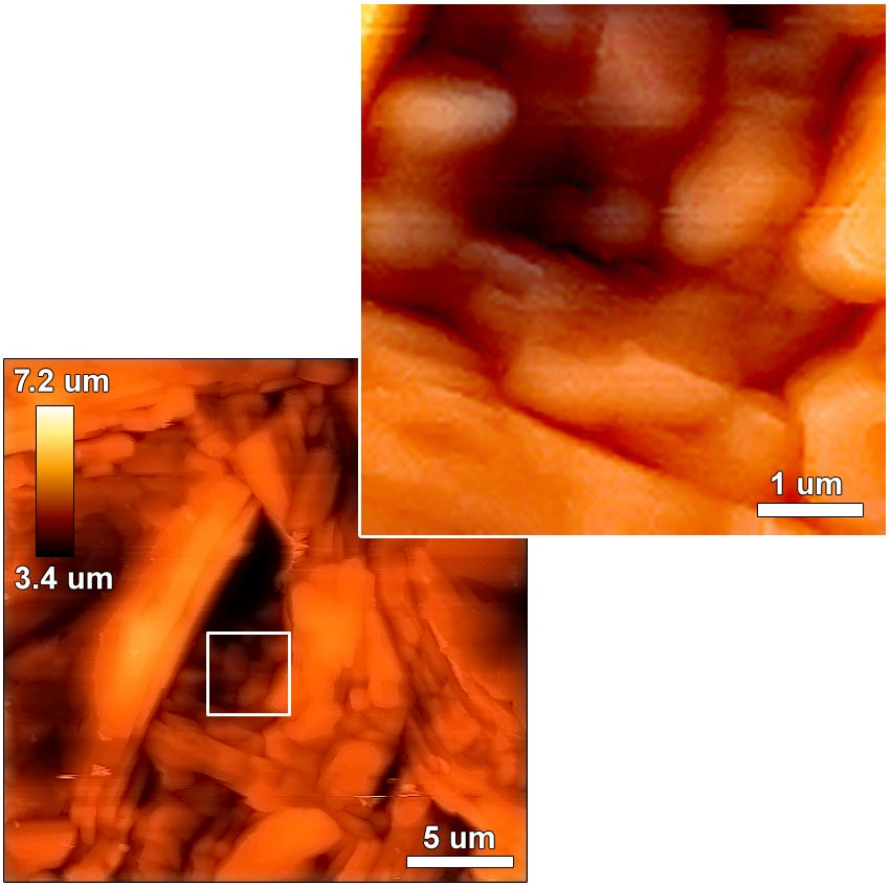

Figure B2 – The topography of samples created by PLIPP of docosane, determined by atomic force microscopy.

The Raman spectra of unaltered docosane (bottom curve) and of this sample (top curve) are presented in Figure B3. Most of the docosane peaks are still present in the processed sample, however; the D and G modes of amorphous carbon are prominent. It is difficult to ascertain if amorphous carbon is simply sitting on the surface of the solid docosane base film or they are becoming interconnected.

In the final PLIPP experiment, the effects of warming time and atmospheric exposure were examined using films created by the PLIPP of decane. Figure B4 shows the topography of thin films that were a) allowed to warm to room temperature *in vacuo* naturally overnight, b) warmed artificially *in vacuo* over a 2 hr period and c) exposed to atmosphere just after the deposition process ended. It is evident that there are changes in the nanostructure due to these factors with the size of nanoparticles

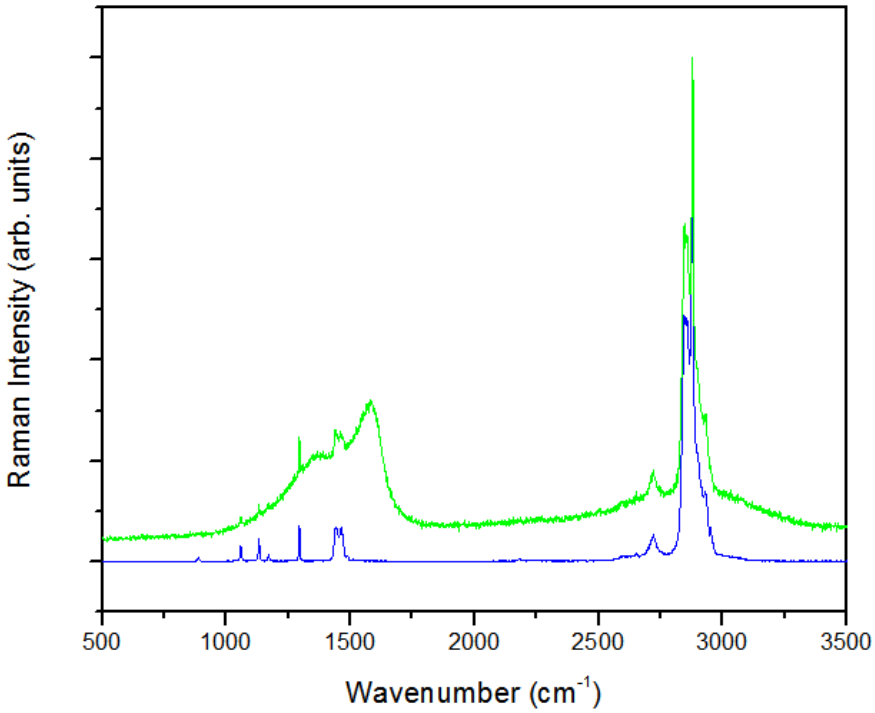

Figure B3 – The Raman spectra of docosane (bottom) and a film created after PLIPP of docosane (top).

decreasing between samples a) and b) and the shape of the particles changing drastically in the case of films immediately exposed to atmosphere. The Raman spectra, which for film a) is the same as presented in Figure 5.15, changes very little between samples and is therefore not presented. The feature of note is an enhanced SERS mode in film c) near 1315 cm^{-1} indicating the presence of nanodiamond in the film, which given the more faceted appearance of the film topography is not surprising.

These results suggest that thermal excitation/relaxation and atmospheric quenching can have a significant effect on the nanostructure of PLIPP films, however; little these processes have little effect on the overall film composition.

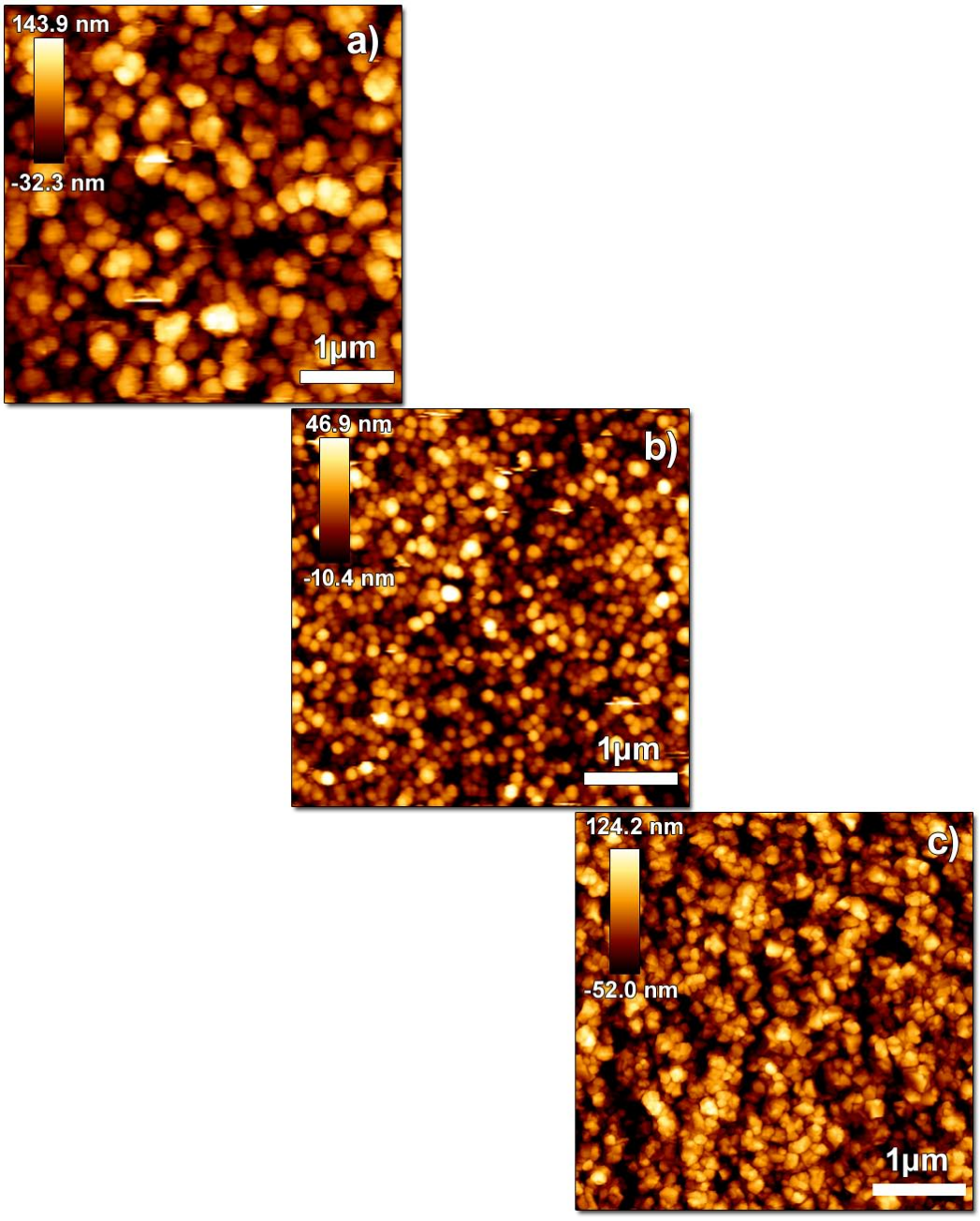

Figure B4 – A series of AFM scans showing the nanostructure of films created by the PLIPP of decane that were allowed to a) warm in vacuum naturally over a 12 hr period, b) warmed quickly in vacuum over a 2 hr period, and c) exposed to atmosphere subsequent to the cessation of deposition.

Bibliography

1. Partoens, B. and F. Peeters, *From graphene to graphite: Electronic structure around the K point.* Physical Review B, 2006. **74**(7).
2. Walter, P., et al., *Making make-up in Ancient Egypt.* Nature, 1999. **397**: p. 483-484.
3. José-Yacamán, M., et al., *Maya Blue Paint: An Ancient Nanostructured Material.* Science, 1996. **273**(5272): p. 223-225.
4. Reibold, M., et al., *Materials: carbon nanotubes in an ancient Damascus sabre.* Nature, 2006. **444**(7117): p. 286.
5. Walter, P., et al., *Early Use of PbS Nanotechnology for an Ancient Hair Dyeing Formula.* Nano Letters, 2006. **6**(10): p. 2215-2219.
6. Freestone, I., et al., *The Lycurgus Cup - A Roman Nanotechnology*. Gold Bulletin, 2007. **40**(4): p. 270-277.
7. Pérez-Villar, S., J. Rubio, and J.L. Oteo, *Study of color and structural changes in silver painted medieval glasses.* Journal of Non-Crystalline Solids, 2008. **354**(17): p. 1833-1844.
8. Faraday, M., *The Bakerian Lecture: Experimental Relations of Gold (and Other Metals) to Light.* Philosophical Transactions of the Royal Society of London, 1857. **147**(145-181).
9. Mogerman, W.D., *Faraday's Lecture on Gold; The Optical Effects of Fine Particles.* Gold Bulletin, 1974. **7**(1): p. 22-24.
10. Von Laue, M., *Concerning the detection of X-ray interferences.* Nobel Lectures, Physics, 1915. **1901-1922**: p. 347-355.
11. Ruska, E., *The Development of the Electron Microscope and of Electron Microscopy.* Bioscience Reports, 1987. **7**(8): p. 607-629.
12. Zworykin, V.K. and E.G. Ramberg, *Surface Studies with the Electron Microscope.* Journal of Applied Physics, 1941. **12**: p. 692-695.
13. Tennant, S., *On the Nature of the Diamond.* Philosophical Transactions of the Royal Society of London, 1797. **87**: p. 123-127.
14. Bragg, W.H. and W.L. Bragg, *The Strucutre of Diamond.* Proceedings of the Royal Society of London. Series A. Containing Papers of a Mathematical and Physical Character, 1913. **89**(610): p. 277-291.
15. Bernal, J.D., *The Structure of Graphite.* Proceedings of the Royal Society of London. Series A. Containing Papers of a Mathematical and Physical Character, 1924. **106**(740): p. 749-773.

16. Cowlard, F.C. and J.C. Lewis, *Vitreous Carbon - A New Form of Carbon.* Journal of Materials Science, 1967. **2**: p. 507-512.
17. Bundy, F.P. and J.S. Kasper, *Hexagonal Diamond - A New Form of Carbon.* Journal of Chemical Physics, 1967. **46**(9): p. 3437-3446.
18. Frondel, C. and U.B. Marvin, *Lonsdaleite, a Hexagonal Polymorph of Diamond.* Nature, 1967. **214**: p. 588-589.
19. Aisenberg, S. and R. Chabot, *Ion-Beam Deposition of Thin Films of Diamondlike Carbon.* Journal of Applied Physics, 1971. **42**(7): p. 2953-2958.
20. Kroto, H.W., et al., *C60: Buckminsterfullerene.* Nature, 1985. **318**: p. 162-163.
21. Li, Y.Y. and C.C. Hsieh, *Synthesis of carbon nanotubes by combustion of a paraffin wax candle.* Micro & Nano Letters, 2007. **2**(3): p. 63.
22. Garvie, L.A.J. and P.R. Buseck, *Nanosized carbon-rich grains in carbonaceous chondrite meteorites.* Earth and Planetary Science Letters, 2004. **224**(3-4): p. 431-439.
23. Iijima, S., *Helical microtubules of graphitic carbon.* Nature, 1991. **354**: p. 56-58.
24. Monthioux, M. and V.L. Kuznetsov, *Who should be given the credit for the discovery of carbon nanotubes?* Carbon, 2006. **44**(9): p. 1621-1623.
25. Rode, A.V., et al., *Structural Analysis of a Carbon Foam Formed by High Pulse-Rate Laser Ablation.* Applied Physics A 1999. **69 S**: p. S755-S758.
26. Baughman, R.H., *Dangerously Seeking Linear Carbon.* Science, 2006. **312**: p. 1009-1010.
27. Lagow, R.J., et al., *Synthesis of Linear Acetylenic Carbon: The "sp" Carbon Allotrope.* Science, 1995. **267**(5196): p. 362-367.
28. Novoselov, K.S., et al., *Electric Field Effect in Atomically Thin Carbon Films.* Science, 2004. **306**: p. 666-669.
29. Pauling, L., *The Nature of the Chemical Bond. Application of Results Obtained from the Quantum Mechanics and from a Theory of Paramagnetic Susceptibility to the Structure of Molecules.* Journal of the American Chemical Society, 1931. **53**: p. 1367-1400.
30. Bundy, F.P., et al., *The Pressure-Temperature Phase and Transformation Diagram for Carbon; Updated through 1994.* Carbon, 1996. **34**(2): p. 141-153.
31. Yang, C.C. and S. Li, *Size-Dependent Temperature-Pressure Phase Diagram of Carbon.* Journal of Chemical Physics, 2008. **112**: p. 1423-1426.
32. McKenzie, D.R., et al., *Synthesis, structure, and applications of amorphous diamond.* Thin Solid Films, 1991. **206**: p. 198-203.

33. Jacob, W. and W. Möller, *On the structure of thin hydrocarbon films.* Applied Physics Letters, 1993. **63**(13): p. 1771-1773.
34. Robertson, J., *Diamond-like amorphous carbon.* Materials Science and Engineering R, 2002. **37**: p. 129-281.
35. Chhowalla, M., et al., *Influence of ion energy and substrate temperature on the optical and electronic properties of tetrahedral amorphous carbon (ta-C) films.* Journal of Applied Physics, 1997. **81**(1): p. 139-145.
36. Friedmann, T.A., et al., *Thick stress-free amorphous-tetrahedral carbon films with hardness near that of diamond.* Applied Physics Letters, 1997. **71**(26): p. 3820-3822.
37. Pharr, G.M., et al., *Hardness, elastic modulus, and structure of very hard carbon films produced by cathodic-arc deposition with substrate pulse biasing.* Applied Physics Letters, 1996. **68**(6): p. 779-781.
38. Teo, K.B.K., et al., *Highest optical gap tetrahedral amorphous carbon.* Diamond and Related Materials, 2002. **11**: p. 1086-1090.
39. Ferrari, A.C. and J. Robertson, *Interpretation of Raman spectra of disordered and amorphous carbon.* Physical Review B, 2000. **61**(20): p. 14095-14107.
40. Savvides, N. and B. Window, *Diamondlike amorphous carbon films prepared by magnetron sputtering of graphite.* Journal of Vacuum Science and Technology A, 1985. **3**(6): p. 2386-2390.
41. Kulikovsky, V., et al., *Study of the structure of hard graphite-like amorphous carbon films by electron diffraction.* Diamond and Related Materials, 2002. **11**: p. 1467-1471.
42. Weiler, M., et al., *Preparation and properties of highly tetrahedral hydrogenated amorphous carbon.* Physical Review B, 1996. **53**(3): p. 1594-1608.
43. Ferrari, A., S. Rodil, and J. Robertson, *Interpretation of infrared and Raman spectra of amorphous carbon nitrides.* Physical Review B, 2003. **67**(15).
44. Cuomo, J.J., et al., *Vapor deposition processes for amorphous carbon films with sp3 fractions approaching diamond.* Journal of Applied Physics, 1991. **70**(3): p. 1706.
45. McKenzie, D.R., et al., *Properties of tetrahedral amorphous carbon prepared by vacuum arc deposition.* Diamond and Related Materials, 1991. **1**: p. 51-59.
46. Fourches, N. and G. Turban, *Plasma deposition of hydrogenated amorphous carbon: growth rates, properties and structures.* Thin Solid Films, 1994. **240**: p. 28-38.

47. Voevodin, A.A. and M.S. Donley, *Preparation of amorphous diamond-like carbon by pulsed laser deposition: a critical review.* Surface Coatings and Technology, 1996. **82**: p. 199-213.
48. Willmott, P.R. and J.R. Huber, *Pulsed laser vaporization and deposition.* Reviews of Modern Physics, 2000. **72**(1): p. 315.
49. Huang, X., et al., *Cancer Cell Imaging and Photothermal Therapy in the Near Infrared Region by Using Gold Nanorods.* Journal of the American Chemical Society, 2006. **128**(2115-2120).
50. Edwards, B.C., *Design and Deployment of a Space Elevator.* Acta Astronautica, 2000. **47**(10): p. 735-744.
51. Chelkowski, S., P.B. Corkum, and A.D. Bandrauk, *Femtosecond Coulomb Explosion Imaging of Vibrational Wave Funtions.* Physical Review Letters, 1999. **82**(17): p. 3416-3419.
52. Itzhaki, L., et al., *Harder than Diamond: Determining the Cross-Sectional Area and Young's Modulus of Molecular Rods.* Angewandte Chemie, 2005. **117**(45): p. 7598-7601.
53. Akagi, K., M. Nishiguchi, and H. Shirakawa, *One-Dimensional Conjugate Carbyne - Synthesis and Properties.* Synthetic Metals, 1987. **17**: p. 557-562.
54. Gamaly, E.G. and V.T. Tikhonchuk, *Effect of intense ultrashort light pulses on a substrate.* Journal of Experimental and Theoretical Physics Letters, 1989. **48**(8): p. 453-455.
55. Rozmus, W. and V. Tikhonchuk, *Heating of solid targets by subpicosecond laser pulses.* Physical Review A, 1992. **46**(12): p. 7810-7814.
56. Gibbon, P. and E. Förster, *Short-pulse laser - plasma interactions.* Plasma Physics and Controlled Fusion, 1996. **38**: p. 769-793.
57. Gamaly, E.G., A.V. Rode, and B. Luther-Davies, *Ultrafast ablation with high-pulse-rate lasers. Part I: Theoretical considerations.* Journal of Applied Physics, 1999. **85**(8): p. 4213-4221.
58. Gamaly, E.G., et al., *Ablation of solids by femtosecond lasers: Ablation mechanism and ablation thresholds for metals and dielectrics.* Physics of Plasmas, 2002. **9**(3): p. 949.
59. Brevik, I., et al., *Analytical and numerical demonstration of how the Drude dispersive model satisfies Nernst's theorem for the Casimir entropy.* Journal of Physics A: Mathematical and Theoretical, 2008. **41**(16): p. 164017.
60. Stuart, B.C., et al., *Nanosecond-to-femtosecond laser-induced breakdown in dielectrics.* Physical Review B, 1996. **53**(4): p. 1749-1761.

61. Perry, M.D., et al., *Ultrashort-pulse laser machining of dielectric materials.* Journal of Applied Physics, 1999. **85**(9): p. 6803.
62. Chichkov, B.N., et al., *Femtosecond, picosecond and nanosecond laser ablation of solids.* Applied Physics A, 1996. **63**: p. 109-115.
63. Banks, P.S., et al., *Short-pulse laser deposition of diamond-like carbon thin film.* Applied Physics A, 1999. **69 S**: p. S347-S353.
64. Qian, F., et al., *High intensity femtosecond laser deposition of diamond-like carbon thin film.* Journal of Applied Physics, 1999. **86**(4): p. 2281-2290.
65. Rode, A.V., B. Luther-Davies, and E.G. Gamaly, *Ultrafast ablation with high-pulse-rate lasers. Part II: Experiments on laser deposition of amorphous carbon film.* Journal of Applied Physics, 1999. **85**(8): p. 4222-4230.
66. Amoruso, S., et al., *Infrared femtosecond laser ablation of graphite in high vacuum probed by optical emission spectroscopy.* Applied Physics A, 2004. **81**(5): p. 981-986.
67. Anisimov, S.I., B.S. Luk'yanchuk, and A. Luches, *An analytical model for three dimensional laser plume expansion into vacuum in hydrodynamic regime.* Applied Surface Science, 1996. **96-98**: p. 24-32.
68. Loir, A.S., et al., *Study of plasma expansion induced by femtosecond pulsed laser ablation and deposition of diamond-like carbon films.* Applied Surface Science, 2003. **208-209**: p. 553-560.
69. Köster, H. and M. K., *Influence of beam parameters on the laser induced particle emission from surfaces.* Applied Surface Science, 1997. **109/110**: p. 428-432.
70. Lifshitz, Y., S. Kasi, and J. Rabalais, *Subplantation model for film growth from hyperthermal species: Application to diamond.* Physical Review Letters, 1989. **62**(11): p. 1290-1293.
71. Lifshitz, Y., et al., *Subplantation model for film growth from hyperthermal species.* Physical Review B, 1990. **41**(15): p. 10468-10480.
72. Lifshitz, Y., G. Lempert, and E. Grossman, *Substantiation of subplantation model for diamondlike film growth by atomic force microscopy.* Physical Review Letters, 1994. **72**(17): p. 2753-2756.
73. Jacob, W., *Surface reactions during growth and erosion of hydrocarbon film.* Thin Solid Films, 1998. **326**: p. 1-42.
74. Wang, X.-M., et al., *Ion-implanted Mechanism of the Deposition Process for Diamond-Like Carbon Films.* Chinese Physics Letters, 2011. **28**(1): p. 016102.

75. Schultrich, B., *Modeling of ta-C growth: Influence of the technological parameters.* Diamond and Related Materials, 2011. **20**(5-6): p. 785-792.
76. Xu, S., et al., *Properties of carbon ion deposited tetrahedral amorphous carbon films as a function of ion energy.* Journal of Applied Physics, 1996. **79**(9): p. 7234.
77. Grossman, E., et al., *Role of ion energy in determination of the sp3 fraction of ion beam deposited carbon films.* Applied Physics Letters, 1996. **68**(9): p. 1214.
78. Couairon, A. and A. Mysyrowicz, *Femtosecond filamentation in transparent media.* Physics Reports, 2007. **441**(2-4): p. 47-189.
79. Marburger, J.H., *Self-Focusing Theory.* Progress in Quantum Electronics, 1975. **4**: p. 35-110.
80. Feit, M.D., *Effect of refraction on spot-size dependence of laser-induced breakdown.* Applied Physics Letters, 1974. **24**(4): p. 169.
81. Raizer, Y.P., *Heating of a gas by a powerful light pulse.* Soviet Physics Journal of Experimental and Theoretical Physics, 1965. **21**(5): p. 1009.
82. Vogel, A., et al., *Mechanisms of femtosecond laser nanosurgery of cells and tissues.* Applied Physics B, 2005. **81**(8): p. 1015-1047.
83. Kennedy, P.K., *A First-Order Model for Computation of Laser-Induced Breakdown Thresholds in Ocular and Aqueous Media: Part I-Theory.* IEEE Journal of Quantum Electronics, 1995. **31**(12): p. 2241-2249.
84. Noack, J., et al., *Influence of pulse duration on mechanical effects after laser-induced breakdown in water.* Journal of Applied Physics, 1998. **83**(12): p. 7488.
85. Schaffer, C.B., et al., *Dynamics of femtosecond laser-induced breakdown in water from femtoseconds to microseconds.* Optics Express, 2002. **10**(3): p. 196-203.
86. Kiselev, S.B., *Kinetic boundry of metastable states in superheated and stretched liquids.* Physica A, 1999. **269**: p. 252-268.
87. Paltauf, G. and E. Dyer, *Photomechanical Processes and Effects in Ablation.* Chemical Reviews, 2003. **103**: p. 487-518.
88. Walker, S.J., *Development and Characterization of a Regeneratively Amplified Ultrafast Laser System with an All Glass Stretcher and Compressor*, in *Physics and Astronomy*2006, University of Waterloo: Waterloo, Ontario, Canada.
89. Binnig, G. and C.F. Quate, *Atomic Force Microscope.* Physical Review Letters, 1986. **56**(9): p. 930-933.

90. OverlordQ, *Atomic Force Microscope Block Diagram*, 2009, Wiki Commons: http://commons.wikimedia.org/wiki/File:Atomic_force_microscope_block_diagram.svg.
91. Knoll, M., *Aufladepotentiel und Sekundäremission elektronenbestrahlter Körper.* Zeitschrift für technische Physik, 1935. **16**: p. 467-475.
92. MarcoTolo, *Schematic of an SEM*, 2010, Wiki Commons: http://en.wikipedia.org/wiki/File:Schema_MEB_%28en%29.svg.
93. Bolotov, A., A. Kozyrev, and Y. Korolev, *A Physical Model of the Low-Current-Density Vacuum Arc.* IEEE Transactions on Plasma Science, 1995. **23**(6): p. 884-892.
94. Fuwa, K. and B.L. Vallee, *The Physical Basis of Analytical Atomic Absorption Spectroscopy; The Pertinence of the Beer-Lamber Law.* Analytical Chemistry, 1963. **35**(8): p. 943-946.
95. Griffiths, P.R. and J.A. De Haseth, *Fourier Transform Infrared Spectrometry*. 2nd ed. 2007, Canada: John Wiley & Sons Inc.
96. Bernath, P.F., *Spectra of Atoms and Molecules*. 2nd ed. 2005, New York, NY, USA: Oxford University Press.
97. Fleischmann, M., P.J. Hendra, and A.J. McQuillan, *Raman Spectra of Pyridine Adsorbed at a Silver Electrode.* Chemical Physics Letters, 1974. **26**(2): p. 163-166.
98. Le Ru, E.C., et al., *Surface Enhanced Raman Scattering Enhancement Factors: A Comprehensive Study*. Journal of Physical Chemistry C, 2007. **111**: p. 13794-13803.
99. Feibelman, P., *Simple Microscopic Theory of Surface Plasmons.* Physical Review, 1968. **176**(2): p. 551-555.
100. Zaidi, A.A., et al., *Time of flight mass spectrometry of polyyne formation in the irradiation of liquid alkanes with femtosecond laser pulses.* Carbon, 2010. **48**(9): p. 2517-2520.
101. Wesolowski, M.J., et al., *Polyyne synthesis and amorphous carbon nano-particle formation by femtosecond irradiation of benzene.* Carbon, 2011. **49**(2): p. 625-630.
102. Smith, H.M. and A.F. Turner, *Vacuum Deposited Thin Films Using a Ruby Laser*. Applied Optics, 1965. **4**(1): p. 147-148.
103. Patil, P., et al., *Pulsed-laser–induced reactive quenching at liquid-solid interface: Aqueous oxidation of iron.* Physical Review Letters, 1987. **58**(3): p. 238-241.
104. Pyatenko, A., et al., *Synthesis of silver nanoparticles by laser ablation in pure water*. Applied Physics A, 2004. **79**(4-6).
105. Ishikawa, Y., et al., *Preparation of zinc oxide nanorods using pulsed laser ablation in water media at high temperature*. J Colloid Interface Sci, 2006. **300**(2): p. 612-5.

106. Zeng, H., et al., *Violet photoluminescence from shell layer of Zn/ZnO core-shell nanoparticles induced by laser ablation.* Applied Physics Letters, 2006. **88**(17): p. 171910.
107. Yang, L., et al., *Growth of diamond nanocrystals by pulsed laser ablation of graphite in liquid.* Diamond and Related Materials, 2007. **16**(4-7): p. 725-729.
108. Wang, Y.-H., et al., *Production of Carbon Nanotubes at Carbon/Water Interface by Pulsed-Laser Ablation.* Acta physico-chimica Sinica, 1996. **10**(905).
109. Ogale, S.B., *Pulsed-Laser-Induced and Ion-Beam-Induced Surface Synthesis and Modification of Oxides, Nitrides and Carbides.* Thin Solid Films, 1988. **163**: p. 215-227.
110. Karimzadeh, R., J.Z. Anvari, and N. Mansour, *Nanosecond pulsed laser ablation of silicon in liquids.* Applied Physics A, 2008. **94**(4): p. 949-955.
111. Lauterborn, W., *High-speed photography of laser-induced breakdown in liquids.* Applied Physics Letters, 1972. **21**(1): p. 27.
112. Rusak, D.A., et al., *Fundamentals and Applications of Laser-Induced Breakdown Spectroscopy.* Critical Reviews in Analytical Chemistry, 1997. **27**(4): p. 257-290.
113. Gruber, J., et al., *Rapid in-situ analysis of liquid steel by laser-induced breakdown spectroscopy.* Spectrochimica Acta Part B, 2001. **56**: p. 685-693.
114. Cravetchi, I.V., et al., *Scanning microanalysis of Al alloys by laser-induced breakdown spectroscopy.* Spectrochimica Acta Part B: Atomic Spectroscopy, 2004. **59**(9): p. 1439-1450.
115. Hu, A., et al., *Direct synthesis of polyyne molecules in acetone by dissociation using femtosecond laser irradiation.* Carbon, 2008. **46**(13): p. 1823-1825.
116. Sato, Y., et al., *Synthesis of polyyne molecules from hexane by irradiation of intense femtosecond laser pulses.* Carbon, 2010. **48**: p. 1670-1697.
117. Castillejo, M., et al., *Ionization and fragmentation of aromatic and single-bonded hydrocarbons with 50 fs laser pulses at 800 nm.* Chemical Physics Letters, 1999. **308**: p. 373-380.
118. Shimizu, S., et al., *Coulomb explosion of benzene irradiated by an intense femtosecond laser pulse.* Chemical Physics Letters, 2000. **317**: p. 609-614.
119. Talebpour, A., A.D. Bandrauk, and S.L. Chin, *Fragmentation of Benzene in an Intense Ti : Sapphire Laser Pulse.* Laser Physics, 2000. **10**(1): p. 210-215.
120. Nakamura, T., Y. Mochidzuki, and S. Sato, *Synthesis of monodispersed DLC nanoparticles in intense optical field by femtosecond laser ablation of liquid benzene.* Conference on Lasers

and Electro Optics/Quantum Electronics and Laser Science Conference and Photonic Applications Systems Technologies, 2007: p. JThD89.

121. Wong, S.S., et al., *Single-walled carbon nanotube probes for high-resolution nanostructure imaging.* Applied Physics Letters, 1998. **73**(23): p. 3465-3467.

122. Jasti, R., et al., *Synthesis, Characterization, and Theory of [9]-, [12]-, and [18 Cycloparaphenylene: Carbon Nanohoop Structures.* Journal of the American Chemical Society, 2008. **130**: p. 17646-17647.

123. Diederich, F., et al., *All-Carbon Molecules: Evidence for the Generation of Cyclo[18]carbon from a Stable Organic Precursor.* Science, 1989. **245**(4922): p. 1088-1090.

124. Baker, C. and D.W. Turner, *High Resolution Molecular Photoelectron Spectroscopy. III Acetylenes and Aza-Acetylenes.* Proceedings of the Royal Society of London. Series A, Mathematical and Physical Sciences, 1968. **308**(1492): p. 19-37.

125. Pfeiffer, R., et al., *Evidence for trans-polyacetylene in nano-crystalline diamond films.* Diamond and Related Materials, 2003. **12**(3-7): p. 268-271.

126. Tabata, H., et al., *Raman and surface-enhanced Raman scattering of a series of size-separated polyynes.* Carbon, 2006. **44**(15): p. 3168-3176.

127. Cataldo, F., *From dicopper acetylide to carbyne.* Polymer International, 1999. **48**: p. 15-22.

128. Wood, T.H., *Enhanced Raman Scattering from Adsorbates on Metal Films in Ultra-High Vacuum.* Surface Science, 1981. **107**: p. 625-635.

129. Hutter, J., H.P. Lüthi, and F. Diederich, *Structures and Vibrational Frequencies of the Carbon Molecules C2-C 18 Calculated by Density Functional Theory.* Journal of the American Chemical Society, 1994. **116**(750-756).

130. Ott, A.K., et al., *Raman spectra and calculated vibrational frequencies of size selected C16, C18, and C20 clusters.* Journal of Chemical Physics, 1998. **109**(22): p. 9652-9655.

131. Hu, A., et al., *Direct synthesis of sp-bonded carbon chains on graphite surface by femtosecond laser irradiation.* Applied Physics Letters, 2007. **91**(13): p. 131906.

132. Nibbering, E.T.J., et al., *Measurement of the nonlinear refractive index of transparent materials by spectral analysis after nonlinear propagation.* Optics Communications, 1995. **119**: p. 497-484.

133. Couris, S., et al., *An experimental investigation of the nonlinear refractive index (n2) of carbon disulfide and toluene by spectral shearing interferometry and z-scan techniques.* Chemical Physics Letters, 2003. **369**(3-4): p. 318-324.

134. Tasumi, M., T. Urano, and M. Nakata, *Some Thoughts on the Vibrational Modes of Toluene as a Typical Monosubstituted Benzene.* Journal of Molecular Structure, 1986. **146**: p. 383-396.

135. Keshtov, M.L., et al., *New phenylated polyphenylenes carrying main-chain bipyridyl groups and their complexes with metal ions.* Polymer Science Series C, 2009. **51**(1): p. 17-25.

136. Lucotti, A., et al., *Raman and SERS investigation of isolated sp carbon chains.* Chemical Physics Letters, 2006. **417**(1-3): p. 78-82.

137. Cataldo, F., *The role of Raman spectroscopy in the research on sp-hybridized carbon chains: carbynoid structures polyynes and metal polyynides.* Journal of Raman Spectroscopy, 2008. **39**(2): p. 169-176.

138. Tabata, H., M. Fujii, and S. Hayashi, *Surface-enhanced Raman scattering from polyyne solutions.* Chemical Physics Letters, 2006. **420**(1-3): p. 166-170.

139. Pavia, D.L., et al., *Introduction to Spectroscopy*. 4th ed. 2009, Belmont CA, USA: Brooks/Cole Cengae Learning.

140. Luo, Y., et al., *Molecular length dependence of optical properties of hydrocarbon oligomers.* Chemical Physics Letters, 1998. **285**: p. 160-163.

141. Eisler, S., et al., *Polyynes as a Model for Carbyne: Synthesis, Physical Properties, and Nonlinear Optical Response.* Journal of the American Chemical Society, 2005. **127**(2666-2676).

142. Chalifoux, W.A., M.J. Ferguson, and R.R. Tykwinski, *Tris(biphenyl-4-yl)silyl-Endcapped Polyynes.* European Journal of Organic Chemistry, 2007. **2007**(6): p. 1001-1006.

143. Kim, S., *Synthesis and structural analysis of one-dimensional sp-hybridized carbon chain molecules.* Angew Chem Int Ed Engl, 2009. **48**(42): p. 7740-3.

144. Müller, A.M., et al., *Photoionization and photofragmentation of gaseous toluene using 80-fs, 800-nm laser pulses.* Journal of Chemical Physics, 2000. **112**(21): p. 9289-9300.

145. Ci, L., et al., *Preparation of carbon nanofibers by the floating atalyst method.* Carbon, 2000. **38**: p. 1933-1937.

146. Rao, C.N.R. and R. Sen, *Large aligned-nanotube bundles from ferrocene pyrolysis.* Chemical Communications, 1998(15): p. 1525-1526.

147. Bai, S., et al., *Influence of ferrocene/benzene mole ratio on the synthesis of carbon nanostructures.* Chemical Physics Letters, 2003. **376**(1-2): p. 83-89.

148. Lu, Y., Z. Zhu, and Z. Liu, *Carbon-encapsulated Fe nanoparticles from detonation-induced pyrolysis of ferrocene.* Carbon, 2005. **43**(2): p. 369-374.

149. Huo, J., H. Song, and X. Chen, *Preparation of carbon-encapsulated iron nanoparticles by co-carbonization of aromatic heavy oil and ferrocene.* Carbon, 2004. **42**(15): p. 3177-3182.

150. Campos-Delgado, J., et al., *Bulk Production of a New Form of sp2 Carbon: Crystalline Graphene Nanoribbons.* Nano Letters, 2008. **8**(9): p. 2773-2778.

151. Deegan, R.D., et al., *Contact line deposits in an evaporating drop.* Physical Review E, 2000. **62**(1): p. 756-765.

152. Cleveland, J.P., et al., *Energy dissipation in tapping-mode atomic force microscopy.* Applied Physics Letters, 1998. **72**(20): p. 2613-2615.

153. Ahlskog, M., et al., *Ring formations from catalytically synthesized carbon nanotubes.* Chemical Physics Letters, 1999. **300**: p. 202-206.

154. Martel, R., H.R. She, and P. Avouris, *Ring Formation in Single-Wall Carbon Nanotubes.* Journal of Physical Chemistry B, 1999. **103**(36): p. 7551-7556.

155. Hu, J., et al., *Growth and Field-Emission Properties of Crystalline, Thin Walled Carbon Microtubes.* Advanced Materials, 2004. **16**(2): p. 153-156.

156. Colfen, H. and S. Mann, *Higher-order organization by mesoscale self-assembly and transformation of hybrid nanostructures.* Angew Chem Int Ed Engl, 2003. **42**(21): p. 2350-65.

157. Bodenheimer, J., E. Loewenthal, and W. Low, *The Raman Spectra of Ferrocene.* Chemical Physics Letters, 1969. **3**(9).

158. Tuinstra, F. and J.L. Koenig, *Raman Spectrum of Graphite.* Journal of Chemical Physics, 1970. **53**(3): p. 1126-1130.

159. Matthews, M.J., et al., *Origin of dispersive effects of the Raman D band in carbon materials.* Physical Review B, 1999. **59**(10): p. R6585-R6588.

160. Pauson, P.I. and G. Wilkinson, *Bis-indenyl Derivatives of Iron and Cobalt.* Journal of the American Chemical Society, 1954. **76**(2024-2026).

161. Okada, Y., et al., *Studies on ferrocene derivatives. Part XIII. Ligand exchange reactions of benzoferrocenes.* Transition Metal Chemistry, 1999. **24**: p. 258-262.

162. Chamritski, I. and G. Burns, *Infrared- and Raman-Active Phonons of Magnetite, Maghemite, and Hematite: A Computer Simulation and Spectroscopic Study*. Journal of Physical Chemistry B, 2005. **109**(4965-4968).

163. Lee, C.T., M.S. Odziemkowski, and D.W. Shoesmith, *An In Situ Raman-Electrochemical Investigation of Carbon Steel Corrosion in Na[sub 2]CO[sub 3]/NaHCO[sub 3], Na[sub 2]SO[sub 4], and NaCl Solutions.* Journal of The Electrochemical Society, 2006. **153**(2): p. B33.

164. Heise, H.M., et al., *Characterisation of carbonaceous materials using Raman spectroscopy: a comparison of carbon nanotube filters, single- and multi-walled nanotubes, graphitised porous carbon and graphite.* Journal of Raman Spectroscopy, 2009. **40**(3): p. 344-353.

165. Butler, I.S., P.D. Harvey, and C. Allen, *Characterization of Some Derivatives of Ferrocene and (N6-Benzene)tricarbonyIchromium(O) by Micro-Raman Spectroscopy*. Journal of Raman Spectroscopy, 1987. **18**: p. 1-7.

166. Fickert, C., et al., *Vibrational analysis and resonance Raman spectra of polycrystalline and matrix-isolated [CpFe(CO) 2] 2*. Inorganic Chimica Acta, 1996. **251**: p. 157-166.

167. Safa, M., et al., *Examining the structural changes in Fe2(CO)9under high external pressures by Raman spectroscopy*. Canadian Journal of Chemistry, 2007. **85**(10): p. 866-872.

168. Dumitrache, F., et al., *Nearly monodispersed carbon coated iron nanoparticles for the catalytic growth of nanotubes/nanofibres.* Diamond and Related Materials, 2004. **13**(2): p. 362-370.

169. Grazulis, S., et al., *Crystallography Open Database – an open-access collection of crystal structures.* Journal of Applied Crystallography, 2009. **42**: p. 726-729.

170. Giambattista, A., B. McCarthy Richardson, and R.C. Richardson, *College Physics*. 2004, New Yor, NY, USA: McGraw-Hill.

171. Sajitha, E.P., et al., *Synthesis and characteristics of iron nanoparticles in a carbon matrix along with the catalytic graphitization of amorphous carbon.* Carbon, 2004. **42**(14): p. 2815-2820.

172. Oprea, C., V. Ciupina, and G. Prodan, *Investigation of Nanocrystals Using TEM micrographs and Electron Diffraction Technique.* Romanian Journal of Physics, 2008. **53**(1-2): p. 223-230.

173. Cabanillas, E.D., et al., *Formation of carbides by electro-discharge machining of alpha iron.* Materials Science and Engineering A, 2000. **276**: p. 133-140.

174. Pauling, L., *Metal-metal bond lengths in complexes of transition metals.* Proceedings of the National Academy of Sciences USA, 1976. **73**(12): p. 4290-4293.

175. Nikitenko, S.I., et al., *Synthesis of Highly Magnetic, Air Stable, Iron-Iron Carbide Nanocrystalline Particles by Using Power Ultrasound.* Angewandte Chemie, 2001. **113**(23): p. 4579-4581.

176. Narkiewicz, U., et al., *XRD, TEM and magnetic resonance studies of iron carbide nanoparticle agglomerates in a carbon matrix.* Carbon, 2004. **42**(5-6): p. 1127-1132.

177. Chen, P., Q.S. Wu, and Y.P. Ding, *Preparation of ferrocene nanocrystals by the ultrasonic-solvent-substitution method and their electrochemical properties.* Small, 2007. **3**(4): p. 644-9.

178. Xu, L., et al., *Formation, Characterization, and Magnetic Properties of Fe3O4 Nanowires Encapsulated in Carbon Microtubes.* Journal of physical Chemistry B, 2004. **108**: p. 10859-10862.

179. Mericam-Bourdet, N., et al., *Experimental investigations of plasma bullets.* Journal of Physics D: Applied Physics, 2009. **42**(5): p. 055207.

180. Raga, A.C., et al., *The Three-Dimensional Structure of a Radiative, Cosmic Bullet Flow.* The Astrophysical Journal, 2007. **668**: p. 310-315.

181. Wu, C.S., C.B. Jia, and M.A. Chen, *A Control System for Keyhole Plasma Arc Welding of Stainless Steel Plates with Medium Thickness.* Welding Journal, 2010. **89**(225s-231s).

182. Hernadi, K., et al., *Fe-Catalyzed Carbon Nanotube Formation.* Carbon, 1996. **34**(10): p. 1249-1257.

183. Nasibulin, A.G., et al., *Correlation between catalyst particle and single-walled carbon nanotube diameters.* Carbon, 2005. **43**(11): p. 2251-2257.

184. Nasibulin, A.G., et al., *A novel hybrid carbon material.* Nat Nanotechnol, 2007. **2**(3): p. 156-61.

185. Kalia, R., et al., *Study of Dielectric Behavior of Nanoporous Polycarbonate Membrane for Future Nano-Electret Applications.* Digest Journal of Nanomaterials and Biostructures, 2008. **3**(4).

186. Wei, J., et al., *Magnetic and electromagnetic properties of ferrocenyl organic metal magnetic resin.* Materials Letters, 2012. **67**(1): p. 135-138.

187. Lee, J., J. Kim, and T. Hyeon, *Recent Progress in the Synthesis of Porous Carbon Materials.* Advanced Materials, 2006. **18**(16): p. 2073-2094.

188. Liang, C., et al., *Synthesis of a large-scale highly ordered porous carbon film by self-assembly of block copolymers.* Angew Chem Int Ed Engl, 2004. **43**(43): p. 5785-9.

189. Li, Z., et al., *Synthesis of Ultrathin Ordered Porous Carbon through Bergman Cyclization of Enediyne Self-Assembled Monolayers on Silica Nanoparticles.* The Journal of Physical Chemistry C, 2011. **115**(32): p. 15829-15833.

190. Olivares, R., S.E. Rodil, and H. Arzate, *Osteoinduction properties of graphite-like amorphous carbon films evaluated in-vitro.* Diamond and Related Materials, 2007. **16**(10): p. 1858-1867.

191. Abramoff, M.D., P.J. Magalhaes, and S.J. Ram, *Image Processing with ImageJ.* Biophotonics International, 2004. **11**(7): p. 36-42.

192. Schwan, J., et al., *Raman spectroscopy on amorphous carbon films.* Journal of Applied Physics, 1996. **80**(1): p. 440.

193. Nemanich, R. and S. Solin, *First- and second-order Raman scattering from finite-size crystals of graphite.* Physical Review B, 1979. **20**(2): p. 392-401.

194. Marchon, B., et al., *Photoluminescence and Raman Spectroscopy in Hydrogenated Carbon Films.* IEEE Transactions on Magnetics, 1997. **33**(5): p. 3148-3150.

195. Vick, D., et al., *Production of porous carbon thin films by pulsed laser deposition.* Thin Solid Films, 1999. **350**: p. 49-52.

196. Krivchenko, V.A., et al., *Nanocrystalline graphite: Promising material for high current field emission cathodes.* Journal of Applied Physics, 2010. **107**(1): p. 014315.

197. Sotiropoulou, S., et al., *Novel carbon materials in biosensor systems.* Biosensors and Electronics, 2003. **18**: p. 211-215.

198. Su, F., et al., *Synthesis of Graphitic Ordered Macroporous Carbon with a Three Dimensional Interconnected Pore Structure for Electrochemical Applications.* Journal of Physical Chemistry B, 2005. **109**: p. 20200-20206.

199. Duley, W.W., *Refractive Indices for Amorphous Carbon.* The Astrophysical Journal, 1984. **287**: p. 694-696.

200. Marquardt, C.L., R.T. Williams, and D.J. Nagel, *Deposition of Amorphous Carbon Films from Laser-Produced Plasmas.* Materials Research Society Symposium Proceedings, 1984. **38**: p. 325.

201. Sato, T., et al., *Diamond-Like Carbon Films Prepared by Pulsed-Laser Evaporation.* Applied Physics A, 1988. **45**: p. 355-360.

202. Hu, A., et al., *Femtosecond pulsed laser deposition and optical properties of diamond-like amorphous carbon films embedded with sp-bonded carbon chains.* Diamond and Related Materials, 2008. **17**(7-10): p. 1643-1646.
203. Wesolowski, M.J., et al., *Synthesis of Polymer-like Hydrogenated Amorphous Carbon by fs-pulsed Laser Induced Plasma Processing of Solid Hexane.* Plasma Processes and Polymers, 2012.
204. Davanloo, F., et al., *Amorphic diamond films produced by a laser plasma source.* Journal of Applied Physics, 1990. **67**(4): p. 2081.
205. Voevodin, A.A., et al., *Pulsed laser deposition of diamond-like amorphous carbon films from graphite and polycarbonate targets.* Journal of Applied Physics, 1995. **78**(6): p. 4123.
206. Murray, P.T. and D.T. Peeler, *Pulsed Laser Deposition of Carbon Films: Dependence of Film Properties on Laser Wavelength.* Journal of Electronic Materials, 1994. **23**(9): p. 855-859.
207. Hu, A., et al., *Spectroscopic characterization of carbon chains in nanostructured tetrahedral carbon films synthesized by femtosecond pulsed laser deposition.* Journal of Chemical Physics, 2007. **126**(15): p. 154705.
208. Qian, F., et al., *Laser deposition of diamondlike carbon films at high intensities.* Applied Physics Letters, 1995. **67**(21): p. 3120-3122.
209. Katsuno, T., et al., *Optical properties of high-density amorphous carbon films grown by nanosecond and femtosecond pulsed laser ablation.* Applied Physics A, 2005. **81**(3): p. 471-476.
210. Levoska, J. and S. Leppavouri, *Effect of laser power density and deposition temperature on electrical and optical properties of pulsed laser ablated diamond-like carbon films.* Applied Surface Science, 1995. **86**: p. 180-184.
211. Polo, M.C., et al., *Pulsed laser deposition of diamond from graphite targets.* Applied Physics Letters, 1995. **67**(4): p. 485.
212. Malshe, A.P., et al., *Properties of carbon films deposited by pulsed laser vaporization from pyrolytic graphite.* Journal of Materials Research, 1989. **4**(5): p. 1238-1242.
213. Bolgiaghi, D., et al., *Pulsed laser deposition of glass-like cluster assembled carbon films.* Carbon, 2005. **43**(10): p. 2122-2127.
214. Grill, A., *Diamond-like carbon: State of the art.* Diamond and Related Materials, 1999. **8**: p. 428-434.

215. Malshe, A.P., et al., *Pulsed laser deposition of diamondlike hydrogenated amorphous carbon films.* Journal of Applied Physics, 1990. **68**(11): p. 5648.

216. Pappas, D.L., et al., *Pulsed laser deposition of diamond-like carbon films.* Journal of Applied Physics, 1992. **71**(11): p. 5675.

217. Ong, H.C. and R.P.H. Chang, *Effect of laser intensity on the properties of carbon plasmas and deposited film.* Physical Review B, 1997. **55**(19).

218. Budai, J., et al., *Reactive pulsed laser deposition of hydrogenated carbon thin films: The effect of hydrogen pressure.* Journal of Applied Physics, 2006. **100**(4): p. 043501.

219. Hu, A. and W.W. Duley, *Surface enhanced Raman spectroscopic characterization of molecular structures in diamond-like carbon films.* Chemical Physics Letters, 2008. **450**(4-6): p. 375-378.

220. Budai, J., et al., *Preparation of hydrogenated amorphous carbon films from polymers by nano- and femtosecond pulsed laser deposition.* Applied Surface Science, 2007. **253**(19): p. 8235-8241.

221. Hanabusa, M. and K. Tsujihara, *Diamond-like carbon films deposited by laser ablation using frozen acetylene targets.* Journal of Applied Physics, 1995. **78**(6): p. 4267.

222. Okoshi, M., S. Higuchi, and M. Hanabusa, *Femtosecond laser ablation of frozen acetone for deposition of diamond-like carbon film.* Journal of Applied Physics, 1999. **86**(3): p. 1768-1770.

223. Scott, A.D., *Laboratory Formation and Analysis of the Materials Comprising interstellar Dust*, in *Physics and Astronomy*1997, University of Waterloo: Waterloo, Ontario, Canada.

224. Witten, T. and L. Sander, *Diffusion-limited aggregation.* Physical Review B, 1983. **27**(9): p. 5686-5697.

225. Baptista, D.L. and F.C. Zawislak, *Hard and sp2-rich amorphous carbon structure formed by ion beam irradiation of fullerene, a-C and polymeric a-C:H films.* Diamond and Related Materials, 2004. **13**(10): p. 1791-1801.

226. Buijnsters, J.G., et al., *Hydrogen quantification in hydrogenated amorphous carbon films by infrared, Raman, and x-ray absorption near edge spectroscopies.* Journal of Applied Physics, 2009. **105**(9): p. 093510.

227. Golanski, A., et al., *Stress field effects on the microstructure and properties of a-C:H thin films.* Journal of Applied Physics, 2002. **92**(7): p. 3662.

228. Filik, J., et al., *XPS and laser Raman analysis of hydrogenated amorphous carbon films.* Diamond and Related Materials, 2003. **12**(3-7): p. 974-978.
229. Gorelik, V.S., et al., *Raman Spectra of Saturated Hydrocarbons and Gasolines.* Journal of Russian Laser Research, 2000. **21**(4): p. 323-334.
230. Socrates, G., *Infrared and Raman Characteristic Group Frequencies: Tables and Charts.* 2001, Chichester, West Sussex, England: John Wiley & Sons.
231. Cleveland, F.F. and P. Porcelli, *Raman Spectra of Hydrocarbons. V. n-Hexane, n-Heptane, 2-Methylpentane, 3-Methylpentane, 2,4-Dimethylpentane, and 2,3-Dimethylbutane.* The Journal of Chemical Physics, 1950. **18**(11): p. 1459-1461.
232. Ravagnan, L., et al., *Influence of Cumulenic Chains on the Vibrational and Electronic Properties of sp-sp2 Amorphous Carbon.* Physical Review Letters, 2007. **98**(21).
233. Veres, M., M. Koós, and I. Pócsik, *IR study of the formation process of polymeric hydrogenated amorphous carbon film.* Diamond and Related Materials, 2002. **11**: p. 1110-1114.
234. Ristein, J., et al., *A comparative analysis of a-C:H by infrared spectroscopy and mass selected thermal effusion.* Journal of Applied Physics, 1998. **84**(7): p. 3836.
235. Retzko, I., et al., *Chemical analysis of plasma polymerized films: The application of X-ray photoelectron spectroscopy (XPS), X-ray absorption spectroscopy (NEXAFS) and fourier transform infrared.* Journal of Electron Spectroscopy and Related Phenomena, 2001. **121**: p. 111-129.
236. Schiller, S., et al., *Chemical Structure and Properties of Plasma-Polymerized Maleic Anhydride Films.* Chemistry of Materials, 2002. **14**: p. 235-242.
237. Truica-Marasescu, F. and M.R. Wertheimer, *Nitrogen-Rich Plasma-Polymer Films for Biomedical Applications.* Plasma Processes and Polymers, 2008. **5**(1): p. 44-57.
238. Ogino, A. and M. Nagatsu, *Gas barrier properties of hydrogenated amorphous carbon films coated on polymers by surface-wave plasma chemical vapor deposition.* Thin Solid Films, 2007. **515**(7-8): p. 3597-3601.
239. Yun, Y., et al., *Oxidation Kinetics of Hydrogenated Amorphous Carbon (a-CHx) Overcoats for Magnetic Data Storage Media.* Langmuir, 2007. **23**: p. 5485-5490.
240. Möller, W., *Plasma and Surface Modeling of the Deposition of Hydrogenated Carbon Films from Low-Pressure Methane Plasmas.* Applied Physics A, 1993. **56**: p. 527-546.

241. Wu, S.M., et al., *Dynamics of Atomic and Molecular Hydrogen Elimination from Small Alkanes Following 157-nm Excitation.* Journal of Physical Chemistry A, 2000. **104**: p. 7189-7199.

242. Compagnini, G., et al., *Ion produced Hydrogenated Amorphous Carbon by irradiation of frozen benzene.* Radiation Effects and Defects in Solids, 1991. **117**(4): p. 299-305.

243. Strazzulla, G. and G.A. Baratta, *Carbonaceous material by ion irradiation in space.* Astronomy and Astrophysics, 1992. **266**: p. 434-438.

244. Wu, Z., et al., *Growth of n-alkane films on a single-crystal substrate.* Chemical Physics Letters, 2001. **348**: p. 168-174.

245. Mo, H., et al., *A novel growth mode of alkane films on a SiO2 surface.* Chemical Physics Letters, 2003. **377**(1-2): p. 99-105.

246. Knüfing, L., et al., *Fractal Analysis Methods for Solid Alkane Monolayer Domains at SiO2/Air Interfaces.* Langmuir, 2005. **21**: p. 992-1000.

247. Quijada, R., et al., *Copolymerization of ethylene with 1-hexene and 1-octene: correlation between type of catalyst and comonomer incorporated.* Macromolecular Chemistry and Physics, 1995. **195**: p. 3991-4000.

248. Morales, P., et al., *Polyethylene Obtained by Plasma Polymerization of Hexene.* Macromolecular Symposia, 2009. **283-284**(1): p. 13-17.

249. Cleveland, F.F., *Raman Spectra of Hydrocarbons I. 1-Octene, cis+trans 2-Octene, trans−3-Octene, trans−4-Octene, 4-Octyne, and 1-Octyne.* The Journal of Chemical Physics, 1943. **11**(1): p. 1.

250. Sears, W.M., *Raman scattering from polymerizing styrene. I. Vibrational mode analysis.* The Journal of Chemical Physics, 1981. **75**(4): p. 1589.

251. Hudson, R.L. and M.H. Moore, *Radiation chemical alterations in solar system ices: An overview.* Journal of Geophysical Research, 2001. **105**(E12): p. 32275-33284.

252. Gibb, E.L., et al., *An Inventory of Interstellar Ices Toward the Embedded Protostar W33A.* The Astrophysical Journal, 2000. **536**: p. 347-356.

253. Gerakines, P.A., M.H. Moore, and R.L. Hudson, *Energetic processing of laboratory ice analogs:UV photolysis versus ion bombardment.* Journal of Geophysical Research, 2001. **106**(E12): p. 33381-33385.

254. Boduch, P., et al., *Production of Oxidants by Ion Bombardment of Icy Moons in the Outer Solar System.* Advances in Astronomy, 2011. **2011**: p. 1-10.

255. Lancaster, G.M., et al., *Secondary Ion Mass Spectrometry of Molecular Solids. Cluster Formation during Ion Bombardment of Frozen Water, Benzene and Cyclohexane.* Journal of the American Chemical Society, 1979. **101**(8): p. 1951-1958.
256. Szakal, C., J. Kozole, and N. Winograd, *Fundamental studies of the cluster ion bombardment of water ice.* Applied Surface Science, 2006. **252**(19): p. 6526-6528.
257. Brenner, D.W. and B.J. Garrison, *Classical dynamics study of the ion bombardment of ice.* Physical Review B, 1986. **34**(8): p. 5782-5787.
258. Paillard, V., *On the origin of the 1100cm-1 Raman band in amorphous and nanocrystalline sp3 carbon.* European Phsyics Letters, 2001. **54**(2): p. 194-198.
259. Skákalová, V., et al., *Intermediate frequency modes in Raman spectra of Ar+-irradiated single-wall carbon nanotubes.* physica status solidi (RRL) – Rapid Research Letters, 2007. **1**(4): p. 138-140.
260. Duley, W.W., *Chemical Evolution of Carbonaceous Material in Interstellar Clouds.* The Astrophysical Journal, 2000. **528**: p. 841-848.
261. Cataldo, F., *From Elemental Carbon to Complex Macromolecular Networks in Space*, in *Astrobiology: Future Perspectives*, P. Ehrenfreund, et al., Editors. 2004, Kluwer Academic Publisher: Dordrecht.
262. Webster, A.S., *Fulleranes, fullerenes and the insterstellar extinction.* Astronomy and Astrophysics, 1992. **257**: p. 750-756.